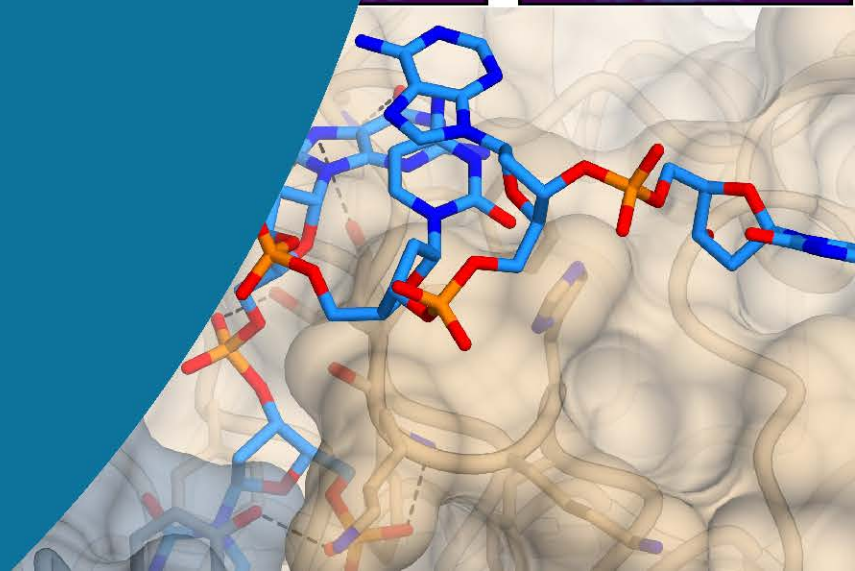
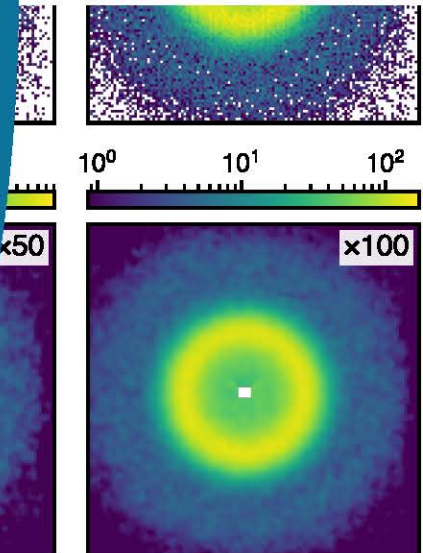
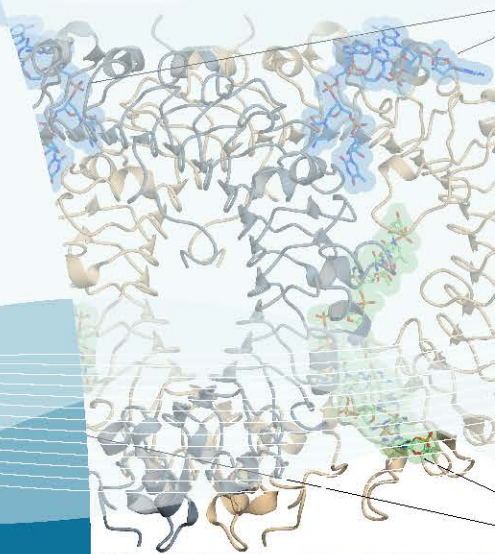
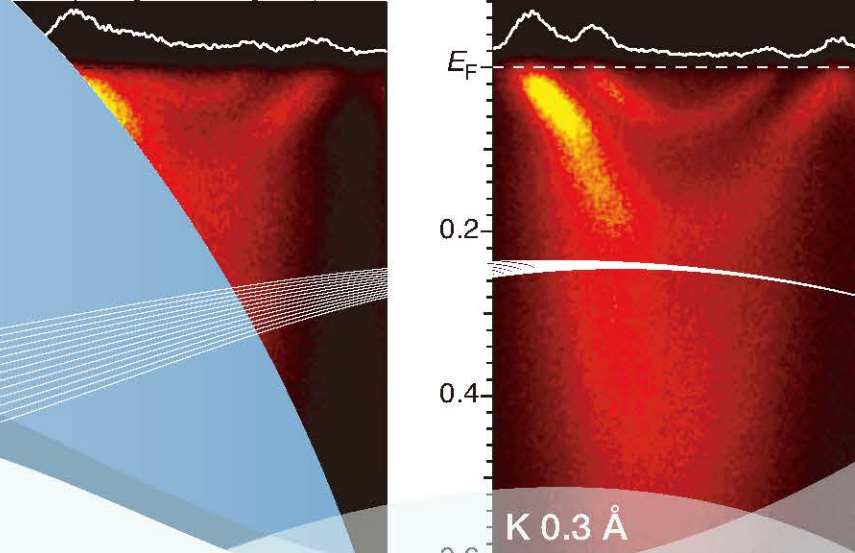


ISSN 2432-4035

Highlights 2018

 Photon Factory



KEK Progress Report 2019-4

© High Energy Accelerator Research Organization (KEK), 2019

KEK progress reports are available from:
High Energy Accelerator Research Organization (KEK)
1-1 Oho, Tsukuba, Ibaraki 305-0801 Japan
Phone: +81-29-864-5137
Fax: +81-29-864-4604
E-mail: irdpub@mail.kek.jp

KEK Top Page URL: <https://www.kek.jp/en/>

Online version of PF Highlights is available at
<https://www2.kek.jp/imss/pf/eng/science/publ/pfhl/>

Photon Factory

Highlights 2018



PREFACE 1

HIGHLIGHTS

1. Materials Science 2

- 1-1 Unexpected Metal–Insulator Transition in $\text{Ca}_{1-x}\text{Sr}_x\text{VO}_3$ Thick Film with Anomalous V Valence State
- 1-2 Single Molecular Bilayers of Organic Semiconductors Realized through Geometrical Frustration
- 1-3 Commensurate vs Incommensurate Charge Ordering near the Superconducting Dome in $\text{Ir}_{1-x}\text{Pt}_x\text{Te}_2$ Revealed by Resonant X-Ray Scattering
- 1-4 A New Structure Family of Oxide-Ion Conductors $\text{Ca}_{0.8}\text{Y}_{2.4}\text{Sn}_{0.8}\text{O}_6$
- 1-5 Magnetic Skyrmion Lattice in Gd_2PdSi_3
- 1-6 Microscopic Origin of the Ferroelectricity in Multiferroics SmMn_2O_5 Studied by Resonant Soft X-Ray Scattering
- 1-7 Helical Ordering of Spin Trimers in $\text{Gd}_3\text{Ru}_4\text{Al}_{12}$ with a Distorted Kagome Lattice
- 1-8 Experimental Evidence of Orbital Ferrimagnetism by X-Ray Magnetic Circular Dichroism
- 1-9 Emergence of Metallic Monoclinic States of Electron-Doped VO_2 Films
- 1-10 Surface Electron Density Analysis of Organic Semiconductors
- 1-11 ARPES Study of the Superconducting Parent Compound Pr_2CuO_4 in Thin Film Form
- 1-12 *In situ* Angle-Resolved Photoelectron Spectroscopy Studies of Two-Dimensional Electronic States at Anatase TiO_2 (001) Surface Controlled by K Adsorption
- 1-13 Anatomy of Interfacial Spin-Orbit Coupling in Co/Pd Multilayers
- 1-14 Detection and Classification of Crystallographic Defects in Wide Bandgap Semiconductor Materials for Next-Generation Power Switching Devices
- 1-15 Discovery of New Chiral Fermions in CoSi
- 1-16 Nanoscale Ice-Type Structural Fluctuation in Spinel Titanates
- 1-17 Coexistence of Magnetism and Superconductivity in EuFe_2As_2 under Pressure

2. Chemical Science 36

- 2-1 Self-Foldable Supramolecular Polymers
- 2-2 An Approach to Produce Uniform Artificial Protein Supramolecules
- 2-3 Photo-Triggered Topology-Reset Execution of Cyclic Polymers for the Tuning of Viscoelasticity
- 2-4 Filamentous Virus-Based Assembly: Relationship between Their Oriented Structures and Thermal Diffusivity
- 2-5 Solid-State Inertial Rotation of a Guest Ball in a Tight Tubular Host
- 2-6 Self-Assembling Supramolecular Nanostructures Constructed from *de Novo* Extender Protein Nanobuilding Blocks

3. Earth Science 48

- 3-1 Multidisciplinary Characterization of Abundant Ferromanganese Microparticles in Deep-Sea Oxidic Sediments: Implications for the Global Manganese Budget
- 3-2 Newly-Developed High-Pressure Small-Angle X-Ray Scattering System at BL-18C Reveals Inhomogeneity in Silica Glass during Structural Transformation

Contents

4. Life Science	52
4-1 Structural Basis for Recognition of Methylated DNA Ligase 1 by UHRF1	
4-2 Structural Analysis Sheds Light on the Heparan Sulfate-Binding Ability of Nonclassical MHC-I Molecule, MILL2	
4-3 Toll-Like Receptor 9 Contains Two DNA Binding Sites that Function Cooperatively to Promote Receptor Dimerization and Activation	
4-4 Crystal Structure of the H3.3 Histone Chaperone Complex Subunit HIRA and its Functional Role	
4-5 Crystal Structure Determination using a Protein Fusion that Forms a Highly Porous Lattice	
4-6 Molecular Basis of Zinc-Dependent Regulation of ERp44 for Protein Quality Control in the Early Secretory Pathway	
5. Instrumentation and Techniques	64
5-1 Shortening Measurement Time without Hardware Investment	
5-2 First Observation of a Low-Energy Positron Diffraction Pattern with a Linac-Based Beam	
5-3 Development of a New Nonevaporable Getter (NEG) Named Oxygen-Free Palladium/Titanium; Surface Analysis by Synchrotron Radiation X-Ray Photoelectron Spectroscopy and Application for NEG Pump	
6. Accelerator	70
6-1 Construction of an Elliptically Polarizing Undulator (U#19) at the Photon Factory	

OPERATION AND PROPOSALS

1. Outline of the Accelerators	72
2. Operation Summary	74
3. Experimental Stations	79
4. Summary of User Proposals	83

APPENDICES

Site and Organization	86
Publication List is available on the PF's website (http://pfwww.kek.jp/acr/2018pdf/pf18pu.pdf).	



PREFACE



It is my great pleasure to share our research highlights based on the Photon Factory (PF) users' program during fiscal 2018 (April 2018 - March 2019). Since the PF users' program started in 1983, more than 17,000 research papers have been published. We are proud to have produced a considerable number of papers describing breakthroughs in broad research areas of materials science, chemical science, earth science, life science, and instrumentation and techniques. I hope that this latest issue of PF Highlights will lead to new discoveries in scientific studies.

The PF ring with the beam energy of 2.5 GeV is the oldest and the PF-AR ring of 6.5 GeV is the third oldest of the nine storage rings in operation in Japan. However, only the PF, PF-AR and SPring-8 storage rings have a beam energy exceeding 2 GeV. The PF has led the way in X-ray science as a key facility in Japan for more than 35 years. X-ray science in the PF is also important in combination with other quantum beams such as neutron, muon, and slow positron beams. These quantum beams have been widely used for academic research via several collaboration programs at the Institute of Materials Structure Science (IMSS), one of the 17 Inter-University Research Institutes.

We have several review committees for our projects in photon science and materials structure science using quantum beams. In March 2019, we held the first meeting of the KEK Scientific Advisory Committee, which reported the following recommendation for the PF:

It is clear that new science at light sources may not always require the brightest and most coherent sources. Rather, as was highlighted in the presentations, there is room for a range of facilities. The PF is well placed to make this evaluation and, based on it, deliver what is needed. It needs to prioritize its areas to develop.

The industry program represents more than an income stream. It is a tool for engaging new users and enhances community outreach. It also highlights to funders a return on investment that is tangible to the community. With this in mind the PF should review its partnership program and extend it to other areas of science. From a purely financial perspective this will offset the reliance on additional income from its crystallography service business.

Multi beamline access at light source facilities is increasing worldwide as a result of demands of multidisciplinary large-scale scientific projects. The PF represents a comparatively large user base within KEK and as such multi beamline access could take on a unique dimension. The KEK quantum beam platform represents an exceptional worldwide opportunity. Synergies between the photon and neutron beam user base might be a good starting point and novice users should be encouraged through a targeted education program and elements of a linked proposal system.

Considering these comments, we started discussing what we and users need from the PF in the short, medium and long term, in leading photon science and in enhancing our quantum beam combination research platform.

Finally, it is with great sadness that we report the passing away of Kazutake Kohra, Professor Emeritus of KEK, on 30 January 2019 at the age of 97. He was the founding director of the PF, which was commissioned in 1982. The realization and success of the PF would have been impossible without his remarkable leadership. We would like to extend our deepest sympathies to his family.

Nobuhiro Kosugi
Director of IMSS

A handwritten signature in black ink, appearing to read 'Nobuhiro Kosugi', written in a cursive style.

Unexpected Metal–Insulator Transition in $\text{Ca}_{1-x}\text{Sr}_x\text{VO}_3$ Thick Film with Anomalous V Valence State

$\text{Ca}_{1-x}\text{Sr}_x\text{VO}_3$ thick films were fabricated on (100)-oriented SrTiO_3 substrates. In contradistinction to previous reports in which only extremely thin film (several nm thick) exhibited metal–insulator transition (MIT), MIT was observed for films with a thickness of 50 nm. To investigate the origin of the MIT, the electronic structure was examined using X-ray photoemission spectroscopy. An anomalous V valence state was observed in $V 2p_{3/2}$ spectra, which comprised four components (V^{5+} , V^{4+} , V^{3+} , and $V^{2+/1+}$). This chemical disorder may be caused by strain from the substrate. The observed MIT can be explained by an increment in electron–electron interactions due to this chemical disorder.

SrVO_3 and the derivative Ca-doped SrVO_3 ($\text{Ca}_{1-x}\text{Sr}_x\text{VO}_3$), which is a $3d^1$ perovskite, are typical bandwidth-controlled metal–insulator transition (MIT) materials, which are attracting attention for application to next-generation nanoelectronics due to their MIT [1–3]. However, MIT has only been achieved for ultrathin films (several nm thick) [1], which are not well suited for practical applications. MIT in an $\text{SrTi}_{1-x}\text{V}_x\text{O}_3$ thick film (16 nm) was reported recently [4]. Possible reasons for the emergence of MIT in the thick film were conjectured to be electron–electron interactions and disorder-induced localization. Thus, MIT in $\text{Ca}_{1-x}\text{Sr}_x\text{VO}_3$ thick film is expected if electron–electron interactions and/or the localization effect can be tuned in some manner.

The normalized electrical resistivity of $\text{Ca}_{1-x}\text{Sr}_x\text{VO}_3$ thick films measured by a four-probe method is shown in **Figs. 1(a)** and **1(b)**. Over the entire range, the resistivity of the films with $x = 0, 0.1$, and 1 can be expressed by a Fermi liquid model, i.e., $\rho = \rho_0 + AT^2$, where ρ_0 is a residual resistivity and A is the temperature coefficient of resistivity quantifying the electron–electron interactions in the strongly correlated Fermi liquid model. In contrast, films with $x = 0.2$ and 0.5 demonstrated resis-

tivity upturns at transition temperatures (T_{MIT}) of 72 and 113 K, respectively (indicated by the arrow). As the temperature was lowered from T_{MIT} , resistivity of these thin films exhibited semiconducting behavior. In a previous report, MIT in an SVO ultrathin film was attributed to dimensional crossover from a three-dimensional metal to a two-dimensional insulator [1]. However, in this study, the effect of dimensional crossover is not appropriate because the film thickness was 50 nm (not an ultrathin film). To determine the reason for the appearance of MIT, the electronic structure of $\text{Ca}_{1-x}\text{Sr}_x\text{VO}_3$ thick films was investigated using hard and soft X-ray photoemission spectroscopy (HX-PES; SX-PES) [5].

All HX-PES and SX-PES measurements were conducted at room temperature. The photon energy was 5953.4 eV for the HX-PES and 1486.6 eV for the SX-PES measurements. The surface sensitive SX-PES spectra of the $V 2p_{3/2}$ core level for the $\text{Ca}_{1-x}\text{Sr}_x\text{VO}_3$ thick films are shown in **Fig. 2(a)**. The spectra were analyzed by deconvolving them into three components, i.e., V^{5+} (517.3 eV), V^{4+} (516.3 eV), and V^{3+} (514.3 eV). The intensity ratio between V^{5+} and V^{3+} was approximately 1:1 in the whole composition, which is attributed to

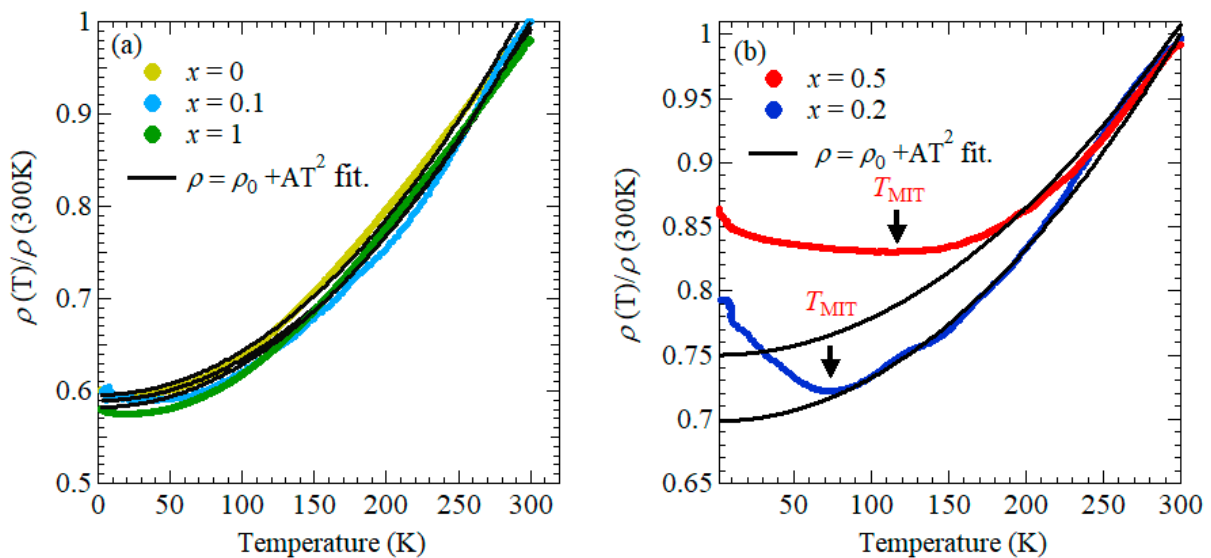


Figure 1: Temperature dependent normalized electrical resistivity for (a) $x = 1, 0.1$, and 0 and (b) $x = 0.5$ and 0.2. $\rho = \rho_0 + AT^2$ fits are also shown.

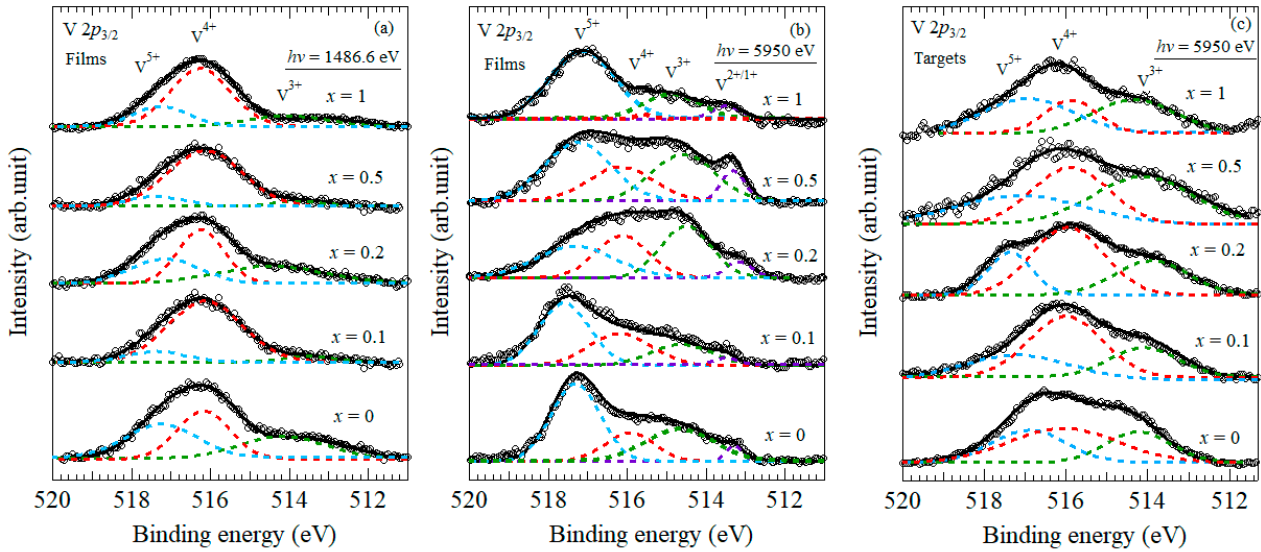


Figure 2: (a) SX-PES spectra of the V $2p_{3/2}$ core level of $\text{Ca}_{1-x}\text{Sr}_x\text{VO}_3$ thick films. HX-PES spectra of the V $2p_{3/2}$ of $\text{Ca}_{1-x}\text{Sr}_x\text{VO}_3$ (b) thick films and (c) targets are shown. Blue, red, green and purple lines indicate V^{5+} , V^{4+} , V^{3+} , and $\text{V}^{2+/1+}$ components, respectively. Black line indicates the sum of all contributing peaks (e.g., V^{n+} peaks).

phase separation of V^{4+} to V^{3+} and V^{5+} ($2\text{V}^{4+} \rightarrow \text{V}^{3+} + \text{V}^{5+}$) due to the strong correlation effects. These SX-PES results agree with the $\text{Ca}_{1-x}\text{Sr}_x\text{VO}_3$ bulk results obtained by Maiti *et al.* [6]. The bulk sensitive HX-PES results are shown in Fig. 2(b). The results differ drastically from those of SX-PES. The V $2p_{3/2}$ spectra comprise four components, i.e., V^{5+} (517.4 eV), V^{4+} (516 eV), V^{3+} (514.6 eV), and $\text{V}^{2+/1+}$ (513.2 eV). The intensity of V^{5+} was the strongest, and this behavior cannot be explained by dismutation of V^{4+} due to the strong correlation. The $\text{Ca}_{1-x}\text{Sr}_x\text{VO}_3$ targets were also investigated by HX-PES, as shown in Fig. 2(c). The V $2p_{3/2}$ spectra comprise V^{5+} , V^{4+} , and V^{3+} , which agree with the bulk results of Maiti *et al.* (including the intensity ratio between V^{5+} and V^{3+}) [6]. Thus, the extra component of $\text{V}^{2+/1+}$ is induced by being thinned. In this study, we focused on strain from the substrate due to lattice mismatch as a probable cause for that component. Generally, strain from the substrate reduces as film thickness increases, and the surface state then resembles the bulk free from strain. An inelastic mean free path calculated using the Tanuma-Powell-Penn equation [7, 8] is ~ 10 nm and ~ 3 nm for HX-PES and SX-PES measurements, respectively. Therefore, the HX-PES results reflect more bulk components with a relatively large strain effect, which can induce the anomalous V valence state. In strongly correlated systems, chemical disorder effects (e.g., $\text{V}^{2+/1+}/\text{V}^{3+}/\text{V}^{4+}/\text{V}^{5+}$) can drive MIT [9]. We have also confirmed that the electron localization effect was not a dominant reason for MIT based on the magnetoresistance behavior as a function of temperature [5]. Thus, we concluded that the dominant reason for MIT in the present case is likely an increment of electron–elec-

tron interactions resulting from the chemical disorder. In future studies, we will investigate how the thick film becomes distorted utilizing *in situ* observation methods including XRD, neutron diffraction, and Raman spectroscopy.

REFERENCES

- [1] K. Yoshimatsu, T. Okabe, H. Kumigashira, S. Okamoto, S. Aizaki, A. Fujimori and M. Oshima, *Phys. Rev. Lett.* **104**, 147601 (2010).
- [2] M. Takayanagi, T. Tsuchiya, W. Namiki, T. Higuchi and K. Terabe, *J. Phys. Soc. Jpn.* **87**, 034802 (2018).
- [3] M. Takayanagi, T. Tsuchiya, W. Namiki, Y. Kitagawa, D. Etoh, D. Nishioka, T. Yamada, T. Higuchi and K. Terabe, *Trans. Mater. Res. Soc. Jpn.* **44**, 57 (2019).
- [4] M. Gu, S. A. Wolf and J. Lu, *Appl. Phys. Lett.* **103**, 223110 (2013).
- [5] M. Takayanagi, T. Tsuchiya, W. Namiki, S. Ueda, M. Minohara, K. Horiba, H. Kumigashira, K. Terabe and T. Higuchi, *Appl. Phys. Lett.* **112**, 133106 (2018).
- [6] K. Maiti, D. D. Sarma, M. J. Rozenberg, I. H. Inoue, H. Makino, O. Goto, M. Pedio and R. Cimino, *Europhys. Lett.* **55**, 246 (2001).
- [7] S. Tanuma, C. J. Powell and D. R. Penn, *Surf. Interface Anal.* **11**, 577 (1988).
- [8] S. Tanuma, C. J. Powell and D. R. Penn, *Surf. Interface Anal.* **35**, 268 (2003).
- [9] M. Gu, J. Laverock, B. Chen, K. E. Smith, S. A. Wolf and J. Lu, *J. Appl. Phys.* **113**, 133704 (2013).

BEAMLIN

BL-2A

M. Takayanagi^{1,2}, T. Tsuchiya², W. Namiki^{1,2}, S. Ueda^{2,3}, M. Minohara⁴, K. Horiba⁴, H. Kumigashira⁴, K. Terabe² and T. Higuchi¹ (¹Tokyo Univ. of Sci., ²NIMS, ³Spring-8, ⁴KEK-IMSS-PF)

Single Molecular Bilayers of Organic Semiconductors Realized through Geometrical Frustration

We have developed a solution-based technology to form ultrathin organic-semiconductor layers with single-molecular-bilayer thickness. We used geometrical frustration to suppress multilayer crystallization, while maintaining intralayer molecular ordering, using an extended π -conjugated framework asymmetrically substituted by an alkyl chain (Ph-BTBT- C_n). Blade-coating with a solution containing two Ph-BTBT- C_n s with different alkyl-chain lengths yielded single-molecular bilayers (SMBs). Synchrotron X-ray diffraction and reflectivity measurements revealed that chain-length disorder did not perturb in-plane crystalline order, but effectively suppressed multilayer crystallization. The uniformity and size of fabricated SMBs were unprecedented compared to other self-assembly processes. This finding should pave the way for SMB-based super-flexible electronics.

Single-molecular bilayers (SMBs) are the basic components of cell membranes of living organisms and have been studied as they are fundamental for molecular nanostructures composed of biological lipids or synthetic amphiphiles. The uniqueness of SMBs is their nanometer-scale controlled thickness, which is well defined by the double length of constituent molecules. However, artificial SMBs produced thus far are unavoidably unstable and fragile under atmospheric conditions [1, 2], limiting their use in next-generation nanotechnology applications such as printed electronics [3]. Their features are closely associated with the fairly weak intermolecular interactions between constituent molecules.

We demonstrate an alternative approach to producing air-stable SMBs using molecules with an extended π -electron skeleton (π -Core). Recently, rod-shaped molecules composed of asymmetrically alkylated π -Cores were developed as high-performance organic semiconductors. These molecules have high-layered crystallinity associated with bilayer herringbone-type molecular packing, as exemplified by 2-phenyl-7-alkylated-[1]benzothieno[3,2-b][1]benzothiophene (Ph-BTBT- C_n [4, 5]) [see Fig. 1(a)]. The crystal structures of these molecules are characterized by molecular bilayers comprising antiparallely aligned polar monomolecular layers, resulting in head-to-head contact of π -Cores. The magnitude of intrabilayer interactions is much stronger than that of interbilayer interactions. The resulting high-layered crystallinity enables efficient two-dimensional carrier transport and the formation of smooth channel/gate-insulator interfaces, leading to the eventual realization of high-performance organic thin-film transistors (TFTs) [6]. To weaken interbilayer interactions, we introduced geometrical frustration to suppress multiple stacking of molecular bilayer units by taking advantage of the controllable nature of substituent alkyl-chain lengths while maintaining the strong intrabilayer interactions. Accordingly, two types of molecules with different alkyl-chain lengths (i.e. Ph-BTBT- C_6 and Ph-BTBT- C_{10})

were dissolved in chlorobenzene at various ratios while maintaining a constant concentration. We set the volume fraction of solutions with longer alkyl chain to 0.1. Note that the π -Cores of these molecules are identical, in contrast to the substituted alkyl chains shown in Fig. 1(a). Thus, the introduction of fewer longer alkyl-chain molecules results in a protuberance that geometrically frustrates the stacking of molecular bilayers, whereas the intralayer packing motif is unaffected by the residual part of longer alkyl chains, as schematically shown in Fig. 1(b). The mixed solutions were blade-coated on a Si-wafer covered with a 100-nm thermally grown silica layer. This methodology enabled the fabrication of a mono-colored ultrathin film of constant thickness with no obvious cracks over nearly the entire wafer area, as presented in Fig. 1(c). Note that the film thickness measured by atomic force microscope corresponds to the c-axis lattice constant (or bilayer thickness) of Ph-BTBT- C_6 .

Through synchrotron X-ray diffraction (XRD) and reflectivity measurements, we demonstrated that the obtained mono-colored films are composed of highly uniform and self-organized SMBs, as shown in Fig. 2. Figure 2(a) shows thin-film XRDs associated with the in-plane crystalline order. A single peak was clearly observed at scattering vector $q = 1.61 \text{ \AA}^{-1}$, which can be attributed to the (020) Bragg reflection of Ph-BTBT- C_6 . Evidence of a Bragg rod is also observed in the image shown in the upper panel of Fig. 2(a). Figure 2(b) presents the X-ray reflectivity (XRR) spectrum of the obtained film, which was simulated based on the assumed structure of SMBs, as schematically shown in Fig. 1(c) (i.e., the SMB is composed of antiparallely aligned polar monomolecular layers with head-to-head contact of π -Cores). Notably, the head-to-head molecular alignment in the SMB is consistent with our hypothesis that the introduction of chain-length disorder prevents multiple stacking of molecular bilayer units through geometrical frustration while minimizing the influence on intrabilayer crystallization.

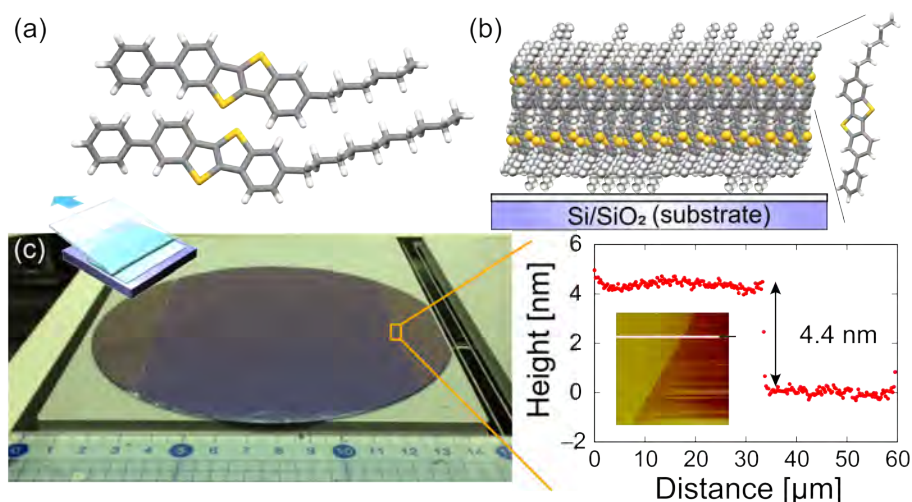


Figure 1: Production of a single-molecular bilayer. (a) Chemical structure of Ph-BTBT- C_n . (b) Schematic representation of geometrical frustration produced by alkyl-chain-length disorder. (c) (left) Photograph of a wafer-scale SMB produced using a mixed solution of Ph-BTBT- C_6 and Ph-BTBT- C_{10} . (right) Height profile of the SMB.

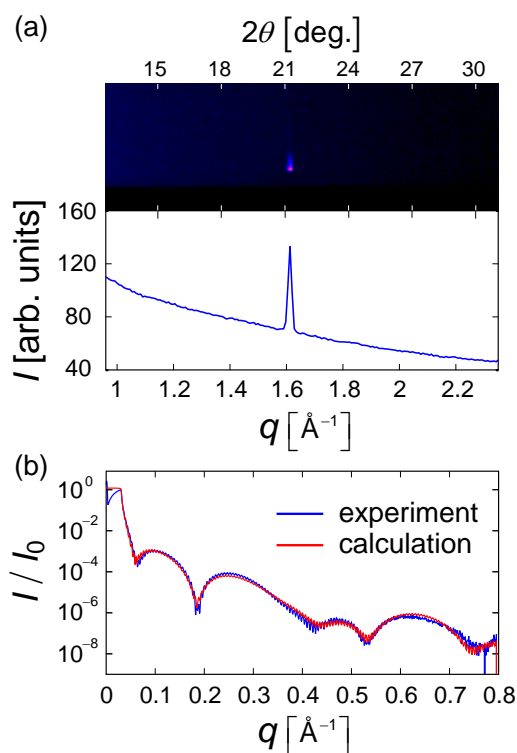


Figure 2: Characterization of fabricated SMB using synchrotron XRD and XRR measurements. (a) In-plane thin-film XRD image and profile of the fabricated SMB. (b) Thin-film XRR spectrum of the fabricated SMB. The incident X-ray photon energy is 9.0 keV.

To investigate the semiconducting properties of SMBs, we fabricated bottom-gate top-contact TFTs based on the fabricated SMBs. Typical mobility was estimated as $6.5 \text{ cm}^2 \text{ V}^{-1} \text{ s}^{-1}$ in the saturation regime [7]. The obtained SMBs exhibited excellent device characteristics, exceeding those of amorphous Si TFTs.

In summary, we successfully developed a technique of manufacturing self-assembled SMBs that have uniformity of both molecular-level thickness and in-plane crystalline order. These SMBs were reproducibly created by a simple blade-coating technique in which geometrical frustration produced by chain-length disorder was introduced. We believe the technique is applicable to a wide variety of molecules composed of π -Cores substituted by alkyl chains. The obtained SMBs also afford high-performance TFTs exceeding those of amorphous Si TFTs. These findings should open a new route to SMB-based ultrathin super-flexible electronics.

REFERENCES

- [1] K. Kurihara, M. Tamura, K. Shohda, T. Toyota, K. Suzuki and T. Sugawara, *Nat. Chem.* **3**, 775 (2011).
- [2] J. Geng, K. Kim, J. Zhang, A. Escalada, R. Tunuguntla, L. R. Comolli, F. I. Allen, A. V. Shnyrova, K. R. Cho, D. Munoz, Y. M. Wang, C. P. Grigoropoulos, C. M. Ajo-Franklin, V. A. Frolov and A. Noy, *Nature* **514**, 612 (2014).
- [3] H. Sirringhaus, *Adv. Mater.* **26**, 1319 (2014).
- [4] H. Iino, T. Usui and J. Hanna, *Nat. Commun.* **6**, 6828 (2015).
- [5] S. Inoue, H. Minemawari, J. Tsutsumi, M. Chikamatsu, T. Yamada, S. Horiuchi, M. Tanaka, R. Kumai, M. Yoneya and T. Hasegawa, *Chem. Mater.* **27**, 3809 (2015).
- [6] T. Hamai, S. Arai, H. Minemawari, S. Inoue, R. Kumai and T. Hasegawa, *Phys. Rev. Appl.* **8**, 054011 (2017).
- [7] S. Arai, S. Inoue, T. Hamai, R. Kumai and T. Hasegawa, *Adv. Mater.* **30**, 1707256 (2018).

BEAMLINES

BL-7C, BL-8A and BL-8B

S. Arai¹, S. Inoue¹, R. Kumai² and T. Hasegawa¹ (¹The Univ. of Tokyo, ²KEK-IMSS-PF)

Commensurate vs Incommensurate Charge Ordering near the Superconducting Dome in $\text{Ir}_{1-x}\text{Pt}_x\text{Te}_2$ Revealed by Resonant X-Ray Scattering

The electronic-structural modulations of $\text{Ir}_{1-x}\text{Pt}_x\text{Te}_2$ have been examined both by resonant elastic and inelastic X-ray scattering (REXS and RIXS) techniques. Charge-density-wave-like superstructures with wave vectors of $Q = (1/5\ 0\ -1/5)$, $(1/8\ 0\ -1/8)$, and $(1/6\ 0\ -1/6)$ are observed on the same sample of IrTe_2 at the lowest temperature. In contrast, superstructures around $Q = (1/5\ 0\ -1/5)$ are observed for doped samples. The superstructure reflections persist to higher Pt substitution than previously assumed. REXS and RIXS results indicate the importance of the Te 5p states rather than the Ir 5d states in the formation of the spatial modulation of these systems.

A charge-density-wave (CDW)-like structural transition was reported in the 5d transition-metal chalcogenide IrTe_2 at $T_s \sim 280$ K. This has attracted great interest because of the recent discovery of superconductivity in Pt- and Pd-substituted compounds [1–3]. With increasing Pt-substitution, the structural transition is suppressed, and a superconducting dome appears in the region of $0.04 \leq x \leq 0.12$, indicating similar diagrams to those of other unconventional superconductors. Although numerous studies have followed these initial works, there is still no consensus on the mechanism of this structural transition. The phase transition of IrTe_2 is accompanied by the emergence of a superstructure lattice modulation, with wave vector $Q_{1/5} = (1/5\ 0\ -1/5)$ as expressed in reciprocal lattice units in trigonal notation. The main elements are the Ir-Ir dimerization along the a -axis with period $5a$, and the consequent distortion of the triangular Ir sublattice in the a - b plane, occurring

together with a trigonal-to-triclinic symmetry reduction. Since in IrTe_2 the formal valence of Ir is +4, the Ir 5d electrons with t_{2g} configuration are the closest to the chemical potential, and they are thus expected to play a central role in the CDW. However, some previous studies indicated that the charge-transfer energy between Ir and Te is close to zero, and that the Te 5p states are also important for the low-energy physics, especially for their surface region. To revisit the superstructures in $\text{Ir}_{1-x}\text{Pt}_x\text{Te}_2$ and to clarify the relation between superconductivity and superstructural modulation, we studied the spatial ordering of electronic states by means of resonant elastic and inelastic X-ray scattering (REXS and RIXS) at both edges of Ir and Te.

Single-crystal samples of $\text{Ir}_{1-x}\text{Pt}_x\text{Te}_2$ ($0.0 \leq x \leq 0.12$) were prepared using a self-flux method. Resonant elastic X-ray scattering (REXS) at the Ir L_3 ($2p$ to $5d$) absorption edge in the hard X-ray region was performed

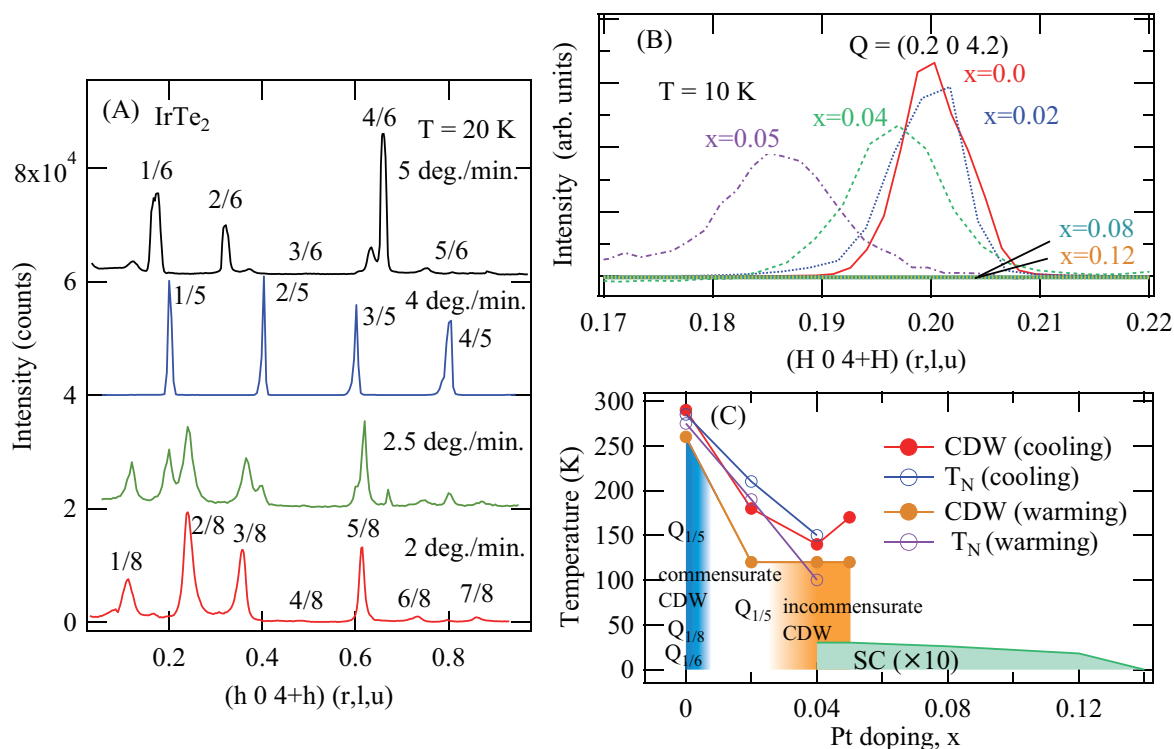


Figure 1: (A) Superstructure peaks for IrTe_2 at $T = 10$ K obtained at various cooling rates: 2, 2.5, 4, and 5 K/min. (B) Superstructure peaks of $Q = (0.2\ 0\ -4.2)$ for $\text{Ir}_{1-x}\text{Pt}_x\text{Te}_2$ ($0.0 \leq x \leq 0.12$). The cooling-warming rates were 4 K/min. (C) Phase diagram of $\text{Ir}_{1-x}\text{Pt}_x\text{Te}_2$.

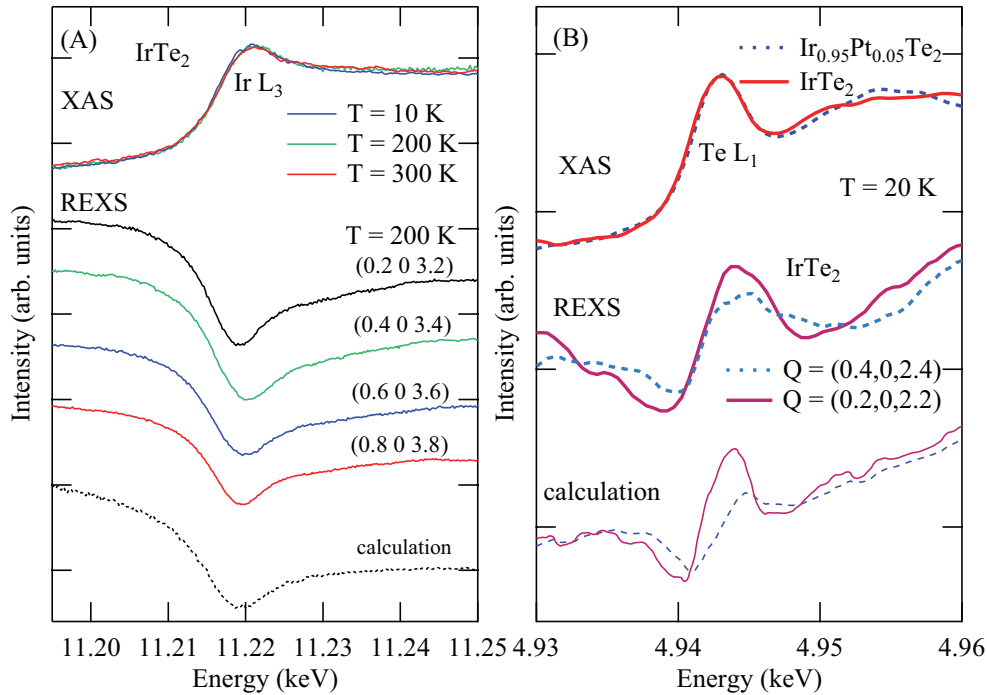


Figure 2: REXS and XAS spectra at the (A) Ir L_3 and (B) Te L_1 edges. The calculated spectra are also shown using the (A) lattice displacement for the Ir sites and (B) valence modulation model for the Te sites, respectively.

at the Photon Factory's BL-4C. REXS at the Te L_1 ($2s$ to $5p$) absorption edge was conducted at BL-22XU of SPring-8. On the other hand, resonant inelastic X-ray scattering (RIXS) at the Ir L_3 edges was carried out at BL-11XU of SPring-8. REXS at the Te $M_{4,5}$ ($3d$ to $5p$) edge in the soft X-ray region was performed at the REIXS beamline of the Canadian Light Source.

Figure 1(A) shows X-ray diffraction along $(0\ 0\ -4)$ to $(1\ 0\ -5)$ through the superstructure peaks for IrTe $_2$ ($x = 0.0$). The $Q = (1/5\ 0\ -1/5)$ -, $(1/8\ 0\ -1/8)$ -, and $(1/6\ 0\ -1/6)$ -type superstructures are observed for IrTe $_2$ at the lowest temperature of $T = 10$ K, whereas only the $Q_{1/5}$ -type superstructures were reported in previous studies for these samples [4, 5]. The periods of the superstructures at low temperature strongly depend on the experimental protocol, or cooling rate. In contrast, incommensurate ordering peaks around $Q = (1/5\ 0\ -1/5)$ are observed for the doped samples of $0.02 \leq x \leq 0.05$ at any cooling rate [Fig. 1(B)]. The superstructures coexist with the superconducting phase for Ir $_{1-x}$ Pt $_x$ Te $_2$ ($x = 0.05$) as shown in Fig. 1(C), suggesting that CDW persists to higher Pt substitution than previously thought. In addition, incommensuration of CDW is observed for $x = 0.04$ and 0.05 samples which coincide with the onset of superconductivity.

Surprisingly, the REXS and RIXS spectra for the Ir L_3 edge scarcely depend on the wavevectors, while the REXS line shape at the Te edges strongly depends on the Q position (Fig. 2), indicating that the spatial charge modulation only exists on the Te sites. Therefore, the charge modulation in the bulk regions resides in the Te orbitals rather than the Ir orbitals. The phase diagram

re-examined in this work suggests that the CDW incommensurability in the Te sites will correlate with the emergence of superconducting states. Ir $_{1-x}$ Pt $_x$ Te $_2$ may harbor similar exotic phases for unconventional superconductors.

REFERENCES

- [1] S. Pyon, K. Kudo and M. Nohara, *J. Phys. Soc. Jpn.* **81**, 053701 (2012).
- [2] J. J. Yang, Y. J. Choi, Y. S. Oh, A. Hogan, Y. Horibe, K. Kim, B. I. Min and S.-W. Cheong, *Phys. Rev. Lett.* **108**, 116402 (2012).
- [3] K.-T. Ko, H.-H. Lee, D.-H. Kim, J.-J. Yang, S.-W. Cheong, M. J. Eom, J. S. Kim, R. Gammag, K.-S. Kim, H.-S. Kim, T.-H. Kim, H.-W. Yeom, T.-Y. Koo, H.-D. Kim and J.-H. Park, *Nature Commun.* **6**, 7342 (2015).
- [4] T. Toriyama, M. Kobori, T. Konishi, Y. Ohta, K. Sugimoto, J. Kim, A. Fujiwara, S. Pyon, K. Kudo, and M. Nohara, *J. Phys. Soc. Jpn.* **83**, 033701 (2014).
- [5] K. Takubo, R. Comin, D. Ootsuki, T. Mizokawa, H. Wadati, Y. Takahashi, G. Shibata, A. Fujimori, R. Sutarto, F. He, S. Pyon, K. Kudo, M. Nohara, G. Levy, I. S. Elfimov, G. A. Sawatzky and A. Damascelli, *Phys. Rev. B* **90**, 081104(R) (2014).

BEAMLINE

BL-4C

K. Takubo¹, K. Yamamoto¹, Y. Hirata¹, H. Wadati¹, T. Mizokawa², R. Sutarto³, F. He³, K. Ishii⁴, Y. Yamasaki⁵, H. Nakao⁶, Y. Murakami⁶, G. Matsuo⁷, H. Ishii⁷, M. Kobayashi⁷, K. Kudo⁷ and M. Nohara⁷ (The Univ. of Tokyo, ²Waseda Univ., ³CLS, ⁴QST, ⁵NIMS, ⁶KEK-IMSS-PF, ⁷Okayama Univ.)

A New Structure Family of Oxide-Ion Conductors $\text{Ca}_{0.8}\text{Y}_{2.4}\text{Sn}_{0.8}\text{O}_6$

Mg_3TeO_6 -type $\text{Ca}_{0.8}\text{Y}_{2.4}\text{Sn}_{0.8}\text{O}_6$ has been found as a new structure family of oxide-ion conductors, by bond-valence-based-energy (BVE) calculations for 147 tin (Sn)-containing compositions [1]. Electrical conductivity measurements and the optical band gap suggested that the dominant carrier of $\text{Ca}_{0.8}\text{Y}_{2.4}\text{Sn}_{0.8}\text{O}_6$ is oxide ions. Synchrotron X-ray powder diffraction data of $\text{Ca}_{0.8}\text{Y}_{2.4}\text{Sn}_{0.8}\text{O}_6$ taken at the BL-4B2 beamline at 300 and 1273 K were successfully analyzed with the Mg_3TeO_6 -type structure. BVE calculations using the refined crystal structure of $\text{Ca}_{0.8}\text{Y}_{2.4}\text{Sn}_{0.8}\text{O}_6$ at 1273 K strongly suggested three-dimensional oxide-ion diffusion. [This article is reproduced from Ref. [1] with permission from The Royal Society of Chemistry.]

Oxide-ion conducting ceramics are important materials, because they can be used in solid oxide fuel cells (SOFCs), batteries, catalysts, gas sensors and oxygen separation membranes. Since most of the researches on oxide-ion conductors are limited to a small number of structure families such as fluorite- and perovskite-type structures, the discovery of a new structure family of oxide-ion conductors would assist the development of materials science and solid state ionics. In the present work, we found that Mg_3TeO_6 -type $\text{Ca}_{0.8}\text{Y}_{2.4}\text{Sn}_{0.8}\text{O}_6$ is a good candidate for an oxide-ion conductor among Sn (tin)-containing oxides. We used the bond-valence method, which is quite fast for calculating the energy landscapes of a test ion in crystal structures [2, 3]. Sn^{4+} has the d^{10} electronic configuration. Since there are many reports of oxide-ion conductors containing d^{10}

electronic configuration cations, such as Ga^{3+} and Ge^{4+} , there are expected to be undiscovered oxide-ion conductors in Sn-containing oxides. There are 119 structure types of oxides containing Sn as an essential element in the inorganic crystal structure database. We selected at least one composition for each structure type and carried out BVE calculations. Finally, we calculated BVE for 147 compositions. The energy barrier for the oxide-ion migration (E_b) of $\text{Ca}_{0.8}\text{Y}_{2.4}\text{Sn}_{0.8}\text{O}_6$ was estimated to be 0.46 eV using the BVE landscape. A majority of other compositions had higher E_b for the oxide-ion migration than that of $\text{Ca}_{0.8}\text{Y}_{2.4}\text{Sn}_{0.8}\text{O}_6$. Therefore, we synthesized $\text{Ca}_{0.8}\text{Y}_{2.4}\text{Sn}_{0.8}\text{O}_6$ by the solid-state reaction method, and investigated its electrical conductivity and crystal structure using high-angular-resolution synchrotron X-ray powder diffraction (SXRPD) data measured *in situ*

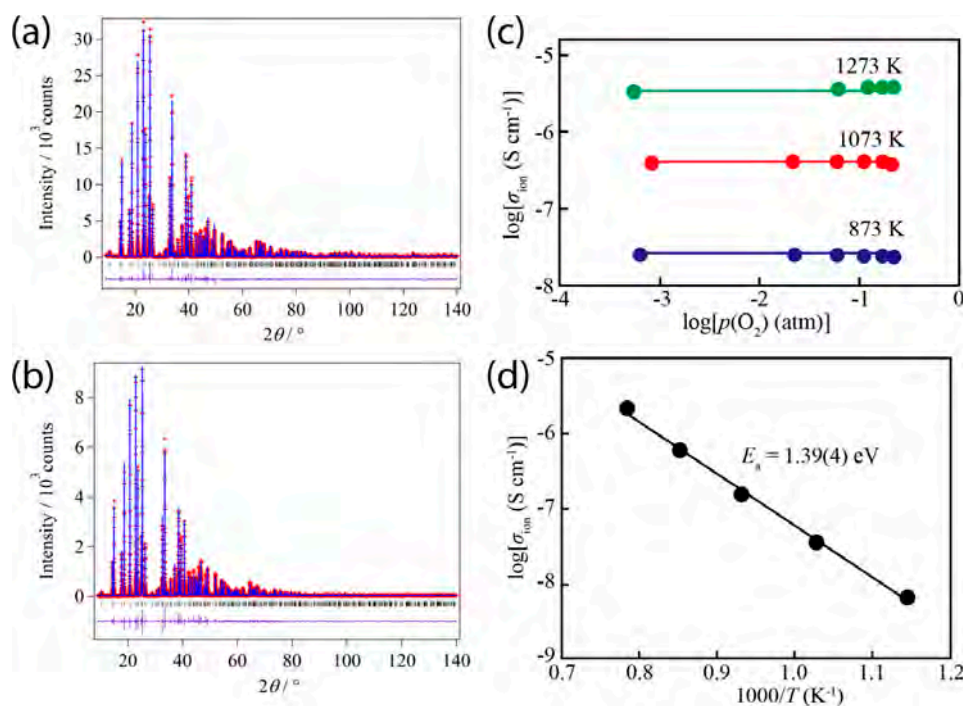


Figure 1: Rietveld patterns of the synchrotron X-ray powder diffraction data of $\text{Ca}_{0.8}\text{Y}_{2.4}\text{Sn}_{0.8}\text{O}_6$ taken in air at (a) 300 K, and (b) 1273 K. (c) Oxygen partial pressure ($p(\text{O}_2)$) dependence of the electrical conductivity of $\text{Ca}_{0.8}\text{Y}_{2.4}\text{Sn}_{0.8}\text{O}_6$ at 843 (blue), 1023 (red), and 1193 K (green). (d) Arrhenius plot of the oxide-ion conductivity σ_{ion} of $\text{Ca}_{0.8}\text{Y}_{2.4}\text{Sn}_{0.8}\text{O}_6$ in air. © Royal Society of Chemistry [1].

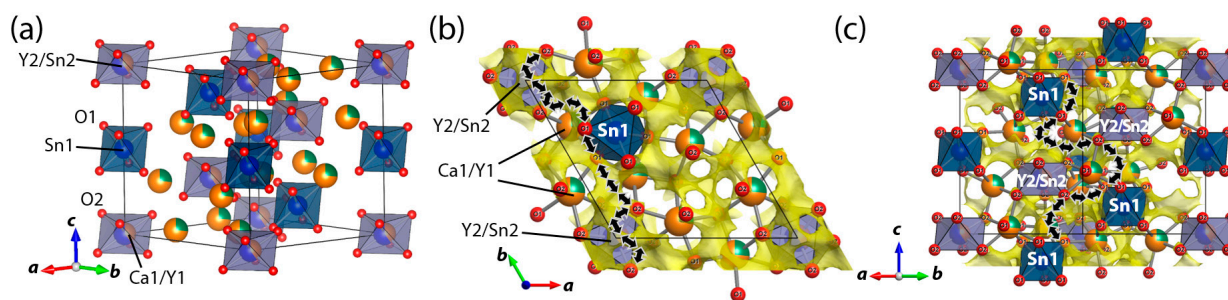


Figure 2: (a) Refined crystal structure of $\text{Ca}_{0.8}\text{Y}_{2.4}\text{Sn}_{0.8}\text{O}_6$ at 1273 K. (b, c) Bond valence-based energy (BVE) landscapes for an oxide ion with an isovalue at 0.6 eV in $\text{Ca}_{0.8}\text{Y}_{2.4}\text{Sn}_{0.8}\text{O}_6$ at 1273 K, which are viewed along the [001] (b) and [110] directions. Arrows represent possible oxide-ion diffusion paths.

at 300 and 1273 K. SXRPD data of $\text{Ca}_{0.8}\text{Y}_{2.4}\text{Sn}_{0.8}\text{O}_6$ were measured using a multiple detector system at the BL-4B₂ beamline. The SXRPD data of $\text{Ca}_{0.8}\text{Y}_{2.4}\text{Sn}_{0.8}\text{O}_6$ taken at 300 K were analyzed by the Rietveld method. The results of Rietveld refinement gave a good fitting and reliable factors were $R_{\text{wp}} = 7.29\%$, $R_{\text{B}} = 3.40\%$, and $\text{GoF} = 1.261$ [Fig. 1(a)]. All the observed reflections of the SXRPD data were indexed by the trigonal cell, which indicates that the product was the single trigonal phase with the $R\bar{3}$ Mg_3TeO_6 -type structure. The refined lattice parameters $a = b = 9.511049(11)$ Å, $c = 11.00686(3)$ Å and atomic coordinates of all atoms agreed well with those reported by Kaminaga *et al.* [4]. The oxygen partial pressure $p(\text{O}_2)$ dependence of total electrical conductivity of $\text{Ca}_{0.8}\text{Y}_{2.4}\text{Sn}_{0.8}\text{O}_6$ measured at 843 K, 1023 K, and 1193 K showed constant conductivity against $p(\text{O}_2)$ [Fig. 1(c)], indicating the dominant charge carrier in $\text{Ca}_{0.8}\text{Y}_{2.4}\text{Sn}_{0.8}\text{O}_6$ is oxide ions at these temperatures. We also confirmed that $\text{Ca}_{0.8}\text{Y}_{2.4}\text{Sn}_{0.8}\text{O}_6$ is an electric insulator from an optical band gap. The possibility of proton conduction was eliminated by conductivity measurements in wet air. From these experimental results, we concluded that Mg_3TeO_6 -type $\text{Ca}_{0.8}\text{Y}_{2.4}\text{Sn}_{0.8}\text{O}_6$ is a new structure family of oxide-ion conductors. SXRPD data of $\text{Ca}_{0.8}\text{Y}_{2.4}\text{Sn}_{0.8}\text{O}_6$ were also measured at 1273 K using a home-made furnace [5, 6]. The Rietveld analysis of the SXRPD data taken at 1273 K was successfully performed by the trigonal $R\bar{3}$ Mg_3TeO_6 -type structure, which gave a good fitting and reliable factors were $R_{\text{wp}} = 9.91\%$, $R_{\text{B}} = 3.93\%$, and $\text{GoF} = 0.90$ [Fig. 1(b)]. The refined crystal structure is shown in Fig. 2(a). The lattice parameters and volume V of $\text{Ca}_{0.8}\text{Y}_{2.4}\text{Sn}_{0.8}\text{O}_6$ at 1273 K ($a = b = 9.60204(3)$ Å, $c = 11.08009(6)$ Å, $V = 884.710(6)$ Å³) were larger than those at 300 K ($a = b = 9.511049(11)$ Å, $c = 11.00686(3)$ Å, $V = 862.285(3)$ Å³) due to thermal expansion. The BVE of an oxide ion was calculated using the refined

crystal structure of $\text{Ca}_{0.8}\text{Y}_{2.4}\text{Sn}_{0.8}\text{O}_6$ at 1273 K, in order to investigate the oxide-ion migration pathway. Figures 2(b) and 2(c) show the yellow isosurfaces of BVE for an oxide ion at +0.6 eV in $\text{Ca}_{0.8}\text{Y}_{2.4}\text{Sn}_{0.8}\text{O}_6$. In these BVE landscapes, the most stable position of an oxide ion was set to 0 eV. An oxide-ion migration path in $\text{Ca}_{0.8}\text{Y}_{2.4}\text{Sn}_{0.8}\text{O}_6$ was found on the ab plane with the energy barrier of 0.53 eV. Arrows in Fig. 2(b) represent an example of the oxide-ion migration paths along the b -axis. The migration path follows the edges of the $\text{Y2/Sn2}(\text{O}2)_6$, $\text{Ca1/Y1}(\text{O}1)_3(\text{O}2)_3$, and $\text{Sn1}(\text{O}1)_6$ octahedra. An equivalent oxide-ion conduction path can be seen along the a -axis, because $\text{Ca}_{0.8}\text{Y}_{2.4}\text{Sn}_{0.8}\text{O}_6$ has a trigonal cell. In addition to these paths, there is a possible migration path of oxide ions along the c -axis with an energy barrier of 0.63 eV as shown by the arrows in Fig. 2(c). Therefore, it is strongly suggested that the oxide ions diffuse three-dimensionally. The possible diffusion path along the c -axis follows the edges of the $\text{Ca1/Y1}(\text{O}1)_3(\text{O}2)_3$, and $\text{Sn1}(\text{O}1)_6$ octahedra.

REFERENCES

- [1] R. Inoue, K. Fujii, M. Shiraiwa, E. Niwa and M. Yashima, *Dalton Trans.* **47**, 7515 (2018).
- [2] S. Adams, *Solid State Ionics* **136–137**, 1351 (2000).
- [3] M. Sale and M. Avdeev, *J. Appl. Cryst.* **45**, 1054 (2012).
- [4] Y. Kaminaga, H. Yamane and T. Yamada, *Acta Crystallogr. C-Struct. Chem.* **62**, 57 (2006).
- [5] M. Yashima, M. Tanaka, K. Oh-uchi and T. Ida, *J. Appl. Cryst.* **38**, 854 (2005).
- [6] M. Yashima, K. Oh-uchi, M. Tanaka and T. Ida, *J. Am. Ceram. Soc.* **89**, 1395 (2006).

BEAMLINE

BL-4B2

K. Fujii, R. Inoue, M. Shiraiwa, E. Niwa and M. Yashima (Tokyo Tech.)

Magnetic Skyrmion Lattice in Gd_2PdSi_3

In the last decade, nanometric spin vortices, referred to as magnetic skyrmions, in noncentrosymmetric magnets have been intensively studied. Some theories have predicted that magnetic frustration may also result in a lattice state of magnetic skyrmions. In this study we have found the emergence of magnetic skyrmion states in a frustrated centrosymmetric magnet Gd_2PdSi_3 . The Hall resistivity is enhanced by the application of a magnetic field of 0.5–1.0 T along the hexagonal c -axis at low temperatures. In this phase, triple in-plane spin modulation of $(q\ 0\ 0)$, $(0\ q\ 0)$, and $(q\ -q\ 0)$ is confirmed by resonant X-ray scattering.

Magnetic skyrmion lattice has been found in cubic chiral MnSi [1] and many other noncentrosymmetric magnets. The lack of inversion symmetry produces the uniform antisymmetric exchange interaction, often called Dzyaloshinski-Moriya interaction, which prefers canting between neighboring spin moments. The competition between ferromagnetic exchange interaction and antisymmetric exchange interaction may result in a helimagnetic state. The helix is modified by the application of a magnetic field and sometimes transformed to the triangular lattice of magnetic skyrmions. However, the helimagnetic state is also found in frustrated magnets. Some theories hence propose the emergence of the skyrmion lattice state in a frustrated magnet in a magnetic field [2, 3]. Nonetheless, no experimental observation has been reported.

Gd_2PdSi_3 consists of Gd triangular lattice and $\text{Pd}_{1/4}\text{Si}_{3/4}$ honeycomb network. Previous studies showed metamagnetic transitions as well as modulation in Gd moments probably due to the so-called Ruderman-Kittel-Kasuya-Yosida (RKKY) type interaction [4]. We

grew single crystals and investigated magnetic and transport properties in detail [5]. **Figure 1** shows the magnetization and Hall resistivity at 2 K. The magnetic field is applied along the c -axis. Two-step metamagnetic transitions are discernible as anomalies at 0.5 T and 1.3 T. It is interesting to note that Hall resistivity exhibits an enhancement in the intermediate-field phase.

The measurement of resonant X-ray scattering was performed on BL-3A. A single crystal with widest planes of $(1\ 1\ 0)$ was loaded in a cryostat with an 8-Tesla superconducting magnet. A magnetic field was applied along the c -axis. The X-ray photon energy was tuned at the Gd L_2 absorption edge (7.932 keV). The polarization of the incident beam was parallel to the scattering plane (or so-called π polarization). The polarization of the scattered beam was analyzed by pyrolytic graphite.

We explored superlattice reflections around the (220) reflections and found peaks at $(1.86, 2, 0)$, $(2, 1.86, 0)$, and $(2.14, 1.86, 0)$, while no peak was observed along the $(2-q, 2-q, 0)$ line in the reciprocal space. We confirmed that the superlattice peak disappears in the

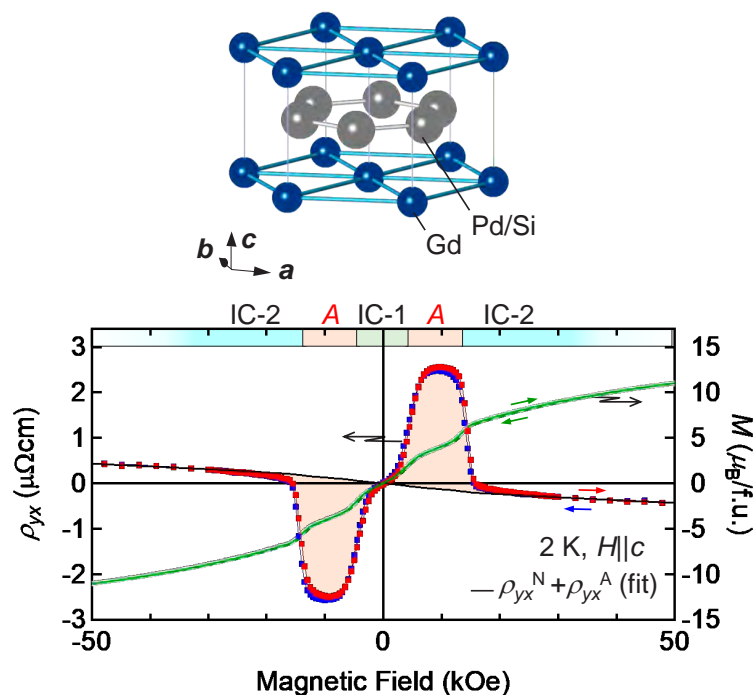


Figure 1: (Upper panel) Crystal structure of Gd_2PdSi_3 . (Lower panel) Magnetization (thin line) and Hall resistivity (dots) in Gd_2PdSi_3 when sweeping a magnetic field along the c -axis at 2 K. Excerpt from Ref. [5].

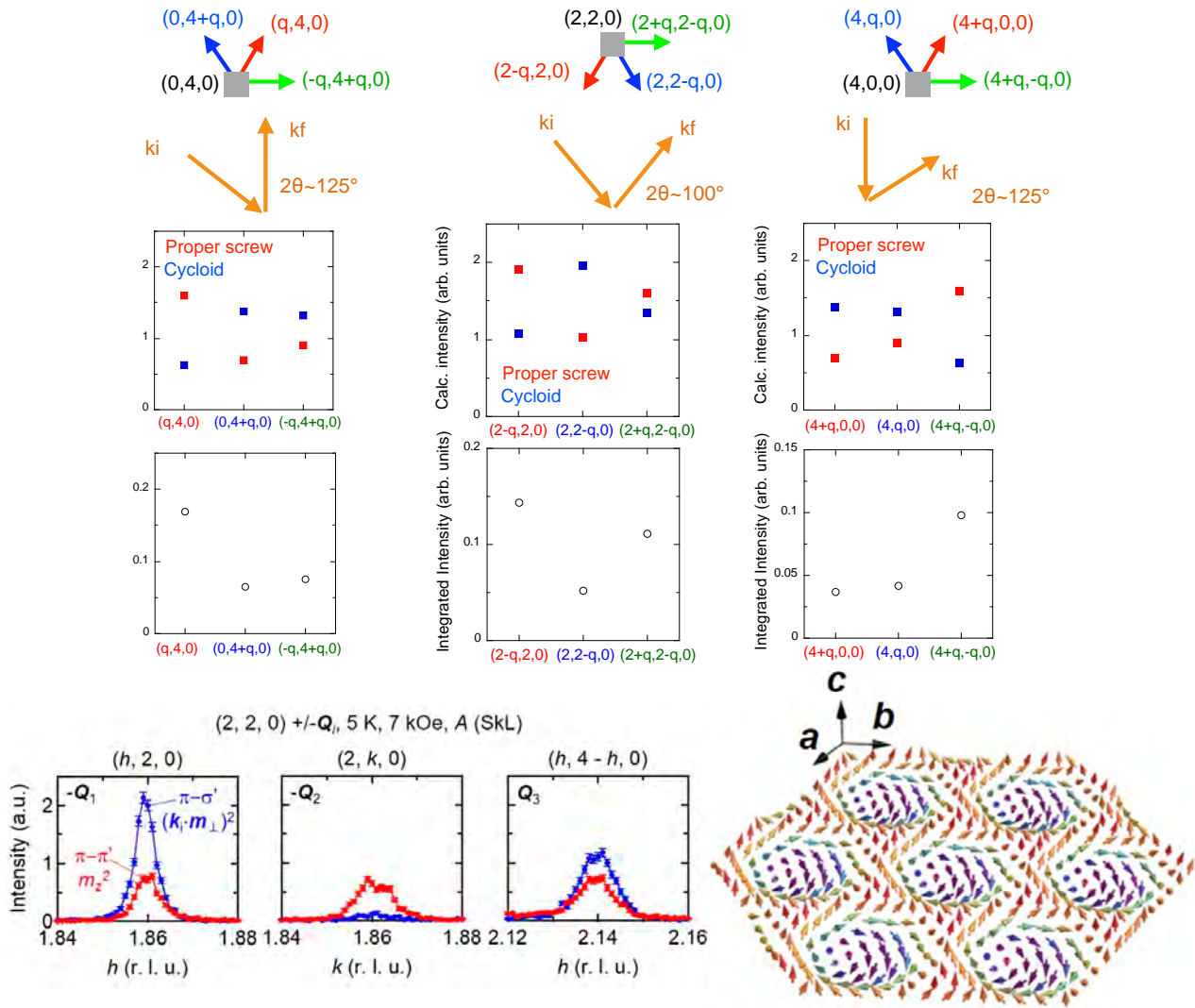


Figure 2: (Upper panel) Comparison of the intensities of superlattice reflections obtained by the present measurement with two models (see main text). (Lower left panel) Polarization analysis of superlattice reflections. Excerpt from Ref. [5]. All the data in this figure are for the intermediate-field phase.

paramagnetic phase above 21 K. We compare the intensities of the superlattice reflections around $(0, 4, 0)$, $(2, 2, 0)$, and $(4, 0, 0)$ in the intermediate-field phase with two magnetic models: triple proper screw modulation and triple cycloidal modulation, as shown in the left panel of **Fig. 2**. In the models, we assume that the amplitudes should be identical. The experimental result agrees well with the triple-screw modulation model. The right upper panel of **Fig. 2** shows the results of polarization analyses of several superlattice reflections. The intensity of $(2, 1.86, 0)$ reflection in the $\pi-\sigma'$ channel is largely suppressed. Since the wavevector of the incident beam is almost parallel to the b^* -axis for the reflection, the intensity of the $\pi-\sigma'$ channel nearly corresponds to the longitudinal spin modulation, which is absent in the proper screw. We hence conclude that the intermediate-field phase is the triangular lattice state of Bloch-type magnetic skyrmions, as shown in the right bottom panel of **Fig. 2**.

REFERENCES

- [1] S. Mühlbauer., B. Binz, F. Jonietz, C. Pfleiderer, A. Rosch, A. Neubauer, R. Georgii and P. Böni, *Science* **323**, 915 (2009).
- [2] T. Okubo, S. Chung and H. Kawamura, *Phys. Rev. Lett.* **108**, 017206 (2012).
- [3] S. Hayami, R. Ozawa and Y. Motome, *Phys. Rev. B* **95**, 224424 (2017).
- [4] S. R. Saha, H. Sugawara, T. D. Matsuda, H. Sato, R. Mallik and E. V. Sampathkumar, *Phys. Rev. B* **60**, 12162 (1999).
- [5] T. Kurumaji, T. Nakajima, M. Hirschberger, A. Kikkawa, Y. Yamasaki, H. Sagayama, H. Nakao, Y. Taguchi, T. Arima and Y. Tokura, *Science* **365**, 914 (2019).

BEAMLINE

BL-3A

T. Kurumaji¹, T. Nakajima¹, M. Hirschberger¹, A. Kikkawa¹, Y. Yamasaki^{1,2}, H. Sagayama³, H. Nakao³, Y. Taguchi¹, Y. Tokura^{1,4} and T. Arima^{1,4} (¹RIKEN-CEMS, ²NIMS, ³KEK-IMSS-PF, ⁴The Univ. of Tokyo,)

Microscopic Origin of the Ferroelectricity in Multiferroics SmMn_2O_5 Studied by Resonant Soft X-Ray Scattering

We investigated magnetic ordering and electronic state in multiferroic SmMn_2O_5 . This material has a relatively large electric polarization among members of the RMn_2O_5 (R = rare earth) family and other type-II multiferroic materials. However, the microscopic origin of this large electric polarization was unknown. Our resonant soft X-ray scattering study at the Photon Factory suggested that ionic displacements via a collinear magnetic structure mainly contribute to the large electric polarization, based on measurements of magnetic ordering of the rare-earth, Mn, and also ligand O ions. In addition, the study revealed unique electronic states of Mn and O ions in SmMn_2O_5 .

So-called type-II multiferroics, where ferroelectricity is driven by magnetic ordering, have attracted intense research interest for several decades. Some of them exhibit a non-linear magnetoelectric (ME) effect, in which the application of an external magnetic (electric) field leads to striking changes of the dielectric (magnetic) properties of the materials. Among them, RMn_2O_5 (R = rare earth) compounds have attracted much attention since they show various ME effects depending on the type of rare-earth ions. Since these

ME effects are believed due to the complex magnetic ordering of rare-earth and Mn ions, revealing the magnetic structure is key to understanding the mechanism of multiferroicity in this family. Neutron scattering has been commonly used to observe the magnetic ordering. Resonant soft X-ray scattering (RSXS) is also an effective tool, particularly for materials containing neutron absorber elements, such as Sm or Gd. Furthermore, RSXS makes it possible to detect the electronic state of ions selectively.

SmMn_2O_5 has a relatively large electric polarization in the RMn_2O_5 family and multiferroic materials. Our previous resonant hard X-ray scattering study [1] reported a collinear magnetic structure of Sm and Mn ions, where the moments point to the c -axis, as shown in Fig. 1(a), which is responsible for the large electric polarization via exchange interaction. However, a more microscopic origin of the electric polarization, such as magnetic-driven ionic displacements and charge transfer between O and Mn ions, remains elusive. Here we employed RSXS for SmMn_2O_5 to observe the magnetic ordering and electronic state of Mn and also O ions, and discuss the mechanism of the ferroelectricity in this material [2].

Figure 1(b) shows RSXS spectra of magnetic reflections around Mn $L_{\text{II,III}}$ edges of SmMn_2O_5 , and also GdMn_2O_5 for comparison. The spectrum of GdMn_2O_5 is similar to those acquired from other RMn_2O_5 [3]. Meanwhile, somewhat different parts were observed in the spectrum of SmMn_2O_5 . The intensity increases around $E = 642$ eV [indicated by A in Fig. 1(b)], while it decreases and another peak appears around $E = 652$ eV (indicated by B). These differences likely reflect the unique electronic state of Mn ions in SmMn_2O_5 .

We also observed a magnetic reflection around the O K edge in both SmMn_2O_5 and GdMn_2O_5 [see Fig. 1(c)]. The spectrum of GdMn_2O_5 has a strong peak around $E = 530$ eV, which indicates the spin polarization of O ions as a result of charge transfer from O to Mn ions. Similar spectra have been also acquired from RMn_2O_5 ($R = \text{Tb}, \text{Y}, \text{Er}$) [3–5]. A previous RSXS study suggested that this charge transfer makes a primary microscopic contribution to the ferroelectricity in RMn_2O_5 [5]. In sharp contrast, SmMn_2O_5 exhibits no evident

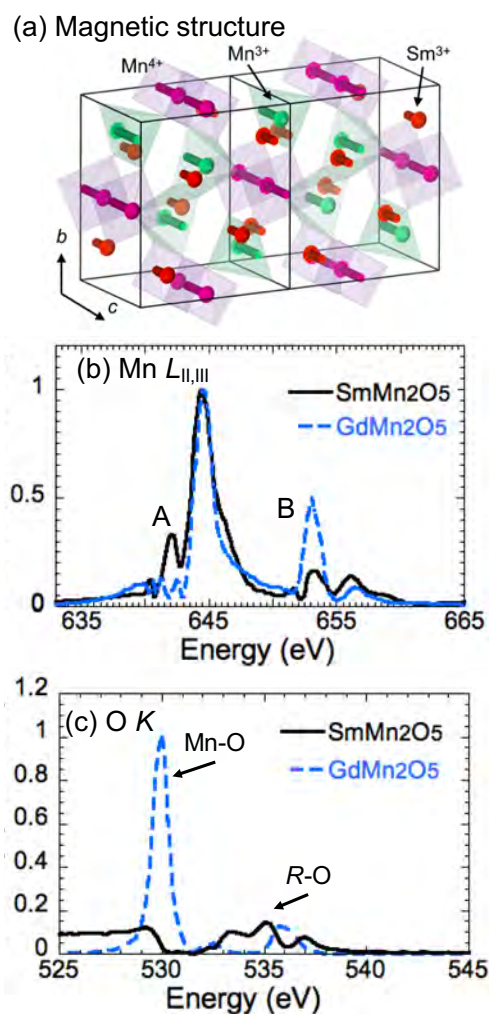


Figure 1: (a) Magnetic structure of Sm and Mn ions. (b) (c) Energy spectra around Mn $L_{\text{II,III}}$ and O K edges, respectively, in SmMn_2O_5 and GdMn_2O_5 .

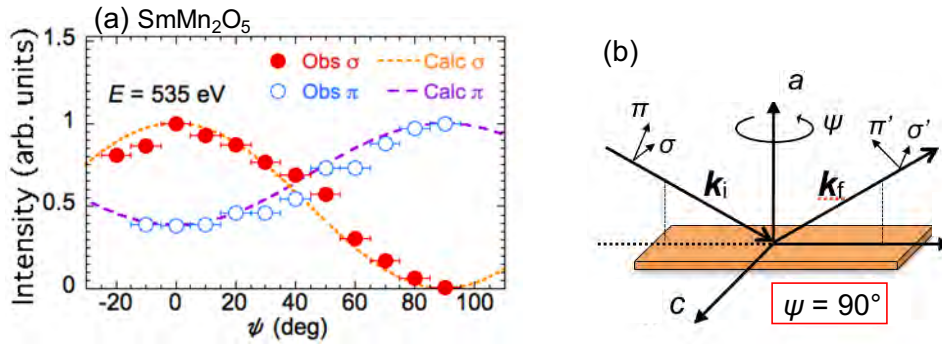


Figure 2: (a) Azimuthal angle dependence of resonant intensities at $E = 535$ eV and calculation values. (b) Experimental geometry at $\psi = 90$ deg.

peak around $E = 530$ eV, which suggests that the large electric polarization is mainly caused by not the charge transfer, but ionic displacements due to exchange interaction. Furthermore, this electronic behavior could lead to changes of the effective charge of Mn ions [6], which results in a different spectrum around Mn $L_{II,III}$ edges.

Meanwhile, several peaks were observed around $E = 535$ eV in SmMn_2O_5 . This energy range is associated with charge transfer to rare-earth $5d$ states. Similar rare-earth $5d$ state contributions have been also observed in GdMn_2O_5 [as shown in Fig. 1(c)] and TbMn_2O_5 [4]. Hence it can be concluded that spin polarization of O ions is induced by charge transfer between only O and Sm ions. Figure 2(a) presents the azimuthal angle (ψ) dependence of the resonant intensity at $E = 535$ eV in SmMn_2O_5 . The experimental geometry is shown in Fig. 2(b), where we defined $\psi = 90$ deg. when the c -axis is perpendicular to the scattering plane. Figure 2(a) also shows calculation values on the assumption that magnetic moments of O ions point in the direction of the c -axis, which reproduces well the experimental values. This is consistent with our conclusion that magnetic moments of O ions are induced by Sm moments. However, the details of these unique electronic states of O and Mn ions are still unclear; further theoretical and experimental studies are required.

REFERENCES

- [1] Y. Ishii, S. Horio, M. Mitarashi, T. Sakakura, M. Fukunaga, Y. Noda, T. Honda, H. Nakao, Y. Murakami and H. Kimura, *Phys. Rev. B* **93**, 064415 (2016).
- [2] Y. Ishii, S. Horio, H. Yamamoto, Y. Noda, H. Nakao, Y. Murakami and H. Kimura., *Phys. Rev. B* **98**, 174428 (2018).
- [3] R. A. de Souza, U. Staub, V. Scagnoli, M. Garganourakis, Y. Bodenthin, S.-W. Huang, M. García-Fernández, S. Ji, S.-H. Lee, S. Park and S.-W. Cheong., *Phys. Rev. B* **84**, 104416 (2011).
- [4] T. A. W. Beale, S. B. Wilkins, R. D. Johnson, S. R. Bland, Y. Joly, T. R. Forrest, D. F. McMorrow, F. Yakhou, D. Prabhakaran, A. T. Boothroyd and P. D. Hatton, *Phys. Rev. Lett.* **105**, 087203 (2010). T. A. W. Beale, S. B. Wilkins, R. D. Johnson, D. Prabhakaran, A. T. Boothroyd, P. Steadman, S. S. Dhesi and P. D. Hatton, *Eur. Phys. J. Special Topics* **208**, 99 (2012).
- [5] S. Partzsch, S. B. Wilkins, J. P. Hill, E. Schierle, E. Weschke, D. Souptel, B. Büchner and J. Geck, *Phys. Rev. Lett.* **107**, 057201 (2011).
- [6] G. Giovannetti and J. van den Brink, *Phys. Rev. Lett.* **100**, 227603 (2008).

BEAMLINES

BL-3A, BL-4C, BL-8A, BL-16A and BL-19B

Y. Ishii¹, H. Yamamoto², Y. Noda², H. Nakao¹, Y. Murakami¹ and H. Kimura² (¹KEK-IMSS-PF, ²Tohoku Univ. -IMRAM)

Helical Ordering of Spin Trimers in $\text{Gd}_3\text{Ru}_4\text{Al}_{12}$ with a Distorted Kagome Lattice

We have found a novel ordering phenomenon of $S_T=21/2$ spin trimers in a distorted kagome lattice of $S=7/2$ 4f-spins of Gd ions in $\text{Gd}_3\text{Ru}_4\text{Al}_{12}$ by resonant X-ray diffraction with polarization analysis. The successive magnetic phase transitions at 18.5 K and 17.5 K were found to be paramagnetic to sinusoidal ordering in the hexagonal c-plane and to helical ordering with both the c-plane and the c-axis components. It is very rare that quantum mechanical multimerization is realized in localized and metallic *f*-electron systems. It is also significant that a spontaneous chiral symmetry breaking was found in the process of sinusoidal to helical successive phase transitions.

In magnetic materials with geometrically frustrated interactions in triangular, kagome, or pyrochlore lattice systems, various kinds of nontrivial orderings are observed: non-collinear and incommensurate spin structures, as well as successive transitions through partially disordered states. Most of them are difficult to predict because a large number of spin structures are generally degenerate. If the magnetic ions are located on a triangular or kagome lattice, and if the exchange interaction is antiferromagnetic, one cannot find a simple structure to satisfy the interactions consistently. In such cases, the system usually ends up with a so-called 120° structure as a result of compromise. In the crystal structure of $\text{Gd}_3\text{Ru}_4\text{Al}_{12}$ shown in Fig. 1, with a distorted kagome, or breathing kagome lattice, one may simply assume that the 120° spin structure should be realized.

However, in $\text{Gd}_3\text{Ru}_4\text{Al}_{12}$, it was recently pointed out by Nakamura that the Gd^{3+} spins of $S=7/2$ on the nearest neighbor triangle form a ferromagnetic “spin trimer” state with $S_T=21/2$ [1]. They showed that the anomalous temperature dependence of the magnetic susceptibility and specific heat can be well explained by a spin trimer model $H = -J(\mathbf{S}_1 \cdot \mathbf{S}_2 + \mathbf{S}_2 \cdot \mathbf{S}_3 + \mathbf{S}_3 \cdot \mathbf{S}_1)$ with a ferromagnetic exchange constant of $J = 13.5$ K, where \mathbf{S}_i ($i = 1-3$) represents the $S=7/2$ spin on the nearest neighbor triangle. Although such quantum spin states are frequently observed in insulating *d*-electron systems with small spin moments, they are rarely observed in mostly metallic *f*-electron systems with relatively large angular mo-

ments. The only exception is a spin dimer formation in YbAl_3C_3 [2]. The spin trimer formation in $\text{Gd}_3\text{Ru}_4\text{Al}_{12}$ may be the first case in *f*-electron systems.

Another interesting property found in $\text{Gd}_3\text{Ru}_4\text{Al}_{12}$ is the antiferromagnetic phase transitions at 18.5 K and 17.5 K. Since the binding energy of the spin trimer is higher than 100 K, these antiferromagnetic transitions at low temperatures are considered as the orderings among the well-developed ferromagnetic spin trimers. To investigate the ordered spin structure, we have utilized resonant X-ray diffraction at beamline 3A. Compared with neutron diffraction, which is a typical method used to investigate magnetic structures, resonant X-ray diffraction offers the advantages of element and orbital selectivity by using X-ray energies near the absorption edge of the target element, effective usage of a polarized incident beam and polarization analysis, high *Q*-resolution, and applicability for tiny samples. In addition, it has been remarked that the present observation performed for a Gd compound with extremely high neutron absorption is almost impossible by neutron diffraction.

From careful measurements and data analysis, especially from the result of polarization analysis, we concluded that the transition at 18.5 K is an ordering of spin trimers from paramagnetic to sinusoidal structure, and that at 17.5 K is a transition from sinusoidal to helical structure, as shown in Fig. 1 [3].

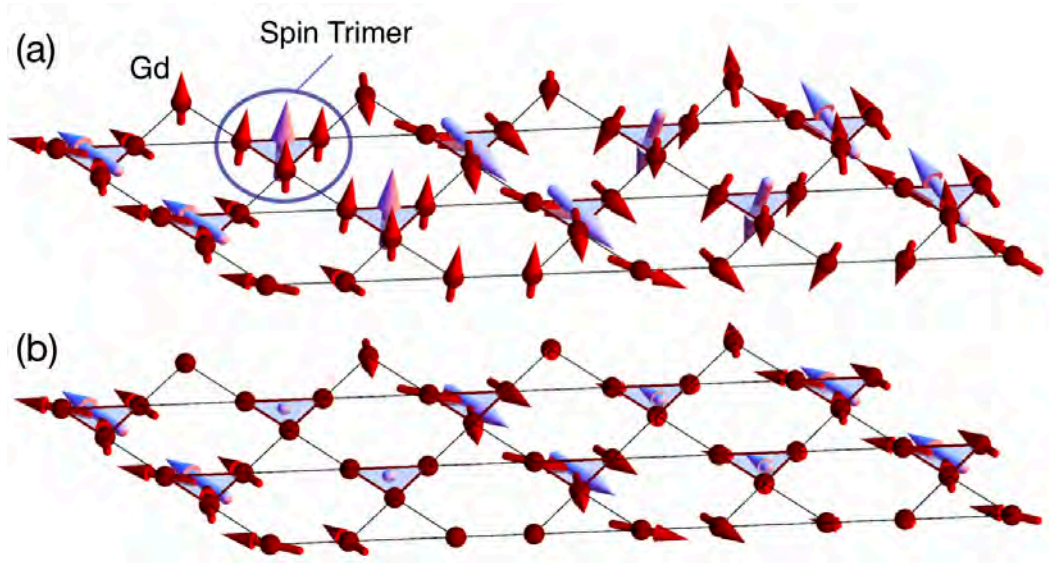


Figure 1: (a) Helical trimer spin structure below 17.5 K, propagating along the a^* -axis. The total spins of each trimer are represented by the bigger arrows at the center of the colored triangles. (b) Sinusoidal trimer spin structure between 17.5 K and 18.5 K.

An important problem of this sinusoidal structure is that there remain magnetic sites with small, or even vanishing, ordered moments. This means that there remains unreleased magnetic entropy, or degeneracy, which must be lifted at lower temperatures. The sinusoidal structure with $\mathbf{q} = (0.27, 0, 0)$ just below the Néel order reflects weak anisotropy in the c -plane and an intrinsic magnetic exchange interaction via the conduction electrons. However, it is not preferable to maintain this collinear structure down to lower temperatures because of the thermodynamic reason of magnetic entropy.

The spin system of Gd₃Ru₄Al₁₂ chooses to become helical below 17.5 K by inducing the c -axis spin component, i.e., by transforming the structure into a non-collinear form. In other words, the chiral degeneracy in the sinusoidal structure is lifted spontaneously by the transition to the helical structure, which allows all the Gd spins to fully develop.

Chirality plays important roles in a wide range of fields in nature from biology and chemistry to particle physics and materials science. In magnetic materials

with chiral crystal structure, the emergence of nontrivial chiral objects such as skyrmions and chiral soliton lattices have recently been attracting widespread interest both for applications and basic science. Although the crystal structure of Gd₃Ru₄Al₁₂ is not chiral, the present discovery of spontaneous breaking of chiral symmetry is expected to stimulate further research and a deeper understanding of chiral magnets [4].

REFERENCES

- [1] S. Nakamura, N. Kabeya, M. Kobayashi, K. Araki, K. Katoh and A. Ochiai, *Phys. Rev. B* **98**, 054410 (2018).
- [2] A. Ochiai, T. Inukai, T. Matsumura, A. Oyamada and K. Katoh, *J. Phys. Soc. Jpn.* **76**, 123703 (2007).
- [3] T. Matsumura, Y. Ozono, S. Nakamura, N. Kabeya and A. Ochiai, *J. Phys. Soc. Jpn.* **88**, 023704 (2019).
- [4] H. Amitsuka, *JPSJ News and Comments* **16**, 06 (2018).

BEAMLINE

BL-3A

T. Matsumura (Hiroshima Univ.)

Experimental Evidence of Orbital Ferrimagnetism by X-Ray Magnetic Circular Dichroism

We have experimentally investigated the magnetic properties of $\text{CoMnO}_3(0001)$ epitaxial films known to exhibit orbital ferrimagnetism. The films were grown by the reactive rf magnetron sputtering method. The magnetic anisotropy of $\text{CoMnO}_3(0001)$ thin films was found to have a large negative value of $K_u = -15.6 \pm 0.8 \text{ Merg/cm}^3$ at 300 K. X-ray magnetic circular dichroism revealed that the spin momenta of Mn and Co ions are oriented opposite to each other and a large orbital momentum comparable to the spin angular momentum emerges only on Co, indicating the orbital ferrimagnetic nature of CoMnO_3 .

CoMnO_3 has an ilmenite structure ($R\bar{3}$)[1–3] in which Co^{2+} and Mn^{4+} layers are alternately stacked along the c -axis [3]. Since Co^{2+} ($d^7\text{HS}$) and Mn^{4+} (d^3) possess $S = 3/2$, and are antiferromagnetically coupled through the superexchange interaction, the spin angular momenta of Co and Mn cancel each other out. However, the orbital angular momentum of Co^{2+} in the crystal field remains [3]. Since the experimentally estimated value of the magnetic moment is $0.72 \mu_B/\text{f.u.}$ ($M_s = 140 \text{ emu/cm}^3$ at 2 K), i.e., the same order of magnitude expected of the orbital angular momentum of Co^{2+} in an octahedral crystal field, this compound is termed an “orbital ferrimagnet.”

Because of the remaining orbital angular momentum, CoMnO_3 possesses significantly large magnetic anisotropy. Cloud and Jesson succeeded in roughly estimating the magnetic anisotropy of $K_{u1} + 2K_{u2} \sim -14 \pm 2 \text{ Merg/cm}^3$. They found that the c -axis is a magnetically hard axis, indicating that CoMnO_3 has a negative magnetic anisotropy constant [4]. Both the large orbital momentum and the large negative uniaxial anisotropy were partially explained within the framework of the single ion model of Co^{2+} , originally adopted for CoFe_2O_4 by Slonczewski [5]. Moreover, CoMnO_3 has a Néel temperature of 391 K [1]. Because of the unique origin of magnetism with a high transition temperature,

CoMnO_3 is an attractive compound from the viewpoint of both fundamental magnetism and applications including novel devices for spintronics based on the orbital angular momentum. However, previous experimental works regarding CoMnO_3 were mainly carried out on miniature single crystals, powder, or ceramic samples, not on sufficiently large single crystals or epitaxial films suitable for investigating the details of various properties [1–3, 6, 7]. Therefore, the magnetic and other physical properties of CoMnO_3 are not yet well understood.

CoMnO_3 thin films were grown by the reactive rf magnetron sputtering technique. X-ray magnetic circular dichroism (XMCD) experiments were also performed at BL-16A to evaluate the element-specific spin angular and orbital angular momenta [8–10]. XMCD measurements for the film were performed at room temperature. The photon energy range was for the Mn and Co $L_{2,3}$ edges. The XAS were determined by the total electron yield (TEY) method. A set of XAS (μ_+ and μ_-) was measured using circularly polarized light with opposite helicity in a magnetic field of 50 kOe, applied parallel to the photon direction. The film plane was inclined at 30° to both the incident photons and the magnetic field. The magnetic anisotropy constant (K_u) was measured by a magnetotorque meter.

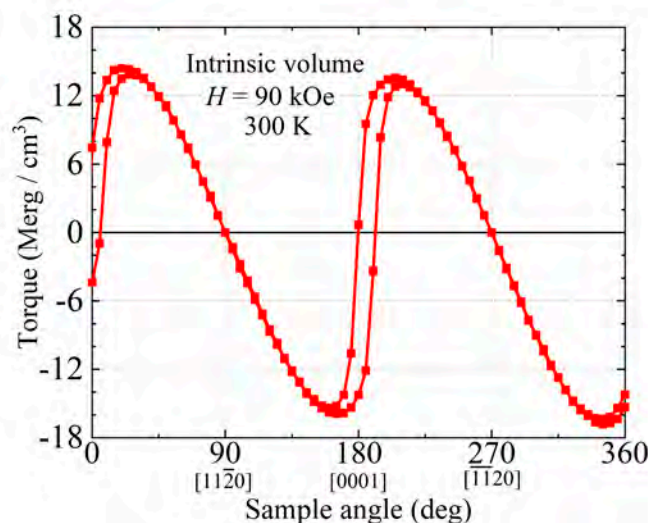


Figure 1: Magnetotorque curve of a CoMnO_3 thin film with a film intrinsic thickness of 69 nm and a nominal thickness of 90 nm at 90 kOe. The intrinsic thickness was evaluated by subtracting the magnetic dead layer from a nominal thickness.

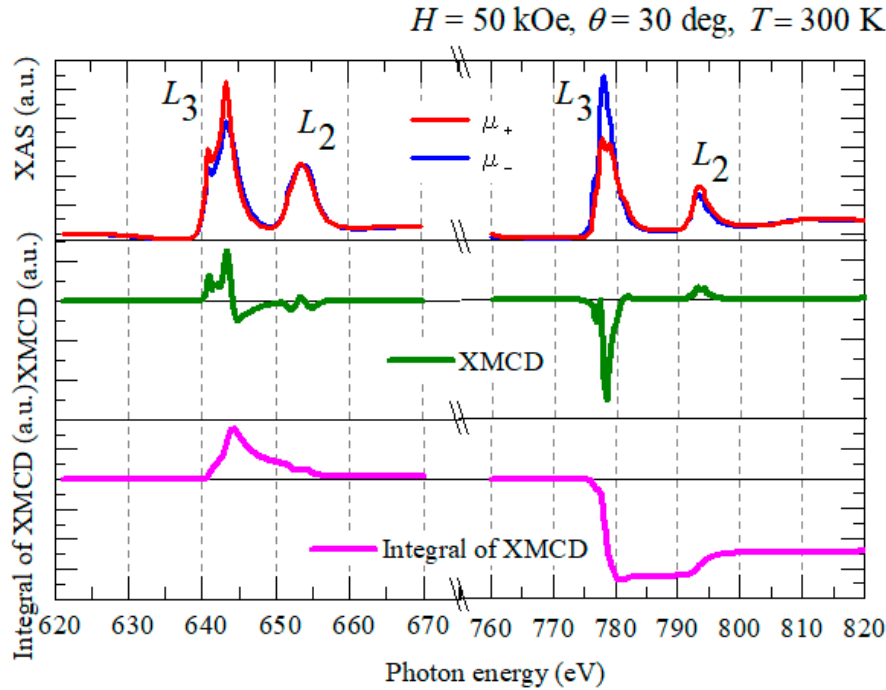


Figure 2: Mn and Co circularly polarized XAS (μ_+ and μ_-), XMCD spectra ($\mu_+ - \mu_-$), and the integral of XMCD spectra.

The magnetotorque curve of the CoMnO_3 thin film at 90 kOe is shown in **Fig. 1**. The measurements were performed at 300 K. The torque curve indicates that the magnetic easy axis lies in plane. Even at 90 kOe, the torque curve exhibits a sawtooth-wave-like shape with clear rotational hysteresis, indicating that the anisotropy field is significantly greater than 90 kOe. The uniaxial magnetic anisotropy energy can be written as $E = K_u^{\text{eff}} \sin^2 \theta$, where K_u^{eff} and θ are the effective uniaxial magnetic anisotropy constant and the angle between magnetization \mathbf{M} and the normal to the film, respectively. The observed K_u^{eff} comprises both magnetic anisotropy contributions from magnetocrystalline anisotropy K_u and shape anisotropy. K_u^{eff} is determined from peak to peak of the torque curve. Note that shape anisotropy is negligibly smaller than the value of K_u . Therefore, the intrinsic $K_u \approx K_u^{\text{eff}}$ of the CoMnO_3 thin film is found to be $-15.6 \pm 0.8 \text{ Merg/cm}^3$ at 300 K, which is almost the same as the previously reported value of $K_u = -14 \pm 2 \text{ Merg/cm}^3$ at room temperature [4].

Figure 2 shows Mn 2p XAS and XMCD spectra as well as those of Co 2p observed for the CoMnO_3 film. From XMCD sum rules of the XMCD spectra shown in **Fig. 2**, the $m_{\text{orb}} / m_{\text{spin}}$ ratios are determined to be 0.02 ± 0.00 for Mn and 0.33 ± 0.03 for Co. It is obvious that the larger contribution of the orbital angular moment comparable to the spin angular moment was found only for Co. In addition, by comparing the shapes of the XMCD spectra for Co and Mn, we can conclude that the

magnetic moments of Mn and Co are oriented in opposite directions. These results strongly indicate the orbital ferrimagnetic nature of CoMnO_3 .

The texts and figures in this article have been adapted from Ref. [11] with the authors' permission.

REFERENCES

- [1] T. J. Swoboda, R. C. Toole and J. D. Vaughan, *J. Phys. Chem. Solids* **5**, 293 (1958).
- [2] W. H. Cloud, *Phys. Rev.* **111**, 1046 (1958).
- [3] R. M. Bozorth and D. E. Walsh, *J. Phys. Chem. Solids* **5**, 299 (1958).
- [4] W. H. Cloud and J. P. Jesson, *J. Appl. Phys.* **37**, 1398 (1966).
- [5] J. C. Slonczewski, *Phys. Rev.* **110**, 1341 (1958).
- [6] A. Petric and H. Ling, *J. Am. Ceram. Soc.* **90**, 1515 (2007).
- [7] I. O. Troyanchuk, A. A. Shemyakov and V. K. Prokopenko, *Physica Status Solidi (a)* **113**, K107 (1989).
- [8] B. T. Thole, P. Carra, F. Sette and G. van der Laan, *Phys. Rev. Lett.* **68**, 1943 (1992).
- [9] P. Carra, B. T. Thole, M. Altarelli and X. Wang, *Phys. Rev. Lett.* **70**, 694 (1993).
- [10] J. Stöhr and H. König, *Phys. Rev. Lett.* **75**, 3748 (1995).
- [11] H. Koizumi, S. Sharmin, K. Amemiya, M. Suzuki-Sakamaki, J. Inoue and H. Yanagihara, *Phys. Rev. Mater.* **3**, 024404 (2019).

BEAMLINES

BL-12C and BL-16A

H. Koizumi¹, S. Sharmin¹, K. Amemiya^{2,3}, M. S-Sakamaki^{2,3,4}, J. Inoue¹ and H. Yanagihara^{1,5} (Univ. of Tsukuba, ²KEK-IMSS-PF, ³SOKENDAI, ⁴Gunma Univ., ⁵TREMS)

Emergence of Metallic Monoclinic States of Electron-Doped VO₂ Films

In order to study the origin of metallization of VO₂ induced by electron injection, we deposited K atoms onto the surface of VO₂ films and investigated the change in the electronic and crystal structures using *in situ* photoemission spectroscopy and X-ray absorption spectroscopy. K deposition onto the surface of insulating monoclinic VO₂ led to a phase transition to metal, in which the V-V dimerization characteristic to monoclinic VO₂ still existed. These results indicate the existence of a novel electronic phase, that is, a metallic monoclinic phase in the case of electron-doped VO₂.

Vanadium dioxide (VO₂) exhibits the metal–insulator transition (MIT) accompanied by a structural phase transition due to the dimerization of V ions at nearly room temperature [1]. Recently, it has been reported that the MIT in VO₂ can be controlled by application of a gate voltage using a field-effect transistor structure. However, the mechanism of the electric-field-induced MIT is still under debate [2, 3]. To understand the origin of the MIT induced by electrostatic injection of charge, it is crucial to obtain information on how the electronic and crystal structures of VO₂ change through the MIT phenomena. In this study, we performed electron doping of a VO₂ surface via *in situ* deposition of K atoms [4, 5], and investigated the change in the electronic and crystal structures via *in situ* photoemission spectroscopy (PES) and X-ray absorption spectroscopy (XAS), respectively.

The experiments were performed using the *in situ* PES–laser molecular beam epitaxy (MBE) system installed at BL-2A MUSASHI. The oxide-film growth, K deposition, and subsequent spectroscopic measurements were performed without exposing the samples

to air by transferring the samples among the chambers connected under ultrahigh vacuum.

Figure 1(a) shows the temperature dependence of the valence-band PES spectra of the VO₂ films (MIT temperature $T_{\text{MIT}} \sim 295$ K) before and after K deposition. For the bare VO₂ films before K deposition, the spectral change across the MIT is in excellent agreement with the results of previous studies [6]. When K atoms are deposited on the surface of the insulating VO₂ films at $T = 250$ K, a distinct Fermi-edge profile appears, indicating the metallization of VO₂ films induced by electron doping upon K deposition. In addition, the temperature-induced MIT also occurs in K/VO₂, while the T_{MIT} value of VO₂ films is suppressed to within 150–250 K by K deposition. The nearly unchanged peak position of the lower Hubbard band in the insulating K/VO₂ from that of insulating bare VO₂ films suggests that the ground states of K/VO₂ are the same as those of VO₂ films. These results suggest that the carrier-induced MIT is realized by surface carrier injection from K into VO₂ films.

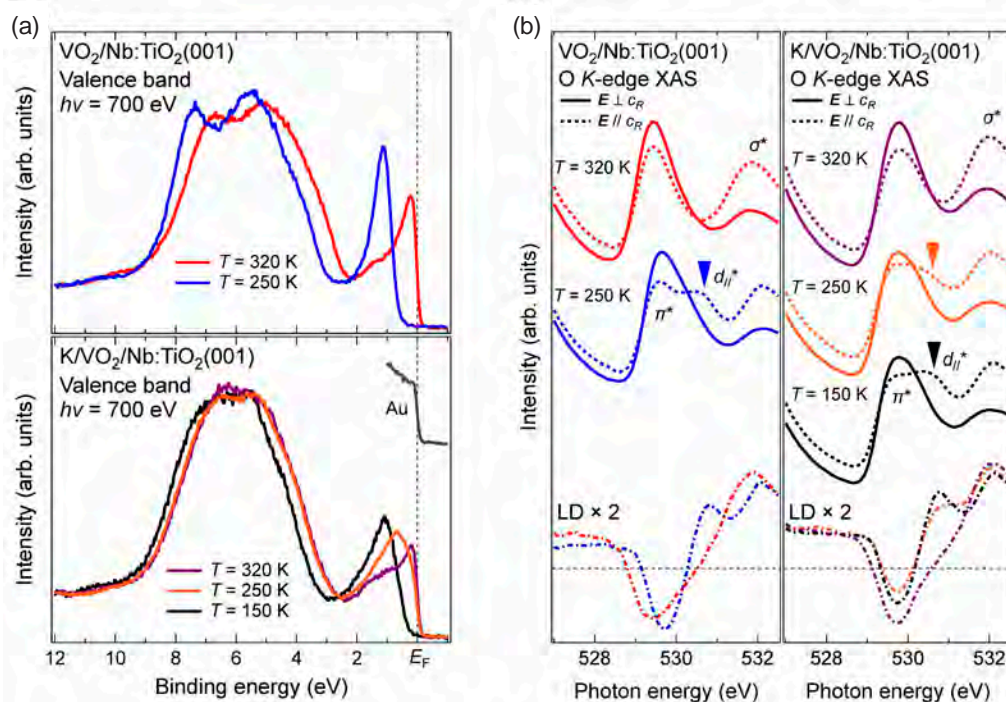


Figure 1: Temperature dependence of (a) valence-band PES spectra and (b) O K-edge XAS spectra with different polarizations and their LD spectra for VO₂/Nb:TiO₂(001) films before and after K deposition.

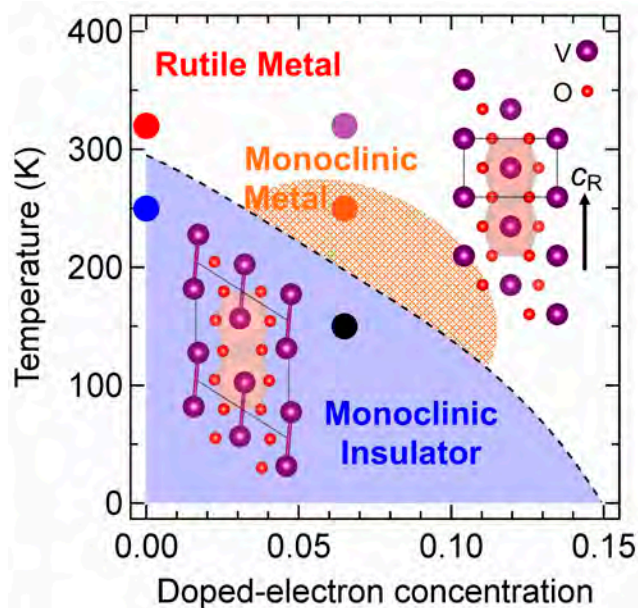


Figure 2: Possible electronic phase diagram of electron-doped VO₂(001) films. Colored solid circles represent spectroscopic measurement points. The inset shows the crystal structure of rutile and monoclinic VO₂. The c_R axis is defined as the c axis of the rutile structure.

On the other hand, when the measurement temperature is raised to 320 K, the coherent states at the Fermi level (E_F) evolve into a sharp peak structure reminiscent of that in the metallic rutile phase of VO₂. This means that the metallization states of K/VO₂ at 250 K might be different from the metallic phase of bare VO₂, as well as the high-temperature phase of K/VO₂. These results suggest that a certain different metallic phase exists at the phase boundary near the MIT in the electron-doped K/VO₂. In order to further investigate the metallization state in K/VO₂ from the viewpoint of crystal structures, we carried out polarization-dependent XAS measurements.

Figure 1(b) shows the temperature dependence of the oxygen K -edge XAS spectra with different polarizations and their linear dichroism (LD) of VO₂ films before and after K deposition. Additional shoulder structures at 530.8 eV can be identified with the $d_{||}^*$ state by inferring the polarization dependence of the XAS spectra, which is used as a fingerprint of the monoclinic structure with the V-V dimer in VO₂ [6]. The $d_{||}^*$ state is clearly observed in the XAS spectra of the insulating monoclinic VO₂ at 250 K, while the state disappears in the metallic rutile phase at 320 K. Intriguingly, the $d_{||}^*$ state indicative of dimerization of V ions in VO₂ is also observed for K/VO₂ at 250 K, although it showed a metallic behavior in the PES spectra [Fig. 1(a)]. These results indicate that the carrier-induced metallic phase in K/VO₂ can be categorized as a novel metallic phase maintaining the dimerization characteristic to the monoclinic phase of VO₂, termed the *metallic monoclinic phase*. Further-

more, the monoclinic metal undergoes a transition to the monoclinic insulator with decrease in temperature (150 K), and to the rutile metal with increase in temperature (320 K). These spectroscopic results suggest that the metallic monoclinic phase exists at the boundary between the insulating monoclinic and metallic rutile phases in the case of electron-doped VO₂ (see Fig. 2) [7].

REFERENCES

- [1] J. B. Goodenough, *J. Solid State Chem.* **3**, 490 (1971).
- [2] M. Nakano, K. Shibuya, D. Okuyama, T. Hatano, S. Ono, M. Kawasaki, Y. Iwasa and Y. Tokura, *Nature (London)* **487**, 459 (2012).
- [3] J. Jeong, N. Aetukuri, T. Graf, T. D. Schladt, M. G. Samant and S. S. P. Parkin, *Science* **339**, 1402 (2013).
- [4] Y. K. Kim, O. Krupin, J. D. Denlinger, A. Bostwick, E. Rotenberg, Q. Zhao, J. F. Mitchell, J. W. Allen and B. J. Kim, *Science* **345**, 187 (2014).
- [5] R. Yukawa, M. Minohara, D. Shiga, M. Kitamura, T. Mitsuhashi, M. Kobayashi, K. Horiba and H. Kumigashira, *Phys. Rev. B* **97**, 165428 (2018).
- [6] T. C. Koethe, Z. Hu, M. W. Haverkort, C. Schüßler-Langeheine, F. Venturini, N. B. Brookes, O. Tjernberg, W. Reichelt, H. H. Hsieh, H.-J. Lin, C. T. Chen and L. H. Tjeng, *Phys. Rev. Lett.* **97**, 116402 (2006).
- [7] D. Shiga, M. Minohara, M. Kitamura, R. Yukawa, K. Horiba and H. Kumigashira, *Phys. Rev. B* **99**, 125120 (2019).

BEAMLINE

BL-2A

D. Shiga^{1,2}, M. Minohara², M. Kitamura², R. Yukawa², K. Horiba² and H. Kumigashira^{1,2} (Tohoku Univ. -IMRAM, ²KEK-IMSS-PF)

Surface Electron Density Analysis of Organic Semiconductors

Surface relaxation in organic semiconductors should affect the performance of organic devices, but there have been few experimental studies. In order to clarify the general tendency of surface relaxation in organic semiconductors, we performed a systematic investigation of the electron density distribution as a function of depth on a series of organic semiconductor [*n*]phenacenes by using surface X-ray scattering measurements combined with holographic analysis and a first principles calculation. We demonstrated that, unlike the case of tetracene that shows a large relaxation, all the [*n*]phenacenes measured have little surface relaxation.

There has been remarkable recent progress in the development of organic device techniques. Organic electroluminescence displays are widely used for cell phones, and laser devices are also being studied. The application of organic semiconductors to various electronic devices requires higher carrier mobility, environmental stability, and smaller contact resistance. All of them are related to the energy level of molecular orbitals, and the mobility depends on the transfer integrals. Since the transfer integrals in molecular crystals depend on intermolecular distance as well as the relative angle of neighboring molecules, a knowledge of the molecular arrangement is desired to design better organic semiconductors. In many organic devices, the place where the carriers move is the surface or interface, and there-

fore the surface/interface structure is of importance. Structural modulation induced by the surface is known as surface relaxation or surface reconstruction, and is one of the central issues of surface science. Surface relaxation may be regarded as a surface induced polymorphism.

To date, the surface structure relaxation of organic semiconductors has been examined for rubrene and tetracene by using the surface X-ray scattering technique [1, 2]. Rubrene has no surface relaxation, while tetracene has significant relaxation. It is unclear whether organic semiconductors often have a relaxed surface. Therefore, we have examined the surface relaxation of organic semiconductors.

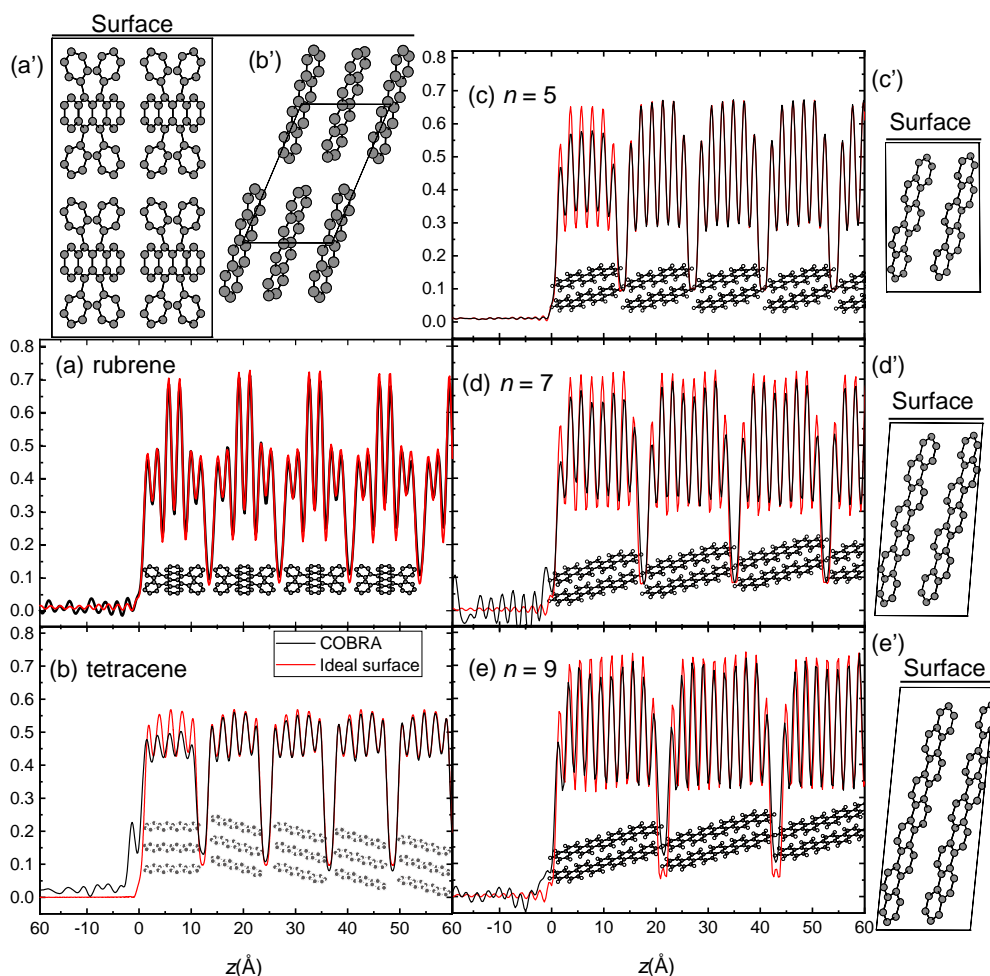


Figure 1: Depth profile of the electron densities for (a) rubrene, (b) tetracene [2], and (c)–(e) [*n*]phenacenes [3]. (a')–(e') show the molecular packing in the bulk unit cell.

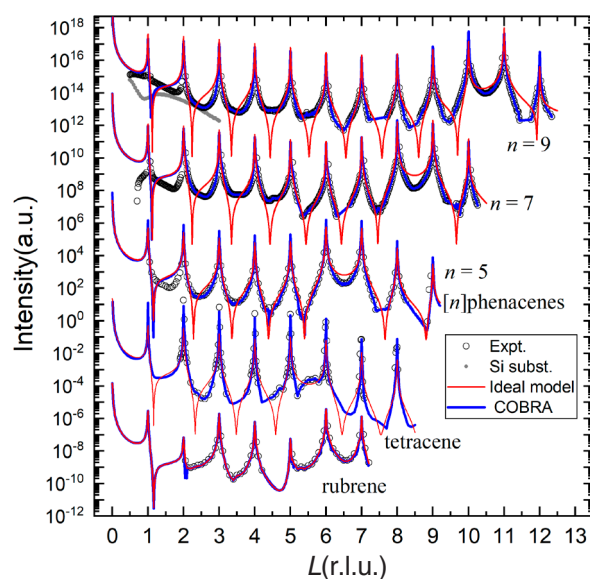


Figure 2: CTR scattering profiles of rubrene, tetracene, and $[n]$ phenacenes ($n = 5, 7$ and 9) single crystals. The unit for the horizontal axis is the length of $2c^*$ for rubrene, and c^* for others [2, 3].

There are several similarities and differences between rubrene and tetracene. Their highest occupied molecular orbitals and lowest unoccupied molecular orbitals are very similar. The main difference between them is the molecular packing as presented in Fig. 1. In order to study the effect of the molecular packing as well as the molecular size, we selected $[n]$ phenacenes as our samples [3].

Single-crystal samples of $[n]$ phenacenes were grown by the physical vapor transport method. The crystals were placed on Si(001) substrate. Surface X-ray scattering experiments along the c^* axis were performed at room temperature in air with the four-circle diffractometer installed at BL-3A. The two-dimensional pixel array detector allows us to measure the intensity profiles in a short time, typically one hour for measurements up to the 2θ angle close to the 004 Bragg reflection of Si substrate. Measured intensity profiles are shown in Fig. 2.

In order to perform phase retrieval analysis, the bulk crystal structure is required. Previous phase retrieval analyses for organic semiconductor surfaces [1, 2] were made with coherent Bragg rod analysis (COBRA) [4] based on the reported results of single-crystal structure analysis. Unfortunately, there is no report on the single-crystal structure analysis of $[n]$ phenacenes ($n \geq 6$) because of the difficulty of growing solid thick crystals; all the crystals were grown in a film shape, which prevents single-crystal structure analysis. To obtain the bulk crystal structure, we performed first principles calculations. Using the theoretically derived bulk structure, we performed COBRA on surface scattering intensity profiles.

The resulting electron density profiles of the $[n]$ phenacenes together with that of tetracene are shown

in Fig. 1. As can be seen, there is little relaxation in $[n]$ phenacenes, which have similar herringbone molecular packing with tetracene. The result shows that the herringbone packing is not the origin of the relaxation.

What makes the surface relaxed? Tetracene has a very similar structure to pentacene, which is known to have various polymorph structures. On the other hand, $[n]$ phenacenes have very stable structures, and no other polymorph structure has been reported. Although the number of examples that show a large surface relaxation is too small to make any decisive conclusion, we propose that the number of possible polymorph structures for the bulk crystal structure reflects the possible degree of surface relaxation.

REFERENCES

- [1] Y. Wakabayashi, T. Kimura and J. Takeya, *Phys. Rev. Lett.* **104**, 066103 (2010).
- [2] H. Morisaki, T. Koretsune, C. Hotta, J. Takeya, T. Kimura and Y. Wakabayashi, *Nature Commun.* **5**, 5400 (2014).
- [3] Y. Wakabayashi, M. Nakamura, K. Sasaki, T. Maeda, Y. Kishi, H. Ishii, N. Kobayashi, S. Yanagisawa, Y. Shimo and Y. Kubozono, *J. Am. Chem. Soc.* **140**, 14046 (2018).
- [4] Y. Yacoby, M. Sowwan, E. Stern, J. O. Cross, D. Brewster, R. Pindak, J. Pitney, E. M. Dufresne and R. Clarke, *Nature Mater.* **1**, 99 (2002).

BEAMLINE

BL-3A

Y. Wakabayashi¹, H. Ishii², N. Kobayashi², S. Yanagisawa³ and Y. Kubozono⁴ (1Tohoku Univ., 2Univ. of Tsukuba, 3Univ. of the Ryukyus, 4Okayama Univ.)

ARPES Study of the Superconducting Parent Compound Pr_2CuO_4 in Thin Film Form

In high-temperature cuprate superconductors, carrier doping has been regarded as essential for superconductivity. Recent studies demonstrated that reduction annealing alone can induce superconductivity in thin films of T' -type cuprates without nominal electron doping through Ce substitutions. In order to reveal the low-energy electronic states relevant to the superconductivity, we have conducted angle-resolved photoemission spectroscopy measurements on thin films of the superconducting Ce-free T' -type cuprate Pr_2CuO_4 . The obtained band structure and Fermi surface of the superconducting Pr_2CuO_4 are similar to those of superconducting Ce-doped bulk single crystals, suggesting that the superconducting Pr_2CuO_4 is doped with electrons despite the absence of Ce substitutions.

High-temperature superconductivity emerges in cuprates when an antiferromagnetic (AF) Mott-insulating parent compound is doped with carriers. In the electron-doped cuprates $\text{Ln}_{2-x}\text{Ce}_x\text{CuO}_4$ (Ln: rare earth) with a so-called T' -type structure, where Cu atoms are coordinated by four O atoms in the square-planar configuration, electron doping is achieved by substituting Ce^{4+} for Ln^{3+} . Recently, the electronic structure of T' -type cuprates has attracted renewed interest since superconductivity is realized without Ce substitutions in thin-film samples [1]. This fact challenges the common belief that the parent cuprates are Mott insulators. An indispensable treatment to realize superconductivity in the T' -type cuprates is post-growth reduction annealing. The primary role of reduction annealing is the removal of impurity apical oxygen atoms [2], thereby suppressing the quasi-particle scattering rate and AF correlation. Furthermore, recent angle-resolved photoemission spectroscopy

(ARPES) studies on bulk crystals have found a significant increase of the doped electron concentration after reduction annealing from estimates of the Fermi surface area [3, 4]. The increase of the electron concentration is associated with the loss of oxygen atoms not only from the apical sites but also from the regular sites. Indeed, the possibility of oxygen-vacancy creation has been pointed out by previous infrared and Raman spectroscopy studies [5]. In this case, Ce concentration no longer represents the doped electron concentration. It is thus imperative to determine the electron concentration of the superconducting (SC) Ce-free T' -type cuprates from direct measurements.

The fact that the superconductivity can only be realized in thin films has impeded studies of the electronic structure of Ce-free T' -type cuprates. Once thin-film surfaces are contaminated upon being taken out from the growth chamber, surface-sensitive probes such as

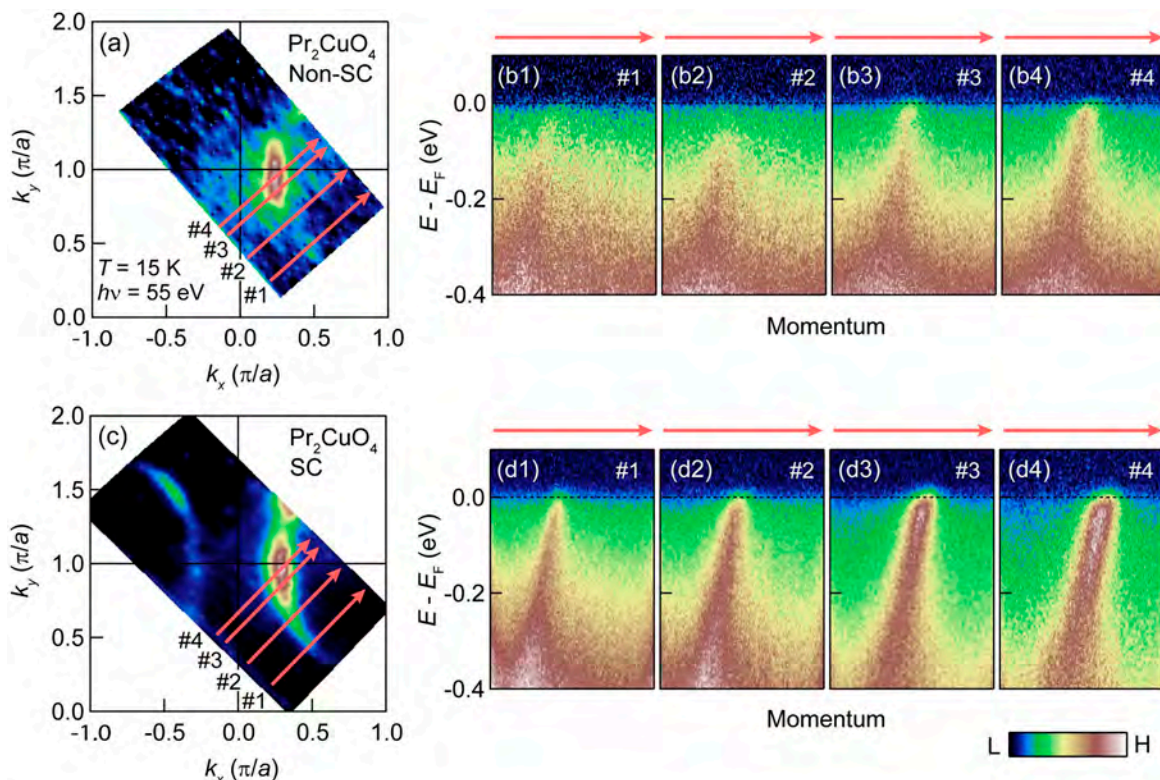


Figure 1: ARPES spectra of Pr_2CuO_4 thin films. (a), (b1)–(b4) Fermi surface and band images along cuts #1–#4, respectively, of the non-SC sample. (c), (d1)–(d4) The same as (a) and (b1)–(b4), respectively, but for the SC sample.

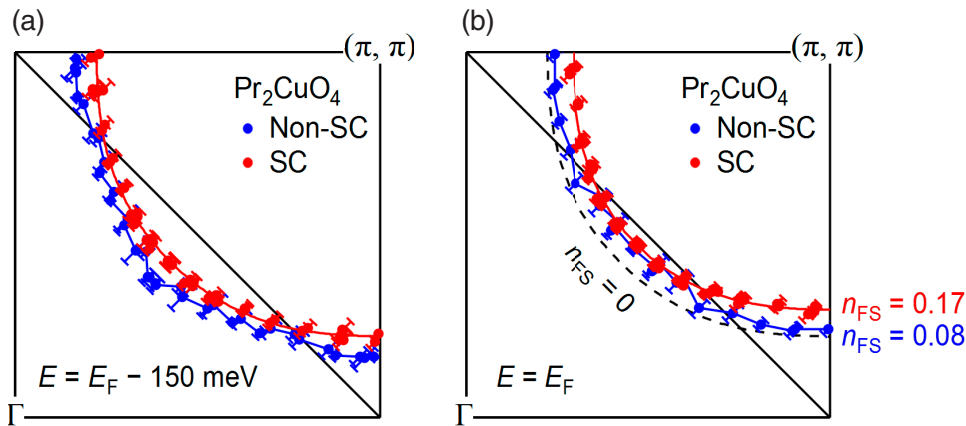


Figure 2: Constant-energy surfaces and Fermi surfaces of Pr_2CuO_4 thin films. (a) Constant energy surfaces of the non-SC (blue) and SC (red) samples at $E = E_F - 150$ meV. (b) Fermi surface displayed in the same color code as (a). Dotted curve represents the hypothetical Fermi surface at half-filling ($n = 0$) for comparison.

ARPES cannot be applied. To overcome this issue, we have developed a capping method. Specifically, two Pr_2CuO_4 thin films [$T_c = 0$ (non-SC), 25.5 K (SC)] for ARPES measurements were first synthesized at NTT Basic Research Laboratories using the molecular beam epitaxy method on GdScO_3 (110) substrates [6]. After the growth, the films were rapidly cooled down to 70°C and amorphous Se was evaporated onto the film surfaces up to a thickness of ~ 50 nm. The films were transferred in air from NTT Basic Research Laboratories to BL-2A. Then, the films were heated inside the preparation chamber at 150°C for 30 minutes under a vacuum of better than 2×10^{-9} Torr to desorb the Se cap, and transferred in vacuo to the measurement chamber. X-ray core-level photoemission spectroscopy measurements performed prior to each ARPES measurement confirmed negligible contamination on the surface after the desorption of the Se layers.

The obtained Fermi surface and ARPES spectra of two Pr_2CuO_4 thin films [7] are summarized in Fig. 1. For the non-SC sample, photoemission intensity is suppressed around the hot spot where the Fermi surface and AF Brillouin zone boundary cross [Fig. 1(b2)]. This is called the AF pseudogap and presumably arises from band folding due to AF short-range order. In contrast, for the SC sample, the suppressed intensity recovers [Fig. 1(d2)] and the Fermi surface becomes continuous over the entire Brillouin zone [Fig. 1(c)]. This observation suggests the strong reduction of AF correlation length and/or magnitude of magnetic moments in the SC sample, consistent with the emergence of superconductivity out of competition with the AF order.

Figure 2(a) displays constant energy surfaces of Pr_2CuO_4 thin films at $E = E_F - 150$ meV. These constant energy surfaces are hole-like and centered at (π, π) . Apparently, the SC sample has a smaller area of the surface, suggesting a larger electron concentration. By directly measuring the area of the Fermi surface [Fig. 2(b)], the doped electron concentration of the non-SC and SC samples were estimated to be $n = 0.08$ and

0.17 per Cu, respectively, considerably deviating from half-filling ($n = 0$). The electron concentration of 0.17 is comparable to that of bulk SC samples (0.13–0.17). Fitting of the band structure to the tight-binding model also yielded nearly the same hopping parameters for the SC Pr_2CuO_4 and SC Ce-doped bulk samples. Therefore, the overall electronic structure is similar between the SC Ce-free T' -type cuprates and SC Ce-doped bulk samples. The present study thus highlights the importance of considering the actual doped electron concentration rather than the Ce concentration when discussing the electronic structure of T' -type cuprate superconductors.

REFERENCES

- [1] A. Tsukada, Y. Krockenberger, M. Noda, H. Yamamoto, D. Manske, L. Alff and M. Naito, *Solid State Commun.* **133**, 427 (2005).
- [2] P. G. Radaelli, J. D. Jorgensen, A. J. Schultz, J. L. Peng and R. L. Greene, *Phys. Rev. B* **49**, 15322 (1994).
- [3] M. Horio, T. Adachi, Y. Mori, A. Takahashi, T. Yoshida, H. Suzuki, L. C. C. Ambolode, K. Okazaki, K. Ono, H. Kumigashira, H. Anzai, M. Arita, H. Namatame, M. Taniguchi, D. Ootsuki, K. Sawada, M. Takahashi, T. Mizokawa, Y. Koike and A. Fujimori, *Nat. Commun.* **7**, 10567 (2016).
- [4] D. Song, G. Han, W. Kyung, J. Seo, S. Cho, B. S. Kim, M. Arita, K. Shimada, H. Namatame, M. Taniguchi, Y. Yoshida, H. Eisaki, S. R. Park and C. Kim, *Phys. Rev. Lett.* **118**, 137001 (2017).
- [5] P. Richard, G. Riou, I. Hetel, S. Jandl, M. Poirier and P. Fournier, *Phys. Rev. B* **70**, 064513 (2004).
- [6] Y. Krockenberger, M. Horio, H. Irie, A. Fujimori and H. Yamamoto, *Appl. Phys. Express* **8**, 053101 (2015).
- [7] M. Horio, Y. Krockenberger, K. Koshiishi, S. Nakata, K. Hagiwara, M. Kobayashi, K. Horiba, H. Kumigashira, H. Irie, H. Yamamoto and A. Fujimori, *Phys. Rev. B* **98**, 020505(R) (2018).

BEAMLINE

BL-2A

M. Horio¹, Y. Krockenberger², K. Koshiishi¹, S. Nakata¹, K. Hagiwara¹, M. Kobayashi³, K. Horiba³, H. Kumigashira³, H. Irie², H. Yamamoto² and A. Fujimori¹ (¹The Univ. of Tokyo, ²NTT-BRL, ³KEK-IMSS-PF)

In situ Angle-Resolved Photoelectron Spectroscopy Studies of Two-Dimensional Electronic States at Anatase TiO₂ (001) Surface Controlled by K Adsorption

The nature of the intriguing metallic electronic structures appearing at the surface of anatase titanium dioxide (a-TiO₂) remains to be elucidated mainly owing to the difficulty of controlling the depth distribution of the oxygen vacancies. In this study, K atoms were adsorbed onto the (001) surface of a-TiO₂ to dope electrons into the a-TiO₂ and to confine the electrons in the surface region. The success of the electron doping and its controllability were confirmed by performing *in situ* angle-resolved photoelectron spectroscopy as well as core-level measurements. Clear subband structures were observed in the surface metallic states, indicating the creation of quasi-two-dimensional electron liquid states in a controllable fashion.

Techniques to control the low-dimensional electronic states appearing at the surface and interface of oxide semiconductors have attracted much attention for designing future quantum electronic devices. Recently, the formation of quasi-two-dimensional electron liquid (q2DEL) states induced by photoirradiation has been reported at the surface of anatase titanium dioxide (a-TiO₂) [1]. However, owing to the difficulty of controlling the distribution of oxygen vacancies in the depth direction, the dimensionality of the electronic states generated by photoirradiation remains a controversial issue [1, 2]. Therefore, in this study, we proposed an alternative route to address the q2DEL states: we adsorbed K atoms on the (001) surface of a-TiO₂ for doping electrons in the surface region and investigated the formed q2DEL states by *in situ* angle-resolved photoemission spectroscopy (ARPES) [3].

Figure 1(a) shows a series of X-ray photoemission spectroscopy (XPS) spectra taken as a function of K adsorption. The K deposition onto the (001) surface of a-TiO₂ causes a weak but distinct structure corre-

sponding to Ti³⁺ states to appear at a binding energy of 457.5 eV, indicating that electrons are transferred from the K atoms to the a-TiO₂ film and that the doped electrons accumulate near the surface region accessible by the present XPS measurements [~ 1 nm away from the a-TiO₂ surface (the interface between K and a-TiO₂)]. As the amount of K deposition increases further, the Ti³⁺ states exhibit systematic evolution. These results imply that a certain amount of electron doping is induced by K deposition. The evolution of the Ti³⁺ states as a function of K deposition is summarized in Fig. 1(b). The occurrence of electron doping is also confirmed by the shift of the Ti⁴⁺ peak by ~ 190 meV due to band bending.

The increment of the sheet carrier density (n_{2D}) associated with K deposition has been clearly observed in *in situ* ARPES measurements. Figure 2(a) shows a series of ARPES images taken along the [100] direction as a function of K adsorption. Clear subband structures are observed in all of the ARPES images for the K-adsorbed surfaces, indicating the 2D nature of the observed conduction bands. By deposition of K atoms onto the a-TiO₂ surface, the Fermi momentum (k_F) determined from momentum distribution curves (MDCs) increases from 0.11 \AA^{-1} for bare a-TiO₂ film to 0.19 \AA^{-1} for a-TiO₂ film with 0.5 \AA K adsorption. Because a-TiO₂ forms a Ti-3d- t_{2g} d_{xy} -derived circular Fermi surface centered at the $\bar{\Gamma}$ point, the increase in k_F may reflect the increase in n_{2D} by K deposition [4]. The n_{2D} values obtained from the Luttinger volumes based on the assumption of spin degeneracy of the subbands are plotted in Fig. 2(b) as a function of K deposition. The n_{2D} value steeply increases with increasing K deposition and seems to saturate at 0.3 \AA . In contrast to the saturation of n_{2D} at 0.3 \AA K deposition, in the Ti 2p core level shown in Fig. 1 the intensity of Ti³⁺ states continues to increase after 0.3 \AA K deposition and seems to saturate at about 0.8 \AA . Assuming that the Ti³⁺ states observed in the Ti-2p core levels reflect the contributions of both localized and mobile electrons (namely, activated carriers whose density corresponds to n_{2D}) [5], these results suggest the charges transferred from K atoms to a-TiO₂ are partially trapped in the surface region.

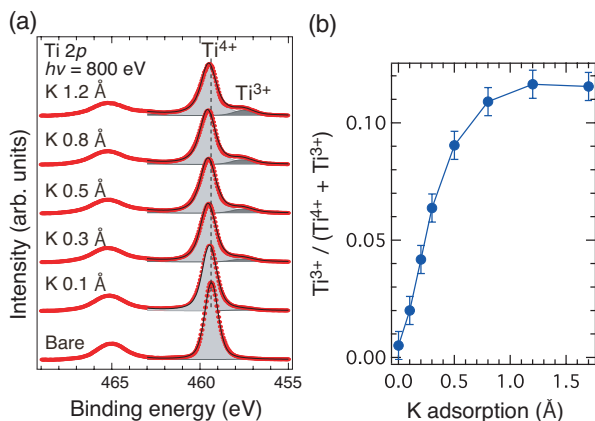


Figure 1: (a) Ti-2p core-level spectra of a-TiO₂ obtained by varying the coverage of adsorbed K atoms. The curve-fitting results for the Ti-2p_{3/2} states are presented, where the components of the Ti⁴⁺ and Ti³⁺ states are indicated by different hatching. The dashed line indicates the peak position of the Ti-2p_{3/2} states for a bare a-TiO₂ (001) surface. (b) The plot of relative intensities of the Ti³⁺ states as a function of adsorbed K.

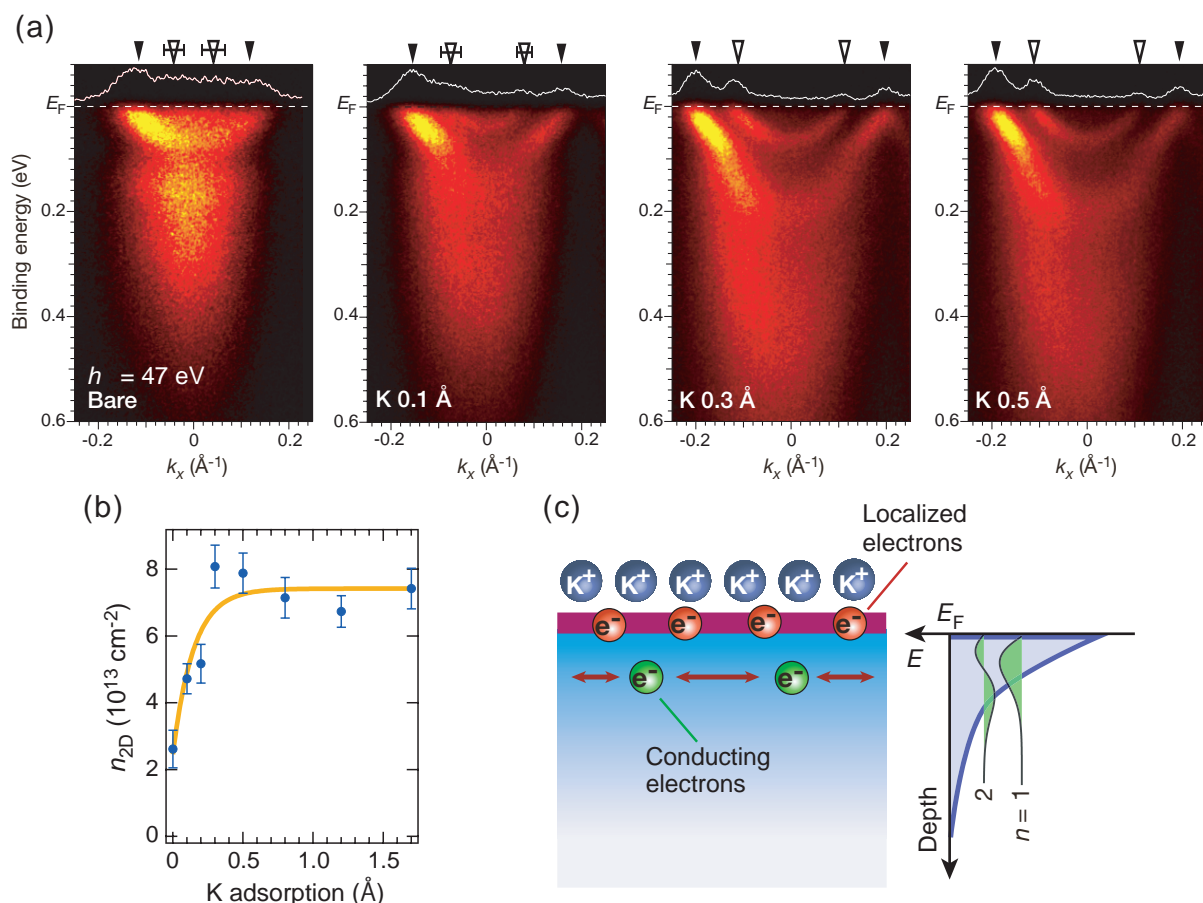


Figure 2: (a) ARPES images taken at $h\nu = 47$ eV for K-adsorbed surfaces of a-TiO₂ with varying K coverage. The ARPES spectra were measured along the k_x direction across the $\bar{\Gamma}_{10}$ point. The MDCs at the Fermi level (E_F) with an energy window of 10 meV are also shown in the respective images. (b) The plot of n_{2D} estimated from ARPES measurements as a function of K coverage. (c) Schematic illustration of the possible structure model explaining the charge transfer from adsorbed K atoms to an a-TiO₂ surface and the resulting accumulation-layer formation. The schematics of the potential structure and the eigenfunctions of the first ($n = 1$) and second ($n = 2$) subbands are shown on the right side.

The possible structure model explaining charge transfer from adsorbed K atoms to an a-TiO₂ surface and the resulting accumulation-layer formation is drawn in Fig. 2(c). Some of the transferred electrons may be preferentially accumulated in the surface regions initially. Analysis of the observed quantized states with a triangular wedge potential suggests that the activated carriers contributing to the formation of q2DEL states are confined in the surface (interface) region extending to a depth of a few nanometers, although the excess electrons could be trapped around K ions and/or oxygen vacancies at the interface between the K and a-TiO₂. Consequently, these results indicate that doping of electrons onto the a-TiO₂ is achieved by chemical adsorption of K atoms onto the a-TiO₂. Clear subband structures are observed in the ARPES images for the surface metallic states, indicating the creation of q2DEL states in a controllable fashion.

REFERENCES

- [1] T. C. Rödel, F. Fortuna, F. Bertran, M. Gabay, M. J. Rozenberg, A. F. Santander-Syro and P. Le Fèvre, *Phys. Rev. B* **92**, 041106 (2015).
- [2] S. Moser, L. Moreschini, J. Jačimović, O. S. Barišić, H. Berger, A. Magrez, Y. J. Chang, K. S. Kim, A. Bostwick, E. Rotenberg, L. Forró and M. Grioni, *Phys. Rev. Lett.* **110**, 196403 (2013).
- [3] R. Yukawa, M. Minohara, D. Shiga, M. Kitamura, T. Mitsuhashi, M. Kobayashi, K. Horiba and H. Kumigashira, *Phys. Rev. B* **97**, 165428 (2018).
- [4] Z. Wang, Z. Zhong, S. McKeown Walker, Z. Ristic, J. Z. Ma, F. Y. Bruno, S. Riccò, G. Sangiovanni, G. Eres, N. C. Plumb, L. Patthey, M. Shi, J. Mesot, F. Baumberger and M. Radovic, *Nano Lett.* **17**, 2561 (2017).
- [5] A. Koitzsch, J. Ocker, M. Knupfer, M. Dekker, K. Dörr, B. Büchner and P. Hoffmann, *Phys. Rev. B* **84**, 245121 (2011).

BEAMLINE

BL-2A

R. Yukawa¹, M. Minohara¹, D. Shiga^{1,2}, M. Kitamura¹, T. Mitsuhashi^{1,2}, M. Kobayashi¹, K. Horiba¹ and H. Kumigashira^{1,2} (¹KEK-IMSS-PF, ²Tohoku Univ.)

Anatomy of Interfacial Spin-Orbit Coupling in Co/Pd Multilayers

Element-specific orbital magnetic moments and their anisotropies in perpendicularly magnetized Co/Pd multilayers are investigated using Co *L*-edge and Pd *M*-edge angle-dependent X-ray magnetic circular dichroism. We show that the orbital magnetic moments in Co are anisotropic, whereas those in Pd are isotropic. First-principles density-functional-theory calculations also suggest similar results through the Co/Pd interfacial proximity effects. We conclude that the orbital-resolved anatomy of Co/Pd interfaces reveals that the orbital moment anisotropy in Co and spin-flipped transition related to the quadrupoles in Pd are essential for the appearance of perpendicular magnetic anisotropy, yielding important guidelines for the design of *spin-orbitronic* materials.

Ultrathin Co/Pd multilayers are artificial nanomaterials that exhibit perpendicular magnetic anisotropy (PMA), due to the spin-orbit interactions, achieved through interfacial chemical bonding. Regarding applications, after the development of artificially synthesized PMA, researchers have pointed out the possibility of ultra-high density recording media [1]. Extensive studies have examined the interfaces of ultra-thin magnetic multilayers and nanostructures. Studies on Co atoms performed using X-ray magnetic circular dichroism (XMCD) have suggested the enhancement of orbital magnetic moments at the interfacial Co that is adjacent to Pd [2]. It is well known that the PMA emerges due to the cooperative effects between spin moments in 3*d* transition metals (TMs) and large spin-orbit interactions in non-magnetic 4*d* or 5*d* TMs. Co/Pd interfaces and multilayers have also been employed to demonstrate the photo-induced precession of magnetization and the creation of skyrmions using the interfacial Dzyaloshinskii-Moriya interaction, and magnetization reversal using the spin-orbit torque phenomena. Despite these promising studies on Co/Pd interfaces, the interfacial PMA, including the anisotropic orbital magnetic moments, has not been fully understood for both Co and Pd sites. Bruno and

van der Laan theoretically proposed an orbital moment anisotropy in 3*d* TMs within the second-order perturbation (the weak coupling) of the spin-orbit interaction for more than half-occupied electrons [3, 4]. However, in the case of strong spin-orbit coupling in 4*d* or 5*d* TMs, the validity of this perturbative formula has been debated. In order to study the mechanisms of PMA in Co/Pd multilayers, the orbital magnetic-moment contributions of each element have to be explicitly considered. However, it is challenging to study the anisotropy of the orbital magnetic moments of both Co and Pd elements using one specific experiment, due to the challenges in detecting the induced magnetic moments, and of Pd in particular.

For the interfacial Pd, the magnetic dipole contribution through the quadrupole interactions between dipoles is assessed quantitatively. We focus on the anisotropy of orbital moments at the Co/Pd interfaces using XMCD and first-principles density functional theory (DFT) calculations, which provide element- and layer-resolved contributions that reveal the mechanism of PMA. Here, we discuss the anisotropies of both spin and orbital moments of Co and Pd using angle-dependent XMCD data and DFT calculations.

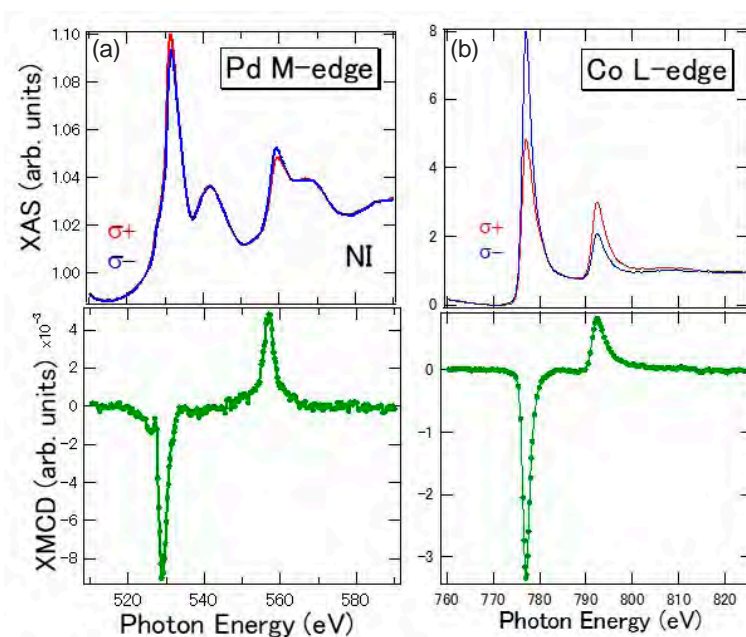


Figure 1: XAS and XMCD of (a) Pd *M*-edge and (b) Co *L*-edge in perpendicularly magnetized Co (0.69 nm)/Pd (1.62 nm) multilayer measured in the normal incidence (NI) configuration.

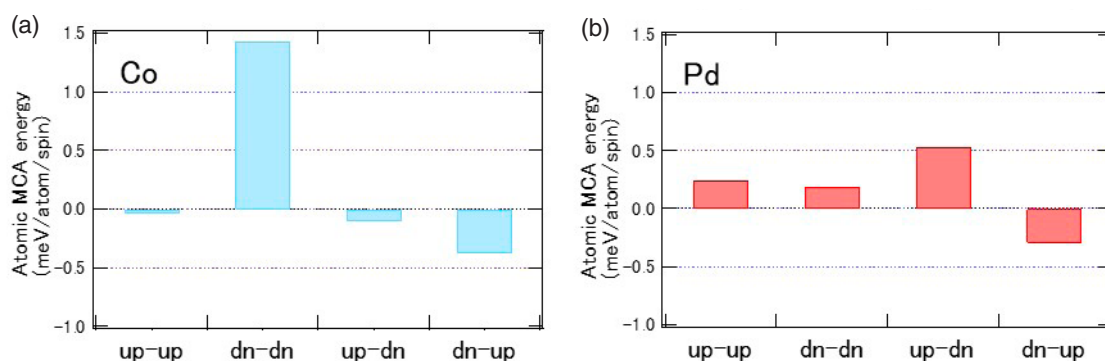


Figure 2: Bar graph of the second-order perturbative contribution of the spin-orbit interaction to the magneto-crystalline anisotropy (MCA) energy at the interfacial atomic sites of (a) Co and (b) Pd for the Pd (8 monolayer (ML))/Co (4 ML) deduced from a DFT calculation, using in-plane lattice constant $a_{||} = 0.391$ nm.

We prepared two kinds of samples of Co/Pd multilayered structures: Co (0.69 nm)/Pd (1.62 nm) for PMA and Co (1.03 nm)/Pd (1.62 nm) for in-plane anisotropy with stacking of five periods on the Si substrates [5]. Sample surfaces were sputtered by Ar ions before the XMCD measurements in order to remove the oxygen contamination. We performed XMCD experiments at BL-7A. Total electron yield mode was adopted. A magnetic field of ± 1.2 T was applied along the direction of the incident polarized soft X-ray.

We successfully observed clear XMCD signals in Pd *M*-edges after the removal of surface contamination, as shown in Fig. 1. Although the XAS line shapes overlap with those of O *K*-edge absorption, clear XMCD signals induced by the proximity with Co layers are observed due to the proper surface cleaning. The Pd *M*-edge XMCD line shapes in both PMA and in-plane anisotropy samples are almost identical, which suggests isotropic orbital moments in Pd, within the detection limits. This indicates that the isotropic finite orbital moments in Pd do not directly contribute to the PMA. On the other hand, for the PMA sample, clear Co *L*-edge XAS and XMCD with angular dependence reveal the enhancement of orbital moments in the surface normal direction because of PMA.

Next, we discuss the quadrupole-like contribution of the interfacial Pd layer from the results of angular dependent XMCD. Our Pd XMCD results indicate that the Pd orbital moments induced at the interface are isotropic. Note that the magnetic dipole term m_T is an order of magnitude smaller than the orbital moments, i.e., $0.005 \mu_B$, comparable with the detectable limits. Therefore, the relatively large spin-orbit coupling constant and small Pd exchange splitting contribute to the appearance of PMA by means of quadrupole-like interactions through the interfacial proximity effects.

Figure 2 represents the contributions of the crystalline magnetic anisotropy at each atomic site by DFT calculations. Four types of spin transition processes occur between the occupied and unoccupied states within the second-order perturbation of the spin-orbit interaction. For Co sites, the transition between down-down spin states is dominant, suggesting the conservation of spin states in the transition, which can be explained using the Bruno model assuming a large spin splitting. In contrast, for Pd, the spin-flipped transitions between up-down and down-up states become dominant due to the small band splitting, hence both spin-preserved and spin-flipped processes occur near the Fermi level. These results are consistent with the angular-dependent XMCD in Co and Pd sites.

In summary, we investigated the orbital-resolved interfacial electronic structures in the Co/Pd system and estimated the spin and orbital moments and magnetic dipole contribution [6].

REFERENCES

- [1] M. T. Johnson, P. J. H. Bloemenz, F. J. A. den Broedery and J. J. de Vries, *Rep. Prog. Phys.* **59**, 1409 (1996).
- [2] Y. Wu, J. Stöhr, B. D. Hermsmeijer, M. G. Samant and D. Weller, *Phys. Rev. Lett.* **69**, 2307 (1992).
- [3] P. Bruno, *Phys. Rev. B* **39**, 865(R) (1989).
- [4] G. van der Laan, *J. Phys. Condens. Matter* **10**, 3239 (1998).
- [5] K. Yamamoto, T. Matsuda, K. Nishibayashi, Y. Kitamoto and H. Munekata, *IEEE Transaction on Magnetism* **49**, 3155 (2013).
- [6] J. Okabayashi, Y. Miura and H. Munekata, *Sci. Rep.* **8**, 8303 (2018).

BEAMLINE

BL-7A

J. Okabayashi¹, Y. Miura² and H. Munekata³ (¹The Univ. of Tokyo, ²NIMS, ³Tokyo Tech.)

Detection and Classification of Crystallographic Defects in Wide Bandgap Semiconductor Materials for Next-Generation Power Switching Devices

Crystallographic defects, especially dislocations in the wide bandgap semiconductors SiC, GaN and AlN, have been revealed and classified using X-ray topography (XRT). By analyzing the geometrical features and the appearances of the dislocation-related contrasts in XRT images, dislocation density, dislocation types in terms of the Burgers vector and their distribution across the entire wafer were obtained.

GaN, SiC and AlN are good candidates for the fabrication of next-generation power switching devices that can operate at high voltage and large current, owing to their remarkable physical properties [1]. However, crystallographic defects, especially dislocations, in these materials are detrimental as they strongly affect the device performance, lifetime and reliability [2, 3]. It is therefore important to reveal and classify dislocations in bulky substrates and epitaxial layers to develop dislocation reduction strategies for crystal growth and for understanding the role that each type of dislocation plays in power devices.

Synchrotron X-ray topography (XRT) is a non-destructive technique to observe dislocations in these materials. It provides a two-dimensional intensity mapping of the X-rays diffracted by a crystal. Because the distortion of crystal planes around a dislocation results in a diffraction direction different to that of the host matrix, dislocations can be visualized by forming contrast different to the background of the defect-free area. A schematic drawing of the experimental setup and principle of XRT observation is shown in Fig. 1. In this report, observation of dislocations in GaN [4] is described as an example; similar observations were carried out for SiC and AlN, which also have a hexagonal crystal structure [5, 6].

A commercial ammono-thermal GaN sample was observed. X-ray diffraction (XRD) measurements showed a radius of curvature of {0001} planes greater than 100 meters. This large radius of curvature is an indispensable characteristic for XRT observation. Synchrotron monochromatic-beam XRT ($\lambda = 1.127 \text{ \AA}$) was recorded from the CMP-treated Ga-face. Asymmetric diffractions with six equivalent diffraction vectors \mathbf{g} of 11–26 were applied by rotating the sample every 60° with respect to its surface normal, in addition to a symmetric diffraction with $\mathbf{g} = 0008$. Diffraction planes (visualized by VESTA [7]) are shown in Fig. 1. Nuclear emulsion plates were used to record XRT images. The topmost $10 \mu\text{m}$ of the surface of the sample makes a major contribution to the XRT images.

Dislocations in GaN are mainly threading dislocations (TD) propagating nearly along the c-axis. They can be categorized into edge-type (ED, $\mathbf{b} = m\mathbf{a}$), screw-type (SD, $\mathbf{b} = n\mathbf{c}$), and mixed-type (MD, $\mathbf{b} = n\mathbf{c} + m\mathbf{a}$, $n, m = 1, 2, \dots$), according to their Burgers vectors. Spot-shaped contrasts in all seven XRT images (not shown) taken with six equivalent \mathbf{g} -vectors of 11–26, and $\mathbf{g} = 0008$ have been found to have a one-to-one correlation in position. According to the $\mathbf{g} \cdot \mathbf{b}$ invisibility criterion (\mathbf{g} is the diffraction vector and \mathbf{b} the Burgers vector), images taken with $\mathbf{g} = 11\text{--}26$ should reveal all three types of TDs,

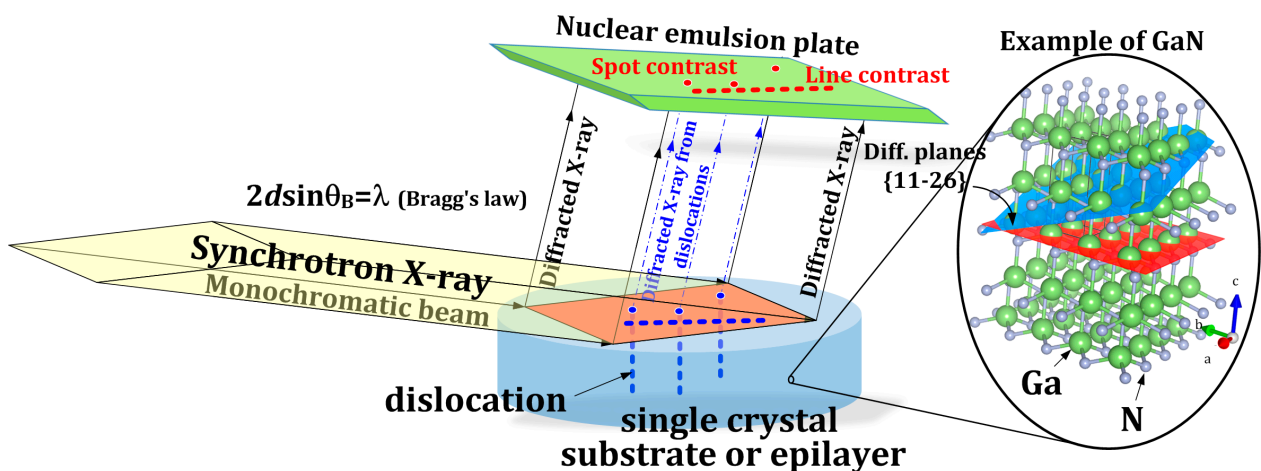


Figure 1: A schematic drawing of the experimental setup and principle of XRT observation. An example of GaN is shown using crystal planes of {11–26} as the diffraction plane.

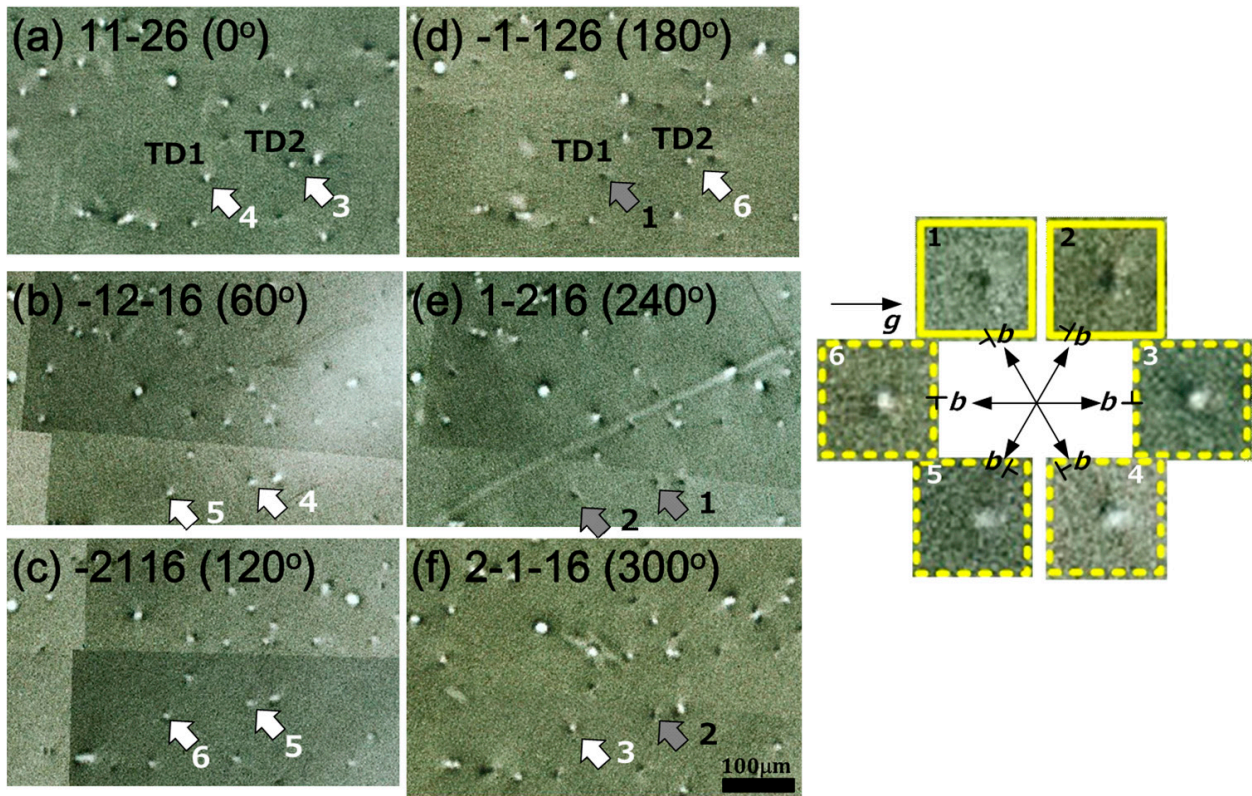


Figure 2: Changes in dark/bright contrast of $c+a$ TD spots when g -vectors are changed among six equivalent 11–26 from (a) to (f).

while the image with $g = 0008$ should reveal TDs whose b contains a c -component (SD or MD). This result indicates that there are no pure EDs in this sample. Most of the TDs (~96%) are MDs with $b = \langle 11\bar{2}0 \rangle / 3 + \langle 0001 \rangle$, the so-called $c+a$ dislocations. Only a very small percentage (~1%) of TDs is pure $1c$ SD with $b = \langle 0001 \rangle$. The other 3% are TDs containing c -component Burgers vector no smaller than $2c$.

In GaN, not only the magnitude but also the direction of the Burgers vectors provides important feedback to the crystal growth. This information can be acquired from the contrast change in the XRT images. **Figure 2** shows the change in dark/bright contrast of $c+a$ TD spots when g -vectors are changed among six equivalent 11–26 (ϕ changes from 0° to 300° every 60°). Using TD1 as an example, it first appears as a dark spot in **Fig. 2(d)** and then **Fig. 2(e)**, and appears as a bright spot in the other four images. TD2 shows similar results with 60° difference in in-plane rotation angle ϕ . Comparing with the XRT spot contrast for threading edge dislocations in 4H-SiC [8], it is clear that the changes in dark or bright contrast (“2 dark+4 bright”) originate from the direction of the a -component of b with respect to the applied g -vector. Thus, the direction of the a -component of $c+a$ TDs in GaN can be unambiguously determined.

In this way, dislocations can be revealed over a wide sample area. Moreover, dislocation types can be deter-

mined by analyzing the dislocation-related contrast. Not only edge-, screw- and mixed-type dislocations can be identified, but also the direction of the a -component in mixed-type dislocations can be accurately determined. These results provide important information for improving crystal growth as well as for analyzing failures in power devices.

REFERENCES

- [1] S. Fujita, *Jpn. J. Appl. Phys.* **54**, 030101 (2015).
- [2] H. Matsuhata and T. Sekiguchi, *Philos. Mag.* **98**, 878 (2018).
- [3] T. Kachi and T. Uesugi, *Sensor Mater.* **25**, 219 (2013).
- [4] Y. Yao, Y. Ishikawa, Y. Sugawara, Y. Takahashi and K. Hirano, *J. Electron. Mater.* **47**, 5007 (2018).
- [5] Y. Yao, Y. Ishikawa, Y. Sugawara, K. Sato, K. Danno, H. Suzuki, T. Bessho, S. Yamaguchi and K. Nishikawa, *J. Cryst. Growth* **364**, 7 (2013).
- [6] Y. Yao, Y. Sugawara, Y. Ishikawa, N. Okada, K. Tadatomo, Y. Takahashi and K. Hirano, *Jpn. J. Appl. Phys.* **58**, SCCB29 (2019).
- [7] K. Momma and F. Izumi, *J. Appl. Crystallogr.* **44**, 1272 (2011).
- [8] I. Kamata, M. Nagano, H. Tsuchida, Y. Chen and M. Dudley, *Mater. Sci. Forum* **600-603**, 305 (2009).

BEAMLINES

BL-3C and BL-14B

Y. Yao¹, Y. Sugawara¹, Y. Ishikawa¹, Y. Takahashi² and K. Hirano³ (¹Japan Fine Ceramics Center, ²Nihon Univ., ³KEK-IMSS-PF)

Discovery of New Chiral Fermions in CoSi

The search for new fermions in condensed matter is currently a hot topic in materials science. Topological semimetals with chiral crystal structure were predicted to host new types of massless fermions distinct from well-known Dirac and Weyl fermions, whereas such exotic fermions are yet to be clarified. Using angle-resolved photoemission spectroscopy (ARPES), we demonstrated that cobalt silicide CoSi hosts two types of exotic fermions, a spin-1 fermion and a double Weyl fermion. We also revealed unusual Fermi-arc surface states connecting the Fermi surfaces associated with these fermions. Our result provides the first experimental evidence for the chiral topological fermions beyond Dirac and Weyl fermions, and paves the way toward realizing exotic electronic properties associated with exotic nodal fermions.

The discovery of Dirac fermions in graphene has accelerated investigations on the physical properties of Dirac-fermion systems and the utilization of Dirac fermions in advanced electronic devices. The Dirac fermion is regarded to be highly useful, for example, in high-speed devices, due to its inherently high mobility. The recent discovery of another type of massless fermion, called the Weyl fermion, increased the categories of nodal fermions and triggered further investigations on unusual magneto-transport properties. Such discoveries naturally pose an essential question as to whether or not more exotic nodal fermions beyond the so-far discovered Dirac and Weyl fermions can be realized. It has been recently proposed by theory that new types of fermions can exist in crystals with specific symmetries and space groups [1–5]. This is exemplified by the prediction of a *spin-1 fermion* containing Dirac-type energy

dispersion and a flat energy band, as well as a *double Weyl fermion* which is composed of two Dirac-cone-like energy dispersions [Fig. 1(A)] [6]. Intriguingly, while Dirac and Weyl fermions could manifest themselves in elementary-particle physics and can exist in vacuum, these new types of massless fermions in condensed-matter systems have no counterparts in elementary particles. Moreover, such fermions likely have topological properties (such as robustness against impurities) and could be useful for advanced applications beyond the framework of so-far realized Dirac and Weyl fermions. It is thus highly desirable to experimentally verify the existence of such new types of nodal fermions.

We have fabricated a high-quality single crystal of cubic CoSi with chiral crystal structure [Fig. 1(B)] which was predicted to host unconventional nodal fermions [6], and have accurately determined its electronic structure

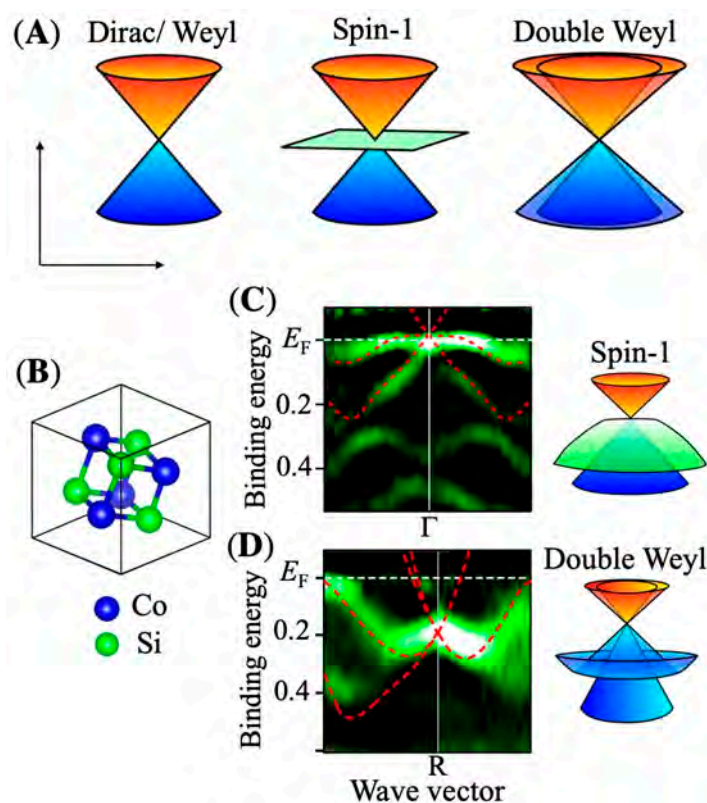


Figure 1: (A) Schematic band dispersion of Dirac/Weyl, spin-1, and double Weyl fermions. (B) Crystal structure of CoSi. (C), (D) Experimental band dispersions (second derivative of ARPES intensity) together with the calculated band dispersions (red curve) around the Γ and R points of the bulk Brillouin zone, measured at $h\nu = 170$ eV and 136.4–181.2 eV, respectively [7].

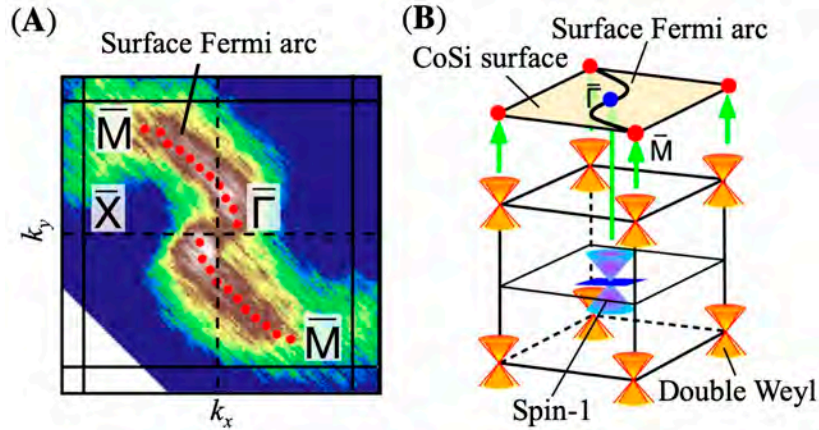


Figure 2: (A) Fermi-surface mapping of CoSi with VUV photons ($h\nu = 67$ eV) supporting the existence of Fermi-arc surface states [7]. (B) Schematic showing the relationship between the bulk nodal-fermion features and the Fermi-arc surface states.

using high-resolution angle-resolved photoemission spectroscopy (ARPES) [7]. By utilizing bulk-sensitive soft-X-ray (SX) photons as well as surface-sensitive vacuum ultraviolet (VUV) photons, we have succeeded for the first time in directly observing the three-dimensional (3D) band structure of the bulk as well as the 2D band structure of the surface. As a result, we revealed two kinds of nodal fermions. The first one is seen around the Γ point of the bulk Brillouin zone and shows an energy dispersion characterized by an X-shaped band and a flat band which intersect exactly at the Γ point [Fig. 1(C)]. This strongly supports the existence of a spin-1 fermion in CoSi. The second one is seen at the R point of the bulk Brillouin zone showing a couple of Dirac-cone-like energy dispersions that intersect exactly at the R point [Fig. 1(D)], supporting the existence of a double Weyl fermion. Intriguingly, experimental band dispersions were found to show good agreement with the calculated band structure obtained by first-principles band calculations for bulk CoSi, as indicated by red curves in Figs. 1(C) and 1(D). We also found that there exist no other bulk Fermi surfaces, suggesting that low-energy excitations in CoSi are solely dictated by the energy bands related to these fermions, providing an excellent opportunity to realize unconventional transport properties.

To search for the possible existence of surface states associated with these fermions, we performed ARPES measurements with VUV photons. As shown in Fig. 2(A), the ARPES intensity is apparently elongated toward two of four adjacent \bar{M} points in the surface Brillouin zone, producing a two-fold-symmetric “Z”-shaped intensity pattern. This feature is commonly observed at other photon energies (not shown), suggestive of its surface origin, and is likely attributed to the predicted Fermi-arc surface states [6], since the calculated surface states exhibit the two-fold-symmetric Fermi contour

and connect with the bulk Fermi surfaces at the $\bar{\Gamma}$ and \bar{M} points [Fig. 2(B)], consistent with the present ARPES results.

Based on the observation of both bulk nodal-fermion features and the Fermi-arc surface states, the present ARPES study on CoSi firmly establishes the existence of new fermions in a solid which have no counterparts in elementary particles. The result also lays a foundation for studying unconventional physical properties related to the chiral fermions, and paves the way toward the possible application of exotic nodal fermions in advanced electronics.

REFERENCES

- [1] J. L. Manès, *Phys. Rev. B* **85**, 155118 (2012).
- [2] B. Bradlyn, J. Cano, Z. Wang, M. G. Vergniory, C. Felser, R. J. Cava and B. A. Bernevig, *Science* **353**, aaf5037 (2016).
- [3] H. Weng, C. Fang, Z. Fang and X. Dai, *Phys. Rev. B* **93**, 241202(R) (2016).
- [4] Z. Zhu, G. W. Winkler, Q.S. Wu, J. Li and A. A. Soluyanov, *Phys. Rev. X* **6**, 031003 (2016).
- [5] B. Q. Lv, Z.-L. Feng, Q.-N. Xu, X. Gao, J.-Z. Ma, L.-Y. Kong, P. Richard, Y.-B. Huang, V. N. Strocov, C. Fang, H.-M. Weng, Y.-G. Shi, T. Qian and H. Ding, *Nature* **546**, 627 (2017).
- [6] P. Tang, Q. Zhou and S.-C. Zhang, *Phys. Rev. Lett.* **119**, 206402 (2017).
- [7] D. Takane, Z. Wang, S. Souma, K. Nakayama, T. Nakamura, H. Oinuma, Y. Nakata, H. Iwasawa, C. Cacho, T. Kim, K. Horiba, H. Kumigashira, T. Takahashi, Y. Ando and T. Sato, *Phys. Rev. Lett.* **122**, 076402 (2019).

BEAMLINES

BL-2 and BL-28A

D. Takane¹, Z. Wang², S. Souma¹, K. Nakayama¹, T. Nakamura¹, H. Oinuma¹, Y. Nakata¹, H. Iwasawa³, C. Cacho³, T. Kim³, K. Horiba⁴, H. Kumigashira^{1,4}, T. Takahashi¹, Y. Ando² and T. Sato¹ (¹Tohoku Univ., ²Univ. Cologne, ³Diamond Light Source, ⁴KEK-IMSS-PF)

Nanoscale Ice-Type Structural Fluctuation in Spinel Titanates

To explore the structural ice-type state, we substituted nonmagnetic Mg ions for Ti ions in spinel titanates MgTi_2O_4 and measured the X-ray diffraction, neutron atomic pair distribution function, and extended X-ray absorption fine structure. We found that a tiny amount of Mg substitution caused the sudden collapse of the tetragonal phase and resurrection of the cubic phase. An analysis of the two-body correlation revealed that the displacement-type ice state, in which two Ti atoms are displaced inward and the other two Ti atoms are displaced outward in the tetrahedra in the pyrochlore lattice, is created during the cubic phase.

Geometrical frustration is a central research topic in the field of condensed matter physics and have given rise to interesting physical properties. The first example of a frustrated system was given as crystalline ice, as reported by Pauling [Fig. 1(a)] [1]. The ice rule, which states that the oxygen is coordinated to two covalently bonded hydrogens and two hydrogen-bonded hydrogens, causes the disorder state in the hydrogen atoms. Anderson applied this ice rule to the spin and charge degrees of freedom. The spin-ice state, in which the spin has a two-in-two-out-type local order, was discovered in pyrochlore titanates [Fig. 1(b)] [2].

To pursue ice physics, realizing the structural ice-type state in strongly correlated electron systems that have high controllability and many degrees of freedom is essential. The structural ice-type state (i.e., “displacement-type ice”) is defined so that two atoms are displaced inward and the other two atoms are displaced outward in the tetrahedra in the pyrochlore lattice [Fig. 1(c)]. The figure shows the original positions (blue) and displaced positions (green) of atoms. Here, the lengths of the red, gray, and blue bonds become short, intermediate, and long, respectively. This displacement follows the ice rule.

In the d^1 electronic system, one valence electron can create a spin singlet pair and a single bond.

This spin-lattice coupling can be a driving force for creating the structural two-in state in the pyrochlore lattice. Thus, we focused on the spinel titanate, MgTi_2O_4 (Ti^{3+} ($3d^1$) $S = 1/2$).

In MgTi_2O_4 , the structural transition from the cubic phase to the tetragonal phase occurs during cooling at $T_c \approx 260$ K and is also accompanied by a transition to the nonmagnetic state (left side of Fig. 2(a)) [3]. Below T_c , the long and short bonds between the Ti ions are arranged alternately along the c axis, as illustrated in the left inset of Fig. 2(a). This Ti atomic displacement follows the ice rule. Unfortunately, this phase transition relieves the frustration originating from the degeneracy of the Ti dimer formation.

To explore the structural ice-type state, we substituted the nonmagnetic Mg ions for Ti ions in MgTi_2O_4 and shortened the correlation length of the tetragonal structure. For its detection, we measured the X-ray diffraction (BL-8A and -8B) and the two-body correlation with Ti ions using the neutron atomic pair distribution function (PDF) (J-PARC BL21) and the extended X-ray absorption fine structure (EXAFS) (BL-9A and -12C). By performing nanoscale structural analyses, we found the nanoscale ice-type structural fluctuation in the cubic phase.

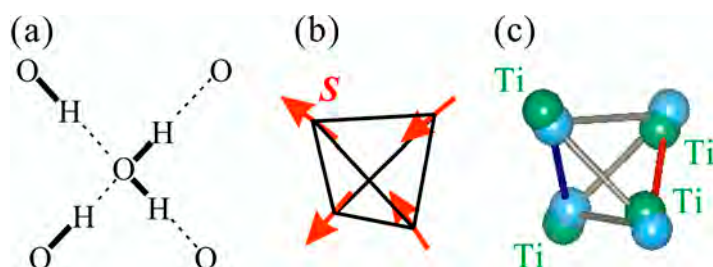


Figure 1: (a) Configuration of H_2O molecules in ice. (b) Spin orientation in the spin-ice state as indicated by the red arrows. (c) Original positions of the atoms (blue spheres) and positions of the displaced atoms (green spheres) in the two-in-two-out-type displacement. The red line indicates the Ti dimer.

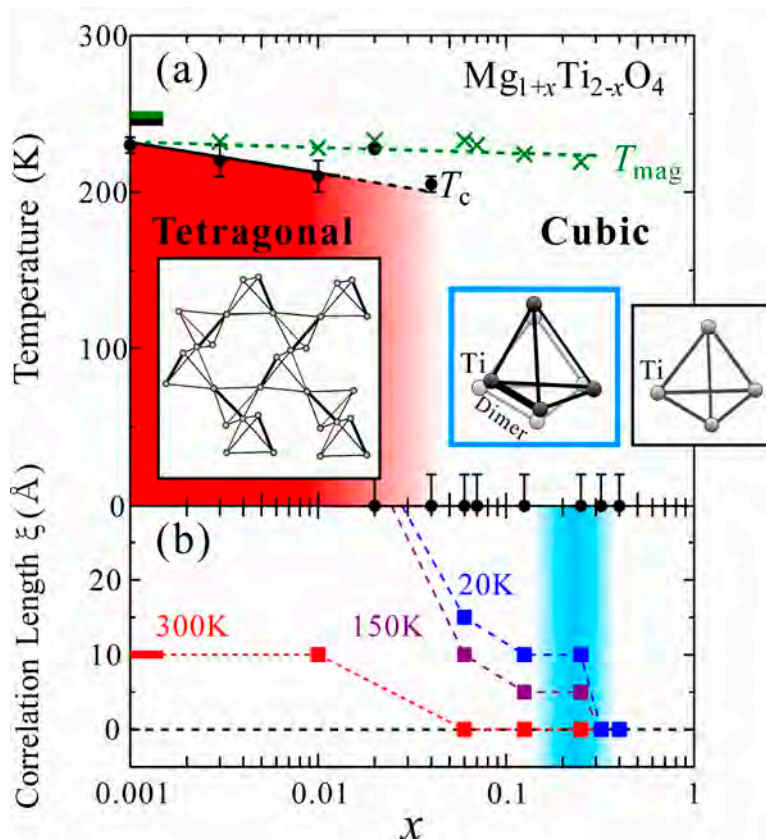


Figure 2: (a) Phase diagram of the lattice structure and the magnetism in $\text{Mg}_{1+x}\text{Ti}_{2-x}\text{O}_4$. The black circles and green crosses indicate the structural transition temperature (T_c) and temperature (T_{mag}) at which the magnetic susceptibility decreases, respectively. The insets illustrate the structure of the Ti tetrahedra. The thick lines indicate the Ti dimer. (b) x dependence of the correlation length ξ of the tetragonal structure obtained by PDF analyses at 20 K (blue), 150 K (purple), and 300 K (red). The blue x region indicates the ice-type state. The thick bars on the left ordinate in (a) and (b) indicate the values at $x = 0$ [4].

Based on experimental results, we present the phase diagram of $\text{Mg}_{1+x}\text{Ti}_{2-x}\text{O}_4$ in Fig. 2(a) [4]. When $x = 0$, the tetragonal phase existed below $T_c \approx 260$ K. For $x > 0.06$, the structural transition temperature T_c dropped to zero, as suggested by the X-ray diffraction measurement. A tiny amount of Mg substitution caused the sudden collapse of the tetragonal phase and the resurrection of the cubic phase. Nevertheless, the reduction of the magnetic susceptibility below T_c was still discernible. The temperature T_{mag} , below which the magnetic susceptibility decreases, remained at ≈ 230 K, indicating the existence of spin-singlet pairs. Indeed, the EXAFS measurement reveals that the two-in-two-out-type displacement of the Ti ions remained at $x < 0.32$. We estimated the correlation length ξ of the tetragonal structure by PDF analysis [Fig. 2(b)]. The correlation length ξ of this tetragonal structure approached zero in $x = 0.25\text{--}0.32$. The nanoscale fluctuation of the local tetragonal structure and the two-in-two-out-type displacement of the Ti ions existed at $x < 0.32$ in the cubic

phase. The displacement-type ice state was created near $x = 0.25$, as indicated by the blue x region.

REFERENCES

- [1] L. Pauling, *J. Am. Chem. Soc.* **57**, 2680 (1935).
- [2] S. T. Bramwell and M. J. P. Gingras, *Science* **294**, 1495 (2001).
- [3] M. Schmidt, W. Ratcliff II, P. G. Radaelli, K. Refson, N. M. Harrison and S. W. Cheong, *Phys. Rev. Lett.* **92**, 056402 (2004).
- [4] S. Torigoe, T. Hattori, K. Kodama, T. Honda, H. Sagayama, K. Ikeda, T. Otomo, H. Nitani, H. Abe, H. Murakawa, H. Sakai and N. Hanasaki, *Phys. Rev. B* **98**, 134443 (2018).

BEAMLINES

BL-8A, BL-8B, BL-9A and BL-12C

S. Torigoe¹, T. Hattori¹, K. Kodama², T. Honda³, H. Sagayama⁴, K. Ikeda³, T. Otomo³, H. Nitani⁴, H. Abe⁴, H. Murakawa¹, H. Sakai¹ and N. Hanasaki¹ (¹Osaka Univ., ²JAEA, ³KEK-IMSS-KENS, ⁴KEK-IMSS-PF)

Coexistence of Magnetism and Superconductivity in EuFe_2As_2 under Pressure

We have investigated the relationship between magnetism and superconductivity in the FeAs-based superconductor EuFe_2As_2 under pressure by measuring the ^{57}Fe nuclear forward scattering (NFS). The antiferromagnetic order in the Fe sublattice coexists microscopically with bulk superconductivity in the pressure range from 2.4 GPa to 3.0 GPa. The spectral features of ^{57}Fe NFS change markedly between the superconducting state at 2.7 GPa and the normal conducting states below 1.9 GPa, indicating modulation of the direction of the magnetic hyperfine field in the Fe sublattice. These results demonstrate the intriguing interplay between magnetism and superconductivity in Fe-based superconductors.

The coexistence between magnetism and superconductivity has aroused great interest in the pairing mechanisms in novel superconductors. Among these novel superconductors, the FeAs-based superconductors AFe_2As_2 (A: Sr, Ba, and Eu) have attracted much attention for the coexistence phases with strong interplays among magnetism, structure, and superconductivity [1].

AFe_2As_2 with a tetragonal structure shows an antiferromagnetic order at $T_0^{\text{Fe}} = 140\text{--}200$ K with the structural change to an orthorhombic one [2, 3]. In the case of EuFe_2As_2 , the Eu^{2+} magnetic moments order antiferromagnetically at $T_0^{\text{Eu}} = 19$ K [4]. The magnetic structure of the Fe sublattice at ambient pressure is the stripe antiferromagnetic (sAFM) one and these magnetic moments are aligned along [100] in the orthorhombic structure [4, 5]. The T_0^{Fe} value is sufficiently suppressed by pressure or substitution, and then bulk superconductivity emerges at low temperature [6–8]. The microscopic coexistences of a long-range magnetic order and superconductivity have been observed in underdoped regions of these substituted AFe_2As_2 superconductors [7–10]. Theoretically, it was predicted using a weak-coupling itinerant model that magnetic states in the coexistence phases are strongly influenced by disorders in compounds due to substitutions [11]. Thus, it is important to investigate the interplay between magnetism and superconductivity of AFe_2As_2 under pressure because hydrostatic pressure controls the electronic state of a material without introducing any disorders. In this article, we report on the magnetic state with superconductivity in EuFe_2As_2 under pressure via the ^{57}Fe nuclear forward scattering (NFS).

^{57}Fe NFS experiments under high pressure at low temperatures were carried out using a clamp-type diamond anvil cell (DAC) on the AR-NE1. The [001] of the single-crystalline sample in DAC was aligned along the propagation vector \mathbf{k}_0 of the incident X-ray.

Figure 1(a) shows the pressure–temperature phase diagram evaluated by the ^{57}Fe NFS and dc magnetic susceptibility under pressure. The T_0^{Fe} value steeply decreases with increasing pressure and then disappears

around 3 GPa, whereas the T_0^{Eu} value gradually increases with no anomaly up to 5 GPa. Superconductivity was observed below $T_{\text{sc}} \sim 25$ K in the pressure range from $p_c^{\text{L}} \sim 2.4$ to $p_c^{\text{H}} \sim 3.0$ GPa [6].

Typical ^{57}Fe NFS spectra at 4 K are shown in Figs. 1(b) and (c). The observed high-frequency quantum beats (QBs) arise from the energy splitting in the nuclear levels by the magnetic hyperfine field $H_{\text{hf}}^{\text{Fe}}$ in the magnetic order: they verify a long-range magnetic order in the Fe sublattice of EuFe_2As_2 below p_c^{H} at 4 K. Note that the features of QBs in the spectrum at 2.7 GPa ($>p_c^{\text{L}}$) are much different from that at 1.9 GPa ($<p_c^{\text{L}}$). Especially, the minima at around 80 and 150 ns in the ^{57}Fe NFS spectrum at 1.9 GPa become shallower than that at 2.7 GPa, as indicated by arrows in Figs. 1(b) and (c). At 2.7 GPa, these shallow minima become deeper with increasing temperature and then the spectral features at 46 K ($>T_{\text{sc}}$) are similar to that at 4 K and 1.9 GPa [Figs. 1(b) and (d)]. These differences in the features of QBs indicate that the magnetic order in the Fe sublattice changes in the superconducting phase.

Since the incident photons are perfectly σ -polarized radiations, the features of QBs in the ^{57}Fe NFS spectra depend on $H_{\text{hf}}^{\text{Fe}}$ and the principal axes of the diagonalized EFG tensor relative to \mathbf{k}_0 . The local environment around the Fe site in the orthorhombic structure is similar to that with $4m2$ in the tetragonal structure [2]. Thus, we assume that the diagonalized EFG tensor has axial symmetry and the principal z-axis is parallel to [001] under pressure at low temperatures. As shown in Figs. 1(b) and (d), the ^{57}Fe NFS spectra in the normal-conducting phase are well analyzed by assuming the sAFM structure ($H_{\text{hf}}^{\text{Fe}} \parallel [100]$) with a structural twinning effect. However, the ^{57}Fe NFS spectrum at 2.7 GPa is not described either by the sAFM structure or by magnetically ordered and paramagnetic Fe states. To analyze the spectrum at 2.7 GPa and 4 K, we need three spectroscopically nonequivalent Fe sites with different directions of $H_{\text{hf}}^{\text{Fe}}$, indicating the directional modulation of the Fe moments from the sAFM state. As shown in Fig. 1(c), the observed spectrum was reproduced using

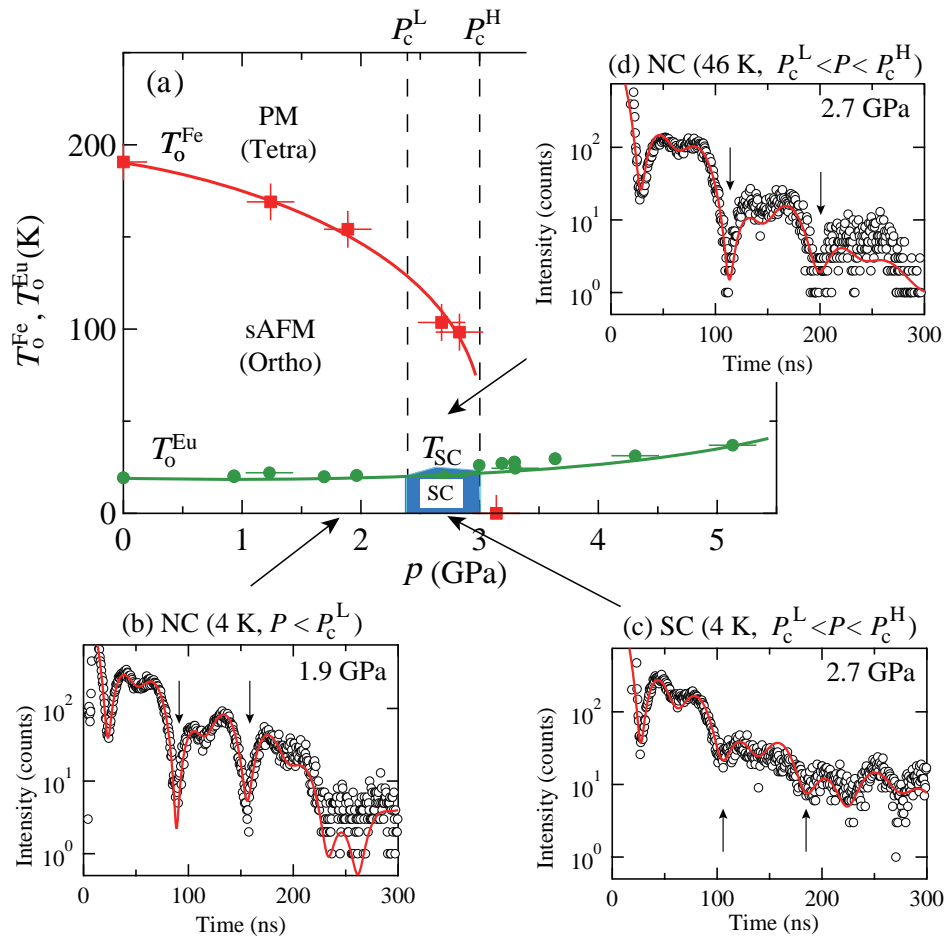


Figure 1: (a) Pressure-temperature phase diagram and (b–d) typical ^{57}Fe nuclear forward scattering spectra of EuFe_2As_2 under pressure. The blue area in (a) represents the superconducting phase. The red lines in (b–d) show the results of fitting.

this assumption with no structural twinning effect. Consequently, the magnetic structure of the Fe sublattice with superconductivity differs from the sAFM one, demonstrating the intriguing relationship between magnetism and superconductivity in EuFe_2As_2 under pressure.

REFERENCES

- [1] E. Abrahams and Q. Si, *J. Phys.: Condens. Matter* **23**, 223201 (2011).
- [2] M. Tegel, M. Rotter, V. Weiß, F. M. Schappacher, R. Pöttgen and D. Johrendt, *J. Phys.: Condens. Matter* **20**, 452201 (2008).
- [3] M. Rotter, M. Tegel, D. Johrendt, I. Schellenberg, W. Hermes and R. Pöttgen, *Phys. Rev. B* **78**, 020503(R) (2008).
- [4] Y. Xiao, Y. Su, M. Meven, R. Mittal, C. M. N. Kumar, T. Chatterji, S. Price, J. Persson, N. Kumar, S. K. Dhar, A. Thamizhavel and Th. Brueckel, *Phys. Rev. B* **80**, 174424 (2009).
- [5] K. Kaneko, A. Hoser, N. Caroca-Canales, A. Jesche, C. Krellner, O. Stockert and C. Geibel, *Phys. Rev. B* **78**, 212502 (2008).
- [6] N. Kurita, M. Kimata, K. Kodama, A. Harada, M. Tomita, H. S. Suzuki, T. Matsumoto, K. Murata, S. Uji and T. Terashima, *Phys. Rev. B* **83**, 214513 (2011).
- [7] F. Waßer, A. Schneidewind, Y. Sidis, S. Wurmehl, S. Aswartham, B. Büchner and M. Braden, *Phys. Rev. B* **91**, 060505(R) (2015).
- [8] J. M. Allred, K. M. Taddei, D. E. Bugaris, M. J. Krogstad, S. H. Lapidus, D. Y. Chung, H. Claus, M. G. Kanatzidis, D. E. Brown, J. Kang, R. M. Fernandes, I. Eremin, S. Rosenkranz, O. Chmaissem and R. Osborn, *Nat. Phys.* **12**, 493 (2016).
- [9] E. Wiesenmayer, H. Luetkens, G. Pascua, R. Khasanov, A. Amato, H. Potts, B. Banusch, H.-H. Klauss and D. Johrendt, *Phys. Rev. Lett.* **107**, 237001 (2011).
- [10] W. T. Jin, S. Nandi, Y. Xiao, Y. Su, O. Zaharko, Z. Guguchia, Z. Bukowski, S. Price, W. H. Jiao, G. H. Cao and Th. Brückel, *Phys. Rev. B* **88**, 214516 (2013).
- [11] M. Hoyer, R. M. Fernandes, A. Levchenko and J. Schmalian, *Phys. Rev. B* **93**, 144414 (2016).

BEAMLINE

AR-NE1

S. Ikeda¹, Y. Tsuchiya¹, X. W. Zhang², S. Kishimoto², T. Kikegawa², Y. Yoda³, H. Nakamura⁴, M. Machida⁴, J. K. Glasbrenner⁵ and H. Kobayashi¹ (¹Univ. of Hyogo, ²KEK-IMSS-PF, ³JASRI, ⁴JAEA, ⁵U.S. NRL)

Self-Foldable Supramolecular Polymers

Folding is an important organization process for proteins which allows them to perform intricate functions. Replicating this process for supramolecular polymers, however, remains a challenging task, as their backbones are based on non-covalent bonds. Here, we report an unprecedented supramolecular polymer system, wherein initially formed misfolded structures self-fold to yield a topology reminiscent of protein tertiary structures. Thermodynamic analysis revealed that the folding is accompanied by a large enthalpic gain. Mechanistic insights revealed that self-folding proceeds via ordering of misfolded domains in the main chain using helical domains as templates.

Figure 1 shows the molecular structures of supramolecular monomers **1–3**. Our group previously discovered that **1** can form uniform toroidal nanofibers by hydrogen-bond assisted supramolecular hexamerization of barbiturate units followed by stacking of the resulting hexamers (rosettes) with intrinsic curvature [1, 2]. Further expanding the molecular structure to **2**, we succeeded in engineering helically folded supramolecular polymers (SP) that can be converted into misfolded fibers by photo-irradiation [3, 4]. However, the misfolded fibers did not recover the original folded structures by any means other than thermal reconstruction. We infer that the increased conformational flexibility of the molecular structure impaired the degree of internal order in the supramolecular polymer backbone, making it difficult to reorganize into the helically folded structures. Accordingly, a more rigid monomer scaffold could improve the degree of internal order of the supramolecular polymer

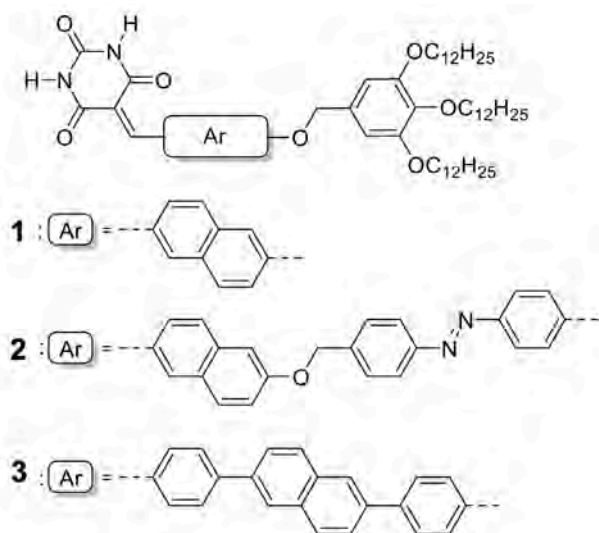


Figure 1: Molecular structures of supramolecular monomers **1–3**.

backbone which led us to molecule **3** after examining several potential candidates. Folding of supramolecular polymers of **3** proceeds on a long time scale, which enabled us to directly visualize intermediate states of the topological transition using atomic force microscopy (AFM) [5].

Slow cooling (1.0 K min^{-1}) of a hot methylcyclohexane (MCH) solution of **3** resulted in the formation of misfolded SP with minor amounts of helically folded conformations [**Fig. 2(A)**]. The resultant solution upon aging at room temperature exhibited a unique self-folding phenomenon of the misfolded domains into helical domains [**Fig. 2(B)**], whereby eventually fully bundled helices with uniform curvature radii ($13 \pm 1 \text{ nm}$) and persistent length ($170\text{--}340 \text{ nm}$), reminiscent of the protein's higher-order topologies, were obtained in quantitative yield over a time period of 5–7 days [**Fig. 2(C)**]. Moreover, these fully bundled helices were interlinked by “turn segments” (dotted squares) [inset, **Fig. 2(C)**]. Further morphological transformations were not observed even after prolonged aging, suggesting that these fully bundled helices constitute the global minimum in the energy landscape. Interestingly, upon cooling the same MCH solution of **3** at a much faster cooling rate (e.g., 10 K min^{-1}), fully misfolded shorter SPs with more inhomogeneous curvature radii ($14 \pm 4 \text{ nm}$) were obtained [**Fig. 2(D)**]. Surprisingly, no morphological evolution over time was observed, suggesting that these fully misfolded SPs are kinetically trapped species. Furthermore, the solutions obtained by mixing separately prepared solutions of fully folded and fully misfolded SPs also did not show any evolution over time, suggesting that the misfolded SPs do not self-fold, neither via an external template mechanism nor by depolymerization–polymerization via monomer exchange. Accordingly, self-folding occurs only when misfolded and folded domains exist in the same SP chain wherein the termini of the helical domains act as a “definite curvature template” for the folding of tethered misfolded chains.

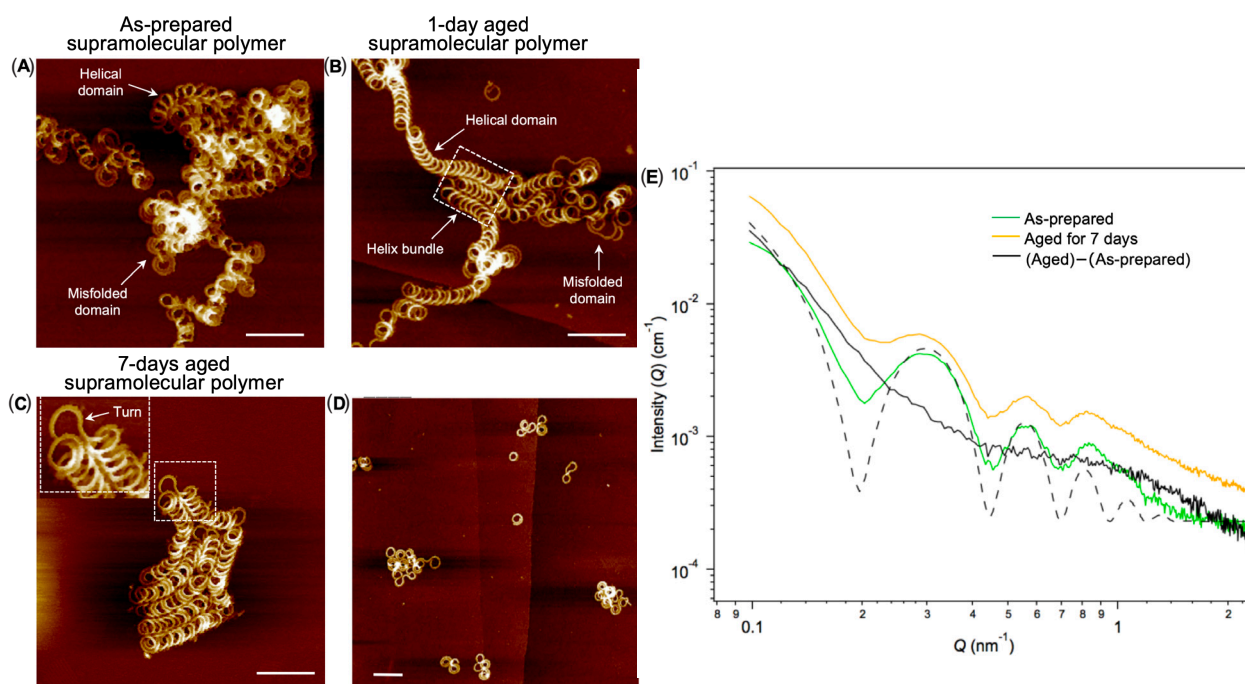


Figure 2: (A to C) AFM images showing the self-folding process of the supramolecular polymers of **3**, after aging the solution at 293 K for 0 min (A), 1 day (B), and 7 days (C). Scale bars, 100 nm. The inset in (C) shows a magnification of the turn segment enclosed by the dotted square. (D) AFM image of fully misfolded supramolecular polymers. Scale bars, 100 nm. (E) SAXS profiles of the as-prepared solution (green curve) and the 7-day-old solution (orange curve) of **3** ($c = 5 \times 10^{-5}$ M) prepared at a cooling rate of 1.0 K min^{-1} . The black curve is the profile obtained by subtracting the two data sets. The black dashed curve is a simulation SAXS profile of the as-prepared sample data using a hollow cylinder model.

The self-folding phenomenon of the above SPs was further probed in solution using small-angle X-ray scattering (SAXS). Both as-prepared supramolecular polymer solution and aged sample displayed identical scattering peaks within the range $Q = 0.2$ to 0.9 nm^{-1} , except the latter showed an increase in SAXS intensity throughout the Q range [Fig. 2(E)]. Data analysis using a hollow cylinder model [Fig. 2(E), dashed curve] provided an average curvature radius of 12.3 nm, which is in agreement with the dimensions measured by AFM. Subtracting the fresh SAXS data from that collected for the aged sample (Fig. 2(E), black curve) resulted in a smooth curve with no observable maxima/minima, suggesting that within this probed size range ($Q = 0.2$ to 0.9 nm^{-1} corresponding to 30 to 7 nm), there is no major change in the structure (that is, it remains, on average, in the coiled state). Also, the subtracted data at $Q < 0.2 \text{ nm}^{-1}$ exhibit a region where $I(Q) \approx Q^{-3}$ and another additional broad contribution centered around $Q = 0.9 \text{ nm}^{-1}$. Because of the limitations of modeling such a complex structure, neither of these features can presently be unambiguously assigned, although the power-law scattering is likely to derive from the more open, equilibrated structures observed by AFM after aging.

REFERENCES

- [1] S. Yagai, Y. Goto, X. Lin, T. Karatsu, A. Kitamura, D. Kuzuhara, H. Yamada, Y. Kikkawa, A. Saeki and S. Seki, *Angew. Chem. Int. Ed.* **51**, 6643 (2012).
- [2] M. J. Hollamby, K. Aratsu, B. R. Pauw, S. E. Rogers, A. J. Smith, M. Yamauchi, X. Lin and S. Yagai, *Angew. Chem. Int. Ed.* **55**, 9890 (2016).
- [3] B. Adhikari, Y. Yamada, M. Yamauchi, K. Wakita, X. Lin, K. Aratsu, T. Ohba, T. Karatsu, M. Hollamby, N. Shimizu, H. Takagi, R. Haruki, S. Adachi and S. Yagai, *Nat. Commun.* **8**, 15254 (2017).
- [4] B. Adhikari, Y. Yamada, M. Yamauchi, K. Wakita, X. Lin, K. Aratsu, T. Ohba, T. Karatsu, M. Hollamby, N. Shimizu, H. Takagi, R. Haruki, S. Adachi and S. Yagai, *PF Highlights* **201731** (2018).
- [5] D. D. Prabhu, K. Aratsu, Y. Kitamoto, H. Ouchi, T. Ohba, M. J. Hollamby, N. Shimizu, H. Takagi, R. Haruki, S. Adachi and S. Yagai, *Sci. Adv.* **4**, eaat8466 (2018).

BEAMLIN

BL-15A2

D. D. Prabhu¹, K. Aratsu¹, Y. Kitamoto¹, H. Ouchi¹, T. Ohba¹, M. J. Hollamby², N. Shimizu³, H. Takagi³, R. Haruki³, S. Adachi³ and S. Yagai¹ (¹Chiba Univ., ²Keele Univ., ³KEK-IMSS-PF)

An Approach to Produce Uniform Artificial Protein Supramolecules

The design of artificial protein supramolecules has attracted great interest in developing novel medical nanomaterials. However, the production of uniform protein supramolecules remains a major challenge. We report a simple approach to produce uniform artificial protein supramolecules based on the geometric features of polyhedra. We demonstrated that the truncated icosahedral structure (soccer-ball shape) was uniformly constructed from the fusion protein composed of pentameric and dimeric protein domains. The supramolecule assembled from our designed fusion proteins was analyzed by small-angle X-ray scattering. Analysis showed that the molecular weight, diameter and overall shape were highly consistent with our designed structure.

Biocompatible protein-based nanomaterials have long been believed to be promising medical materials such as for vaccines and drug carriers [1]. Although various approaches to produce protein-based nanomaterials have been developed, most of them were based on random protein aggregations giving non-uniform materials, which is not desirable for applications. The key to producing uniform protein materials is the design of protein supramolecules produced by specific protein-protein interactions without random aggregation. One simple way to form protein supramolecules is to design a fusion protein composed of two different naturally oligomeric proteins. For example, Yeates' group successfully produced cubic protein supramolecules by using a fusion protein composed of the subunits from dimeric and trimeric proteins, respectively [2]. Although this is a very simple method of constructing protein supramolecules, three different shapes of protein supramolecule—cube, triangle prism, and triangle pillar—are produced at the same time owing to the geometric features of polyhedra.

In accordance with Euler's polyhedron formula (Eq. 1), we found that soccer-ball shape polyhedra (truncated icosahedron) could be produced as the sole structure if we designed a fusion protein composed of pentameric and dimeric proteins:

$$V + E - F = 2 \quad (\text{Eq. 1})$$

where V , E and F are the number of vertices, edges and faces of polyhedra, respectively. The equation suggests that the number of pentagons is always 12 if a polyhedron is only composed of pentagons and hexagons such as a soccer-ball shape [3]. The hexagonal planes of the soccer-ball shape can be depicted by six line-segments provided from three different pentagonal planes (each pentagonal plane provides one line-segment) and three line-segments connecting the vertices of the pentagonal planes. The dimeric protein units in the fusion proteins connect the pentagonal protein units to form hexagonal planes, followed by forming a soccer-ball shape structure as shown in Fig. 1. We thus selected the template proteins, LSm protein as a pentameric protein unit and a coiled coil part of Myosin X (MyoX-coil), as a dimeric protein unit [4].

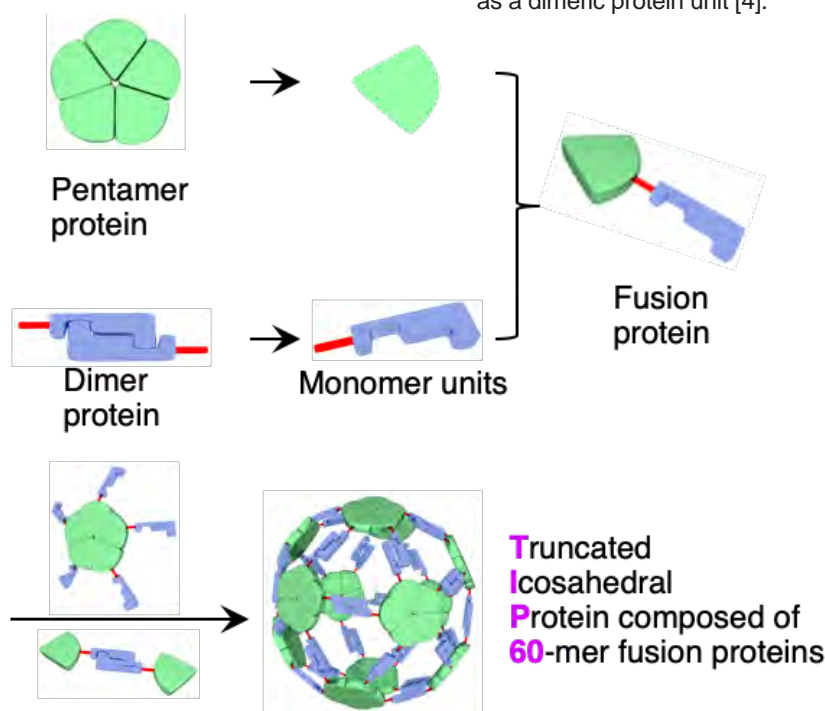


Figure 1: Schematic representation of our design approach to produce uniform protein supramolecules. Green colored pentamer and blue colored dimer proteins correspond to LSm and MyoX-coil, respectively. Copyright (2018) Wiley-VCH. Used with permission from ref. [4].

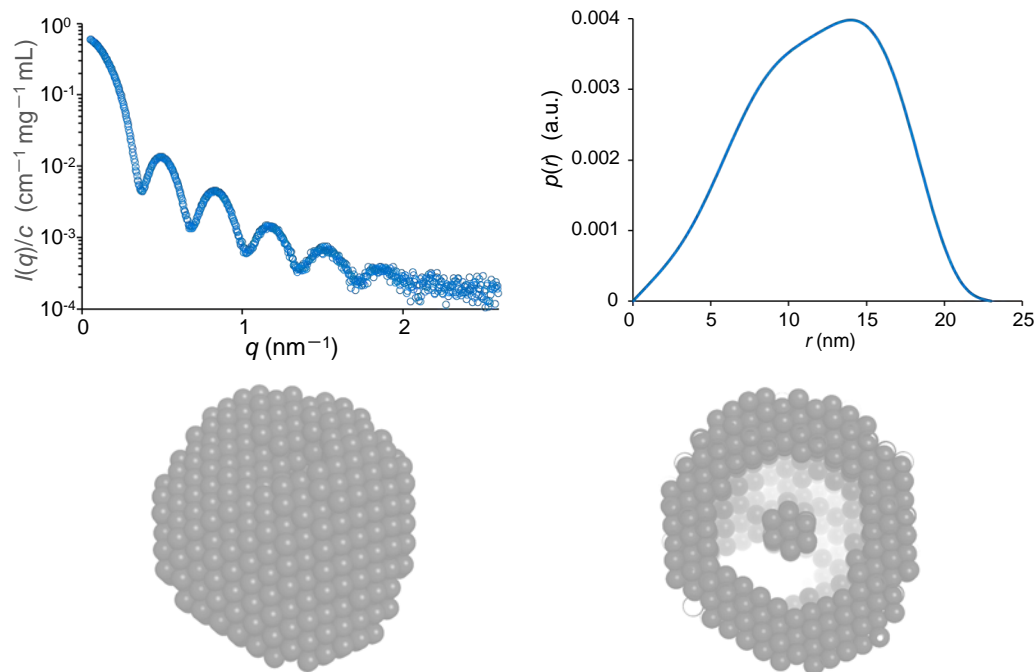


Figure 2: SAXS analysis data. The SAXS intensity of the protein supramolecule (upper left) and its pair-distribution function (upper right). A dummy atom model of the protein supramolecule: a full view (lower left) and cross-sectional view (lower right). (SASBDB accession code: SASDDZ8). Copyright (2018) Wiley-VCH. Used with permission from ref. [4].

The designed fusion protein was expressed in *E. coli* and purified by a Ni column. Complex formation of the purified protein was first analyzed by Blue-Native PAGE. The result clearly showed a single band at the molecular weight position corresponding to 960 kDa, suggesting that the molecular weight value was consistent with 1070 kDa calculated based on our designed 60-meric protein supramolecule. We therefore analyzed the structure by small-angle X-ray scattering (SAXS). For the SAXS analysis, the protein complex was further purified by an anion exchange column, followed by a size exclusion column. The SAXS profile of the purified protein complex showed the typical pattern of uniform spherical particles (Fig. 2). The radius of gyration and the molecular weight of the protein complex supramolecule were determined from the Guinier plots as 9.47 nm and 1063 kDa, respectively. The pair-distance distribution function $p(r)$ obtained from the SAXS data gave the maximum particle distance (D_{max}) as 23 nm. Interestingly, the shape of the distribution pattern was slightly left skewed, suggesting that the protein supramolecule has an inner space as reported in apo-ferritin, which is a natural hollow protein supramolecule [5]. The dummy atom model of the protein complex was reconstructed from the SAXS data using the *ab initio* modeling program DAMMIF [6]. The model structure also indicated that the protein supramolecule had a hollow spherical shape.

The shape, molecular weight and diameter of this protein supramolecule were also confirmed by transmis-

sion electron microscopy, dynamic light scattering analysis and SEC-MALS analysis [4]. All the analyses gave values that were consistent with those obtained from SAXS analysis. We thus designated the protein complex supramolecule as TIP60 (Truncated Icosahedral Protein composed of 60-mer fusion proteins). We also demonstrated that both the interior and exterior surfaces of TIP60 were functionalized by chemical modification [4]. Therefore, we believe that TIP60 can be used as a biomedical nanomaterial for various applications.

REFERENCES

- [1] L. P. Herrera Estrada and J. A. Champion, *Biomater. Sci.* **3**, 787 (2015).
- [2] Y. T. Lai, E. Reading, G. L. Hura, K. L. Tsai, A. Laganowsky, F. J. Asturias, J. A. Tainer, C. V. Robinson and T. O. Yeates, *Nat. Chem.* **6**, 1065 (2014).
- [3] P. Schwerdtfeger, L. N. Wirz and J. Avery, *WIREs Comput. Mol. Sci.* **5**, 96 (2015).
- [4] N. Kawakami, H. Kondo, Y. Matsuzawa, K. Hayasaka, E. Nasu, K. Sasahara, R. Arai and K. Miyamoto, *Angew. Chem. Int. Ed.* **57**, 12400 (2018).
- [5] L. Melníková, V. I. Petrenko, M. V. Avdeev, V. M. Garamus, L. Almásy, O. I. Ivankov, L. A. Bulavin, Z. Mitroová and P. Kopčanský, *Colloids Surf. B* **123**, 82 (2014).
- [6] D. Franke and D. I. Svergun, *J. Appl. Crystallogr.* **42**, 342 (2009).

BEAMLINE

BL-6A

N. Kawakami¹ and R. Arai² (¹Keio Univ., ²Shinshu Univ.)

Photo-Triggered Topology-Reset Execution of Cyclic Polymers for the Tuning of Viscoelasticity

Repeatable topological transformation of polymers has been a challenge for modulating material functions. We synthesized cyclic poly(dimethylsiloxane)s (PDMSs) containing various ring sizes in-chain linked with hexaarylbiimidazoles (HABIs) from linear PDMSs with 2,4,5-triphenylimidazole (lophine) end groups. The physical state of PDMS turned into liquid simply by converting lophines into HABIs from the former solid state of linear PDMS. Based on the photochemistry of HABI, cyclic PDMSs were successfully reset to linear PDMSs having triphenylimidazolyl radical (TPIR) end groups upon photoirradiation, and subsequent termination of photoirradiation enabled recyclization into cyclic PDMSs again. Moreover, photoirradiation of cyclic PDMSs enabled solvent-free switching of rheological properties.

Advances in synthetic polymer chemistry have produced various nonlinear polymers such as cyclic, star, comb-like, and network polymers. There is much interest in studying topology–property relationships because the topology of polymers often dramatically differentiates their properties. An ongoing challenge in this field is to establish a reversible topological transformation system for switching their properties [1–5]. Obviously, it is important to develop a solventless repeatable topological transformation process, but this remains mostly unrealized.

On the other hand, changes in the physical states of materials are a familiar phenomenon in daily life. Such changes between physical states or viscoelasticity are generally caused by heat stimulation. However, materials displaying a change in viscoelasticity including a liquid–solid change upon receiving external stimuli

other than heat are rare. The conventional approach to attaining such materials is to use photoisomerizable molecules. Notable examples are isothermal melting and crystallization of multi-azobenzene-containing branched small molecules [6, 7] based on photo-induced phase transition [8] and reversible shift in the glass transition temperature of side-chain azobenzene-containing polymers [9]. In contrast, we have focused on network materials containing reversibly cleavable and reformable covalent linkings. In particular, we have used the photochemistry of hexaarylbiimidazole (HABI) [10]. HABI undergoes cleavage of the covalent bond between the two imidazoles to generate a pair of triphenylimidazolyl radicals (TPIRs) upon photoirradiation and the generated TPIRs readily recouple into HABI upon terminating photoirradiation [Fig. 1(a)]. Importantly, TPIRs are stable even in the presence of oxygen and thus the photochemistry can be achieved in air [11]. We have used this photoreaction for repeatable transformation of the topologies of polymers and realized photo-triggered solvent-free isothermal liquid–nonliquid conversion of network poly(dimethyl siloxane)s (PDMSs) at room temperature [12]. To extend the current frontier of this chemistry, the construction of a simple topological transformation system and nanoscale analysis of these materials for more sophisticated polymer design remain crucial issues to be tackled.

We synthesized cyclic PDMSs linked with HABIs (C_{mix}) from linear PDMSs having lophine end groups (L). The lophine end groups of L were oxidized to produce linear PDMS with TPIR end groups (L^*) and subsequent coupling of TPIRs into HABI occurred intra- and inter-molecularly to afford C_{mix} [Fig. 1(b), top]. Although L and C_{mix} have quite similar chemical compositions and C_{mix} has a much higher molecular weight, the appearance of L and C_{mix} was completely different; that is, while L was solid, C_{mix} was viscous liquid [Fig. 2(a)]. Related to this, DSC and IR analyses indicated the existence of hydrogen bonding (H-bonding) only in L . We have further analyzed synchrotron radiation small angle X-ray scattering (SAXS) profiles of L and C_{mix} to evaluate the molecular ensemble on a nanoscale. Analogous to thermoplastic elastomers formed by triblock

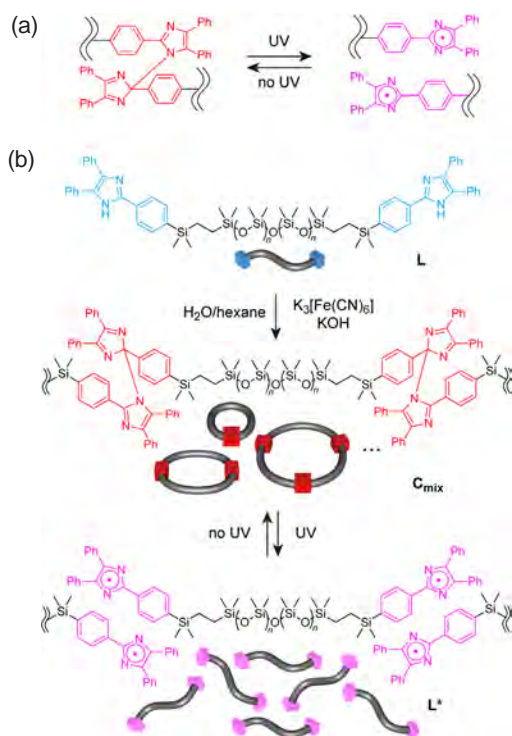


Figure 1: (a) Photochemistry of HABI. (b) Synthesis of in-chain HABI-functionalized C_{mix} and cyclic–linear topological transformation based on photo-triggered cleavage and reformation of HABI.

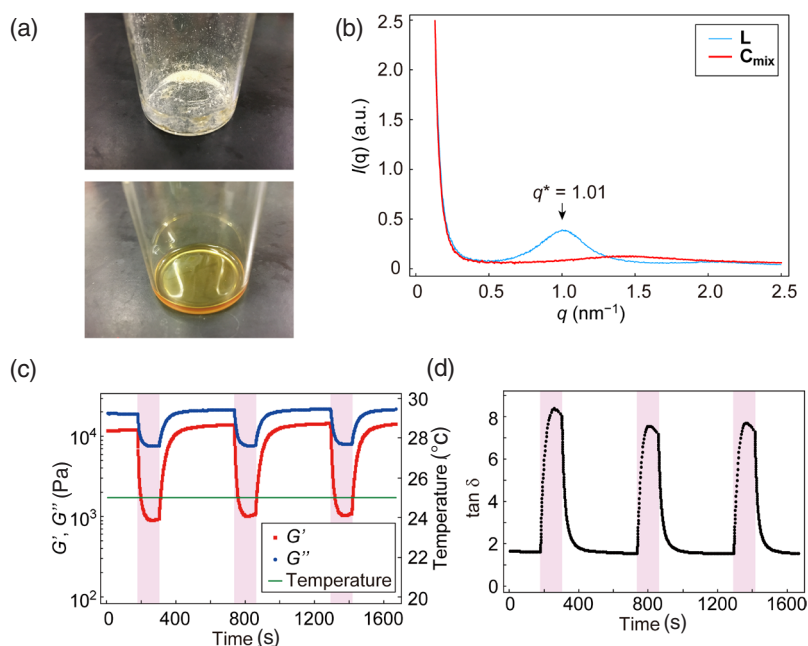


Figure 2: (a) Appearance of **L** (top) and **C_{mix}** (bottom). (b) SAXS intensity profiles of **L** (light blue) and **C_{mix}** (red). Time-dependent plots of (c) G' and G'' and (d) $\tan \delta$ of **C_{mix}** upon ON–OFF UV irradiation cycles (the periods of UV irradiation are colored in pink).

copolymers, linear polymers having H-bonding end groups cause microphase separation. As was studied by SAXS, such materials show scattering derived from end groups. The SAXS profile of **L** showed a scattering similar to the reported one and the peak scattering vector (q^*) was 1.01, corresponding to an averaged distance of about 6 nm between two aggregates formed by end groups [Fig. 2(b), light blue line]. In contrast, SAXS of **C_{mix}** showed no aggregates-derived scattering [Fig. 2(b), red line]. It is noteworthy that the simple conversion of lophines into HABIs changes the material to a homogeneous liquid.

By taking advantage of the liquid character of **C_{mix}**, we conceived of solvent-free repeatable tuning of viscoelasticity upon photoirradiation of **C_{mix}** while retaining the liquid state. Time-dependent plots of G' and G'' of **C_{mix}** upon ON–OFF UV (365 nm, 150 mW/cm²) irradiation cycles showed their sudden decrease and increase [Fig. 2(c)]. Both of G' and G'' repeatably decreased to converged values within 2 min upon UV irradiation and reverted within 4 min after terminating irradiation. As shown in the time-dependent plots of loss tangent ($\tan \delta = G''/G'$), UV irradiation suddenly increased $\tan \delta$ from 1.6 to almost 8 [Fig. 2(d)], indicating the UV-irradiated product has a more liquid-like character.

Solventless photo-triggered repeatable transformation of cyclic and linear topologies resulted in dramatic changes in the rheological properties of PDMS while retaining the liquid state, which is arguably important for a broad range of applications. The key process here is resetting a polymer topology into that of precursor, and thus we have named this strategy “topology-reset execution (T-rer)” [13]. Work on expanding the T-rer strat-

egy to different combinations of polymer topologies and characterizing unprecedented properties is currently in progress.

REFERENCES

- [1] D. Aoki, S. Uchida and T. Takata, *Angew. Chem. Int. Ed.* **54**, 6770 (2015).
- [2] T. Ogawa, N. Usuki, K. Nakazono, Y. Koyama and T. Takata, *Chem. Commun.* **51**, 5606 (2015).
- [3] T. Ogawa, K. Nakazono, D. Aoki, S. Uchida and T. Takata, *ACS Macro Lett.* **4**, 343 (2015).
- [4] S. Valentina, T. Ogawa, K. Nakazono, D. Aoki and T. Takata, *Chem. - Eur. J.* **22**, 8759 (2016).
- [5] T. Yamamoto, S. Yagyu and Y. Tezuka, *J. Am. Chem. Soc.* **138**, 3904 (2016).
- [6] M. Hoshino, E. Uchida, Y. Norikane, R. Azumi, S. Nozawa, A. Tomita, T. Sato, S.-i. Adachi and S.-y. Koshihara, *J. Am. Chem. Soc.* **136**, 9158 (2014).
- [7] H. Akiyama and M. Yoshida, *Adv. Mater.* **24**, 2353 (2012).
- [8] S. Koshihara, Y. Tokura, T. Mitani, G. Saito and T. Koda, *Phys. Rev. B* **42**, 6853 (1990).
- [9] H. Zhou, C. Xue, P. Weis, Y. Suzuki, S. Huang, K. Koynov, G. K. Auernhammer, R. Berger, H.-J. Butt and S. Wu, *Nat. Chem.* **9**, 145 (2017).
- [10] T. Hayashi and K. Maeda, *Bull. Chem. Soc. Jpn.* **33**, 565 (1960).
- [11] L. A. Cescon, G. R. Coraor, R. Dessauer, A. S. Deutsch, H. L. Jackson, A. MacLachlan, K. Marcali, E. M. Potrafke and R. E. Read, E. F. Silversmith and E. J. Urba, *J. Org. Chem.* **36**, 2267 (1971).
- [12] S. Honda and T. Toyota, *Nat. Commun.* **8**, 502 (2017).
- [13] S. Honda, M. Oka, H. Takagi and T. Toyota, *Angew. Chem. Int. Ed.* **58**, 144 (2019).

BEAMLINE

BL-10C

M. Oka¹, H. Takagi², T. Toyota¹ and S. Honda¹ (¹The Univ. of Tokyo, ²KEK-IMSS-PF)

Filamentous Virus-Based Assembly: Relationship between Their Oriented Structures and Thermal Diffusivity

Organic polymers are generally regarded as thermal insulators because amorphous arrangement of molecular chains reduces the mean free path of heat-conducting phonons. However, recent studies revealed that highly oriented single polymeric chains could have higher thermal conductivity than bulk polymers because stretched polymer chains effectively conduct phonons through polymeric covalent bonds. Here, we demonstrate the possibility of non-covalent virus assembly prepared by simple flow-induced methods toward the creation of high thermal conductive polymeric materials. Films with high thermal diffusivity composed of non-covalent bond-based assemblies of liquid crystalline filamentous viruses were prepared using a simple flow-induced orientation method. Structural and thermal characterization demonstrated that the highly oriented structures of the viruses in the films affected the high thermal diffusivity.

Organic polymers with high thermal conductivity have been of great interest for flexible electronic devices due to their lightweight and (typically) electronic insulation properties. However, the thermal conductivity of bulk polymers is very low because of strong phonon scattering caused by various defects, interfaces, and the isotropic molecular orientations in amorphous regions. Highly oriented polymers such as liquid crystalline polymers are promising candidates because the well-oriented polymer chains effectively conduct phonons through polymeric covalent bonds. Although significant efforts have focused on the development of various technologies to increase their thermal conductivity, the design of a simple control method to achieve high thermal conductivity via non-covalently assembled structures has attracted little attention.

M13 bacteriophage (phage), one of the filamentous viruses [Fig. 1(a)], is a regular assembly of plural proteins and genetic DNA. Recently, it has been reported that the phages can be utilized as a material component in various fields due to their unique functions, which are easily integrated into the phages by genetic or chemical modification of the coat proteins on surfaces. Further-

more, the frameworks of phages are competent liquid crystal mesogens that are capable of forming various phases due to their high aspect ratio (4.5 nm width and 900 nm length), dipole properties, and charge densities. The liquid crystalline structures are controlled using various methods, and, in particular, a method using substrates (i.e., solid/liquid interfaces) has recently been used to create liquid crystalline virus materials, such as sensors, electronics, and devices.[1, 2] Although a phage comprises a supramolecular assembly of well-packed coat proteins, the phage acts as a potential thermal conductive material component due to its filamentous structure and liquid crystallinity.

Here, we demonstrate a straightforward technique for the preparation of phage films with highly oriented liquid crystalline structures using flow-induced methods and glass plates circularly patterned with a highly water-shedding coating [Fig. 1(b)]. The thickness of the outside of the film was visibly thicker than other positions on the film. Because a drop of solution on a solid surface leaves a dense ring-like deposit along the perimeter (coffee-ring effect), the increased thickness on the film outside may be caused by the capillary

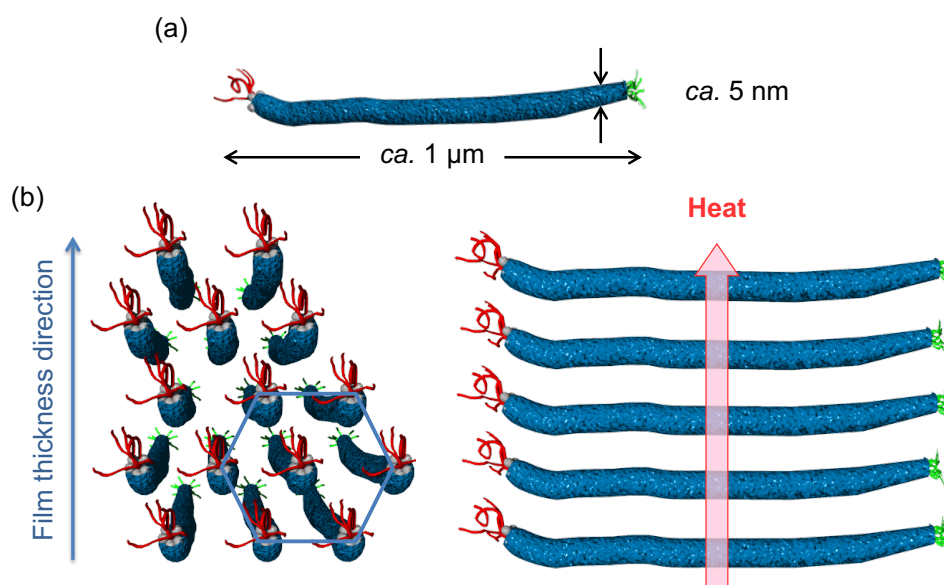


Figure 1: Schematic representations. (a) Phage and (b) hexagonally assembled structures of the phages in the film.

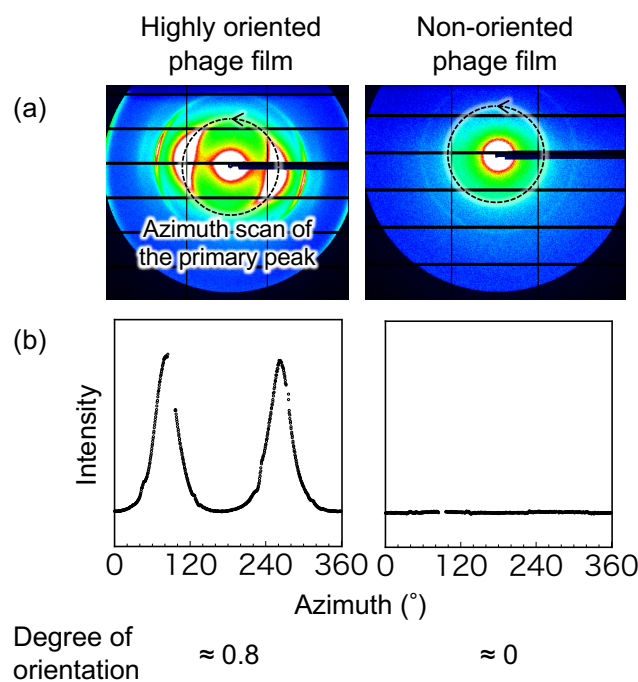


Figure 2: SAXS analyses of the phage films. **(a)** Two-dimensional patterns for the highly oriented (outside) and non-oriented phage films. **(b)** Azimuth scan of the primary peaks and resultant degree of orientation values.

flow of solutes. Thermal diffusivity values of the phage films at the outside, midpoint, and center of the film in a perpendicular (thickness) direction were measured by temperature wave analysis. The thermal diffusivity value on the outside ($6.3 \times 10^{-7} \text{ m}^2 \text{ s}^{-1}$) was approximately 10 times greater than that of the non-oriented film and approximately 7 times greater than those at other points, demonstrating the extremely high thermal diffusivity on the outside of the film.

To characterize the oriented structures of the phages, small-angle X-ray scattering (SAXS) experiments were performed on the outside, midpoint, and center of the film as well as the non-oriented film. Typical results are shown in Fig. 2. In the resulting scattering profiles for all the positions, intense peaks with a reciprocal d -spacing ratio of $1:\sqrt{3}:2$, which indicates hexagonally packed structures of the phages, were observed. The primary peak intensities and positions (7.9–8.3 nm) were comparable irrespective of the positions, and so packing of the phages on a molecular level is essentially the same. To quantitatively investigate the oriented structures of the phages, an azimuth scan of the primary peaks at approximately 8 nm was performed. Full width at half maximum (FWHM) was determined by fitting with the pseudo-Voigt function to calculate the degree of orientation, which indicates the orientation of the phages within the volume of irradiation. In this calculation, the degree of orientation ranges from 0 to 1, and a higher value represents a higher degree of orientation. The resulting degree of orientation of the outside of the film (0.81) was extremely high compared with those of the other positions, suggesting that the assembled phages on the outside of the film are highly oriented. The de-

gree of orientation for the non-oriented film with the lowest thermal diffusivity could not be determined because no peaks for the azimuth scan were detected. A comparison of the values of thermal diffusivity and orientation degrees indicated that no linear correlation existed between them, and only films with a high degree of orientation (0.81) exhibited high thermal diffusivity. These results suggested that the highly oriented structures of the assembled phages with a scale of several hundred μm (area measured by SAXS) resulted in a high thermal diffusivity, which may be due to highly efficient phonon transport. Therefore, the increase in the thermal diffusivity was not substantially influenced by the moderate orientation of the domains of the assembled phages. Based on all the structural and thermophysical characterizations, the thermal diffusivity of the liquid crystalline phage film measured in the perpendicular direction substantially increased due to the highly oriented assembly of the phages, which may be due to a decrease in phonon scattering at structural defects in the phage-assembled structures [3].

REFERENCES

- [1] T. Sawada, *Polym. J.* **49**, 639 (2017).
- [2] T. Sawada and T. Serizawa, *Bull. Chem. Soc. Jpn.* **91**, 455 (2018).
- [3] T. Sawada, Y. Murata, H. Marubayashi, S. Nojima, J. Morikawa and T. Serizawa, *Sci. Rep.* **8**, 5412 (2018).

BEAMLINES

BL-10C and BL-6A

T. Sawada^{1,2}, Y. Murata¹, H. Marubayashi¹, S. Nojima¹, J. Morikawa¹ and T. Serizawa¹ (Tokyo Tech.² JST)

Solid-State Inertial Rotation of a Guest Ball in a Tight Tubular Host

The dynamics of molecules in the solid state are greatly influenced by molecular contact and are usually restricted. We found that rotational motions of C_{60} , a spherical carbonaceous ball, were liberated in a tight tubular host in the solid state. The rotational motions reached an inertial regime, and variable-temperature crystallographic analyses and solid-state ^{13}C NMR spectroscopy revealed the detailed dynamics of C_{60} . The rotational frequency at 335 K was determined to be 213 GHz.

The dynamics of molecules in the solid state are an interesting subject, which can connect molecular-scale events with properties of bulk materials. However, molecular motions are severely restricted in solids. Thus, although a fullerene molecule, C_{60} , is known to rotate in solids, its dynamics are not free from restrictions: a restricted ratchet phase emerges by intermolecular face-to-face contacts, and motions below 260 K are severely restricted [1, 2]. As a tight host to trap C_{60} , a finite segment of helical carbon nanotubes, [4]cyclo-2,8-chrysenylene ([4]CC), has previously been synthesized [Fig. 1(a)] [3]. Although the enthalpy gain of the complex formation is as large as 14 kcal/mol, the ball guest in the tube host was found to be rotating in solution and, interestingly, in the solid state [4, 5]. In this work, we reveal a unique, complete picture of the solid-state dynamics of the guest in [4]CC \supset C_{60} [6].

The solid-state motions of C_{60} in [4]CC \supset C_{60} were first indicated by variable-temperature crystallographic analyses. Six single crystals of [4]CC \supset C_{60} were in-

dependently subjected to X-ray diffraction analysis at AR-NE3A, which were respectively performed at 95, 140, 180, 220, 260, and 295 K. A molecular structure at 95 K is shown in Fig. 1(b). Throughout the temperature range, one C_{60} molecule was commonly observed at several disordered orientations with the center of gravity being unchanged in the tube. Electron densities visualized for different temperature conditions (95, 180, 220 and 260 K) are shown in Fig. 1(c). The electron density mapping ($2F_o - F_c$) showed that biased locations of electrons of C_{60} (95 and 180 K) became blurred upon elevating the temperature (220 and 260 K), which could be ascribed to the dynamic motions of the guest at the higher temperatures.

The solid-state dynamics of C_{60} in [4]CC \supset C_{60} were next investigated by solid-state ^{13}C NMR analysis in a quantitative manner. The spectra were recorded without using magic angle spinning (MAS) which is normally required to obtain sharp resonance peaks. In the absence of MAS conditions, however, a sharp peak of

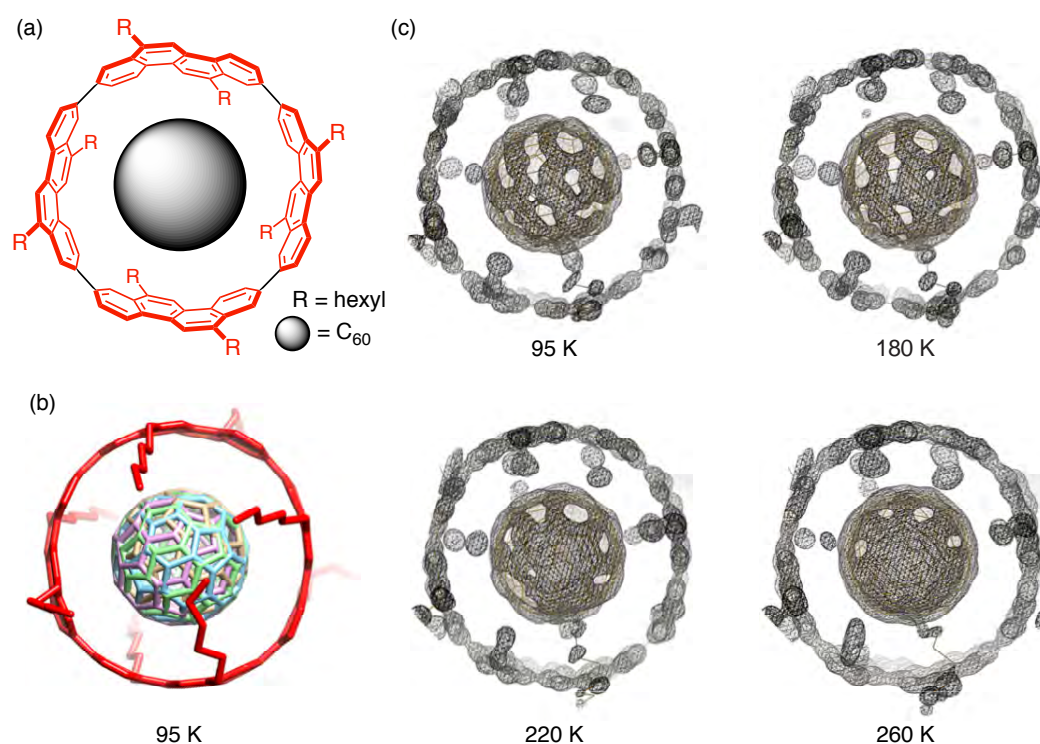


Figure 1: Crystallographic analyses of (*P*)-(12,8)-[4]CC \supset C_{60} . (a) Chemical structure of molecular bearing. (b) A crystal structure at 95 K. Disordered alkyl chains and hydrogen atoms are omitted for clarity. (c) Temperature-dependent electron density mappings with $2F_o - F_c$ (RMSD: 1.5 σ).

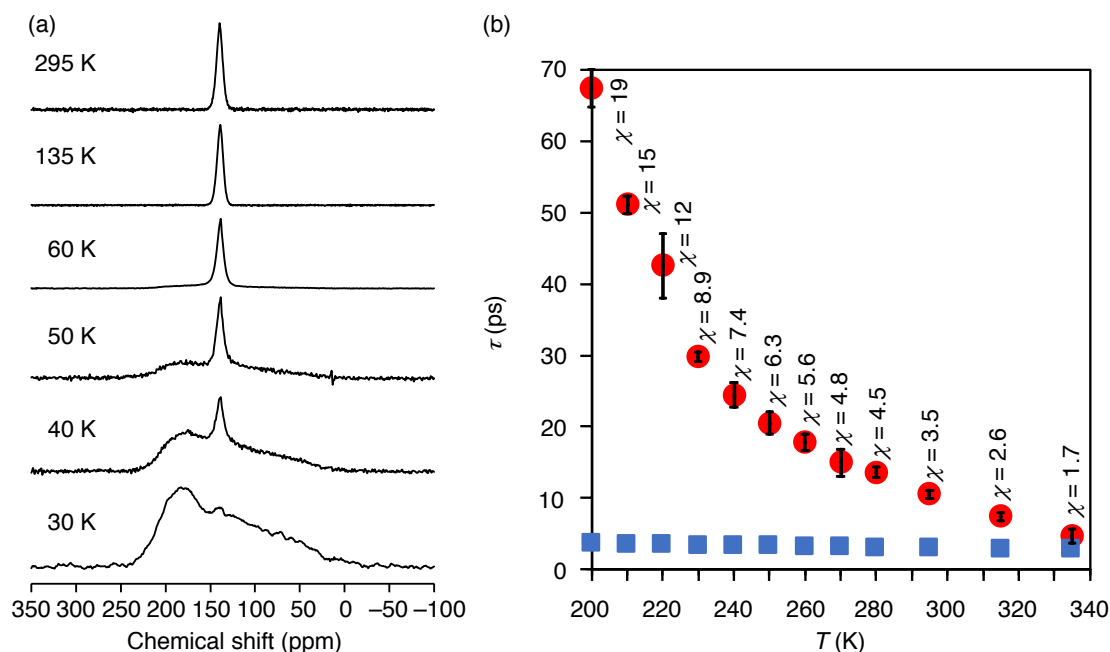


Figure 2: NMR analyses of solid-state dynamics. **(a)** Variable-temperature solid-state ^{13}C NMR of $[4]\text{CC}@C_{60}$ under static conditions without MAS. **(b)** Temperature-dependence of rotational correlation time τ obtained from field-dependent spin-lattice relaxation. Red dots and blue squares indicate τ and τ_{FR} , respectively.

C_{60} was observed at 295 K [Fig. 2(a)], which remained unchanged at a lower temperature down to 60 K. When we further cooled the specimen, a broad shoulder peak started to appear from 50 K, and at 30 K a powder pattern was observed from non-averaged chemical shift anisotropy (CSA). The peak at 50 K for $[4]\text{CC}@C_{60}$ was similar to that of intact C_{60} at 143 K [1], which indicated the liberation of C_{60} from motional restrictions in the presence of the tubular host. Rotational kinetics such as rotational correlation time (τ) and rotational frequency (k_{rot}) were determined by measurements of spin-lattice relaxation time (T_1). A series of T_1 values was obtained under three different magnetic fields to exclude field-independent non-CSA contributions contained in the T_1 values, which allowed us to determine the τ values. For instance, the temperature-dependent τ values were 4.7 ps at 335 K, which was converted to an extremely high k_{rot} value of 213 GHz. The τ values as well as the theoretical limit, τ_{FR} , of the inertial motions are plotted in Fig. 2(b).

An interesting test, the so-called χ -test, clarified the presence of unique dynamics. The χ value is defined as τ/τ_{FR} , which gives a good measure of motional regimes. Thus, it is suggested that when the χ value is less than 2, the rotational motion can be regarded as non-Brownian in the inertial regime [7]. As shown in Fig. 2(b), the χ value of our system started from 19 at 200 K, and gradually decreased upon elevating the temperature. The smallest χ value was recorded at 335 K and was 1.7, which was indeed smaller than 2. The χ -test thus demonstrated the presence of inertial motions of C_{60} that was trapped in the tubular $[4]\text{CC}$ host.

The solid-state dynamics of C_{60} were liberated from

restricting intermolecular contact by encapsulation in a tubular host. Interestingly, the association enthalpy was as large as 14 kcal/mol, which did not hamper the rotational motions. On the contrary, the tight host allowed the guest to rotate freely in the inertial regime in the solid state. Furthermore, we recently found a method of manipulating the direction of rotation via CH- π hydrogen bonds without changing the rotational enthalpy barrier [8]. An additional unique feature of the host is the presence of chirality: the rotational dynamics took place in a (*P*)-helical environment of the segmental nanotube. Exploration of the chirality-related phenomena should be of great interest in future.

REFERENCES

- [1] R. D. Johnson, C. S. Yannoni, H. C. Dorn, J. R. Salem and D. S. Bethune, *Science* **255**, 1235 (1992).
- [2] R. Tycko, G. Dabbagh, R. M. Fleming, R. C. Haddon, A. V. Makhija and S. M. Zahurak, *Phys. Rev. Lett.* **67**, 1886 (1991).
- [3] S. Hitosugi, W. Nakanishi, T. Yamasaki and H. Isobe, *Nat. Commun.* **2**, 492 (2011).
- [4] H. Isobe, S. Hitosugi, T. Yamasaki and R. Iizuka, *Chem. Sci.* **4**, 1293 (2013).
- [5] S. Sato, T. Yamasaki and H. Isobe, *Proc. Nat. Acad. Sci. U.S.A.* **111**, 8374 (2014).
- [6] T. Matsuno, Y. Nakai, S. Sato, Y. Maniwa and H. Isobe, *Nat. Commun.* **9**, 1907 (2018).
- [7] W. A. Steele, *J. Chem. Phys.* **38**, 2404 (1963).
- [8] T. Matsuno, M. Fujita, K. Fukunaga, S. Sato and H. Isobe, *Nat. Commun.* **9**, 3779 (2018).

BEAMLINE

AR-NE3A

T. Matsuno, S. Sato and H. Isobe (The Univ. of Tokyo)

Self-Assembling Supramolecular Nanostructures Constructed from *de Novo* Extender Protein Nanobuilding Blocks

To construct chain-like polymeric nanostructures, we designed *de novo* extender protein nanobuilding blocks (ePN-Blocks) by tandemly fusing two *de novo* binary-patterned proteins with various linkers. The ePN-Blocks with long helical linkers or flexible linkers were constructed and analyzed by native PAGE, size exclusion chromatography-multiangle light scattering (SEC-MALS), small-angle X-ray scattering (SAXS), and transmission electron microscopy, suggesting the formation of various structural homooligomers. Subsequently, we reconstructed heterooligomeric complexes from extender and stopper PN-Blocks by denaturation and refolding. The SEC-MALS and SAXS analyses showed that extender and stopper PN-Block (esPN-Block) heterocomplexes formed different types of extended chain-like conformations depending on their linker types.

Living organisms are maintained by various self-assembling biomolecules including proteins, nucleic acids, sugars, and lipids. The structural and functional design of artificial proteins and protein complexes as desired is one of the ultimate goals of protein science and protein engineering. To achieve this goal, we consider that the design of artificial proteins that self-assemble into supramolecular complexes is an important step in the emerging field of “synthetic structural biology.” Several years ago, we solved the three-dimensional structure of a *de novo* protein WA20 designed by binary patterning. The WA20 formed an intermolecularly folded dimeric 4-helix bundle structure [1]. Recently, we designed and constructed a protein nanobuilding block (PN-Block), WA20-foldon, by fusing an intermolecularly folded dimeric *de novo* protein WA20 and a trimeric foldon domain of T4 phage fibritin [2]. WA20-foldon formed several types of self-assembling nanoarchitectures in multiples of 6-mers, including a barrel-like hexamer and a tetrahedron-like dodecamer.

In this study, to construct chain-like polymeric nanostructures, we designed *de novo* extender protein nanobuilding blocks (ePN-Blocks) by tandemly fusing two *de novo* binary-patterned WA20 proteins with heli-

cal or flexible linkers (Fig. 1) [3]. The ePN-Blocks with long helical linkers or flexible linkers were expressed in soluble fractions of *Escherichia coli*, and the purified ePN-Blocks were analyzed by native PAGE, size exclusion chromatography-multiangle light scattering (SEC-MALS), small-angle X-ray scattering (SAXS), and transmission electron microscopy. These results suggest the formation of various structural homooligomers.

Subsequently, we reconstructed heterooligomeric complexes from extender and stopper PN-Blocks by denaturation and refolding. The SEC-MALS and SAXS analyses showed that extender and stopper PN-Block (esPN-Block) heterocomplexes formed different types of extended chain-like conformations depending on their linker types. Figure 2 shows three-dimensional structural modeling of the esPN-Block (HL4) heterocomplex, e1s2 (HL4), based on SAXS analysis [3]. A rigid-body model structure of one extender and two stopper PN-Blocks [e1s2 (HL4)] was constructed based on the crystal structure of the WA20 dimer (PDB code 3VJF) [1] to explain the experimental $p(r)$ with consideration of the helical linker rigidity following linking of C and N terminals. The rigid-body model [Fig. 2(A)] shows an extended Z shape, and the simulated $I(q)$ and $p(r)$ from

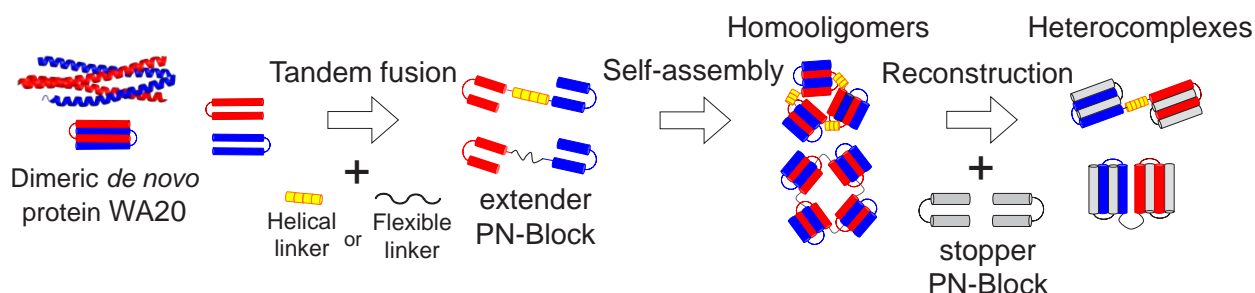


Figure 1: Schematic illustration of design and construction of extender protein nanobuilding blocks (ePN-blocks) and their complexes [3].

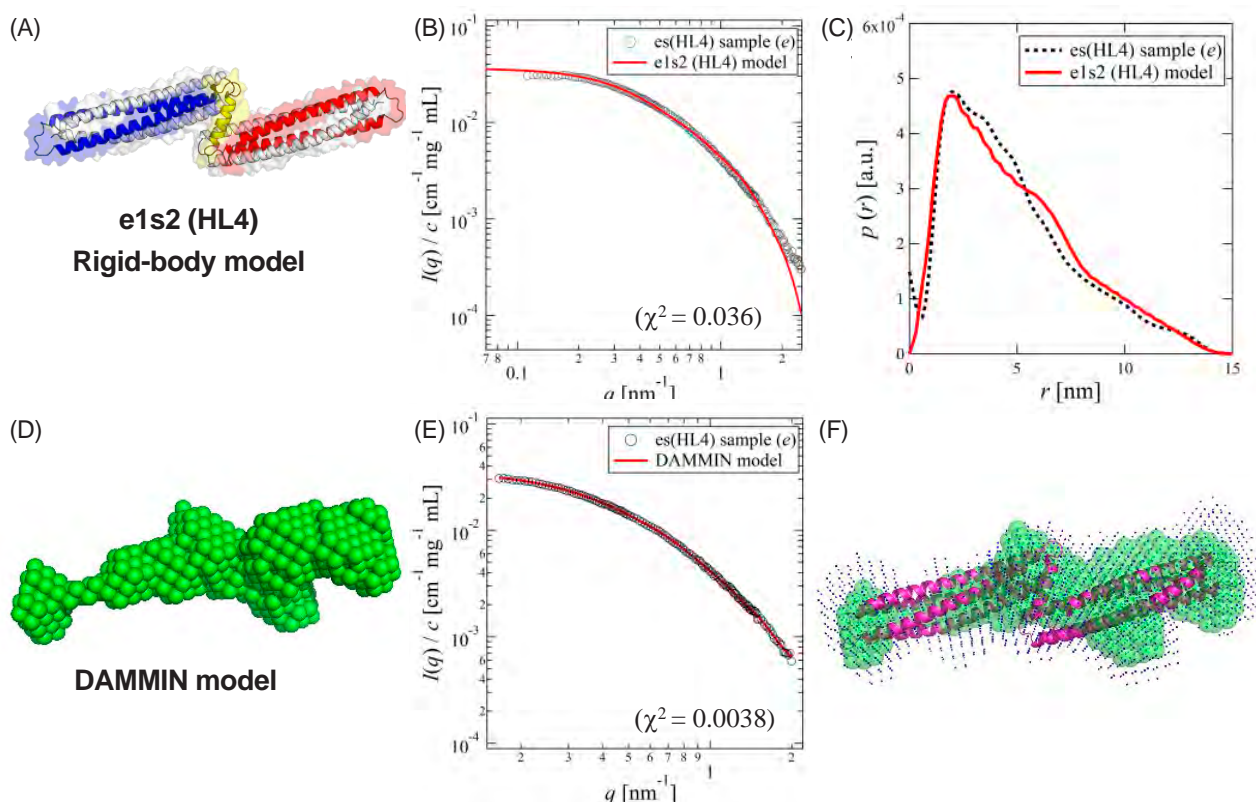


Figure 2: Three-dimensional structural modeling of the esPN-Block (HL4) heterocomplex [e1s2 (HL4)] based on SAXS analysis. **(A)** A rigid-body model structure of one extender and two stoppers (e1s2) of the esPN-Block (HL4) heterocomplex. **(B)** The concentration-normalized scattering intensity of the esPN-Block (HL4) heterocomplex [es (HL4)] sample obtained by the SAXS experiment (open circles) and fitting of $I(q)$ simulated from the rigid-body model of e1s2 (HL4) (red line). **(C)** The pair-distance distribution function $p(r)$ of the esPN-Block (HL4) heterocomplex sample (e) calculated from the SAXS data (black dash line) and $p(r)$ simulated from the rigid-body model of e1s2 (HL4) (red line). **(D)** A dummy atom model of e1s2 (HL4) reconstructed from the SAXS data using *ab initio* modeling programs DAMMIF and DAMMIN. **(E)** The concentration-normalized scattering intensity of the esPN-Block (HL4) heterocomplex sample (black open circles) and fitting of $I(q)$ simulated from the DAMMIN model of e1s2 (HL4) (red line). **(F)** Superimposition of the rigid-body model (magenta ribbon representation) and the dummy atom model (green) of e1s2 (HL4). Blue dots represent an averaged model from ten structural models calculated by DAMMIF. Reprinted from reference [3] with permission. Copyright © 2018, American Chemical Society.

the rigid-body model closely resemble those from the SAXS experiment [Fig. 2(B) and 2(C)]. Moreover, the low-resolution dummy atom model was reconstructed from the SAXS data using *ab initio* shape modeling programs DAMMIF and DAMMIN [Fig. 2(D) and 2(E)]. The DAMMIN model is superimposed on the rigid-body model as shown in Fig. 2(F).

Moreover, atomic force microscopy imaging in liquid suggests that the esPN-Block heterocomplexes with metal ions further self-assembled into supramolecular nanostructures on mica surfaces. Taken together, the present study demonstrates that the design and construction of self-assembling PN-Blocks with *de novo* proteins is a useful strategy for building polymeric nano-architectures of supramolecular protein complexes.

REFERENCES

- [1] R. Arai, N. Kobayashi, A. Kimura, T. Sato, K. Matsuo, A. F. Wang, J. M. Platt, L. H. Bradley and M. H. Hecht, *J. Phys. Chem. B* **116**, 6789 (2012).
- [2] N. Kobayashi, K. Yanase, T. Sato, S. Unzai, M. H. Hecht and R. Arai, *J. Am. Chem. Soc.* **137**, 11285 (2015).
- [3] N. Kobayashi, K. Inano, K. Sasahara, T. Sato, K. Miyazawa, T. Fukuma, M. H. Hecht, C. Song, K. Murata and R. Arai, *ACS Synth. Biol.* **7**, 1381 (2018).

BEAMLIN

BL-10C

N. Kobayashi^{1,2} and R. Arai¹ (¹Shinshu Univ., ²NINS-ExCELLS)

Multidisciplinary Characterization of Abundant Ferromanganese Microparticles in Deep-Sea Oxidic Sediments: Implications for the Global Manganese Budget

Abundant (10^8 – 10^9 particles cm^{-3}) micrometer-scale ferromanganese mineral particles (Mn-microparticles) were found in deep-sea oxidic sediments of the South Pacific Gyre from the seafloor to the ~100 million-year-old sediments. Microtexture, major and trace element composition, and synchrotron-based redox state analyses revealed that these Mn-microparticles consist of poorly crystalline ferromanganese oxides precipitating from bottom water. We extrapolate that 1.5 – 8.8×10^{28} Mn-microparticles, accounting for 1.28–7.62 Tt of manganese, are present globally. This estimate is at least two orders of magnitude larger than the manganese budget of manganese nodules and crusts on the seafloor. Thus, Mn-microparticles contribute significantly to the global manganese budget.

Manganese is the third most abundant metallic element, after iron and titanium, in the Earth's crust, and ferromanganese minerals are sensitive to changes in redox condition. The redox-sensitive dynamics and budget of ferromanganese minerals are important for understanding the global cycling of manganese and numerous associated trace elements [1]. At present, the most extensive deposition of ferromanganese minerals occurs on the deep-seafloor in oceanic abyssal plains, including those below open-ocean gyres. However, the extent of ferromanganese minerals buried in subseafloor sediments remains unclear.

During the Integrated Ocean Drilling Program (IODP) Expedition 329, we drilled the entire sedimentary sequence at six sites in the ultra-oligotrophic region of the South Pacific Gyre (SPG), where dissolved O_2 and aerobic microbial communities are present from the seafloor to the ~100 million-year-old sediment-basement interface [2]. By establishing an improved method for the observation of sediment microstructure [3], we found abundant (10^8 – 10^9 particles/ cm^3 ; average, 3.34×10^8 particles/ cm^3) micrometer-scale ferromanganese mineral particles (Mn-microparticles) (Fig. 1) in the oxidic pelagic clays of the SPG [4]. Furthermore, we established a microparticle separation technique by the combined use of density concentration [5] and flow cytometer/particles sorting [6]. Major and trace element compositional

analyses by inductively coupled plasma-mass spectrometry (ICP-MS) revealed that iron and manganese were the major components of Mn-microparticles, while they also contained rare-earth elements (REEs). REE concentration patterns in these Mn-microparticles reveal predominantly positive cerium anomalies.

Bulk sample X-ray absorption fine structure (XAFS) analysis indicates the manganese oxidized state. The X-ray absorption near-edge structure (XANES) spectra at the Mn K-edge [Fig. 2(a)] of the bulk sediments herein exhibited absorption maxima similar to that of MnO_2 references such as δ - MnO_2 and birnessite. The extended X-ray absorption fine structure (EXAFS) spectra of selected samples [Fig. 2(b)] also showed dominant Mn(IV) in the bulk sample studied herein. However, scanning transmission X-ray microscopy (STXM) analysis of a separated Mn-microparticle indicated the manganese reduced state. The near-edge X-ray absorption fine structure (NEXAFS) spectra of manganese at the Mn L-edge of the separated Mn-microparticle exhibited absorption patterns similar to spectra of Mn(II) reference. Thermodynamic calculations of the redox state of the SPG sediment porewater suggest that Mn(II) minerals are unsaturated, which precludes precipitation of Mn(II) minerals in the oxidic subseafloor environment. We conclude that (1) the primary redox state of manganese in the Mn-microparticles is oxidized and

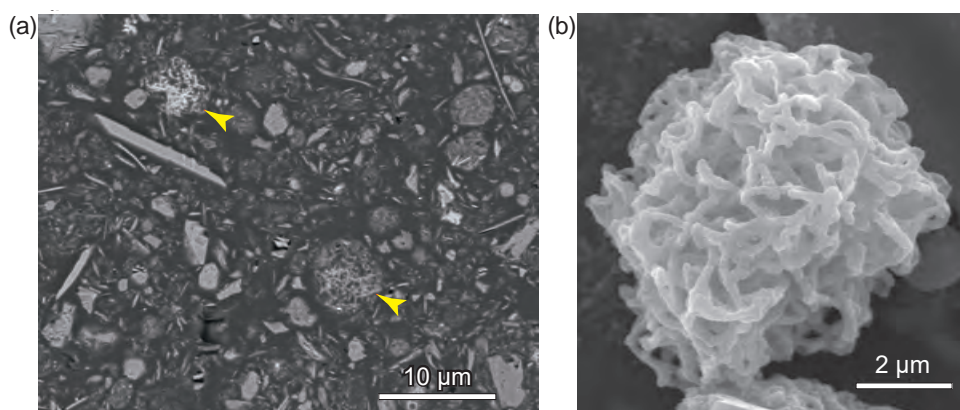


Figure 1: Representative electron micrographs of Mn-microparticles in sediment samples. (a) Cross-sectional scanning electron microscopy (SEM) images of resin-embedded oxidic pelagic clay. Arrows indicate Mn-microparticles. (b) SEM image of a Mn-microparticle in a density-separated sample (sample U1365C-1H-2 0/20).

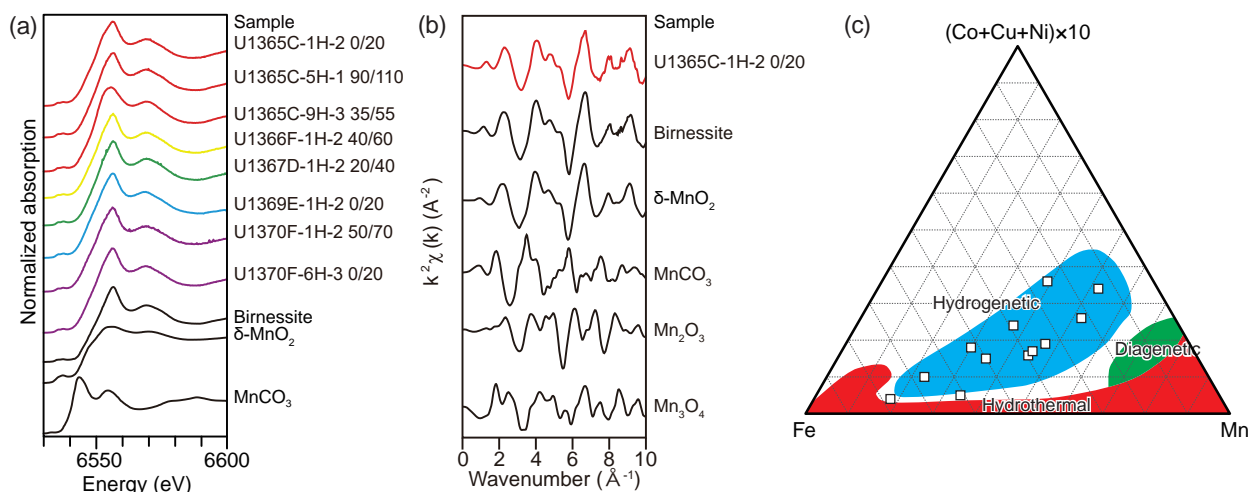


Figure 2: Geochemical characteristic of manganese in Mn-microparticles in oxic pelagic sediments. **(a)** XANES spectra of selected and standard samples. **(b)** Representative normalized k^2 -weighted EXAFS spectra for sample U1365C-1H-2 0/20 and standard samples. **(c)** Fe-Mn-(Co + Cu + Ni) $\times 10$ ternary diagram showing the origin of Mn-microparticles.

(2) photoreduction of manganese in Mn-microparticles may have occurred via irradiation by the intense X-rays during STXM measurements. Careful adjustment of the absorbed number of photons in a unit volume of sample and X-ray exposure time enables precise determination of the manganese redox state in Mn-microparticles.

Based on the major and trace elemental composition of Mn-microparticles (such as Fe-Mn-(Co+Cu+Ni) $\times 10$ ternary diagram [7] and values of Ce anomaly) and primary redox state of manganese in sediments, we interpret that Mn-microparticles in oxic SPG sediments were formed primarily by the hydrogenetic precipitation of manganese oxides from bottom water [Fig. 2(c)]. Together with this, the distribution of Mn-microparticles even in deep and old (~100 Ma) sediment indicates that the Mn-microparticles have been stable since their deposition over ~100 Ma. Since the Mn-microparticles are thought to be stable in the sediment, we can infer the flux of Mn-microparticles into the oxic sediments from the abundance in the sediment and its sedimentation rate. The Mn-microparticles are calculated to form and precipitate at a rate of 108 ± 35 microparticles/cm²-sediment per day.

This study based on the multidisciplinary characterization of Mn-microparticles provides a basis for understanding the global distribution and budget of manganese contained in Mn-microparticles within deep-sea oxic sediments. If we assume that the number of Mn-microparticles in the SPG pelagic clay is roughly constant at 3.34×10^8 cm⁻³, and accounts for changes in manganese content in Mn-microparticles with sediment depth (>40–70% in shallow sediments and <1.8% in deep sediments) and the global distribution of oxic pelagic clay [2], an estimated $1.5\text{--}8.8 \times 10^{28}$ Mn-microparticles are present in the oxic pelagic clays, corresponding to 1.28–7.62 Tt of manganese. Our manganese budget estimate from Mn-microparticles is at least 2–3 orders of magnitude higher than those presented in

previous studies based on seafloor manganese nodules and crusts [8]. Along with the examination of manganese input, formation, and preservation, the discovery of abundant Mn-microparticles provides new insight into the global manganese budget.

REFERENCES

- [1] J. E. Post, *Proc. Natl. Acad. Sci. U. S. A.* **96**, 3447 (1999).
- [2] S. D'Hondt, F. Inagaki, C. A. Zarikian, L. J. Abrams, N. Dubois, T. Engelhardt, H. Evans, T. Ferdelman, B. Gribsholt, R. N. Harris, B. W. Hoppie, J.-H. Hyun, J. Kallmeyer, J. Kim, J. E. Lynch, C. C. McKinley, S. Mitsunobu, Y. Morono, R. W. Murray, R. Pockalny, J. Sauvage, T. Shimono, F. Shiraishi, D. C. Smith, C. E. Smith-Duque, A. J. Spivack, B. O. Steinsbu, Y. Suzuki, M. Szpak, L. Toffin, G. Uramoto, Y. T. Yamaguchi, G.-I. Zhang, X.-H. Zhang and W. Ziebis, *Nat. Geosci.* **8**, 299 (2015)
- [3] G.-I. Uramoto, Y. Morono, K. Uematsu and F. Inagaki, *Limnol. Oceanogr. Methods* **12**, 469 (2014).
- [4] G.-I. Uramoto, Y. Morono, N. Tomioka, S. Wakaki, R. Nakada, R. Wagai, K. Uesugi, A. Takeuchi, M. Hoshino, Y. Suzuki, F. Shiraishi, S. Mitsunobu, H. Suga, Y. Takeichi, Y. Takahashi and F. Inagaki, *Nat. Comm.* **10**, 400 (2019).
- [5] R. Wagai, M. Kajjura, M. Asano and S. Hiradate, *Geoderma* **241**, 295 (2015).
- [6] Y. Morono, T. Terada, J. Kallmeyer and F. Inagaki, *Environ. Microbiol.* **15**, 2841 (2013).
- [7] E. Bonatti, T. Kraemer and H. Rydell, "Classification and Genesis of Submarine Iron-Manganese Deposits" in *Ferromanganese Deposits on the Ocean Floor*, edited by R. H. David, p.149-166 National Science Foundation, 1972.
- [8] J. M. Broadus, *Science* **235**, 853 (1987).

BEAMLINES

BL-9A and BL-13A

G.-I. Uramoto^{1,2}, Y. Morono¹, N. Tomioka¹, S. Wakaki¹, R. Nakada¹, R. Wagai³, K. Uesugi⁴, A. Takeuchi⁴, M. Hoshino⁴, Y. Suzuki^{4,5}, F. Shiraishi⁶, S. Mitsunobu⁷, H. Suga⁵, Y. Takeichi⁸, Y. Takahashi⁵ and F. Inagaki¹ (¹JAMSTEC, ²Kochi Univ., ³NARO, ⁴JASRI, ⁵The Univ. of Tokyo, ⁶Hiroshima Univ., ⁷Ehime Univ., ⁸KEK-IMSS-PF)

Newly-Developed High-Pressure Small-Angle X-Ray Scattering System at BL-18C Reveals Inhomogeneity in Silica Glass during Structural Transformation

Glass is usually considered to be homogeneous, but it is also known to show phase transformations called “polyamorphism” during which it could be inhomogeneous. To detect nanoscale inhomogeneity, we have developed a high-pressure small-angle X-ray scattering system at BL-18C and succeeded in detecting the signal from the transient state of pressure-induced phase transformation of silica glass. The data suggests that the size of inhomogeneity is sub-nanometer ($\sim 6 \text{ \AA}$) and the boundary between low- and high-density domains is unsharp.

Silica glass is one of the most studied noncrystalline materials. Despite its simple chemical composition, this material shows interesting behaviors such as anomalous elasticity, permanent densification, and gradual structural changes in short-range order [1]. These phenomena are related to some amorphous-amorphous phase transformations (polyamorphism). However, little is known about the intermediate state of pressure-induced polyamorphism because of the lack of suitable experimental techniques.

The gradual phase transformation in short-range order of silica glass occurs between 20 and 35 GPa and is accompanied by a $\sim 30\%$ increase in density [2]. Despite such large changes in density, silica glass remains optically homogeneous during the transformation. X-ray diffraction reveals that the average silicon coordination number gradually increases from four to six as the

transformation proceeds. However, no information on the inhomogeneity has been obtained because X-ray diffraction only provides information on the average atomic arrangement of noncrystalline materials. Small-angle X-ray scattering is a method that covers the length scale between optical microscopy (micron scale) and X-ray diffraction (angstrom scale). It provides information about the inhomogeneity of a sample on a nanometer scale. In this study, we developed small-angle X-ray scattering techniques to study the inhomogeneity of glass at high pressures, and used them to unveil the intermediate state of the transformation in silica glass.

High-pressure in-situ small-angle X-ray scattering experiments for silica glass were conducted using a newly-developed system at BL-18C [3]. **Figure 1** shows the setup for measuring X-ray scattering in the low- Q range for samples in diamond-anvil high-pressure cells (DAC). The system is very simple with two collimators and a vacuum chamber. The lower limit of the Q range is about 0.1 \AA^{-1} . The X-ray energy was set to around 15 keV considering the X-ray absorption and glitches of the anvils.

Figure 2(a) shows the pressure dependence of the scattering intensity averaged over the low- Q range (I_{av}) and the position of the first sharp diffraction peak (FSDP). Upon compression, the position of the FSDP changes monotonically with pressure, whereas I_{av} shows a maximum at $\sim 25 \text{ GPa}$. Upon decompression, the position and the height of the FSDP change drastically between 15 and 10 GPa. This is accompanied by a more obvious maximum in I_{av} . These drastic changes observed upon decompression can be attributed to the transformation from the sixfold-coordinated structure to the fourfold-coordinated structure. As the pressure-induced transformation in short-range order of silica glass occurs mainly between 20 and 35 GPa, the increase in the intensity of the small-angle X-ray scattering provides definitive evidence of a heterogeneous intermediate state during the transformation.

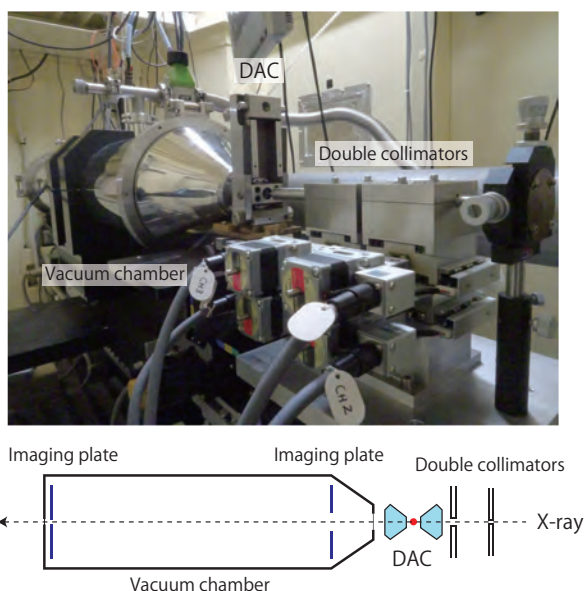


Figure 1: High-pressure small-angle X-ray scattering system at BL-18C.

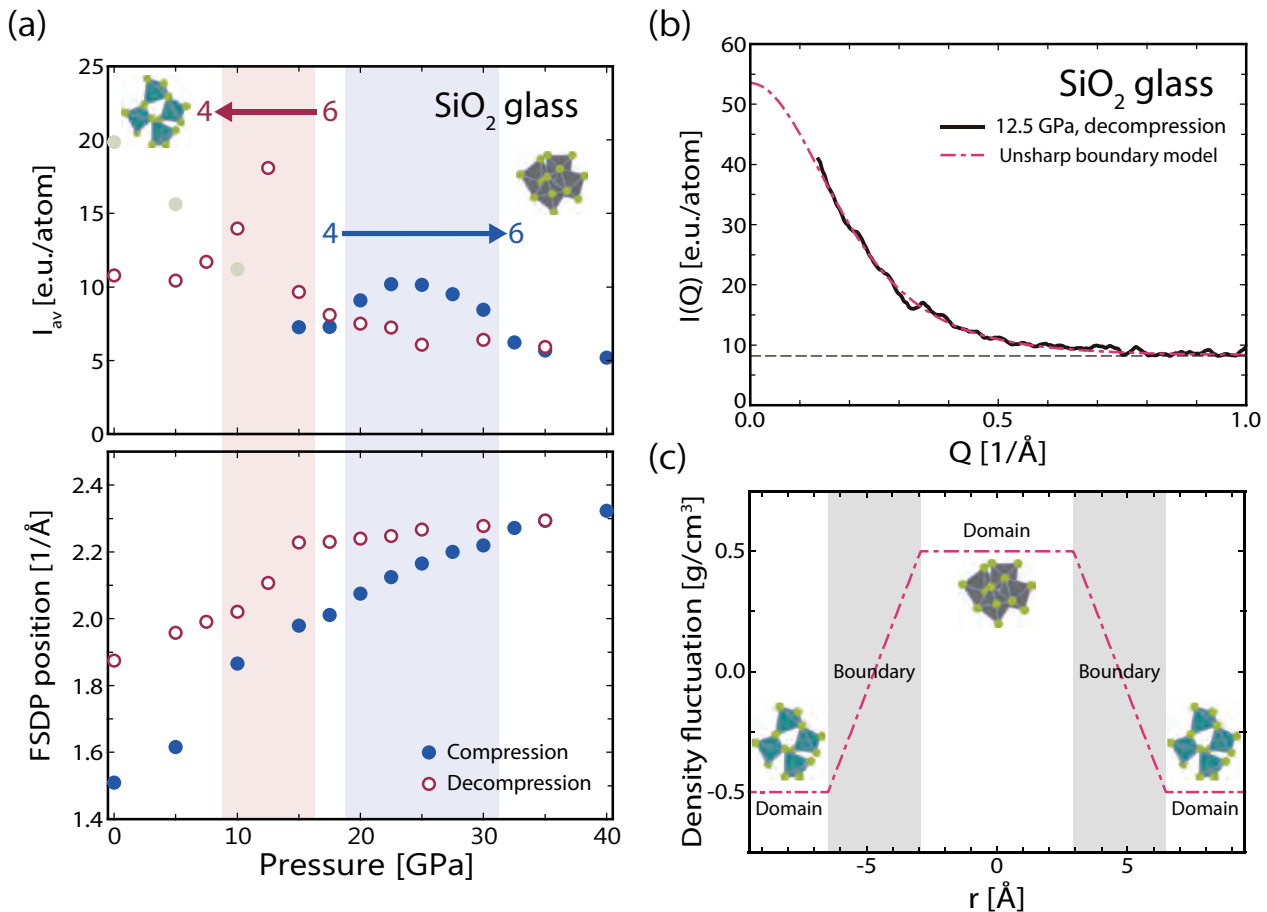


Figure 2: (a) Pressure dependence of I_{av} , the average scattering intensity at $Q = 0.14\text{--}0.60 \text{ \AA}^{-1}$, and the position of the FSDP. Gray symbols for I_{av} denote the data upon compression affected by the tail of the FSDP. (b) Low-Q X-ray scattering pattern of silica glass at 12.5 GPa upon decompression and (c) corresponding one-dimensional density-fluctuation model.

Figure 2(b) shows the low-Q X-ray scattering pattern of silica glass at 12.5 GPa on decompression. We have fitted the data with the two-phase mixing model extended to the case of an unsharp domain boundary [3] and obtained the parameters of the correlation length ζ and the boundary width E . Figure 2(c) shows the one-dimensional density-fluctuation model with the best-fitted parameters. The average domain size and boundary width are estimated to be $\sim 6 \text{ \AA}$ and $3\text{--}4 \text{ \AA}$, respectively. Considering that the Si-O bond length is $1.6\text{--}1.7 \text{ \AA}$ both in the fourfold-coordinated structure and the sixfold-coordinated structure, several SiO_4 tetrahedrons and SiO_6 octahedrons likely form one domain. The structure in the boundary region may be classified as a fivefold-coordinated structure. The result well explains the lack of heterogeneous features such as grain boundaries and cracks in optical microscopy, although

the two structures coexist in silica glass during the transformation. First, optical microscopy cannot identify domains that are smaller than the wavelength of visible light. Second, the broad boundary region with an intermediate structure likely works as a buffer.

REFERENCES

- [1] T. Sato and N. Funamori, *Phys. Rev. B* **82**, 184102 (2010).
- [2] T. Sato and N. Funamori, *Phys. Rev. Lett.*, **101**, 255502 (2008).
- [3] T. Sato, N. Funamori, D. Wakabayashi, K. Nishida and T. Kikegawa, *Phys. Rev. B* **98**, 144111 (2018).

BEAMLINE

BL-18C

T. Sato¹, N. Funamori² and D. Wakabayashi² (¹Hiroshima Univ., ²KEK-IMSS-PF)

Structural Basis for Recognition of Methylated DNA Ligase 1 by UHRF1

DNA methylation defines the gene expression patterns of somatic cells and is faithfully inherited after each cycle of replication to maintain cell identity. UHRF1 is an essential factor for the maintenance of DNA methylation, and recruits DNA methyltransferase to the methylation sites. Recently, replication factor DNA ligase1 (LIG1) has been shown to bind UHRF1 and recruit UHRF1 to the replication sites. Here, we determined the crystal structure of UHRF1 in complex with methylated LIG1, which reveals the details of the interaction between UHRF1 and LIG1. SAXS analysis demonstrated the structural change of UHRF1 from closed to open form upon binding of methylated LIG1. These structural data provide novel insights into the molecular mechanism of maintenance of DNA methylation coupled with DNA replication.

A fundamental role of biology is robust inheritance of genomic information. In addition to the genomic sequence, DNA methylation, which occurs at the C5 position of a cytosine in the CG dinucleotide sequence, is also known to be inheritable information.

DNA methylation contributes to gene silencing through heterochromatin formation. DNA methylation defines tissue-specific gene expression patterns, therefore, somatic cells have a unique feature. Importantly, DNA methylation patterns in the cells are inherited after each cycle of DNA replication to uphold the cell identity. UHRF1 is an essential factor for the maintenance of DNA methylation. UHRF1 has five functional domains: UBL, TTD, PHD SRA and RING domains. After DNA replication, UHRF1 binds to hemimethylated DNA, which is methylated at only the parent strand, and subsequently ubiquitinates histone H3. The ubiquitylated histone H3 functions as a binding platform for DNA methyltransferase, DNMT1. Finally, DNMT1 is recruited to hemimethylation sites by the ubiquitylated histone H3 and remethylates the nascent strand. Maintenance of DNA methylation occurs immediately after DNA replication, however, the mechanism underlying the functional

and structural relationship between replication and maintenance of DNA methylation is unclear.

DNA ligase 1 (LIG1) has emerged as a factor for recruiting UHRF1 to replication sites, thus LIG1 links replication and maintenance of DNA methylation [1]. LIG1 accumulates at replication sites during S-phase and catalyzes the ligation reaction of Okazaki fragments in lagging strands. Intriguingly, the N-terminal of LIG1 has a histone H3-like sequence and the side chain of Lys126 is methylated by lysine methyltransferase, G9a/GLP (H3: ⁴KQTARK⁹, LIG1: ¹²¹RRTARK¹²⁶, underline means methylated lysine residue). UHRF1 tandem tudor domain (TTD) binds to the methylated LIG1. The UHRF1 TTD domain is known to function as a hub that is involved in inter- and intramolecular interactions, such as histone H3 containing trimethylated K9 (H3K9me₃; known as an epigenetic mark for heterochromatin formation) and UHRF1 linkers [2]. Interestingly, despite the sequence similarity, UHRF1 TTD domain binds to trimethylated K126 in LIG1 (LIG1K126me₃) with the dissociation constant K_d of 9 nM, whereas the K_d between TTD and H3K9me₃ is 1 μ M. How can LIG1K126me₃ bind to UHRF1 TTD domain with high affinity?

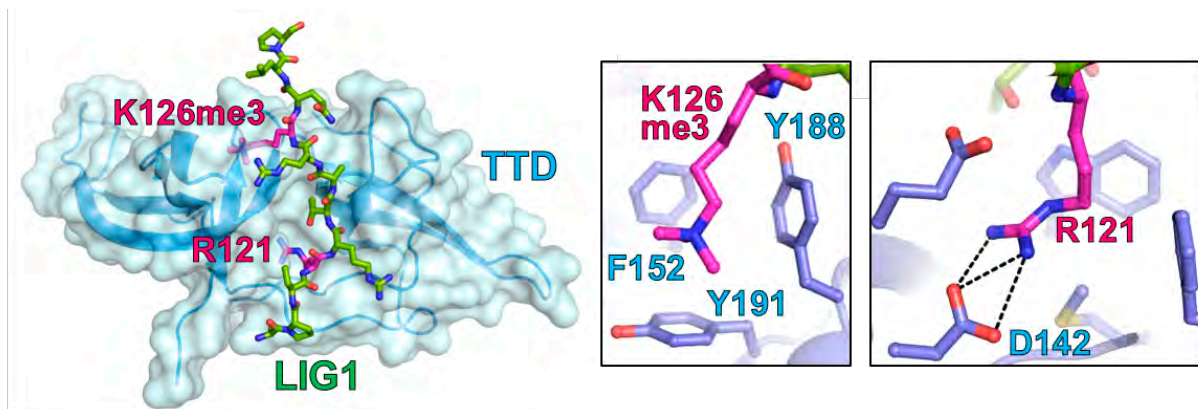


Figure 1: Crystal structure of UHRF1 TTD (blue cartoon model overlaid on surface model) bound to the LIG1K126me₃ peptide (green stick model). Arg121 and K126me₃ of LIG1 are colored magenta. Bottom panels are magnified views of recognition of Arg121 and K126me₃ of LIG1 by UHRF1 TTD.

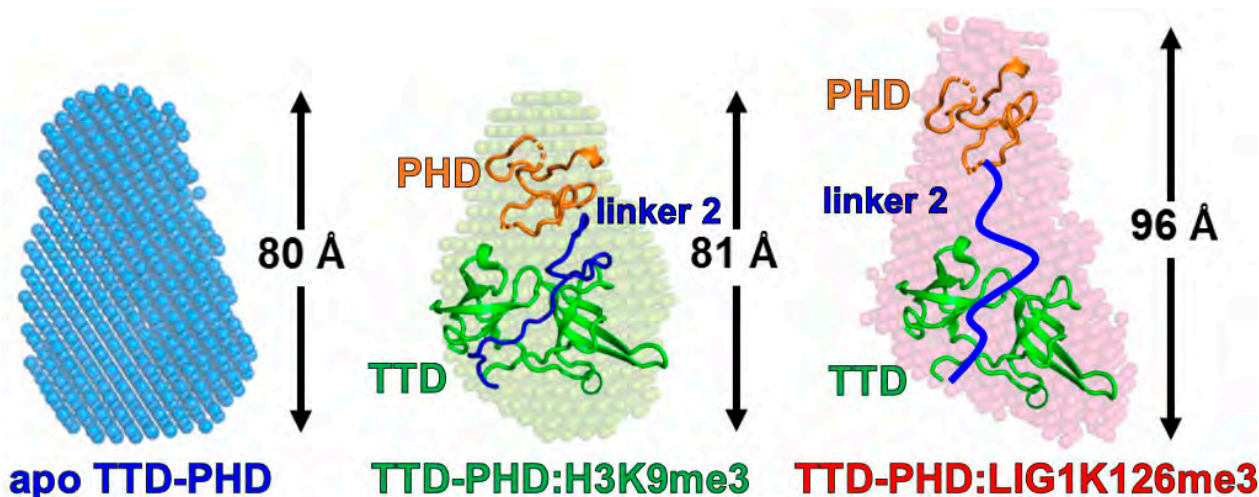


Figure 2: Low-resolution beads models of apo TTD-PHD (left) and when bound to H3K9me3 (middle) and LIG1K126me3 peptide (right). The crystal structure of TTD-PHD in complex with H3K9me3 and the open-form model of TTD-PHD upon binding of LIG1K126me3 are superimposed on the corresponding beads models, respectively.

To reveal the mechanism of the high affinity binding, we determined the crystal structure of UHRF1 TTD bound to the LIG1K126me3 peptide at BL-17A [3]. LIG1 binds to the groove of TTD (TTD groove) (Fig. 1). Two dense contacts were observed: K126me3 in LIG1 is recognized by an aromatic cage comprising F152, Y188 and Y191 of UHRF1 TTD, and Arg121 in LIG1 forms hydrogen bonds with Asp142 in the acidic pocket of UHRF1 TTD (Fig. 1). Structural and mutational analysis clearly showed that the interaction between Arg121 of LIG1 and the acidic pocket of UHRF1 TTD is critical for the high affinity binding, because only one amino-acid residue mutation (Lys4 to Arg, corresponding to Arg121 in LIG1) in histone H3 greatly enhanced the binding affinity to UHRF1 TTD with K_d of 22 nM, which is nearly identical to that of LIG1K126me3.

We also revealed the structural change of UHRF1 upon binding to LIG1K126me3 by SEC-SAXS at BL-10C (Fig. 2). The TTD-PHD module of UHRF1 has a compact structure in which the linker 2 between TTD and PHD interacts with the TTD groove [4]. The TTD-PHD module is known to bind to H3K9me3, where residues 1–4 and K9me3 are simultaneously recognized by PHD and TTD, respectively. SEC-SAXS analysis showed that binding of H3K9me3 leads to no structural change of TTD-PHD, which is still a compact structure. In contrast, binding of LIG1K126me3 to the TTD-PHD module is limited to the TTD region, as a result of which the structure of the TTD-PHD module is changed from closed to open form (Fig. 2).

Taken together, this study clarified the structural mechanism by which replication factor LIG1 could recruit UHRF1 to the replication site. In addition, we identified the important interaction point for the high affinity binding between UHRF1 and LIG1. It has been shown that overexpression of UHRF1 in various cancer cells is involved in aberrant DNA methylation which leads to silencing of tumor suppressor genes. The small molecule that binds to the acidic pocket in the TTD groove of UHRF1 may inhibit the interaction with LIG1, paving the way for the development of cancer drugs.

REFERENCES

- [1] L. Ferry, A. Fournier, T. Tsusaka, G. Adelmant, T. Shimazu, S. Matano, O. Kirsh, R. Amouroux, N. Dohmae, T. Suzuki, G.J. Filion, W. Deng, M. de Dieuleveult, L. Fritsch, S. Kudithipudi, A. Jeltsch, H. Leonhardt, P. Hajkova, J.A. Marto, K. Arita, Y. Shinkai and P.-A. Defossez, *Mol. Cell.* **67**, 550 (2017).
- [2] C. Bronner, M. Alhosin, A. Hamiche and M. Mousli, *Genes.* **10**, 65 (2019).
- [3] S. Kori, L. Ferry, S. Matano, T. Jimenji, N. Kodera, T. Tsusaka, R. Matsumura, T. Oda, M. Sato, N. Dohmae, T. Ando, Y. Shinkai, P.-A. Defossez and K. Arita, *Structure.* **27**, 485 (2019).
- [4] K. Arita, S. Isogai, T. Oda, M. Unoki, K. Sugita, N. Sekiyama, K. Kuwata, R. Hamamoto, H. Tochio, M. Sato, M. Ariyoshi and M. Shirakawa, *Proc. Natl. Acad. Sci. U.S.A.* **109**, 12950 (2012).

BEAMLINES

BL-10C and BL-17A

S. Kori and K. Arita (Yokohama City Univ.)

Structural Analysis Sheds Light on the Heparan Sulfate-Binding Ability of Nonclassical MHC-I Molecule, MILL2

MILL2 is a nonclassical major histocompatibility complex class-I molecule associated with β_2 -microglobulin. Previous reports suggested that MILL2 is involved in wound healing or nutrient metabolism; however, its molecular mechanisms remain unclear. Crystal structural analysis revealed that MILL2 has a unique basic patch located on the exposed surface of the α_3 domain. Further functional study identified the patch as a binding site to heparan sulfate on the cell surface of fibroblast. Interestingly, two forms (open and closed) of MILL2 with different orientation onto β_2 -microglobulin were observed. Binding study demonstrated that only MILL2 lacking β_2 -microglobulin binds the heparin column. This structural plasticity supports the idea that MILL2 constitutively associates with β_2 -microglobulin but releases it when bound to heparan sulfate.

Classical major histocompatibility complex class-I (MHC-I) molecules are type-I transmembrane proteins composed of extracellular α_1 , α_2 and α_3 domains associated with β_2 -microglobulin (β_2m). They ubiquitously express on the surface of nucleated cells to present peptides derived from intracellular proteins. Cytotoxic T lymphocytes survey classical MHC-I molecules presenting abnormal peptides derived from viral or tumor proteins, and eliminate the cells expressing them. Thus, classical MHC-I molecules play a key role in adaptive immunity against viral infection and malignant transformation.

On the other hand, genes encoding proteins similar to classical MHC-I α chains are found in mammalian genomes. These MHC-I-like proteins are called nonclassical MHC-I molecules and play diverse roles such as in the regulation of natural killer cells or NKT cells, lipid metabolism, iron transfer, IgG transportation and so on. MHC class I-like located near the leukocyte receptor complex (*Mill*) gene family were identified in the genomes of rodents, marsupials and odd-toed ungulates [1–3]. The members of *Mill* encoding proteins, MILL1 and MILL2, are nonclassical MHC-I proteins associated with β_2m [4]. MILLs were reported to be involved in wound healing [5]; however, the molecular function remains largely unknown.

Recently, we successfully determined the crystal structure of MILL2 extracellular domain as a heterodimer

with β_2m at 2.15 Å resolution [6]. The overall structure of MILL2 closely resembles that of other MHC-I molecules [Fig. 1(A)]. β_2m is located to the side of the α_3 domain. The α_1 and α_2 domains have two α -helices lying on the β -sheet platform formed by seven β -strands. In ligand-presenting MHC-I molecules, antigen peptide or small molecules fit in the groove of these helices; however, the distance between the two helices of MILL2 is too narrow to permit ligand binding. Electrostatic analysis of MILL2 revealed a remarkable basic patch on the exposed surface [Fig. 1(B)]. Six basic amino acids forming this patch (Arg194, Arg200, Lys229, Arg232, Arg247 and Arg251) are located at the α_3 domain near the β_2m interacting site [Fig. 1(C)]. Since this basic patch is unique to MILL2 among all classical and nonclassical MHC-I molecules, we hypothesized that it interacts with putative receptors or ligands by electrostatic interaction. MILL2 is known to bind to the cell surface of the fibroblast cell line NIH-3T3 [5]. We too confirmed that wild-type MILL2 tetramer bound to the surface of NIH-3T3 cells. In contrast, mutant tetramers in which some basic residues were replaced with alanine completely abolished binding to NIH-3T3 cells. In addition, treatment with trypsin, heparan sulfate (HS)-specific endoglycosidases or excess concentrations of heparin inhibited MILL2 tetramer-binding to NIH-3T3 cells. These results suggest that MILL2 binds to HS of glycoproteins on the cell surface of fibroblast.

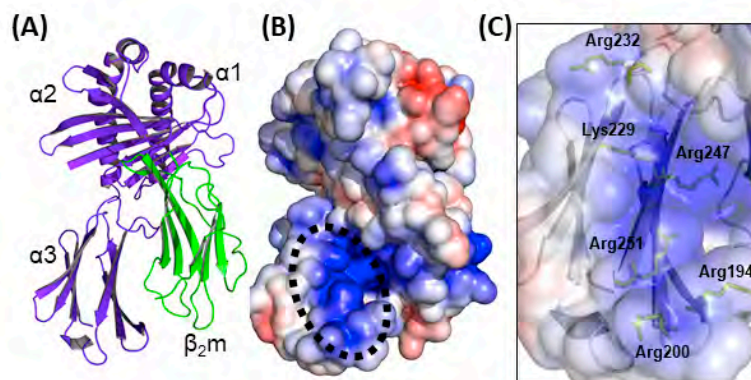


Figure 1: (A) Overall structure of MILL2 (closed form, green: β_2m , purple: MILL2 α chain). (B) Electrostatic surface potential of MILL2. Red and blue indicate negatively and positively charged areas, respectively. The black dotted circle indicates the MILL2-specific basic patch. (C) Magnified image of the basic patch area on the α_3 domain.

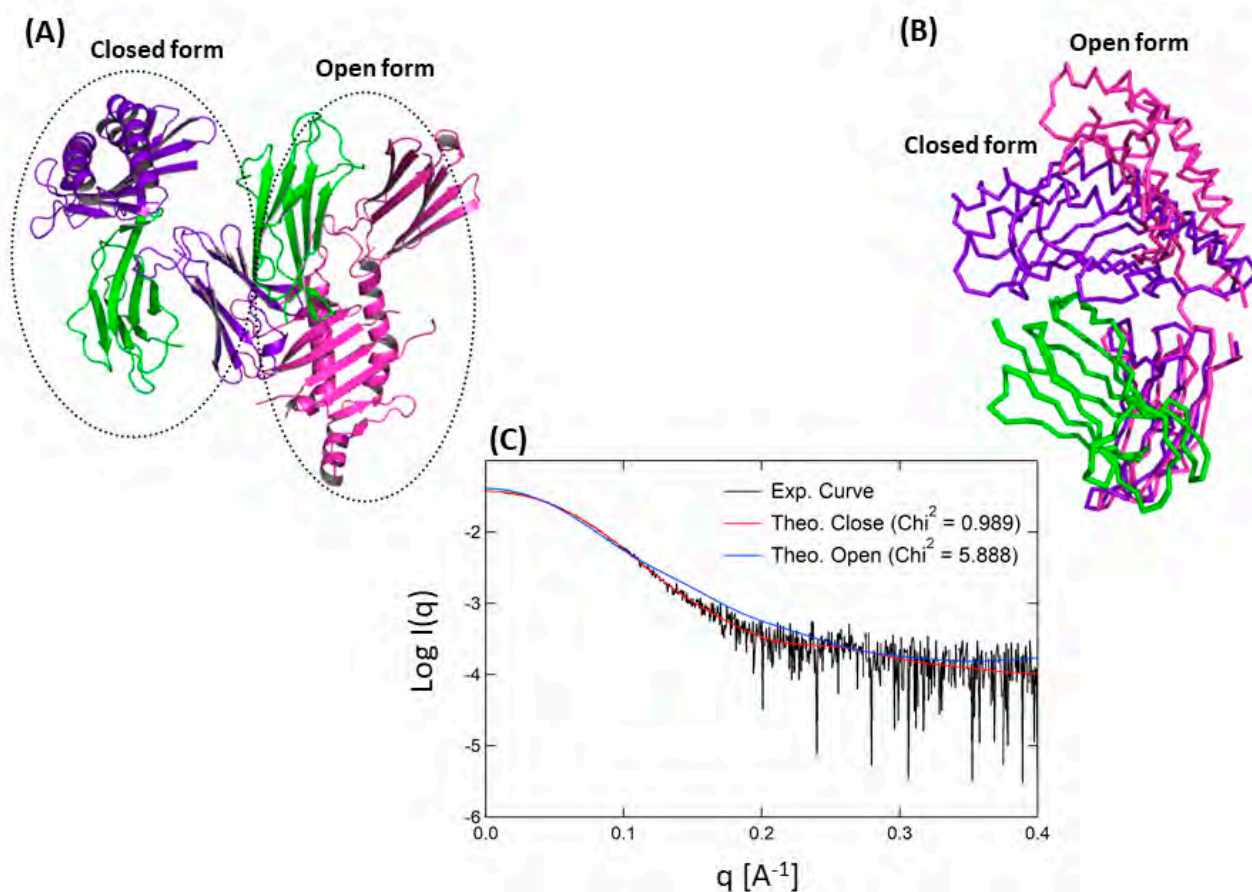


Figure 2: (A) Crystal packing of MILL2 (open and closed forms, green: $\beta_2 m$, purple and magenta: MILL2 α chain). (B) Superimposition of the two conformations based on the position of $\beta_2 m$. The coloring is the same as (A). (C) SAXS profiles of MILL2 (black line: experimental data, red and blue lines: theoretical model of closed and open forms, respectively).

Interestingly, two conformations of MILL2 are observed in the crystals [Fig. 2(A)]. In one form, the $\alpha 1$ - $\alpha 2$ domains are anchored with $\beta_2 m$ (closed form), similar to typical MHC-I molecules. On the other hand, in another form, the $\alpha 1$ - $\alpha 2$ domains are not associated with $\beta_2 m$ and are located far from the $\alpha 3$ - $\beta_2 m$ domains (open form) [Fig. 2(B)]. Small-angle X-ray scattering (SAXS) profiles demonstrated that the majority of MILL2 in solution exists in the closed conformation [Fig. 2(C)]. On the other hand, heparin affinity chromatography revealed that $\beta_2 m$ dissociates from MILL2 when MILL2 binds to heparin. MILL2 should exist in the open conformation since the fixing of the $\alpha 1$ - $\alpha 2$ domain by $\beta_2 m$ is completely lost. These observations suggested that MILL2 constitutively associates with $\beta_2 m$ but releases it when bound to HS on the surface of fibroblast. Since $\beta_2 m$ generally supports the structural stability of MHC-I molecules, $\beta_2 m$ likely contributes to the proper folding and stability of MILL2. On the other hand, upon binding to HS, the dissociation of $\beta_2 m$ from MILL2 might contribute to increasing the binding surface toward HS of heavily glycosylated cell surface proteins.

Taken together, structural analysis revealed that the “orphan molecule” MILL2 is the first MHC-I-like molecule having HS-binding ability. MILL2 presumably associates with HS-proteoglycans (HSPG) on the surface of fibro-

blast, which include the syndecan family important in the progression of wound healing. Further investigations for ligand evaluation, especially syndecans, will clarify MILL2-mediated wound healing.

REFERENCES

- [1] M. Kasahara, Y. Watanabe, M. Sumasu and T. Nagata, *Proc. Natl. Acad. Sci. U.S.A.* **99**, 13687 (2000).
- [2] Y. Watanabe, T. Maruoka, L. Walter and M. Kasahara, *Eur. J. Immunol.* **34**, 1597 (2004).
- [3] M. Kondo, T. Maruoka, N. Otsuka, J. Kasamatsu, K. Fugo, N. Hanzawa and M. Kasahara, *Immunogenetics* **62**, 441 (2010).
- [4] M. Kajikawa, T. Baba, U. Tomaru, Y. Watanabe, S. Koganei, S. Tsuji-Kawahara, N. Matsumoto, K. Yamamoto, M. Miyazawa, K. Maenaka, A. Ishizu and M. Kasahara, *J. Immunol.* **177**, 3108 (2006).
- [5] B. A. Rabinovich, R. R. Ketchum, M. Wolfson, L. Goldstein, M. Skelly and D. Cosman, *Immunol Cell Biol.* **86**, 489 (2008).
- [6] M. Kajikawa, T. Ose, Y. Fukunaga, Y. Okabe, N. Matsumoto, K. Yonezawa, N. Shimizu, S. Kollnberger, M. Kasahara and K. Maenaka, *Nat. Commun.* **9**, 4330 (2018).

BEAMLINES

BL-17A and BL-10C

M. Kajikawa^{1,2}, T. Ose³, K. Yonezawa⁴, N. Shimizu⁴ and K. Maenaka^{2,3} (¹Showa Pharm. Univ., ²Kyushu Univ., ³Hokkaido Univ., ⁴KEK-IMSS-PF)

Toll-Like Receptor 9 Contains Two DNA Binding Sites that Function Cooperatively to Promote Receptor Dimerization and Activation

Innate immunity is essential for host defense against microbial infections and relies on pattern recognition receptors (PRRs) such as Toll-like receptors (TLR) for pathogen recognition. TLR9 is known as a sensor of unmethylated CpG motif of DNA (CpG DNA) derived from pathogens. Structural and biochemical analyses demonstrate that TLR9 recognizes not only CpG DNA but also 5'-xCx motif containing DNA (5'-xCx DNA) and the latter binds to TLR9 in the presence of CpG DNA and promotes dimerization and activation of TLR9. The findings of this study will help understand the mechanism of TLR9 activation and the development of therapeutic agents targeting TLR9.

Toll-like receptor (TLR) recognizes molecular patterns from pathogenic microorganisms and activates an innate immune response through inducing the production of type I interferons and pro-inflammatory cytokines. TLR is a type-I transmembrane receptor and, to date, 10 TLRs have been identified in humans. Structural analyses have revealed that ectodomains of TLRs form a homo- or hetero-dimer upon binding of ligands. Members of the TLR7 subfamily, including TLR7, 8 and 9, are localized in endosome and participate in the sensing of nucleic acids derived from microbes, namely, ssRNA (TLR7/8) and ssDNA with CpG motifs (TLR9). So far, the crystal structure of TLR9 complexed with CpG DNA (2:2 complex) has been determined [1], where the two CpG DNAs are recognized by both TLR9 protomers and contribute to the TLR9 dimerization (Fig. 1A). A recent study has shown that DNAs containing the TCG or TCC motif at the 5' end in addition to the CpG motif activate TLR9 more effectively than DNAs with the CpG motif alone [2, 3] length, and dimerization properties of ODNs modulate their activation of TLR9. We performed a systematic investigation of the sequence motifs of B-class and C-class phosphodiester ODNs to identify the sequence properties that govern TLR9 activation. ODNs shorter than 21 nt and with the adenosine adja-

cent to the cytidine-guanosine (CG. Moreover, in TLR7 and TLR8, mononucleoside and ssRNA bind to distinct sites and exhibit synergistic effects in the dimerization of TLR7 and TLR8 [4, 5]. Because of functional and structural similarities among TLR7 subfamily members, there is the possibility that a second binding site also exists in TLR9.

Assuming that the second binding site of TLR9 might recognize 5'-TCG or 5'-TCC motif, a binding assay of 10-mer CpG DNA (AGGCGTTTTT) and 6-mer 5'-TCG DNA (TCGCCC) for TLR9 was conducted. ITC experiments showed that CpG DNA alone bound to TLR9 with a K_d value of 97 nM, while 5'-TCG DNA alone did not bind to TLR9. However, 5'-TCG DNA bound to TLR9 in the presence of CpG DNA with a K_d of 21 nM. Moreover, size-exclusion chromatography analysis showed that 5'-TCG DNA promotes dimerization of TLR9 in the presence of CpG DNA. Detailed analyses of the sequence specificity of the 5'-TCG DNA binding site in TLR9 using 5'-TCG DNA sequence variants revealed that DNAs with a cytosine nucleotide at the second position from the 5' end (hereafter referred to as 5'-xCx DNA) bound strongly to TLR9, and this binding participated in TLR9 dimerization [6].

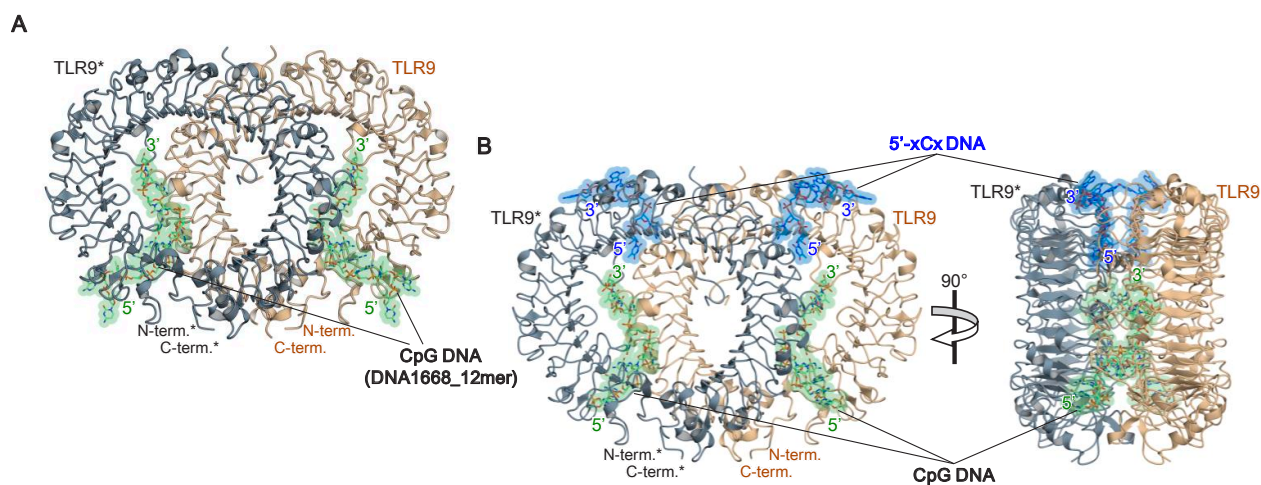


Figure 1: Activated dimer structures of TLR9. **A** Structure of horse TLR9 in complex with CpG DNA (PDB ID: 3WPC). **B** Structure of horse TLR9 in complex with CpG DNA and 5'-xCx DNA.

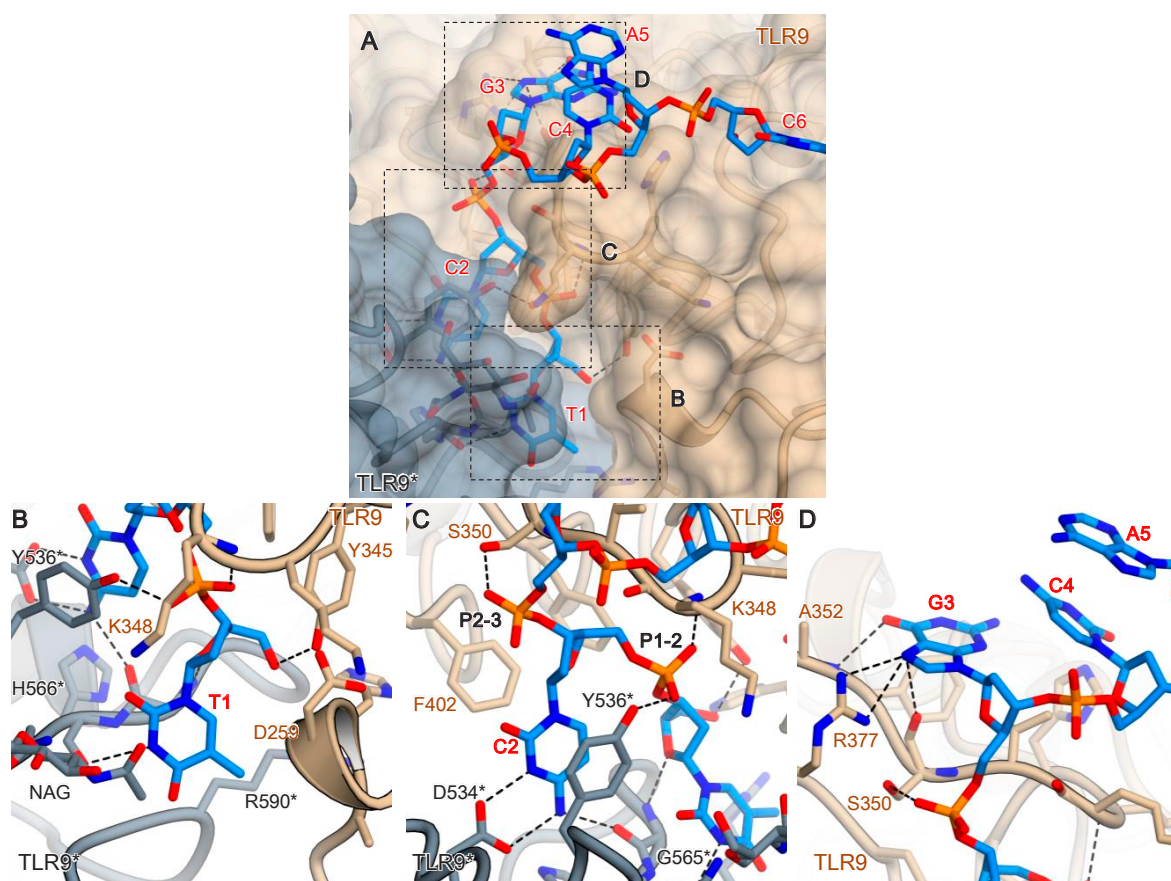


Figure 2: **A** Overview of 5'-xCx DNA binding site. **B-D** Close-up views of the first three nucleotide recognitions by TLR9. Hydrogen bonds are indicated with dashed lines.

To elucidate the structural mechanism by which two DNA motifs promote effective dimerization of TLR9, crystal structures of the TLR9 complexed with CpG and 5'-xCx DNA were determined using beamline AR-NE3A [6]. The structure formed a 2:2:2 complex and the overall structure was found to be essentially the same as the previously determined 2:2 complex of TLR9 and CpG DNA (Fig. 1). CpG DNA in the ternary complex bound to TLR9 in a manner similar to the 2:2 complex, while 5'-xCx DNA was observed in the newly identified binding site. The first three nucleotides of 5'-xCx DNA (T1, C2, G3) made multiple interactions with TLR9, which contributed mainly to the TLR9 binding and dimerization (Fig. 2A). The 5'-OH group of T1 was engaged with Tyr345 by hydrogen bonding and there was no space for an additional base at the 5'-end and C2 was tightly recognized by both TLR9 and TLR9* (Fig. 2C). These interactions determine the specificity of 5'-xCx DNA for TLR9 binding. The T1 and G3 nucleotides were loosely recognized by TLR9 (Fig. 2B, 2D). These observations were consistent with the result by ITC and SEC that DNA with cytosine nucleotide at the second position from the 5'-end strongly bound to TLR9. Interestingly, C2 in the 5'-xCx DNA was located at the identical position corresponding to guanosine and uridine complexed with TLR7 and TLR8, respectively.

This study demonstrated that TLR9 senses two different types of DNAs using two distinct sites, and that such a synergistic activation mechanism of two ligands is common among the TLR7 subfamily. These structural insights into the dimerization and activation mechanism of TLR9 may contribute to drug designs for regulating TLR9 activity.

REFERENCES

- [1] U. Ohto, T. Shibata, H. Tanji, H. Ishida, E. Krayukhina, S. Uchiyama, K. Miyake and T. Shimizu, *Nature* **520**, 702 (2015).
- [2] J. Pohar, A. Kužnik Krajnik, R. Jerala and M. Benčina, *J. Immunol.* **194**, 3901 (2015).
- [3] J. Pohar, D. Lainšček, K. Ivičak-Kocjan, M.-M. Cajnko, R. Jerala and M. Benčina, *Nat. Commun.* **8**, 15363 (2017).
- [4] H. Tanji, U. Ohto, T. Shibata, M. Taoka, Y. Yamauchi, T. Isobe, K. Miyake and T. Shimizu, *Nat. Struct. Mol. Biol.* **22**, 109 (2015).
- [5] Z. Zhang, U. Ohto, T. Shibata, E. Krayukhina, M. Taoka, Y. Yamauchi, H. Tanji, T. Isobe, S. Uchiyama, K. Miyake and T. Shimizu, *Immunity* **45**, 737 (2016).
- [6] U. Ohto, H. Ishida, T. Shibata, R. Sato, K. Miyake and T. Shimizu, *Immunity* **48**, 649 (2018).

BEAMLIN

AR-NE3A

H. Ishida, U. Ohto and T. Shimizu. (The Univ. of Tokyo)

Crystal Structure of the H3.3 Histone Chaperone Complex Subunit HIRA and its Functional Role

The HIRA complex, which comprises HIRA, UBN1, and CABIN1, is a histone chaperone for histone variant H3.3, mediating the incorporation of H3.3 into nucleosomes at transcribed regions and DNA repair sites. We found that HIRA acts as a trimer, as revealed by X-ray crystallographic and biochemical analyses. HIRA trimerization is essential for its localization at UV damage sites, H3.3 deposition, and interaction with its partner protein, CABIN1. The homotrimeric HIRA may serve as a platform interacting with components of transcription or repair machinery present at DNA bubble structures.

Eukaryotic chromatin consists of a repeat of nucleosomes, in which DNA is wrapped around a protein complex called a histone octamer. The histone octamer contains two molecules of each core histone, H2A, H2B, H3, and H4. Inheritance, expression, and repair of eukaryotic genetic materials usually involve chromatin remodeling, including nucleosome assembly and/or disassembly. The nucleosome assembly/disassembly is facilitated by a group of proteins called histone chaperones. Histone chaperones are associated with histones and stimulate a reaction involving histone transfer without being a part of the final product. The histone regulator A (HIRA) is a histone chaperone for the histone variant H3.3, mediating its incorporation to nucleosomes at transcribed regions and DNA repair sites [1, 2]. HIRA forms a complex with Calcineurin-binding protein 1 (CABIN1) and Ubinuclein 1 (UBN1) [3]. In order to reveal a functional oligomerization state of the HIRA complex, we conducted biochemical and crystallographic analyses [4].

After expression by *E. coli*, the C-terminal region of human HIRA (aa 644-1017) was purified in 300 mM NaCl (Fig. 1a). However, the purified protein was precipitated during concentration, and it could not be concentrated to higher than 1 mg/ml. Analysis of size-

exclusion chromatography with in-line multi-angle light scattering (SEC-MALS) detected an unstable refractive index (Fig. 1b). This problem was solved by increasing the NaCl concentration to 500 mM. Under this condition, HIRA(644-1017) could be concentrated to more than 10 mg/ml (Fig. 1c). SEC-MALS analysis indicated that the molecular weight of HIRA(644-1017) was $111,400 \pm 2.3\%$, which was comparable to the theoretical molecular weight of a trimer, 125,815 (Fig. 1d).

The purified HIRA(644-1017) (Fig. 1c) was crystallized using an automated protein crystallization and monitoring system, PXS [5]. The initial crystallization screening gave crystals from no. 14 of the Stura Footprint (Molecular Dimensions). The crystallization condition was further optimized based on the above condition by changing the concentration of the precipitant and pH. Moreover, Additive Screen (Hampton Research) and microseeding were used for the optimization. Finally, we obtained single crystals of HIRA(644-1017). Diffraction data for Se-SAD (single wavelength anomalous diffraction) phasing was collected with an X-ray of wavelength 0.9790 Å at beamline BL41XU of SPring-8 (Hyogo, Japan). Native-SAD data was collected with an X-ray of wavelength 1.9000 Å at beamline BL-17A at Photon Factory (KEK, Ibaraki, Japan). While initial

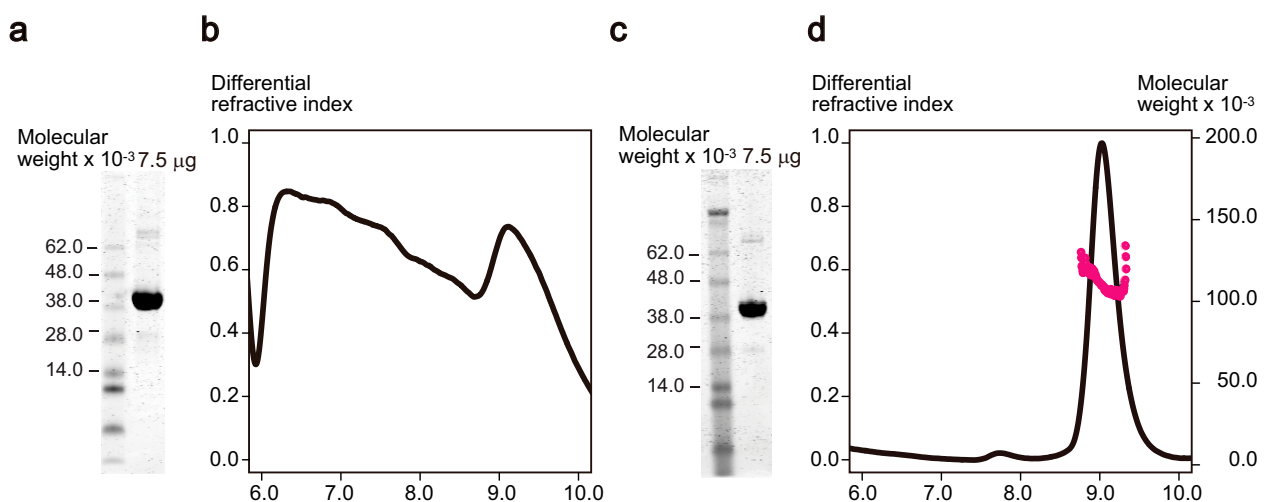


Figure 1: SEC-MALS analysis of HIRA(644-1017). **a** SDS-PAGE gel for HIRA(644-1017) in 300 mM NaCl and **b** SEC-MALS analysis of HIRA(644-1017) in 300 mM NaCl. **c** SDS-PAGE gel for HIRA(644-1017) in 500 mM NaCl and **d** SEC-MALS analysis of HIRA(644-1017) in 500 mM NaCl. The line indicates differential refractive index (left axis) and the dots indicate molecular weight (right axis).

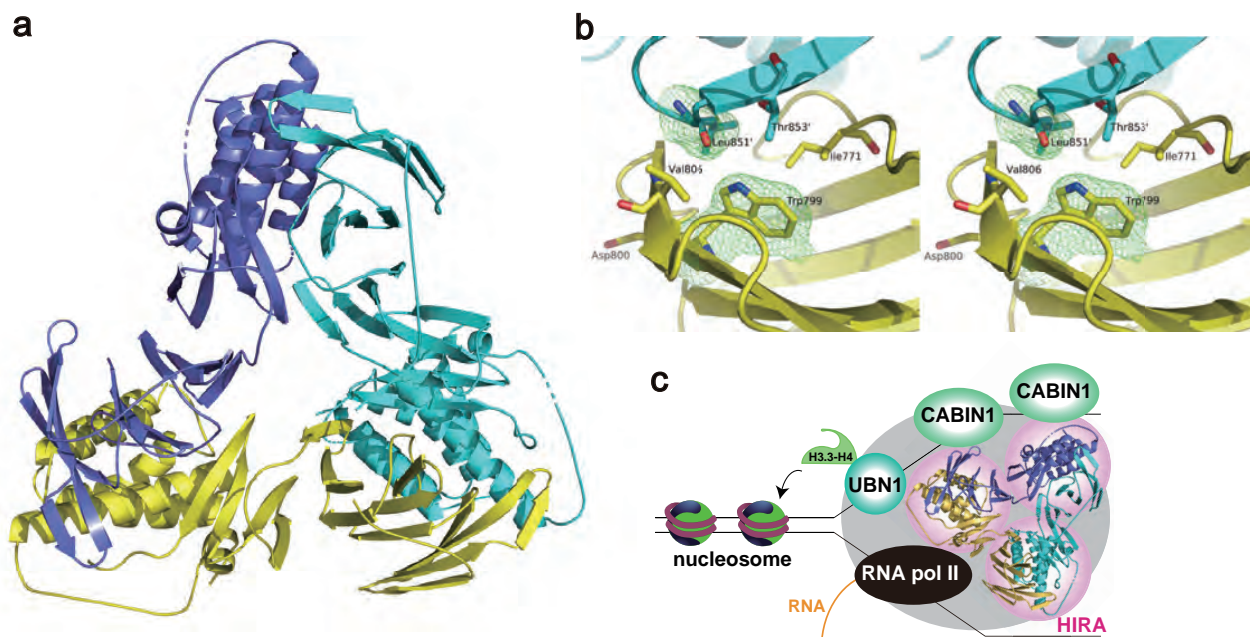


Figure 2: Crystal structure of HIRA(644-1017). **a** Overall structure of homotrimeric HIRA(644-1017). Subunits A, B, and C are shown in yellow, cyan and blue, respectively. **b** Trp799 located at the interface between subunits A and B, shown in the stereo image. The mFo-DFc simulated annealing (SA)-omit map for Trp799 in subunit A and Leu851 in subunit B is shown in green. The density map was countered at 3 σ . **c** Model for HIRA homotrimer function.

phases of the HIRA(644-1017) were obtained by the Se-SAD method, it was not possible to build the model for the C-terminal region of HIRA(644-1017) due to poor electron density. Accordingly, we obtained the molecular replacement (MR)-native SAD electron density map. The anomalous difference Fourier map gave coordinates of sulfur atoms in not only Met but also Cys residues, which helped us to construct the HIRA(644-1017) model. The crystal structure of HIRA(644-1017) was crystallographically refined at 2.45 Å resolution, of which diffraction data was collected with an X-ray of wavelength 0.9800 Å at beamline BL-17A (PF). The asymmetric unit of the crystal contained a homotrimer of HIRA(644-1017) (Fig. 2a). SEC-MALS analysis also showed that HIRA(644-1017) forms a trimer in solution (Fig. 1d). Immunoprecipitation analysis using YFP-tagged HIRA(492-1017) and YFP-tagged HIRA(1-440) revealed that endogenous HIRA co-immunoprecipitated with YFP-tagged HIRA(492-1017) but not with YFP-tagged HIRA(1-440), suggesting that HIRA(644-1017) forms an oligomer (probably a trimer) in cells. Immunoprecipitation analysis demonstrated that point mutations in Trp799 and Asp800 hampered homo-oligomerization of HIRA. While Asp800 does not interact with an adjacent subunit in the crystal structure of HIRA(644-1017), Trp799 is located at the interface of two subunits and forms a hydrophobic patch with Ile771 and Val806. Since this hydrophobic patch interacts with Leu851 and Thr853 of an adjacent subunit (Fig. 2b), substitution of Trp799 seems to reduce the hydrophobic interaction between the subunits. Further cell biological experiments

confirmed that HIRA homotrimerization is essential for its localization at UV damage sites, H3.3 deposition and interaction with CABIN1. Sedimentation analysis with CABIN1 revealed that the HIRA (aa 661-1017)-CABIN1 complex contains three HIRA and two CABIN1 molecules. These observations strongly suggest that the functional oligomeric state of HIRA is a homotrimer. We speculate that homotrimeric HIRA acts as a platform for multiple players of transcription or repair machineries present at DNA bubble structures (Fig. 2c).

REFERENCES

- [1] H. Tagami, D. Ray-Gallet, G. Almouzni and Y. Nakatani, *Cell* **116**, 51 (2004).
- [2] D. Ray-Gallet, A. Woolfe, I. Vassias, C. Pellentz, N. Lacoste, A. Puri, D. C. Schultz, N. A. Pchelintsev, P. D. Adams, L. E. Jansen and G. Almouzni, *Mol. Cell* **44**, 928 (2011).
- [3] M. D. Ricketts and R. Marmorstein, *J. Mol. Biol.* **429**, 1924 (2017).
- [4] D. Ray-Gallet, M. D. Ricketts, Y. Sato, K. Gupta, E. Boyarchuk, T. Senda, R. Marmorstein and G. Almouzni, *Nat. Commun.* **9** 1 (2018).
- [5] M. Hiraki, R. Kato, M. Nagai, T. Satoh, S. Hirano, K. Ihara, N. Kudo, M. Nagae, M. Kobayashi, M. Inoue, T. Uejima, S. Oda, L. M. Chavas, M. Akutsu, Y. Yamda, M. Kawasaki, N. Matsugaki, N. Igarashi, M. Suzuki and S. Wakatsuki, *Acta Crystallogr. D* **62**, 1058 (2006).

BEAMLINES

BL-1A, BL-5A, BL-17A and AR-NE3A

Y. Sato¹ and T. Senda^{2,3} (¹Tohoku Univ., ²KEK-IMSS-PF/SBRC, ³SOKENDAI)

Crystal Structure Determination using a Protein Fusion that Forms a Highly Porous Lattice

Protein crystallization requires numerous screenings, which hinders structural studies. To overcome this, an R1EN-fusion method was developed, which consists of preparing an R1EN-protein fusion and assembling the same crystal lattice as R1EN, consequently obtaining the crystal structure of the fusion guest. R1EN-ubiquitin fusions were prepared and crystals with the same lattice under the same conditions as the original R1EN were successfully obtained. The crystals diffracted to 1.7–2.4 Å resolution, and the ubiquitin structure could be determined by molecular replacement using R1EN. The R1EN-fusion method eliminates the need for crystallization screening and is useful for *de novo* protein structure determination.

A crystallization process requires setting a large number of conditions for screening and requires a large amount of high-purity protein, hindering crystal structure analysis. Accordingly, it is extremely difficult to develop an easy and versatile protein crystallization technique. In 1982, Seeman suggested a strategy of protein crystallization in which a crystal lattice made of DNA origami is used as a scaffold and a DNA-binding protein is arranged therein, consequently solving the crystal structure [1]; however, a long-stretched DNA itself is too flexible to retain the crystal lattice. Instead of DNA, using a protein that assembles a highly porous crystal lattice is a simple way to incorporate the protein of interest to the crystalline framework just by constructing a protein fusion. A previous study [2] focused on R1EN, which forms a hollow honeycomb crystal lattice with an inner diameter of ~110 Å (Fig. 1) [3], and demonstrated that R1EN-ubiquitin fusion protein (R1EN-Ub) could be assembled with the same honeycomb crystalline framework as R1EN, thus determining the X-ray structure of ubiquitin.

At first, a series of R1EN-Ub with various linker lengths were prepared and crystallized by the micro-seeding technique, resulting in the same hexagonal crystals under the same condition as the R1EN. X-ray diffraction data with 1.7–2.4 Å resolution were collected at AR-NW12A (PF) and BL44XU (SPring-8). The phases were obtained by molecular replacement using R1EN (PDB:2EI9) and ubiquitin (1UBQ). In R1EN₂₂₃-Ub (linker length: 3aa), the electron density of ubiquitin in the central cavity was observed, while in the long (≥ 11 aa) linker constructs, the electron density of ubiquitin could not be observed. There are two contact faces between ubiquitin and symmetric ubiquitin [Fig. 2(a)], one of which (contact-A) seems to be too close to neighboring ubiquitin. The steric collision in contact-A was not fixed even when the space group was converted to P1. The R1EN moiety was almost the same as the previous structure. Interestingly, the electron density of Met5-Pro9, which was disordered in the previous R1EN structure, was observed. There are four hydrogen bonds between ubiquitin Lys33 and Met5-Pro9, and

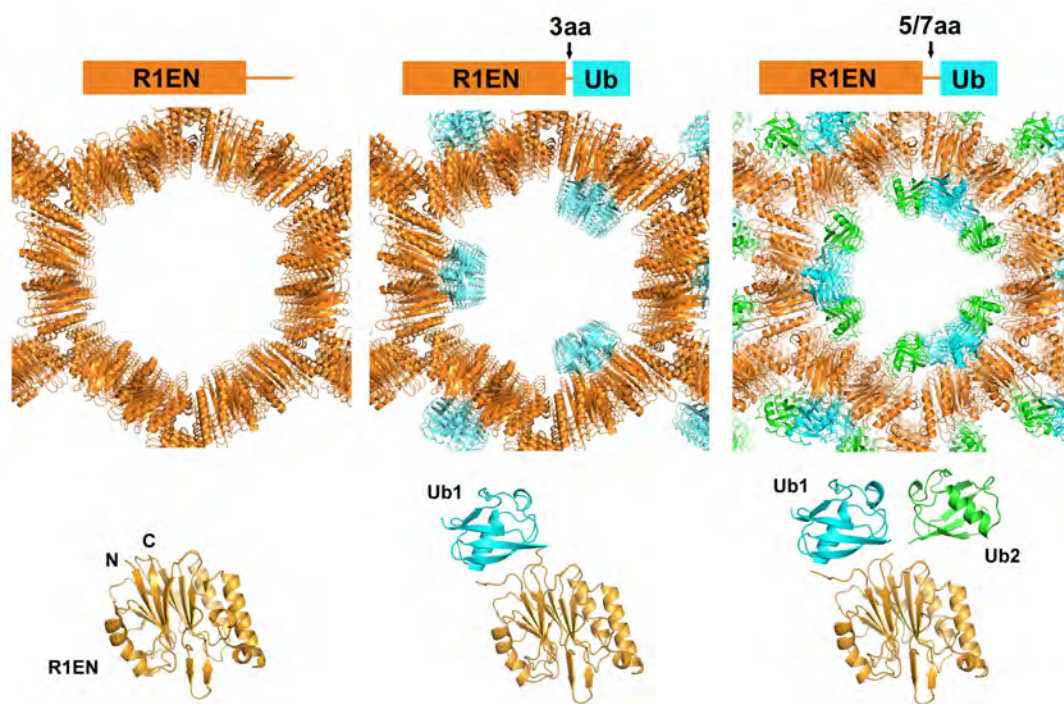


Figure 1: Crystal lattices of R1EN (left), R1EN₂₂₃-Ub (center), and R1EN_{225/227}-Ub (right).

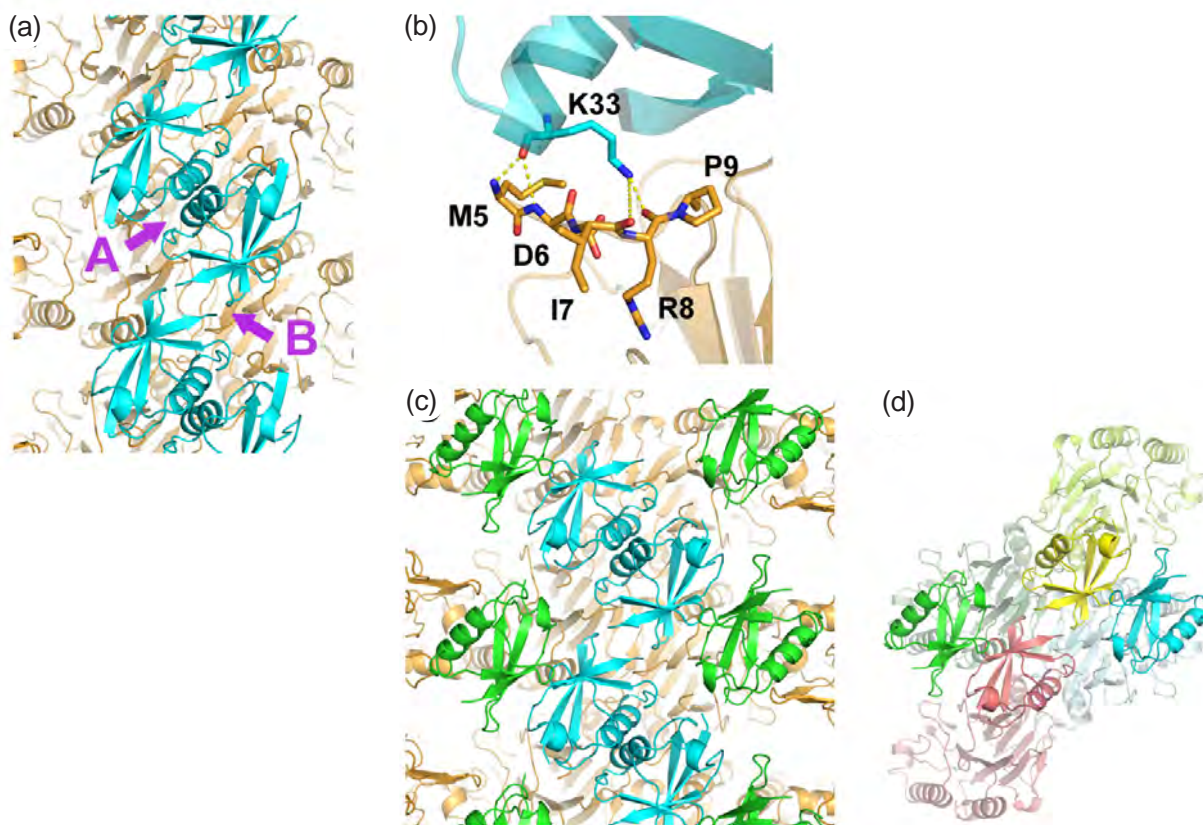


Figure 2: Interaction of ubiquitin moiety. **(a)** Two contact faces of Ub1. Steric collision in contact-A was observed. **(b)** Interaction between the N-terminal region of R1EN and Ub1. **(c)** Symmetry-related contacts of Ub1 and Ub2 in R1EN_{225/227}-Ub. **(d)** The proposed model of tetrameric R1EN-Ub unit in R1EN_{225/227}-Ub crystal. For clarity, R1EN-Ubs are colored yellow, green, cyan, and red, respectively.

presumably the Met5-Pro9 region interacted with ubiquitin, stabilizing each other [Fig. 2(b)].

Next, an attempt was made to solve the ubiquitin structure by the phases calculated from molecular replacement of R1EN alone. Phase improvement and auto-building were performed, and the resulting ubiquitin model contained 65 out of 72 residues of the main chain, including 36 of the correctly modelled side chains.

In R1EN₂₂₅-Ub (linker length: 5aa) and R1EN₂₂₇-Ub (linker length: 7aa), another ubiquitin subunit was observed [Fig. 1, 2(c)]. For clarity, the ubiquitin observed in R1EN₂₂₃-Ub is referred to as Ub1, and the second ubiquitin as Ub2. Since the N-terminus of Ub1 and Ub2 are close to each other, Ub2 is considered to be Ub1's multi-conformer. The distance between the Met1 in Ub2 and the C-terminus R1EN is 9.4 Å, which is too far for the R1EN₂₂₃-Ub to place the ubiquitin at the Ub2 position. Ub2 has no definite interaction with cis-R1EN, however, the Gln31-Gly35 region of Ub2 interacts with symmetry-related R1EN by water-mediated interactions. Moreover, Lys6 in Ub2 interacts with Asn60 and Gln62 in symmetry-related Ub1. Collectively, the Ub1-Ub1 interface at α 1 (contact-A) is too close, while other Ub1-Ub1 (contact-B) and Ub2-Ub1 interfaces are quite reasonable [Fig. 2(c)]. These observations suggest that in the crystalline lattice, four R1EN-Ubs compose one unit: two Ub1s in contact-B relationships

and the other two are placed in Ub2 [Fig. 2(d)]. The four R1EN-Ubs conformation is able to complete along the c-axis arrangement and compose one side of the hexagon, however, each side of the hexagon is independent in assembling the honeycomb structure, resulting in the overlapped electron density which seems to cause crushing of Ub1 at α 1. Similarly, in R1EN₂₂₃-Ub, two Ub1s may be in contact-B and other two subunits are disordered.

The refined ubiquitin structures in all fusion proteins are almost identical to the reported structure (1UBQ) with the main chain C α positional root mean square deviation range of 0.46–0.55 Å, indicating that the structure determined by the R1EN-fusion method is quite reliable. In conclusion, it is demonstrated that highly porous protein crystal could be used as a novel protein crystallization and structure determination tool by the fusion technique.

REFERENCES

- [1] N. C. Seeman, *J. Theor. Biol.* **99**, 237 (1982).
- [2] N. Maita, *J. Am. Chem. Soc.* **140**, 13546 (2018).
- [3] N. Maita, H. Aoyagi, M. Osanai, M. Shirakawa and H. Fujiwara, *Nucl. Acids Res.* **35**, 3918 (2007).

BEAMLINE

AR-NW12A

N. Maita (Tokushima Univ.)

Molecular Basis of Zinc-Dependent Regulation of ERp44 for Protein Quality Control in the Early Secretory Pathway

ERp44 is a PDI family member involved in the transport of various secretory proteins and some ER-resident proteins from the endoplasmic reticulum (ER) to the Golgi. Here, we found that Zn^{2+} binds to ERp44 with high affinity, modulating its intracellular localization and ability to retrieve clients. Crystal structures of Zn^{2+} -bound ERp44 reveal that Zn^{2+} binds to a conserved histidine-cluster, inducing large conformational changes. Consequently, the substrate-binding region of ERp44 is fully exposed to solvent, enhancing interactions with clients. These observations suggest a new physiological role of Zn^{2+} as a key regulator for protein quality control in the early secretory pathway.

ERp44, a member of the protein disulfide isomerase (PDI) family, is involved in the transport of various secretory proteins and several ER-resident proteins from the endoplasmic reticulum (ER) to the Golgi. ERp44 traps its clients in the Golgi, retrieving them to the ER in a pH-dependent manner. High-resolution crystal structures of ERp44 at pH 7.2 and 6.5 revealed that protonation of key histidine and cysteine residues induces pH-dependent conformational changes in the protein, leading to exposure of the positively charged client-binding site including the essential cysteine Cys29 [1]. The structures also suggested that metal ions can bind to a histidine-clustered site (His-cluster) comprising three highly conserved histidines (His299, His328, His332).

In this study, we found that ERp44 specifically binds Zn^{2+} with submicromolar affinity to form a Zn^{2+} -dependent homodimer [2]. Depletion of intracellular zinc by a Zn^{2+} chelator altered subcellular localization of ERp44. Furthermore, silencing the Zn^{2+} transporters localized

at the Golgi resulted in dysfunction of this chaperone, and increased secretion of its clients. To elucidate the detailed mechanism of how Zn^{2+} regulates ERp44, we determined the crystal structure of the Zn^{2+} bound form of ERp44 at 2.45Å resolution by the SAD method using the anomalous signals of Zn^{2+} . X-ray diffraction data were collected on the BL-1A beamline.

The overall structure of ERp44 consists of three thioredoxin (Trx)-like domains (**a**, **b**, and **b'**) and a C-terminal tail (C-tail). The crystal structure of the Zn^{2+} -bound ERp44 reveals that ERp44 forms a Zn^{2+} -bridged homodimer, where the **b'** domains from two protomers are bridged by a Zn^{2+} ion (Fig. 1). Three types of Zn^{2+} -binding sites (sites 1, 2 and 3) are found at the interface of the ERp44 homodimer. Site 1 is formed by the His-cluster in each protomer, at which a Zn^{2+} ion is coordinated by His299, His328, His332 and a water molecule in a tetrahedral geometry (Fig. 1, left lower inset). At the center of the dimer interface (site 2), two histidine pairs (His277 and His288) from the **b'** domains

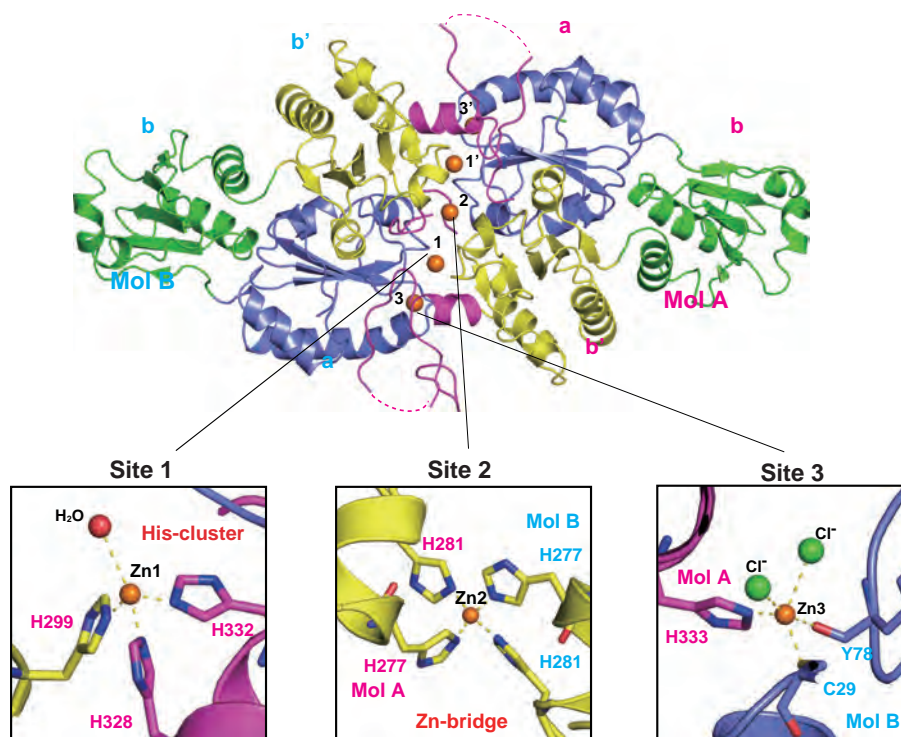


Figure 1: Crystal structure of the Zn-bridged ERp44 homodimer. The **a**, **b**, **b'** domains and C-tail of Mol A and Mol B are shown in blue, green, yellow, and magenta, respectively. The Zn^{2+} ions are shown as orange spheres. The lower insets display close-up views of the three Zn^{2+} -binding sites: site 1 (left), site 2 (middle) and site 3 (right).

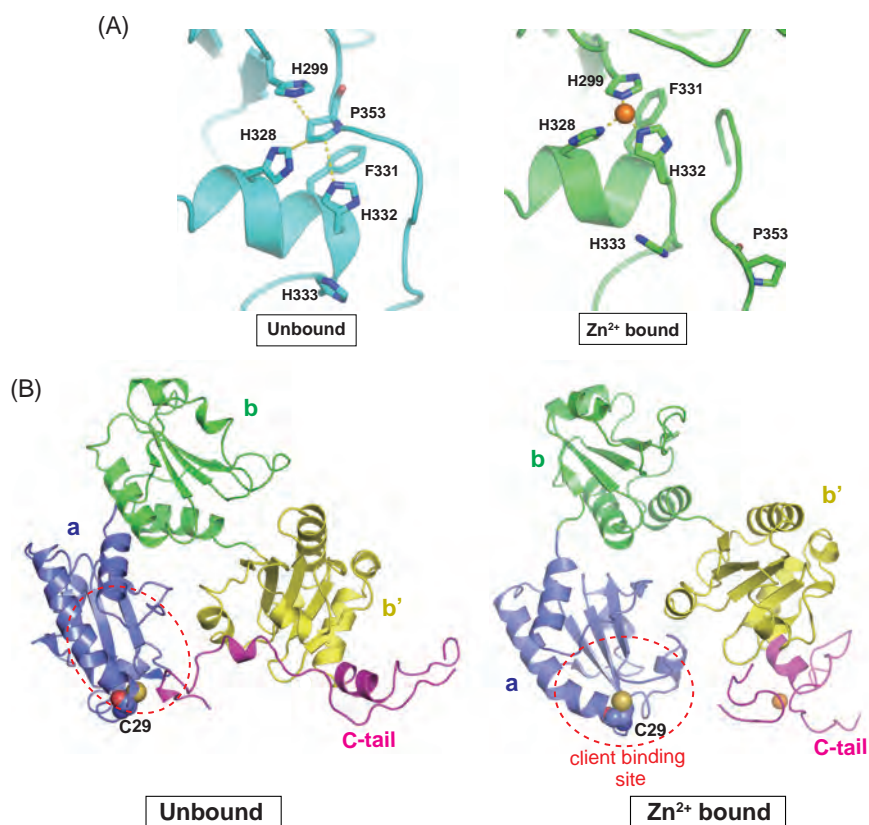


Figure 2 : Zn²⁺-dependent conformational changes of ERp44 **(A)** Structural comparison of the His-cluster region in the metal-unbound (left) and Zn²⁺-bound (right) ERp44. **(B)** Comparison of the overall domain arrangement in the metal-unbound (left) and Zn²⁺-bound (right) states of ERp44 monomer. The essential cysteine (Cys29) is represented as spheres. Red-dashed circles indicate a client binding site.

coordinate a Zn²⁺, playing an essential role in homodimerization of ERp44 (**Fig. 1**, middle lower inset). The Zn-bridged ERp44 homodimer possesses a third Zn²⁺-binding site (site 3), which is unexpected because our ITC analyses suggested the presence of only two Zn²⁺-binding sites in ERp44. At site 3, Zn²⁺ is coordinated by the thiol group of Cys29, the main-chain carbonyl oxygen of Tyr74 of one protomer, the N δ of His333 of another protomer, and two chloride ions (**Fig. 1**, right lower inset). The coordination mode at site 3 is rarely found in other metalloproteins of known structures. Based on the ITC and other biochemical results, Zn²⁺ binding to site 3 does not seem necessary for dimerization.

The present structure further reveals that Zn²⁺ binding to site 1 induces large displacement of the C-tail, resulting in significant movements of the Trx-like domains (**Fig. 2**). In the metal-unbound state, Pro353 intervenes between His299, His328 and His332 in the His-cluster [**Fig. 2(A)**, left]. In the Zn²⁺ bound state, however, Pro353 is largely moved out and these three histidines get closer to one another, adopting a configuration suitable for Zn²⁺ binding (site 1) [**Fig. 2(A)**, right]. The large movement of Pro353 also accompanies a striking C-tail movement toward the **b'** domain, impairing the interactions between the C-tail and the **a** domain. As a result, the client binding site in the Zn²⁺-bound form becomes fully exposed to the solvent [**Fig. 2(B)**, right],

in contrast to the closed conformation in the metal-unbound state [**Fig. 2(B)**, left]. These observations suggest that the Zn²⁺-bound form of ERp44 recognizes its client proteins with higher affinity than the metal-free form. Indeed, our ITC analysis revealed that interactions of ERp44 with its clients were further enhanced in the presence of Zn²⁺.

Based on the present results, we propose a new model of Zn²⁺-dependent protein quality control in the early secretory pathway [2]. Relative to pH changes, Zn²⁺ binding to ERp44 induces even larger conformational changes, leading to the enhanced interactions between ERp44 and its clients. These findings shed light on a new physiological role of cellular Zn²⁺ as a key regulator for protein quality control.

REFERENCES

- [1] S. Watanabe, M. Harayama, S. Kanemura, R. Sitia and K. Inaba, *Proc. Natl. Acad. Sci. U.S.A.* **114**, E3224 (2017).
- [2] S. Watanabe, Y. Amagai, S. Sannino, T. Tempio, T. Anelli, M. Harayama, S. Masui, I. Sorrentino, M. Yamada, R. Sitia and K. Inaba, *Nat. Commun.* **10**, 603 (2019).

BEAMLIN

BL-1A

S. Watanabe¹ and K. Inaba¹ (Tohoku Univ. -IMRAM)

Shortening Measurement Time without Hardware Investment

We propose a simple method to shorten the measurement time of experiments using a two-dimensional detector by exploiting spatial correlation in a smooth intensity distribution. We use kernel density estimation (KDE), a statistical tool to estimate the true probability density distribution from observed data, to exploit spatial correlation via a Gaussian kernel. The improvement of statistical quality (variance) by time accumulation and KDE was investigated using a short-time measurement dataset of silica nanoparticles. The time required to achieve a certain variance was reduced by one order of magnitude. For the case of anisotropic data where the strong noise reduction ability of radial averaging is not available, KDE can reduce measurement time by half.

Scientific research is experiencing a new paradigm called data-intensive science, or data-centric science. Materials informatics is one example of an emerging interdisciplinary research field that has arisen under the new paradigm. The aim of the field is to make materials development procedures more efficient by exploiting large or minimum datasets with the help of statistical and/or machine-learning analysis techniques. The first step in a research cycle in the field is data acquisition or preparation, and is often achieved by using existing databases or creating a new one experimentally or computationally. In this regard, large experimental facilities including the Photon Factory have the potential to make significant contributions to database preparation. Some studies have already used experimental data obtained at synchrotron facilities as the input for data-centric materials science studies owing to the capability of synchrotron facilities to generate a massive amount of data [1, 2]. In contrast, data from neutron facilities have not yet been used for such purposes presumably due to the low measurement throughput. In general, such a drawback can be overcome only by costly hardware upgrades to increase the beam flux or to reduce the overhead time for changing the sample. The Photon Factory and the Paul Scherrer Institute (PSI) have developed a method that, under certain conditions, reduces the measurement time by introducing a well-established tool in statistics without expensive hardware upgrades.

There are two types of correlation in a smooth two-dimensional (2D) intensity distribution with no sharp peaks: temporal correlation and spatial correlation. The former relates to the fact that the count rate per unit time at a pixel always lies in a certain range for multiple measurements following Poisson statistics. The latter means that the count rate of a pixel is similar to those of adjacent pixels because of smoothness. The statistical quality of many kinds of counting experiments has been guaranteed by a simple strategy using temporal correlation, that is, a strategy to reduce the uncertainty of observed counts by accumulating enough counts. On the other hand, a similar approach to improve the statistical quality of a 2D count distribution using spatially-correlated values, which is practically smoothing, has not been widely used, probably because such data processing is regarded as unfavorable data manipulation just to visually deceive other researchers. In fact, however, weighted-averaging based on spatial correlation is called kernel density estimation (KDE) in statistics and is widely used to estimate the true probability density distribution from observed values. Considering that the 2D intensity distribution is equal to the probability density distribution of detection events, it is natural to apply KDE to 2D count maps.

We collected one hundred small-angle neutron scattering (SANS) datasets of silica nanoparticles with low statistical quality by repeating a short measurement at

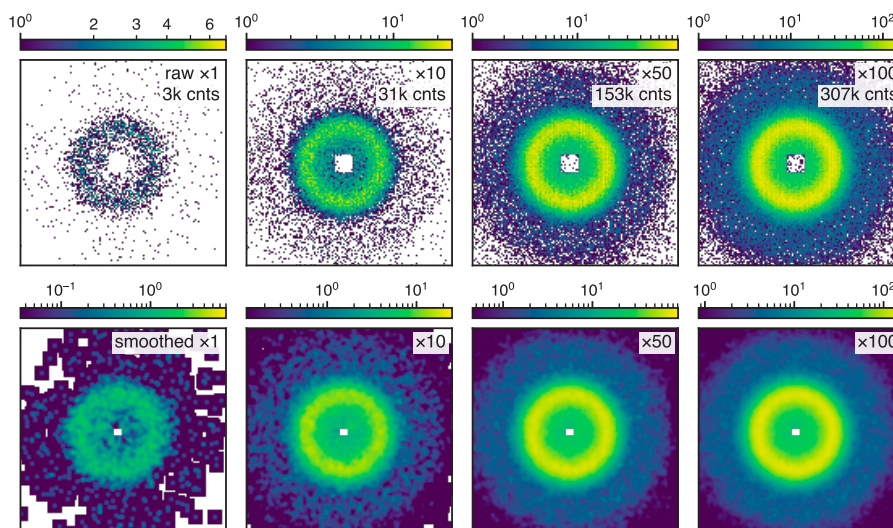


Figure 1: The effect of KDE on 2D SANS data. Raw (upper) and KDE-smoothed (lower) data. White pixels are null pixels [3].

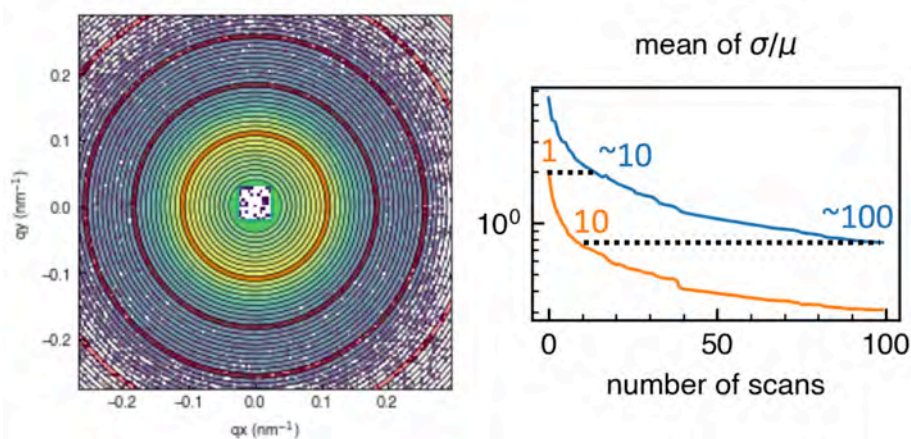


Figure 2: Mean of variances of pixel intensities in 50 concentric rings (left) normalized by the mean intensity of each ring. The blue line is time-averaged data and the orange line is KDE-smoothed data.

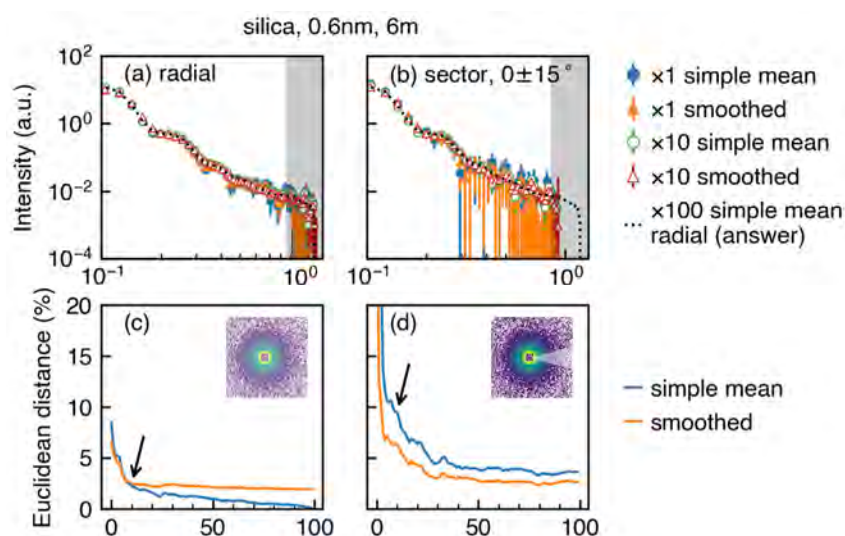


Figure 3: The effect of KDE on 1D intensity. Radial averaging (left column) and sector averaging (right column) [3].

SANS-I, SING (PSI). The measurement time was set so that the total counts of the one hundred datasets reached a conventional standard, 300k counts, which is thought to be enough counts to secure statistical quality. **Figure 1** shows raw 2D SANS datasets and the effect of KDE on them. It can be clearly seen that KDE makes the datasets with shorter measurement time close to the raw datasets with longer measurement time. As our datasets are isotropic, we can examine this effect by taking the variance of pixel intensities within concentric rings. The mean of the variances of fifty rings normalized by average counts for each ring is shown in **Fig. 2**. KDE significantly reduces the variance to the same level as that of raw datasets with ten-times longer measurement time, meaning that the measurement time required to obtain a certain level of variance in a 2D SANS dataset can be shortened by one order of magnitude. However, in practice, researchers often use radially-averaged 1D SANS intensity for isotropic data to perform model fitting, and radial averaging also has a strong ability to reduce variance. For this reason, we examined the effect of KDE on radially-averaged 1D intensity and sector-averaged 1D intensity used for anisotropic 2D SANS

data. The results are shown in **Fig. 3**. We confirmed that, while the advantage of KDE is less significant for radially-averaged 1D SANS intensity, KDE is still effective on sector-averaged intensity for anisotropic cases, which means that KDE can shorten the measurement time for anisotropic SANS data.

Although it would depend on the samples and other conditions, we believe this method is valid for most 2D scientific data obtained with 2D pixel detectors. Simple ideas in other fields may improve research efficiency without huge investment. We believe there is still room for this type of improvement in synchrotron and neutron experiments.

REFERENCES

- [1] F. Ren, L. Ward, T. Williams, K. J. Laws, C. Wolverton, J. Hattrick-Simpers and A. Mehta, *Sci. Adv.* **4**, eaaq1566 (2018).
- [2] I. Akai, K. Iwamitsu, Y. Igarashi, M. Okada, H. Setoyama, T. Okajima and Y. Hirai, *J. Phys. Soc. Jpn.* **87**, 074003 (2018).
- [3] K. Saito, M. Yano, H. Hino, T. Shoji, A. Asahara, H. Morita, C. Mitsumata, J. Kohlbrecher and K. Ono, *Sci. Rep.* **9**, 1526 (2019).

K. Saito¹ and K. Ono² (¹PSI-LNS, ²KEK-IMSS-PF)

First Observation of a Low-Energy Positron Diffraction Pattern with a Linac-Based Beam

In this study, an experimental station is developed for studying low-energy positron diffraction (LEPD) with a slow-positron beam generated by a linear-electron-accelerator (linac). Diffraction patterns of a Ge(001)-2×1 surface structure are observed with a normal positron incidence. This is the first LEPD observation with a linac-based high-intensity pulsed slow-positron beam. LEPD is expected to be particularly useful for structural analysis of surfaces containing heavy atoms, which are difficult to analyze using low-energy electron diffraction. LEPD can be applied to surfaces of poor flatness and is expected to develop into a method for analyzing local surface structures. It can thus be a complementary method to total-reflection high-energy positron diffraction.

Low-energy positron diffraction (LEPD), which is the positron counterpart of low-energy electron diffraction (LEED), has been evaluated by a LEED theorist as an ideal surface structure analysis method [1]. In 1979, the first LEPD was observed by the Brandeis University group with a channel electron multiplier using a slow-positron beam from a radioisotope (RI) source emitting positrons through β^+ -decay [2]. Subsequently they developed a system for observing an LEPD pattern with multiple spots and demonstrated that LEPD experimental results are more closely reproduced by a dynamical diffraction theory than in LEED [3]. Unfortunately, however, LEPD experimental research has been discontinued for about the last two decades because of the difficulty in obtaining a low-energy positron beam with sufficient intensity and adequate quality.

Theoretical works revealed that LEPD has several advantages over LEED [1]. First, LEPD is more surface sensitive than LEED. This is because inelastic scattering cross-sections of the positron are about 1.5 to 2 times larger than those of the electron while elastic backscattering cross-sections are several times to

nearly an order of magnitude smaller than those of the electron. This makes the ratio of the inelastic scattering cross-section to the elastic back scattering cross-section, which is a crucial factor for the surface sensitivity, one order of magnitude greater for LEPD than LEED. As a result, LEPD is sensitive to 3 to 5 atomic layers from the surface. Second, positron diffraction suffers less multiple elastic-scattering than electron diffraction for the same reason. Third, scattering factors of positron are simple with a small angular dependence, like those of X-rays. This comes from the fact that the positive charge keeps the positrons away from the inner shell of the atoms, while the electrons are attracted into the core, resulting in complex scattering factors.

Despite the promising properties of LEPD as an ideal technique for studying surface structure, no further experimental LEPD research followed the pioneering work of the Brandeis University group. The difficulty in obtaining sufficient beam intensities, as mentioned above, discouraged researchers from starting LEPD experiments.

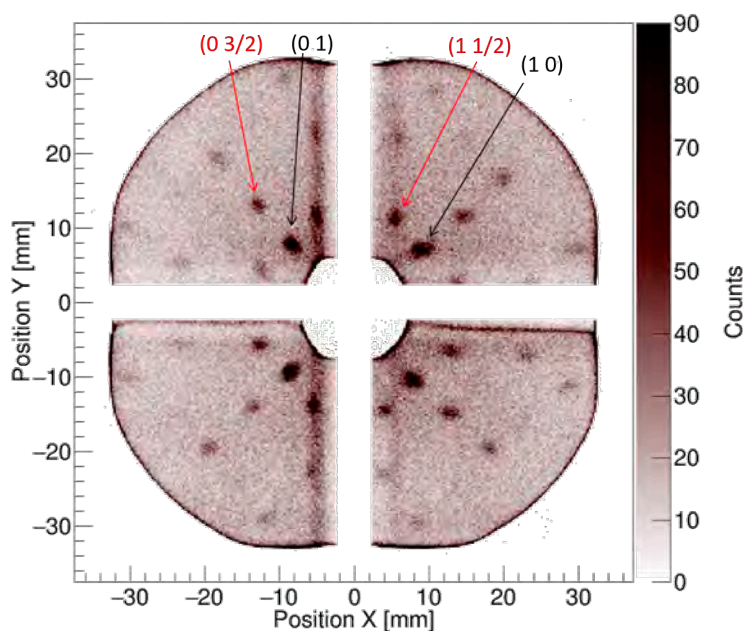


Figure 1: A diffraction pattern of a Ge(001)-2×1 structure observed with a 144.5-eV positron beam generated by a linac [4].

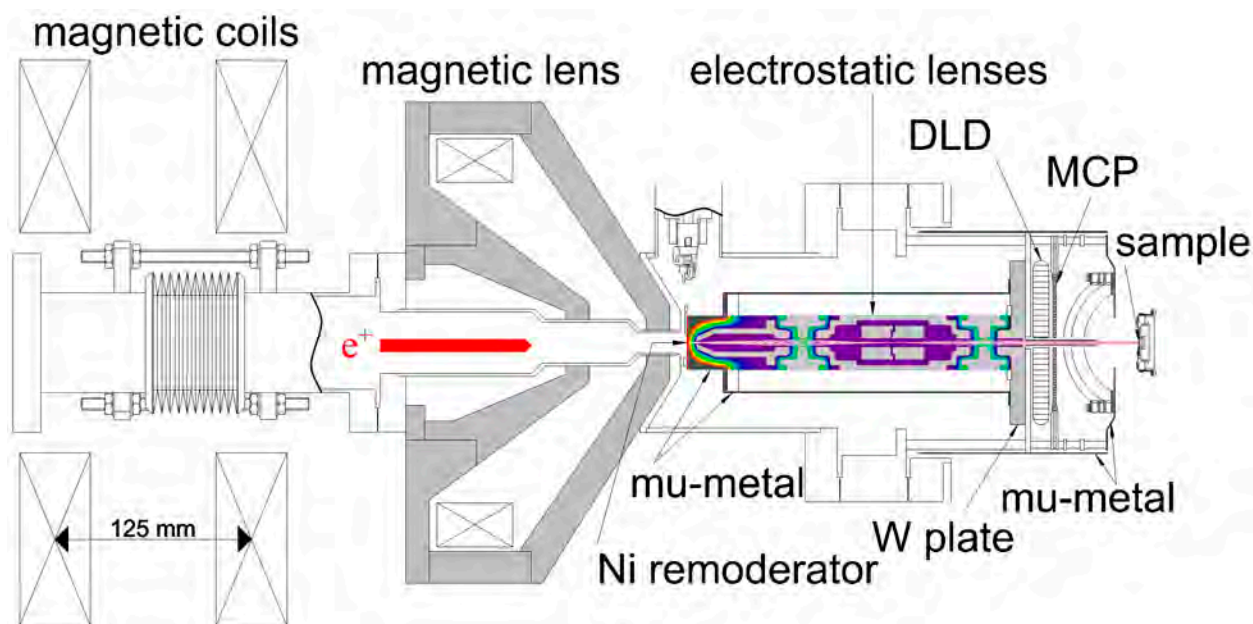


Figure 2: The present LEPD experimental station developed at IMSS-SPF [4]. "DLD" and "MCP" denote delay-line detector and multi-channel plate, respectively.

Slow Positron Facility (SPF) at Institute of Materials Structure Science (IMSS) has overcome this difficulty by utilizing a high-intensity slow-positron beam generated by a linear-electron-accelerator (linac) and succeeded in observing diffraction patterns of a Ge(001)-2x1 surface structure (Fig. 1) [4]. This is the first LEPD observation with a linac-based slow-positron beam, and is expected to lead the way in providing another fundamental tool for surface structure analysis for KEK facility users, in addition to total-reflection high-energy positron diffraction (TRHEPD) [5].

There are a number of differences between an RI-based LEPD system and a linac-based one. One difference is the time structure of the beam. While an RI-based system provides a continuous beam resulting from the Poisson random process for positron emission through β^+ -decay, a slow-positron beam generated with a normal-conducting linac has a pulsed time-structure reflecting that of the linac beam. A high-intensity pulsed slow-positron beam could cause a multi-hit problem in the detection system with a position-sensitive detector. To address this problem, a pulse stretcher with a Penning-Malmberg trap, approximately 6 m long, has been developed.

Another difference is in the beam transportation methods. The RI-based LEPD system employed electrostatic lenses along the whole beam-line, while linac-based systems transport the beam from a remote positron production unit along the beam-line with a magnetic field. It is more difficult to shield the diffraction observation system from a magnetic field than from an electric field. A new transmission-type brightness-enhancement system with electrostatic lenses has been developed

to produce low-energy positron beams, interacting with a sample in a non-magnetic field region, with sufficient intensity and adequate quality (Fig. 2).

LEPD is expected to be particularly useful for structural analysis of the surfaces containing heavy atoms, which are difficult to analyze by LEED. As LEPD patterns have properties more suitable for inversion by the Patterson function and holography than LEED, the experimental demonstrations of these are also attractive. LEPD is even applicable to a crystal surface with poor flatness, because of its normal incidence, and is also expected to develop into a method for the analysis of local surface structure.

REFERENCES

- [1] S. Y. Tong, *Surf. Sci.* **457**, L432 (2000).
- [2] I. J. Rosenberg, A. H. Weiss and K. F. Canter, *Phys. Rev. Lett.* **44**, 1139 (1980).
- [3] C. B. Duke, "Low-Energy Positron and Electron Diffraction by Solids: Concepts, Models, Calculations and Surface Structure Analyses" in *Positron Spectroscopy of Solids* edited by A. Dupasquier and A. P. Mills Jr. (IOS. Press Ebooks, Amsterdam, 1995.) p. 317.
- [4] K. Wada, T. Shirasawa, I. Mochizuki, M. Fujinami, M. Maekawa, A. Kawasuso, T. Takahashi and T. Hyodo, *e-J. Surf. Sci. Nanotech.* **16**, 313 (2018).
- [5] Y. Fukaya, A. Kawasuso, A. Ichimiya and T. Hyodo, *J. Phys. D: Appl. Phys.* **52**, 013002 (2019).

BEAMLINE

SPF-A4

K. Wada¹, T. Shirasawa², I. Mochizuki³, M. Fujinami⁴, M. Maekawa¹, A. Kawasuso¹, T. Takahashi⁵ and T. Hyodo³ (¹QST, ²AIST, ³KEK-IMSS-PF, ⁴Chiba Univ., ⁵Tokyo Gakugei Univ.)

Development of a New Nonevaporable Getter (NEG) Named Oxygen-Free Palladium/Titanium; Surface Analysis by Synchrotron Radiation X-Ray Photoelectron Spectroscopy and Application for NEG Pump

We have developed a novel nonevaporable getter named oxygen-free Pd/Ti. After activation at 133°C, oxygen-free Pd/Ti evacuates H₂ and CO. Its pumping speeds do not decrease even after repeated venting–activating cycles. Surface analysis by synchrotron radiation X-ray photoelectron spectroscopy showed that carbon contamination decreased to an extent on heating in ultra-high vacuum, but decreased considerably on heating under an O₂ pressure. The pumping speeds of the oxygen-free Pd/Ti coated chamber improved remarkably after O₂ baking. The new NEG pump using oxygen-free Pd/Ti was commercialized in March 2019.

A nonevaporable getter (NEG) is a material that evacuates active residual gases when activated under clean ultra-high vacuum (UHV) conditions. Typical NEG materials are Al, Ti, V, Zr, Fe, and their alloys. Pumps using NEG (NEG pumps) are widely used in UHV apparatus because of their high pumping speeds for H₂ and active gases in the UHV region. However, the conventional NEG pump has the following drawbacks: 1) its pumping speeds decrease after repeated venting–activating cycles; 2) it requires relatively high activation temperature (typically 350°C for 24 h when ZrVFe alloy is used [1], and typically 180°C for 24 h when TiZrV film is used [2]); and 3) it requires a dedicated power supply and current feedthroughs. In order to overcome these disadvantages, we developed a new NEG with an activation temperature of 133°C using Ti sublimation followed by Pd sublimation under UHV, and named it oxygen-free Pd/Ti [3]. The activation and pumping mechanisms of oxygen-free Pd/Ti are shown in Fig. 1 [4]. During the activation of oxygen-free Pd/Ti, hydrogen atoms diffuse from the Ti film through the Pd overcoat to the surface and desorb as H₂ into vacuum leaving oxygen-free Pd/Ti available to H₂ absorption. In the same activation process, CO desorbs from the Pd surface making the Pd surface available for CO adsorption. Therefore, hydrogen diffusion and desorption as well as CO desorption determine the activation temperature of oxygen-free Pd/Ti, which is as low as 133°C.

When oxygen-free Pd/Ti is exposed to air, the Pd

overcoat prevents the Ti thin film from oxidation, but the Pd surface becomes contaminated to some degree with carbon [3]. This contamination is supposed to reduce the pumping speeds of oxygen-free Pd/Ti for H₂ and CO [4]. To find an effective and simple method for removing carbon contamination, we investigated oxygen-free Pd/Ti samples heated in an UHV or under an O₂ pressure of 1.3×10^{-4} Pa by synchrotron radiation X-ray photoelectron spectroscopy (SR-XPS) at BL-13B [5]. The Pd 3d_{5/2} SR-XPS spectra shown in Fig. 2(a) suggested that the number of less-coordinated Pd atoms decreases after heating. This result is consistent with the secondary electron microscopy (SEM) images of the unheated and UHV-heated oxygen-free Pd/Ti samples [5]. On the other hand, the deconvoluted C 1s peaks indicated that the carbon contamination is mainly graphene and molecules containing carbon as shown in Fig. 2(b). The graphene is supposed to be generated by catalytic chemical reaction from hydrocarbons adsorbed on Pd. The graphene coverage of the unheated sample was estimated to be 0.9 monolayer (ML), whereas those of the UHV-heated and O₂-heated samples were estimated to be 0.3 and 0.04 ML, respectively. The pumping speeds of the oxygen-free Pd/Ti coated chamber for H₂ and CO were measured by using the orifice method, and were found to be improved after O₂ baking as shown in Fig. 3. Therefore, we concluded that removal of carbon contamination on oxygen-free Pd/Ti improves the pumping speeds for H₂ and CO.

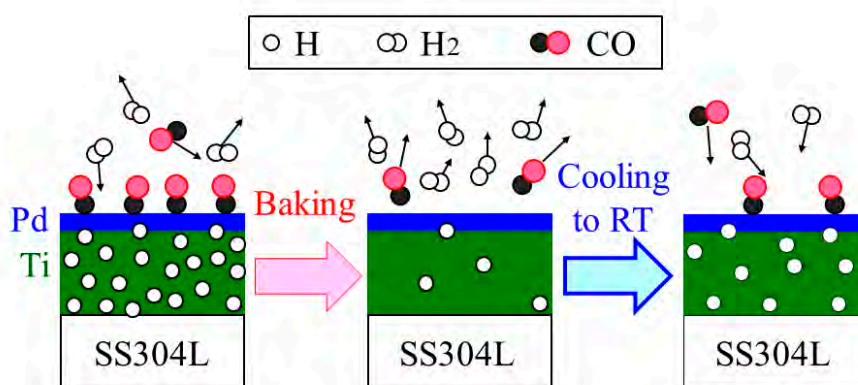


Figure 1: Schematic of the activation and pumping mechanisms of oxygen-free Pd/Ti coated on SS304L. Reproduced from Ref. 4, with the permission of AIP Publishing.

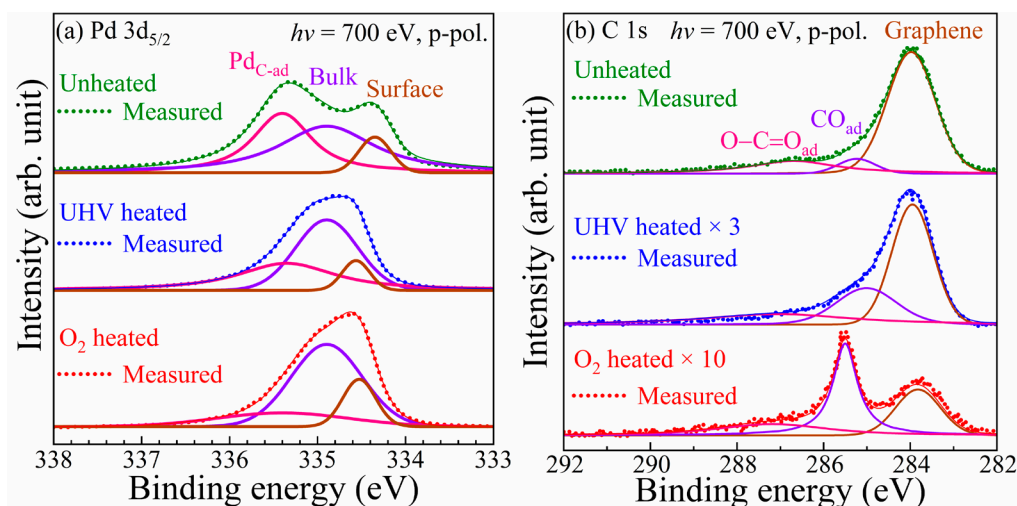


Figure 2: Measured, fitted, and deconvoluted peaks of (a) Pd 3d_{5/2} and (b) C 1s. Reproduced from Ref. [5], with the permission of AIP Publishing.

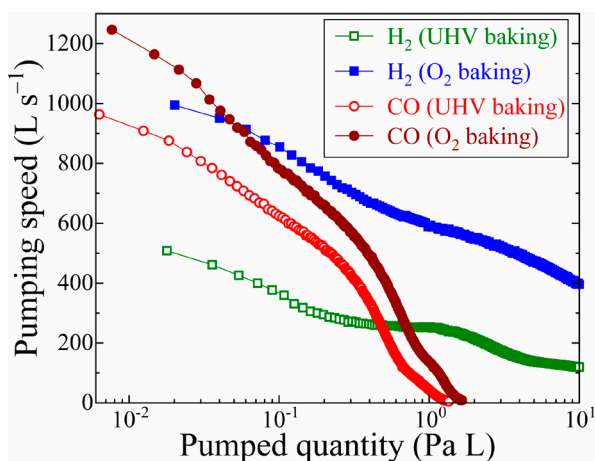


Figure 3: Measured pumping speeds of the oxygen-free Pd/Ti coated chamber with an inner diameter of 147 mm and inner length of 236 mm for H₂ or CO after UHV or O₂ baking at 150°C for 12 hours. Reproduced from Ref. 5, with the permission of AIP Publishing.

The new NEG pump using oxygen-free Pd/Ti was commercialized in March 2019. The advantages of the new NEG pump are as follows: 1) it can be activated by baking at 150°C for 6 h, and pumps H₂ and CO efficiently; 2) its pumping speeds do not decrease even after repeated venting–activating cycles; 3) there is no need for a dedicated power supply or current feedthroughs; and 4) the pumping speeds can be improved by O₂ baking. A comparison of the commercially-available ICF203 NEG pump [6] and the present new ICF203 NEG pump [7] is summarized in Table 1. Since we were able to quickly feed back the results obtained by SR-XPS to the oxygen-free Pd/Ti development, we could commercialize the new NEG pump in one year from publication of the first paper on oxygen-free Pd/Ti [3]. This is a good example of how the SR facility is making a major contribution to the research and development of new functional materials and products using them.

Table 1: Comparison of commercially-available ICF203 NEG pump [6] and the present new ICF203 NEG pump [7]

	Capaci Torr® D 2000 [6]	Present NEG pump [7]
Activation conditions	450°C, 10 min	150°C, 12 h
Gases that can be pumped	H ₂ , H ₂ O, O ₂ , N ₂ , CO, CO ₂	H ₂ and CO
Initial pumping speed for H ₂	2,000 L/s	2,200 L/s
Initial pumping speed for CO	1,000 L/s	1,500 L/s
Influence of repeated venting and activation cycles	Pumping speed decreases	Pumping speed does not decrease
Current feedthroughs	Necessary	Unnecessary
Dedicated power supply	Necessary	Unnecessary

REFERENCES

- [1] C. Benvenuti and P. Chiggiato, *J. Vac. Sci. Technol. A* **14**, 3278 (1996).
- [2] C. Benvenuti P. Chiggiato, F. Cicoira and V. Ruzinov, *Vacuum* **50**, 57 (1998).
- [3] T. Miyazawa, M. Kurihara, S. Ohno, N. Terashima, Y. Natsui, H. Kato, Y. Kato, A. Hashimoto, T. Kikuchi and K. Mase, *J. Vac. Sci. Technol. A* **36**, 051601 (2018).
- [4] T. Kikuchi, T. Miyazawa, H. Nishiguchi and K. Mase, *AIP Conf. Proc.* **2054**, 060046 (2019).
- [5] T. Miyazawa, Y. Kano, Y. Nakayama, K. Ozawa, T. Iga, M. Yamanaka, A. Hashimoto, T. Kikuchi and K. Mase, *J. Vac. Sci. Technol. A* **37**, 02160 (2019).
- [6] SAES Group, CapaciTorr Products, <https://www.saesgetters.com/sites/default/files/CapaciTorr%20D.pdf>, (Last accessed: 2019-07-29)
- [7] <https://www.baroque-inc.co.jp/custom.html>, (Last accessed: 2019-07-29).

BEAMLINE

BL-13B

T. Miyazawa¹, Y. Kano², Y. Nakayama², K. Ozawa³, T. Kikuchi⁴ and K. Mase^{1,4} (¹SOKENDAI, ²Tokyo Univ. of Sci., ³Tokyo Tech, ⁴KEK-IMSS-PF)

Construction of an Elliptically Polarizing Undulator (U#19) at the Photon Factory

We are constructing a new elliptically polarizing undulator (U#19) as a light source for soft X-ray scattering, spectroscopy and scanning transmission X-ray microscopy (STXM) experiments. U#19 is an EPU with an APPLE-II-type magnetic arrangement to obtain various polarization states. We designed U#19 to utilize the extended straight section as much as possible. The target photon energy region of U#19 is from 100 eV to 2 keV under various polarization states. We installed U#19 in the ring in the summer of 2018 and its operation for user experiments was successfully begun during the autumn operation of the ring.

We have renewed the undulators for the vacuum ultraviolet and soft X-ray (VUV-SX) light source renewal project after the reconstruction of the Photon Factory (PF) [1]. Step-by-step, we constructed five elliptically polarizing undulators (EPUs): U#02-2, U#13, U#16-1, U#16-2, and U#28 for the beamlines BL-02, BL-13, BL-16, and BL-28, respectively. For the remaining beamline BL-19, we are constructing U#19 as a light source for soft X-ray scattering, spectroscopy, and STXM experiments. U#19 is the fourth EPU with the APPLE-II-type magnetic arrangement [2] to obtain vari-

ous polarization states. **Table 1** shows the basic parameters of the EPUs at the ring.

Table 2 shows the characteristic parameters of U#19. The target photon energy region of U#19 is from 100 eV to 2 keV under various polarization states. **Figure 1(a)** shows the calculated spectrum of U#19. The basic design of the mechanical system to move the gap and the magnet rows of U#19 is the same as that of the previous APPLE-II-type EPU (U#13). **Figure 1(b)** shows a photograph of U#19 after assembling the magnet arrays.

Table 1: Basic parameters of the EPUs at the PF ring

Name	Period length (mm)	Number of periods	Maximum B_y , B_x (T)	Photon energy region (eV)	Type of EPU	Installation year
U#16-1 & 2	56	44	0.6, 0.38	200–1000	APPLE-II	2008, 2010
U#02-2	160	17	0.33, 0.33	30–300	six movable rows	2014
U#13	76	48	0.68, 0.34	50–1500	APPLE-II	2015
U#28	160	22	0.33, 0.33	30–300	six movable rows	2015
U#19	68	55	0.71, 0.46	100–2000	APPLE-II	2018

Table 2: Characteristic parameters of U#19

Magnetic block size (mm)	Magnet material	Maximum magnetic force F_x , F_y , F_z (kN)	Gap operation range (mm)
40x40x17	Nd-Fe-B (NEOMAX-S49CH)	42.6, 17.5, 43.5	24–150

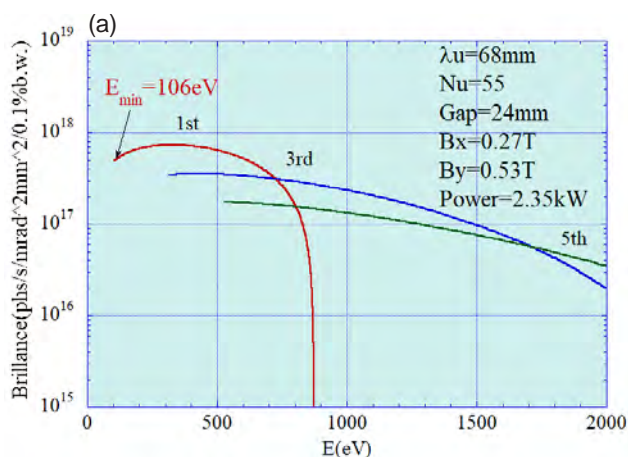


Figure 1: (a) Calculated spectrum of U#19 in the elliptical polarization mode ($B_y/B_x = 2$), (b) Picture of U#19

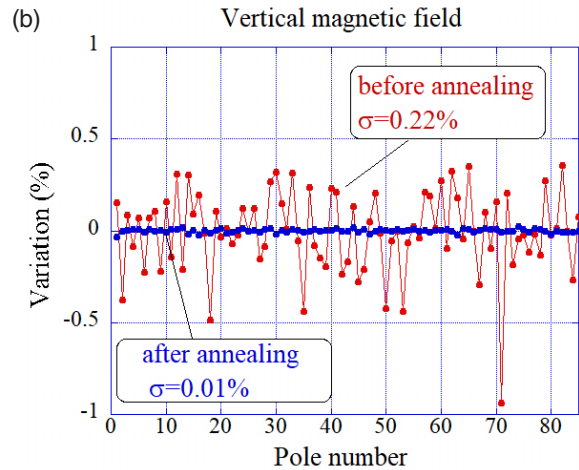
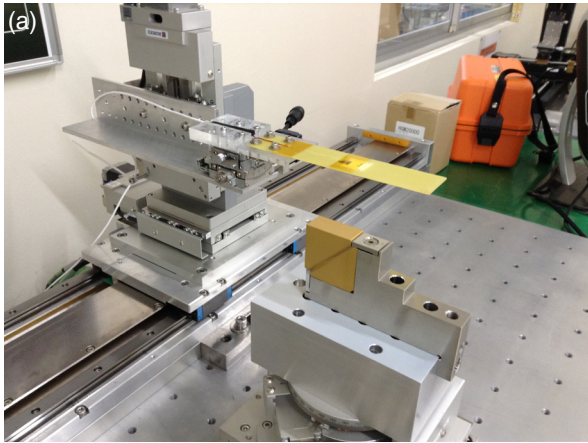


Figure 2: (a) Measurement setup for individual magnetic blocks along the beam axis. (b) Distribution of the first integrals of the magnetic field every half period along the z-axis at individual magnetic poles compared before and after the sorting simulation in the horizontally linear polarizing mode. The variation from the average value is expressed.

For the magnetic adjustments of the EPUs at the PF, we have developed a practical method of determining an excellent initial arrangement of the magnetic arrays [3]. In this method, the longitudinal magnetic field distribution of each magnet is measured with a high spatial resolution using a Hall probe system that moves along the beam axis. We measured the vertical and horizontal fields simultaneously. **Figure 2(a)** shows the setup used for this measurement. The total number of measured magnets was 920. We optimized the initial arrangement of the magnet arrays by analyzing the superposition of all distribution data. The simulation results for U#19 are summarized in **Fig. 2(b)**. We optimized the magnetic arrangement in the horizontal polarizing mode and the vertical polarizing mode simultaneously. We compared the properties of the superposed magnetic field distribution at the calculated arrangement of the magnets and the case of the initial state. In the initial state, we set the magnetic blocks randomly. The figures show the results of the first integral distributions of the magnetic field every half period along the z-axis at the individual magnetic poles.

For the operation of all APPLE-II-type EPUs (U#16-1 & 2, U#13, and U#19) at the ring, we control our EPUs as adjustable phase undulators (APUs) by individually shifting the four magnetic array rows [4, 5]. We control the photon energy by shifting the upper pair of the magnet rows longitudinally with respect to the lower pair or by shifting the right pair of the magnet rows with respect to the left pair; however, the gap is kept fixed [1, 6, 7]. The COD caused by changes in this APU mode is clearly small compared to the usual variable-

gap mode. The APU mode offers a highly useful feature for the operation of EPUs as it allows the polarization state and photon energy to be controlled without spectral degradation or the large disturbance of the electron beam caused by changing the gap of the EPU.

The U#19 vacuum chamber is made of aluminum alloy (A6060-T6), and its inner wall is coated with a non-evaporable getter (NEG) thin film. The beam channel has an elliptical aperture; the vertical opening of 15 mm is required by the beam dynamics and the horizontal opening of 90 mm is identical to those of the adjacent chambers. The external height of the chamber is 20 mm because the minimum gap of the magnet arrays is 24 mm, and the 0.6-mm-thick flat wires are placed at the top and bottom of the chamber.

REFERENCES

- [1] K. Tsuchiya, M. Adachi, T. Shioya, T. Honda, Y. Tanimoto, T. Nogami, S. Asaoka and K. Ueda, *AIP Conf. Proc.* **1741**, 020023 (2016).
- [2] S. Sasaki, K. Kakuno, T. Takada, T. Shimada, K. Yanagida and Y. Miyahara, *Nucl. Instrum. Methods Phys. Res. A* **331**, 763 (1993).
- [3] K. Tsuchiya and T. Shioya, *Rev. Sci. Instrum.* **86**, 043305 (2015).
- [4] R. Carr, *Nucl. Instrum. Methods Phys. Res. A* **306**, 391 (1991).
- [5] S. Lidia and R. Carr, *Nucl. Instrum. Methods Phys. Res. A* **347**, 77 (1994).
- [6] T. Schmidt and D. Zimoch, *AIP Conf. Proc.* **879**, 404 (2007).
- [7] T. Schmidt, M. Calvi, T. Schmitt, V. N. Strocov and D. Zimoch, *J. Phys. Conf. Ser.* **425** 032020 (2013).

K. Tsuchiya^{1,2}, M. Adachi^{1,2}, T. Shioya¹, S. Eguchi¹, Y. Tanimoto^{1,2} and R. Kato^{1,2} (¹KEK-ACCL, ²SOKENDAI)

OPERATION and PROPOSALS

1. Outline of the Accelerators

Two electron storage rings, namely the PF ring and the PF-AR, have been stably operated as dedicated light sources at the Photon Factory. The KEK linear accelerator (LINAC) with a maximum electron energy of 8 GeV is employed to inject electron beams into the rings. After the 2018 summer shutdown when modification of the LINAC for enabling simultaneous injections to the four different rings (the PF ring, PF-AR, SuperKEKB

HER and LER) was completed, user operation of both light sources was performed with the top-up injection. This was the first time that the PF-AR introduced the top-up injection to its user operation.

The machine parameters of the rings and the calculated spectral performances are listed in **Table 1** and **Table 2**, respectively. The spectral distributions of synchrotron radiation (SR) from the bending magnets and the insertion devices are shown in **Fig. 1**.

Table 1: Principal beam parameters of the PF ring and PF-AR.

	PF ring	PF-AR
Energy	2.5 GeV	6.5 GeV
Natural emittance	34.6 nm rad	293 nm rad
Circumference	187 m	377 m
RF frequency	500.1 MHz	508.6 MHz
Bending radius	8.66 m	23.2 m
Energy loss per turn	0.4 MeV	6.66 MeV
Damping time		
Vertical	7.8 ms	2.5 ms
Longitudinal	3.9 ms	1.2 ms
Natural bunch length	10 mm	18.6 mm
Momentum compaction factor	0.00644	0.0129
Natural chromaticity		
Horizontal	-12.9	-14.3
Vertical	-17.3	-13.1
Stored current	450 mA	60 mA
Normal filling	250 bunches	Single
Beam lifetime	20 h (at 450 mA)	13 h (at 50 mA)
Hybrid filling	Single (50 mA) + 131 bunches (400 mA)	
Beam lifetime	8 h (450 mA)	

Table 2: Calculated spectral performances of the bending source and all the insertion devices at the PF ring (2.5 GeV, 450 mA) and the PF-AR (6.5 GeV, 60 mA). λ_u : period length, N : number of periods, L : length of undulator or wiggler, $G_y(G_x)$: minimum vertical (horizontal) gap height, $B_y(B_x)$: maximum vertical (horizontal) magnetic field, type of magnet, H: hybrid configuration, S.C.: super-conducting magnet, σ_x, σ_y : horizontal or vertical beam size, σ_x, σ_y : horizontal or vertical beam divergence, $K_y(K_x)$: vertical (horizontal) deflection parameter, D : photon flux density (photons/sec/mrad²0.1%b.w.), B : brilliance (photons/sec/mm²/mrad²0.1%b.w.), P_T : total radiated power. MPW#05 and EMPW#NE01 are operated in wiggler mode denoted by -W.

Name	E/I GeV/mA	λ_u cm	N	L m	$G_y(G_x)$ cm	$B_y(B_x)$ T	Type of magnet	σ_x mm	σ_y mm	σ_x mrad	σ_y mrad	$K_y(K_x)$	ϵ_x/ϵ_c keV	D	B	P_T kW
PF 2.5/450																
Bend								0.41	0.059	0.178	0.012	4	5.38E+13	3.48E+14		
SGU#01		1.2	39	0.5	0.4	0.7	P(NdFeB)	0.6	0.012	0.088	0.029	0.78	4.56E+16	9.90E+17	0.4	
U#02-1		6	60	3.6	2.8	0.4	H(NdFeB)	0.65	0.042	0.054	0.008	2.3	2.73E+17	1.55E+18	1.07	
U#02-2		16	17	2.72	2.6	0.33(0.33)	P(NdFeB)	0.65	0.042	0.054	0.008	4.93(4.93)	9.53E+15	4.58E+16	0.53	
SGU#03		1.8	26	0.5	0.4	1	P(NdFeB)	0.6	0.012	0.088	0.029	1.68	2.50E+16	5.44E+17	0.82	
MPW#05-W		12	21	2.5	2.64	1.4	H(NdFeB)	0.71	0.045	0.078	0.009	16	2.22E+15	1.10E+16	8.83	
U#13		7.6	47	3.6	2.3	0.68(0.34)	P(NdFeB)	0.74	0.02	0.094	0.019	4.84(2.42)	6.85E+16	4.70E+17	3.7	
VW#14					5	5	S.C.	0.53	0.045	0.128	0.008	20.8	5.42E+13	3.59E+14		
SGU#15		1.76	27	0.5	0.4	0.97	P(NdFeB)	0.6	0.012	0.088	0.029	1.37	4.38E+15	9.44E+16	0.75	
U#16-1 & 16-2		5.6	44	2.5	2.1	0.6(0.38)	P(NdFeB)	0.654	0.042	0.055	0.008	3(2)	1.42E+17	7.87E+17	2.2	
SGU#17		1.6	29	0.5	0.4	0.92	P(NdFeB)	0.6	0.012	0.088	0.029	1.37	7.88E+15	1.71E+17	0.69	
U#19		6.8	55	3.74	2.4	0.71(0.46)	P(NdFeB)	0.71	0.045	0.078	0.009	4.5(2.92)	1.14E+17	5.08E+17	4.76	
U#28		16	22	3.52	2.7	0.33(0.33)	P(NdFeB)	0.53	0.045	0.127	0.008	4.93(4.93)	1.39E+16	6.59E+16	1.36	
PF-AR 6.5/60																
Bend								1	0.2	0.593	0.036	26	3.90E+13	3.11E+13		
EMPW#NE01-W		16	21	3.36	3(11)	1(0.2)	P(NdFeB)	1.07	1.07	0.268	0.032	15(3)	28(90%)	1.84E+15	2.54E+15	5.52
U#NE03		4	90	3.6	1	0.8	P(NdFeB)	1.57	0.17	0.312	0.029	3	1.29E+16	7.66E+15	3.708	
U#NW02		4	90	3.6	1	0.8	P(NdFeB)	1.57	0.17	0.312	0.029	3	1.29E+16	7.66E+15	3.708	
U#NW12		4	95	3.8	1	0.8	P(NdFeB)	1.57	0.17	0.312	0.029	3	1.29E+16	7.66E+15	3.912	
U#NW14-36		3.6	79	2.8	1	0.8	P(NdFeB)	1.35	0.14	0.338	0.036	2.8	7.69E+15	6.49E+15	3.12	
U#NW14-20		2	75	1.5	0.8	0.63	P(NdFeB)	0.75	0.07	0.383	0.038	1.17	7.69E+15	6.49E+15	0.936	

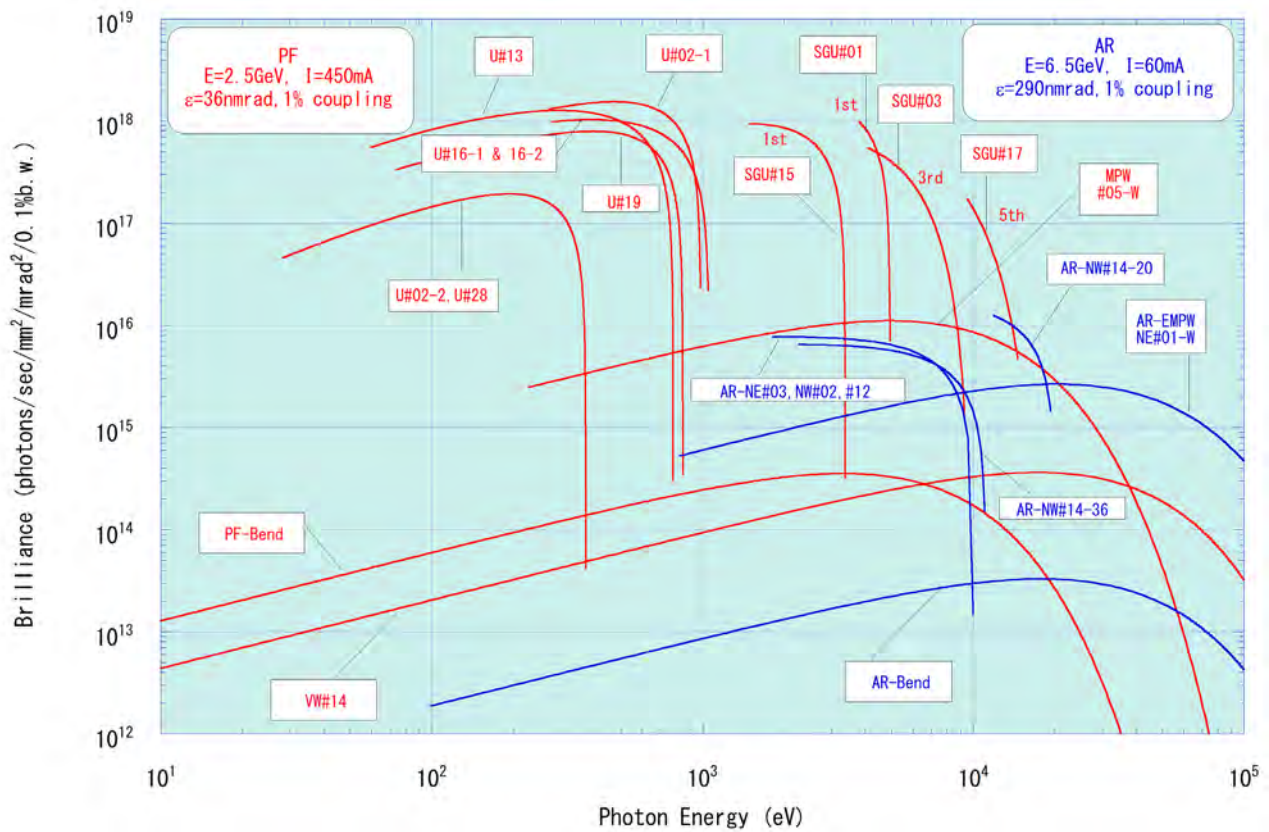


Figure 1: Synchrotron radiation spectra available at the PF ring (2.5 GeV) and the PF-AR (6.5 GeV). Brilliance of the radiation vs. photon energy is denoted by red curves for the insertion devices, SGU#01, U#02-1 & 02-2, SGU#03, MPW#05, U#13, VW#14, SGU#15, U#16-1 & 16-2, SGU#17, U#19 and U#28, and the bending magnets (PF-Bend) at the PF ring. Blue curves denote those for the insertion devices, EMPW#NE01, U#NE03, U#NW02, U#NW12, U#NW14-36 and U#NW14-20, and the bending magnets (AR-Bend) at the PF-AR. The name of each source is listed in **Table 2**. The spectral curve of each undulator (or undulator mode of multipole wiggler) is the locus of the peak of the first harmonic within the allowance range of K parameter. For SGU#01 and SGU#15, the first harmonic regions are shown. For SGU#03, the third harmonic region is shown. For SGU#17, the fifth harmonic region is shown.

2. Operation Summary

The operation schedule of the PF ring and PF-AR in FY2018 is shown in **Fig. 2**. The statistics of the accelerator's operation for the past decade are shown in **Fig. 3**. The scheduled user time in the PF ring increased by 120 hours over FY2017. In the PF-AR, the time decreased by about 500 hours owing to the reduction of the operational budget and the low-energy operation tested for a week.

For the PF ring, more detailed operation statistics and the number of failures from FY2008 to FY2018 are listed in **Table 3** and **Table 4**, and a pie chart of the down time in FY2018 is shown in **Fig. 4**. While the total down time increased by 12 hours compared to FY2017, the failure rate was kept at 1% or less. The mean time between failures (MTBF) was 184 hours, indicating that the PF-ring operation in FY2018 was sufficiently stable. A breakdown of the down time shows that 69% was due to issues with the magnet power supplies and 28% was due to the RF system. The old power supplies for

the quadrupole magnets which caused frequent issues owing to aging were replaced on the FY2018 budget. The renewal of an old septum chamber which caused a serious vacuum leak in FY2015 is also in progress. The new septum chamber will be installed in the injection section with a new septum magnet during the 2020 summer shutdown.

The upgrade project of the SR beamline #19 (BL-19) is planned for three years starting in FY2017. During the 2018 summer shutdown, the removal of an old revolver-type undulator and the installation of a new APPLE-II type elliptically polarizing undulator were performed. A vacuum chamber for the new undulator received a Ti-Zr-V Non-Evaporable Getter (NEG) coating on the inner surface; this is the first attempt to use a NEG-coated chamber for undulators in Japanese light sources. The start-up and tuning of BL-19 components including the new undulator started in November 2018, and will be available to users in the first operation period of FY2019. **Figure 5** shows a photo of the new undulator installed in the PF-ring tunnel.

	MON 9 17	TUE 9 17	WED 9 17	THU 9 17	FRI 9 17	SAT 9 17	SUN 9 17	MON 9 17	TUE 9 17	WED 9 17	THU 9 17	FRI 9 17	SAT 9 17	SUN 9 17	MON 9 17	TUE 9 17	WED 9 17	THU 9 17	FRI 9 17	SAT 9 17	SUN 9 17
Date	30	5.1	2	3	4	5	6	7	8	9	10	11	12	13	14	15	16	17	18	19	20
PF																					
AR																					
Date	21	22	23	24	25	26	27	28	29	30	31	6.1	2	3	4	5	6	7	8	9	10
PF																					
AR																					
Date	11	12	13	14	15	16	17	18	19	20	21	22	23	24	25	26	27	28	29	30	7.1
PF																					
AR																					
Date	2	3	4	5	6	7	8	9	10	11	12	13	14	15	16	17	18	19	20	21	22
PF																					
AR																					
Date	11.5	6	7	8	9	10	11	12	13	14	15	16	17	18	19	20	21	22	23	24	25
PF																					
AR																					
Date	26	27	28	29	30	12.1	2	3	4	5	6	7	8	9	10	11	12	13	14	15	16
PF																					
AR																					
Date	17	18	19	20	21	22	23	24	25	26	27	28	29	30	31						
PF																					
AR																					
Date	2.11	12	13	14	15	16	17	18	19	20	21	22	23	24	25	26	27	28	3.1	2	3
PF																					
AR																					
Date	4	5	6	7	8	9	10	11	12	13	14	15	16	17	18	19	20	21	22	23	24
PF																					
AR																					
Date	25	26	27	28	29	30															
PF																					
AR																					

PF: PF ring
AR: PF-AR

- Tuning and ring machine study
- Short maintenance and /or machine study
- Ring machine study
- Experiment using SR
- Hybrid Mode Operation
- B Bonus

Figure 2: Operation schedule of PF ring and PF-AR in FY2018

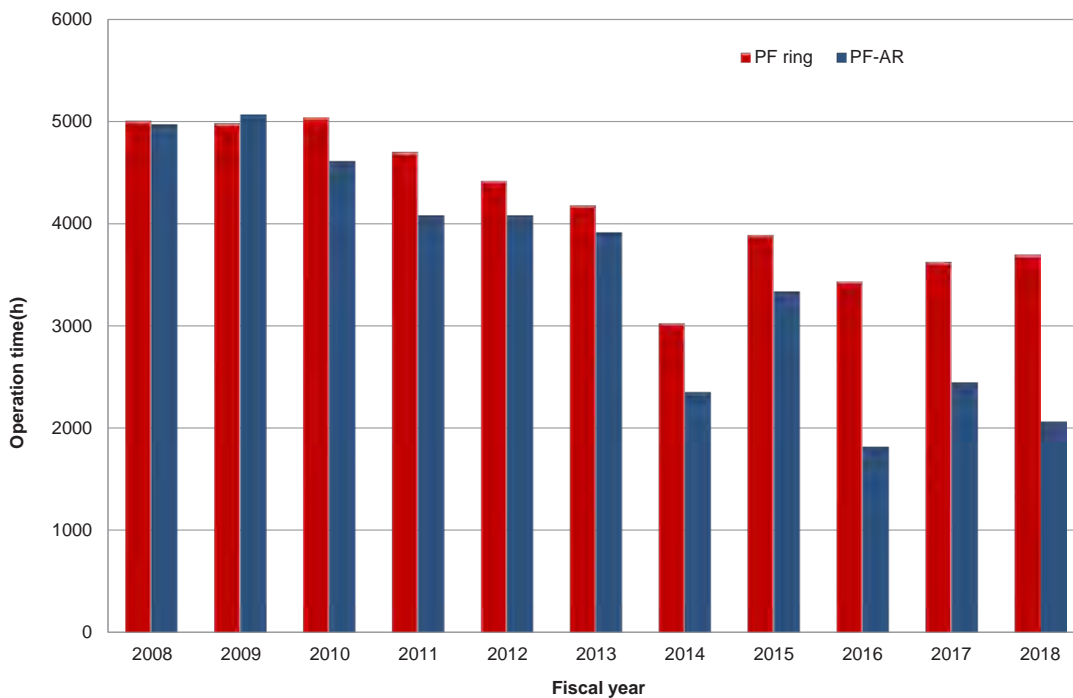


Figure 3: Total operation time for PF ring and PF-AR.

In the PF-AR, similar statistics are listed in **Table 5** and **Table 6**, and a pie chart of the down time in FY2018 is shown in **Fig. 6**. Although the number of failures significantly decreased since the problem of accidental discharges of the injection kickers installed at the end of the direct BT line was solved, the total down time was almost the same as that of FY2017. The failure rate and MTBF were 1.6% and 64 hours, respectively. A breakdown of the down time shows that 75% was due to issues with the RF system, 14% was due to the injection devices, and 8% was due to sudden beam loss caused by dust trapping. The old programmable logic controllers in high-voltage power supplies for klystrons, which were manufactured in 1988 and became difficult to maintain, were renewed in the 2018 summer shutdown.

In addition, beam dumps caused by the temperature interlock of cables for extracting and damping the higher order modes (HOMs) in acceleration cavities frequently occurred in FY2018. The cause of the heating of the HOM cables is considered to be aging and deterioration by radiation. All of the 70 HOM cables will be replaced during the 2019 summer shutdown.

The user operation of the PF-AR has continued with a 6.5-GeV full-energy injection using the direct beam transport (BT) line completed in FY2016. In FY2017, preparations required for the introduction of the top-up injection such as the radiation survey during the injection with the main beam shutters of the SR beamlines opened were completed. Since modification of the LINAC for the pulse-by-pulse switching of the electron

Table 3: Operation statistics for PF ring from FY2008 to FY2018.

Fiscal Year	2008	2009	2010	2011	2012	2013	2014	2015	2016	2017	2018
Total operation time (h)	5000	4976	5064	4728	4416	4176	3024	3888	3432	3624	3696
Scheduled user time (h)	4032	4008	4080	2832	3792	3504	2328	3048	2928	3000	3120
Ratio of user time (%)	80.6	80.5	80.6	59.9	85.9	83.9	77.0	78.4	85.3	82.8	84.4
No. of failures	18	24	18	18	23	22	15	23	18	14	17
Total down time (h)	23.8	42.7	29.2	14.9	37.6	52.1	11.4	14.4	17.3	16.6	28.4
Failure rate (%)	0.6	1.1	0.7	0.5	1.0	1.5	0.5	0.5	0.6	0.6	0.9
MTBF (h)	224.0	167.0	226.7	157.3	164.9	159.3	155.2	132.5	162.7	214.3	183.5
Mean down time (h)	1.3	1.8	1.6	0.8	1.6	2.4	0.8	0.6	1.0	1.2	1.7

Table 4: Number of failures for PF ring from FY2008 to FY2018.

Fiscal Year	2008	2009	2010	2011	2012	2013	2014	2015	2016	2017	2018
RF	5	12	13	5	10	8	1	1	1	1	7
Magnet	3	4	0	2	0	2	4	7	7	6	8
Injection	4	0	1	0	0	1	3	6	0	3	0
Vacuum	0	0	0	0	0	0	0	1	2	0	0
Dust trap	0	1	0	0	0	0	0	0	0	0	0
Insertion Devices	3	1	1	4	3	0	1	1	0	2	0
Control/ Monitor	0	3	0	1	6	5	3	3	5	0	1
Cooling water	1	1	0	0	0	0	0	0	0	0	0
Safety/ Beamline	1	2	2	1	1	1	3	2	1	1	1
Earthquake	1	0	0	4	3	1	0	2	2	0	0
Electricity	0	0	1	1	0	4	0	0	0	1	0
Total	18	24	18	18	23	22	15	23	18	14	17

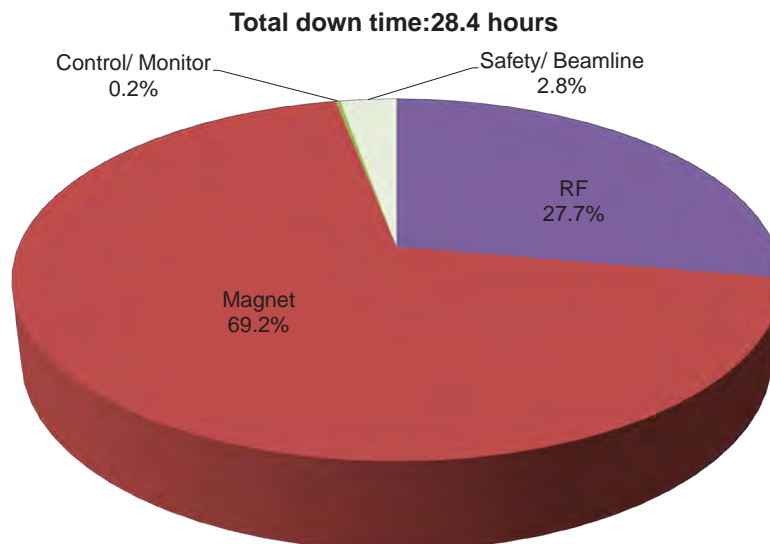


Figure 4: Pie chart of down time for PF ring in FY2018.



Figure 5: New APPLE-II type undulator installed for BL-19.

Table 5: Operation statistics for PF-AR from FY2008 to FY2018.

Fiscal Year	2008	2009	2010	2011	2012	2013	2014	2015	2016	2017	2018
Total operation time (h)	4969	5063	4608	4080	4080	3912	2352	3336	1821	2448	2064
Scheduled user time (h)	4344	4392	4032	2904	3672	3478	1992	2784	1104	2136	1608
Ratio of user time (%)	87.4	86.7	87.5	71.2	90.0	88.9	84.7	83.5	60.6	87.3	77.9
No. of failures	40	41	74	49	33	47	22	18	13	55	25
Total down time (h)	41.7	91.0	73.7	38.7	29.7	99.6	37.0	31.0	18.3	24.7	26.4
Failure rate (%)	1.0	2.1	1.8	1.3	0.8	2.9	1.9	1.1	1.7	1.2	1.6
MTBF (h)	108.6	107.1	54.5	59.3	111.3	74.0	90.5	154.7	84.9	38.8	64.3
Mean down time (h)	1.0	2.2	1.0	0.8	0.9	2.1	1.7	1.7	1.4	0.4	1.1

Table 6: Number of failures for PF-AR from FY2008 to FY2018.

Fiscal Year	2008	2009	2010	2011	2012	2013	2014	2015	2016	2017	2018
RF	4	8	10	5	4	5	2	1	3	5	4
Magnet	2	2	10	8	3	4	9	4	5	1	0
Injection	9	1	6	4	3	18	7	1	2	19	6
Vacuum	0	2	1	0	1	0	0	1	1	0	0
Dust trap	15	16	24	20	13	3	2	1	1	22	14
Insertion Devices	0	0	0	0	0	0	0	0	0	0	0
Control/ Monitor	1	1	2	1	2	8	0	0	0	0	0
Cooling water	3	4	4	1	0	2	0	0	0	0	0
Safety/ Beamline	5	7	17	3	4	3	1	8	0	8	1
Earthquake	0	0	0	5	3	1	0	2	1	0	0
Electricity	1	0	0	2	0	3	1	0	0	0	0
Total	40	41	74	49	33	47	22	18	13	55	25

guns and the injection parameters for the four different rings was finished in the 2018 summer shutdown, the top-up injection using the direct BT line was introduced to the user operation for the first time. This top-up injection no longer disturbs those of the other three rings since the injection parameters are switched within the minimum injection period of 40 ms. It has also contributed to reducing the frequency of the re-injection for recovering the sudden drop of the beam lifetime caused by dust trapping and to stabilizing the user operation.

The operation time of the PF-AR in recent years has been much less than the target value of 3,000 hours because its operational cost is twice that of the PF-ring. In order to improve this situation within the limited budget, a test operation with the beam energy reduced from 6.5 GeV to 5 GeV was conducted for one week. The power consumption of the 5-GeV operation is expected

to be around 60% of the 6.5-GeV operation. **Figure 7** shows the SR spectra measured at the sample position of the SR beamline AR-NW10A, whose light source is a bending magnet. The vertical axis indicates the photon flux at the stored current of 50 mA. The flux rapidly decreases in the high-energy region of more than 14 keV and becomes half of that of the 6.5-GeV operation at around 27 keV. However, it exceeds the calculated estimation at all energies. This is because the SR vertical beam size at the optical slit of the beamline decreases with the energy and emittance of the electron beam. Such a decrease in the photon flux in the high-energy region can be compensated by increasing the stored current, extending the measurement time, or using higher order SRs. In FY2019, however, we plan to conduct the 6.5-GeV operation at a set ratio since some SR beamlines need high-energy X-rays of 50 keV or more.

Total down time: 26.4 hours

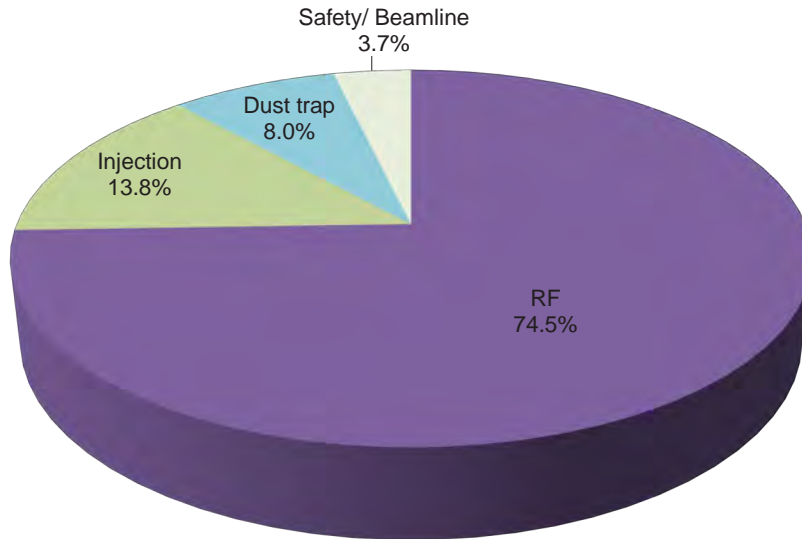


Figure 6: Pie chart of down time for PF-AR in FY2018.

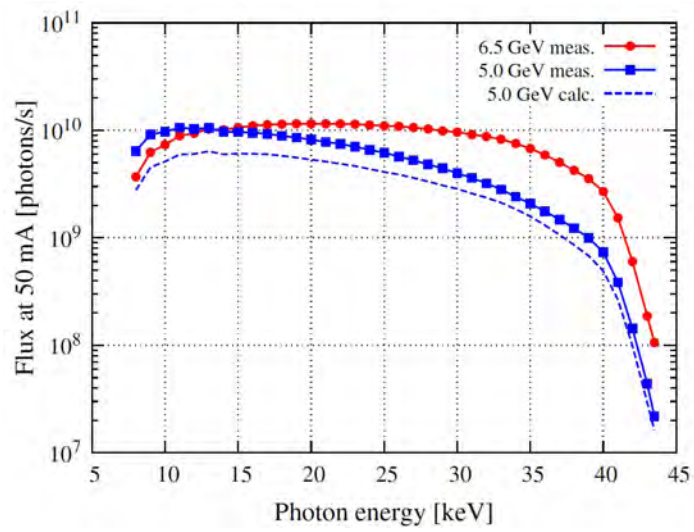


Figure 7: Comparison of SR spectra at AR-NW10A between the 6.5-GeV and 5-GeV operations. The dashed line shows the calculated

3. Experimental Stations

Fifty-three experimental stations are in operation at the PF ring, PF-AR and slow positron facility (SPF), as shown in **Figs. 8, 9** and **10**. Thirty-seven stations are dedicated to research using hard X-rays, 12 stations

for studies in the VUV and soft X-ray energy regions, and 4 stations for studies using slow positrons. **Tables 7, 8** and **9** summarize the areas of research being carried out at the experimental stations at the PF ring, PF-AR and SPF.

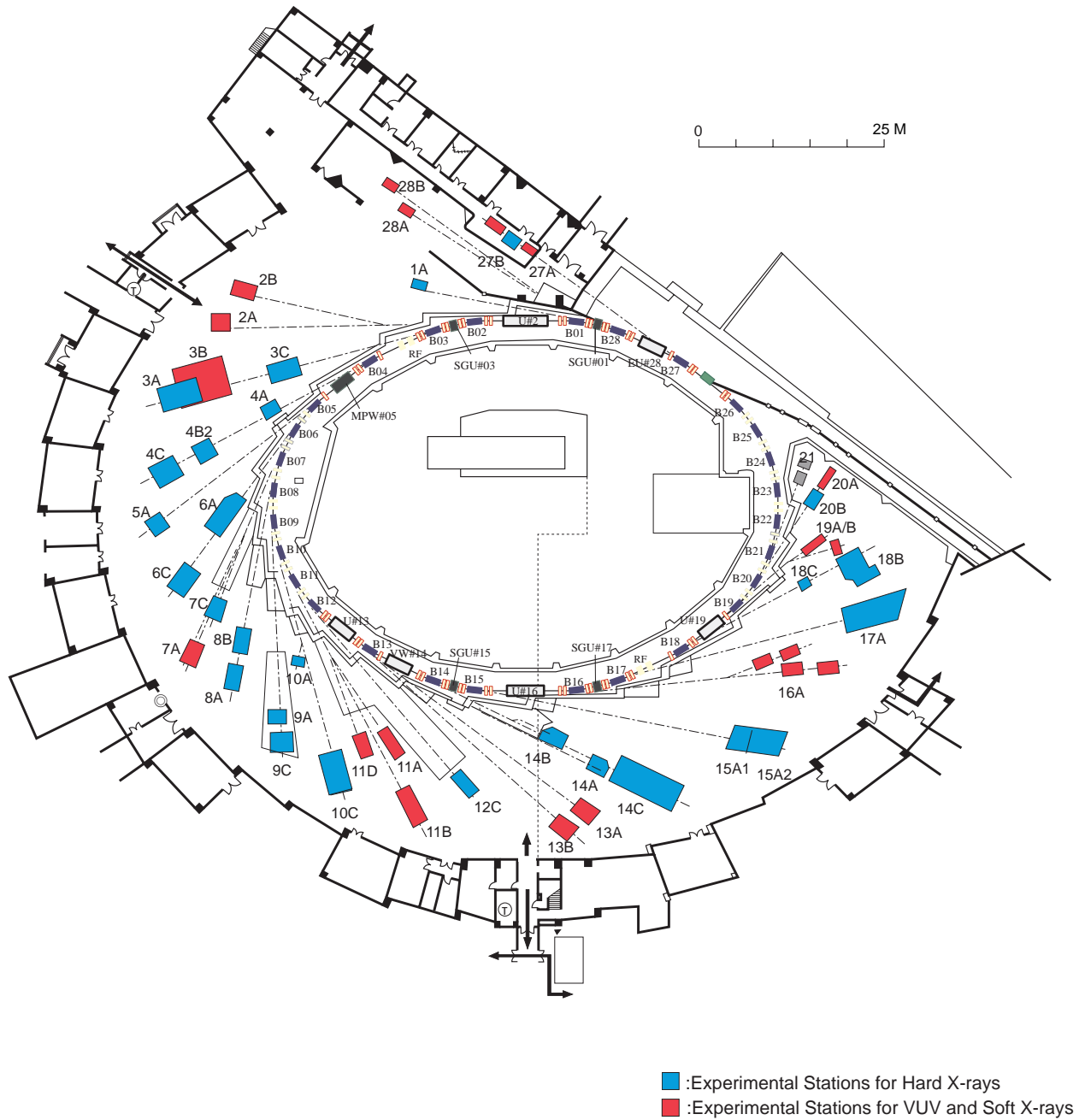


Figure 8: Plan view of the PF experimental hall, showing hard X-ray experimental stations (blue), and VUV and soft X-ray experimental stations (red).

Table 7: List of the experimental stations available for users at the PF ring.

Experimental Station		Person in Charge
BL-1 A	(Short Gap Undulator) Macromolecular crystallography	N. Matsugaki
BL-2 A B	(Variable Polarization Undulator for VUV and planer undulator for SX) High-resolution VUV-SX beamline for angle-resolved photoemission spectroscopy High-resolution VUV-SX spectroscopies	K. Horiba K. Horiba
BL-3 A B C	(A: Short Gap Undulator) X-ray diffraction for material structural science VUV and soft X-ray spectroscopy (♠) Characterization of X-ray optical elements/White X-ray magnetic diffraction	H. Nakao K. Edamoto [Rikkyo Univ.], J. Yoshinobu [The Univ. of Tokyo], K. Mase K. Hirano
BL-4 A B2 C	Trace element analysis, X-ray microprobe (♠) High resolution powder diffraction (♠) X-ray diffraction for material structural science	Y. Takahashi [The Univ. of Tokyo], M. Kimura, Y. Niwa H. Uekusa [Tokyo Tech.], H. Nakao H. Nakao
BL-5 A	(Multipole Wiggler) Macromolecular crystallography	N. Matsugaki
BL-6 A C	Small-angle X-ray scattering X-ray diffraction and spectroscopy (♠)	N. Igarashi N. Happo [Hiroshima City Univ.], H. Nakao
BL-7 A C	Soft X-ray spectroscopy (◆) X-ray spectroscopy and diffraction	J. Okabayashi [RCS, The Univ. of Tokyo], K. Amemiya H. Sugiyama
BL-8 A B	Weissenberg camera for powder/Single-crystal measurements under extreme conditions Weissenberg camera for powder/Single-crystal measurements under extreme conditions	H. Sagayama H. Sagayama
BL-9 A C	XAFS XAFS	H. Abe H. Abe
BL-10 A C	X-ray diffraction and scattering (♠) Small-angle X-ray Scattering	A. Yoshiasa [Kumamoto Univ.], R. Kumai N. Shimizu
BL-11 A B D	Soft X-ray spectroscopy Soft X-ray spectroscopy Characterization of optical elements used in the VSX region	Y. Kitajima Y. Kitajima K. Mase
BL-12 C	XAFS	H. Nitani

Experimental Station		Person in Charge
BL-13 A/B	(Variable Polarization Undulator) VUV and soft X-ray spectroscopies with circular and linear polarization	K. Mase
BL-14 A B C	(Vertical Wiggler) Crystal structure analysis and detector development High-precision X-ray optics Medical applications and general purpose (X-ray)	S. Kishimoto K. Hirano K. Hyodo
BL-15 A1 A2	(Short Gap Undulator) Semi-microbeam XAFS High brilliance small-angle X-ray scattering	Y. Takeichi N. Shimizu
BL-16 A	(Variable Polarization Undulator) Soft X-ray spectroscopies with circular and linear polarization	K. Amemiya
BL-17 A	(Short Gap Undulator) Macromolecular crystallography	Y. Yamada
BL-18 B C	Multipurpose monochromatic hard X-ray station (◆) High pressure X-ray powder diffraction (DAC) (♠)	G. Das [JNCASR], R. Kumai H. Kagi [The Univ. of Tokyo], N. Funamori
BL-19 A/B	(Variable Polarization Undulator) Soft X-ray microscopy and spectroscopy (under commissioning)	K. Ono
BL-20 A B	VUV spectroscopy (◇) White & monochromatic X-ray topography and X-ray diffraction experiment	N. Kouchi [Tokyo Tech], J. Adachi H. Sugiyama
BL-27 A B	(Beamline for radioactive samples) Radiation biology, soft X-ray photoelectron spectroscopy Radiation biology, XAFS	N. Usami N. Usami
BL-28 A B	(Variable Polarization Undulator) High-resolution angle-resolved photoemission spectroscopy with circular and linear polarization High-resolution VUV spectroscopies with circular and linear polarization	K. Horiba K. Horiba

- ♠ User group operated beamline
◆ External beamline
◇ Operated by University

RCS: Research Center for Spectrochemistry, the University of Tokyo
JNCASR: Jawaharlal Nehru Centre for Advanced Scientific Research

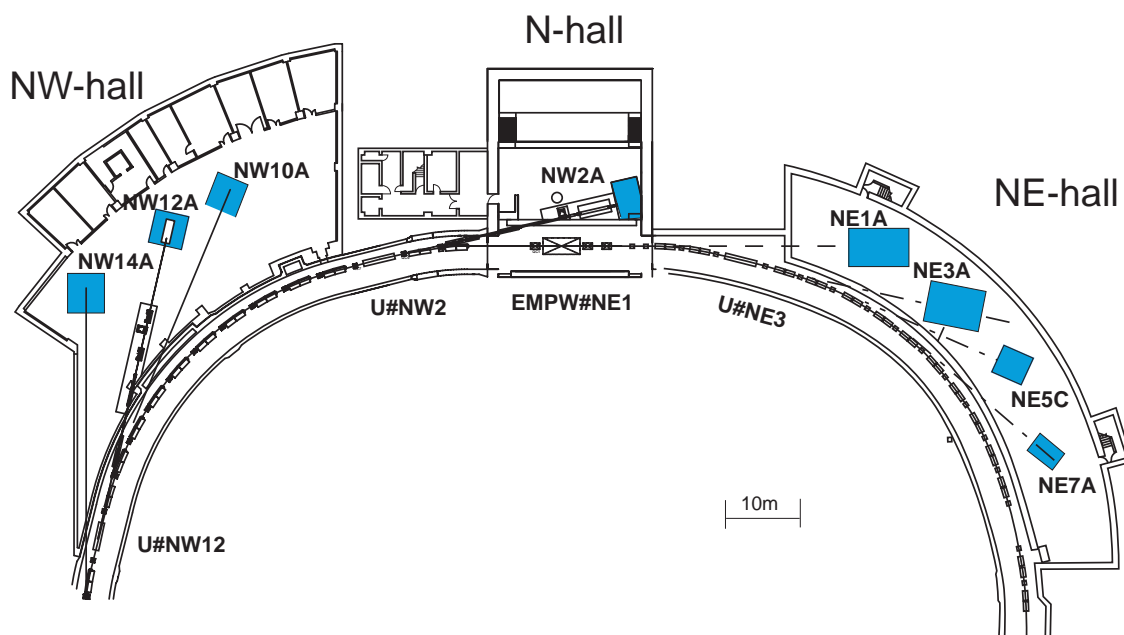


Figure 9: Plan view of the beamlines in the PF-AR north-east, north, and north-west experimental halls.

Table 8: List of the experimental stations at the PF-AR.

Experimental Station		Person in Charge
AR-NE1	(Multipole Wiggler)	
A	Laser-heating high pressure X-ray diffraction and nuclear resonant scattering (DAC)	N. Funamori
AR-NE3	(In-vacuum Undulator)	
A	Macromolecular crystallography	Y. Yamada
AR-NE5		
C	High pressure and high temperature X-ray diffraction (MAX-80)	N. Funamori
AR-NE7		
A	High pressure and high temperature X-ray diffraction (MAX-III) (♥), X-ray imaging	K. Hyodo, A. Suzuki [Tohoku Univ.]
AR-NW2	(In-vacuum Type Tapered Undulator)	
A	Time-resolved Dispersive XAFS/XAFS/X-ray Diffraction	Y. Niwa
AR-NW10		
A	XAFS	H. Nitani
AR-NW12	(In-vacuum Type Tapered Undulator)	
A	Macromolecular crystallography	M. Hikita
AR-NW14	(In-vacuum Undulator)	
A	Time-resolved X-ray diffraction, scattering and absorption	S. Nozawa

♥ User group operated experimental equipment

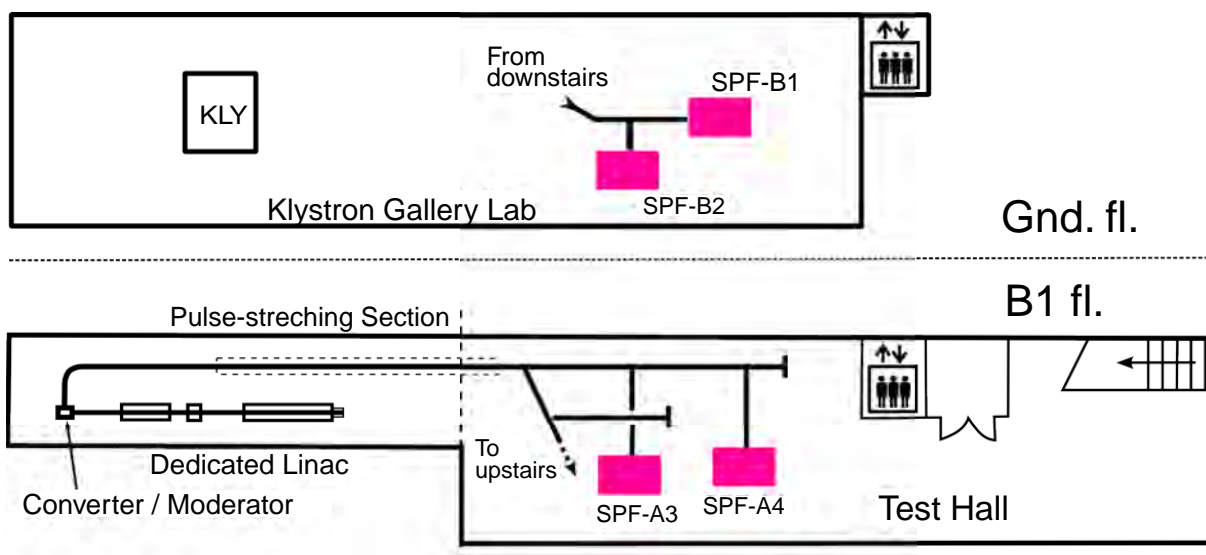


Figure 10: View of the beamlines in the Slow Positron Facility.

Table 9: List of the experimental stations in the Slow Positron Facility.

Experimental Station		Person in Charge
SPF-A3	Total-reflection high-energy positron diffraction	I. Mochizuki
SPF-A4	Low-energy positron diffraction	I. Mochizuki
SPF-B1	General purpose (Positronium laser cooling)	I. Mochizuki
SPF-B2	Positronium time-of-flight	I. Mochizuki

4. Summary of User Proposals

The Photon Factory accepts experimental proposals submitted by researchers mainly at universities and research institutes inside and outside Japan. The PF Program Advisory Committee (PF-PAC) reviews the proposals, and the Advisory Committee for the Institute of Materials Structure Science approves those that are favorably recommended. The number of accepted proposals over the period 2007–2018 is shown in Table 10, where S1/S2, U, G, P, and MP denote Special, Urgent, General, Preliminary, and Multi-Probe proposals, respectively. Category T is a proposal for supporting researches by PhD students. Category MP is a proposal in which at least two of the four beams, synchrotron radiation at the PF, slow positron beam at the Slow Positron Facility, and neutron and muon beams at the Materials and Life Science Experimental Facility (MLF) in J-PARC, are required to be used, as a multi-probe experiment.

Category C is a proposal for collaboration between

KEK and a research institute including a private company. Category I is a non-proprietary proposal for the integrated promotion of social system reform and research and development, supported by the Ministry of Education, Culture, Sports, Science and Technology (from 2009 to 2015). Category V is a non-proprietary grant-aided proposal that has already been reviewed and approved for a research grant; beam time for proposals in this category is allocated with high priority, and applicants are required to pay the regulation fees for the beam time. Category Y is a proprietary proposal; applicants are required to pay the regulation fees for the beam time. The number of current G-type proposals each year has exceeded 700 for the past few years. In addition to these proposals, 32 projects in the BINDS program (Basis for Supporting Innovative Drug Discovery and Life Science Research) were performed at the PF in FY2018. A full list of the proposals effective in FY2018 and their scientific output can be found in the Photon Factory Activity Report (<https://www2.kek.jp/imss/pf/science/publ/acrpubl.html>).

Table 10: Number of proposals accepted for the period 2007–2018.

category	FY-2007	2008	2009	2010	2011	2012	2013	2014	2015	2016	2017	2018
S1	0	0	0	0	0	0	0	0	0	0	0	1
S2	1	4	6	3	2	4	5	4	7	6	1	6
U	7	3	2	2	0	4	1	0	1	0	0	0
G	403	402	397	407	415	454	447	407	361	372	392	321
P	14	14	14	16	11	18	18	5	16	10	16	16
T								6	4	3	3	2
MP									3	0	0	1
C	24	18	12	15	19	20	20	25	24	19	21	21
I			9	17	13	17	13	16	11	-	-	-
V						1	2	2	2	4	4	10
Y	23	22	29	31	30	30	41	22	33	39	30	39

S-type proposals consist of two categories, S1 and S2. S1 proposals are self-contained projects of excellent scientific quality, and include projects such as the construction and improvement of beamlines and experimental stations which will be available for general users after the completion of the project. S2 proposals are superior-grade projects that require the full use of synchrotron radiation or long-term beam time. Proposals are categorized into five scientific disciplines, and reviewed by the five subcommittees of PF-PAC: 1) electronic structure, 2) structural science, 3) chemistry and materials, 4) life science I (protein crystallography), and 5) life science II (including soft matter science). **Figure 11** shows the distribution by research field of the proposals accepted by the subcommittees in FY2018.

The number of users for all types of proposals is about 3,000. About 20% of the proposals are conducted by new spokespersons, indicating that the Photon Factory is open to public academic users. **Figure 12** shows the distribution of users by institution and their positions. Over three-quarters of the users belong to universities. About two-thirds of the university users are graduate and undergraduate students, clearly showing the important role that the Photon Factory plays in both

research and education. The geographical distribution of the Photon Factory users is shown in **Figs. 13** and **14**, which also indicates the immense contribution of the Photon Factory to research and education throughout Japan. The registered number of papers published in 2018 based on experiments at the PF was 554 at the time of writing (July 1, 2019). In addition, 58 doctoral and 221 master theses have been presented.

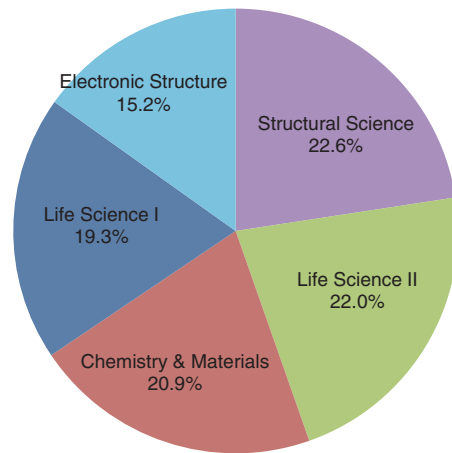


Figure 11: Distribution by scientific field of experimental proposals accepted in FY2018.

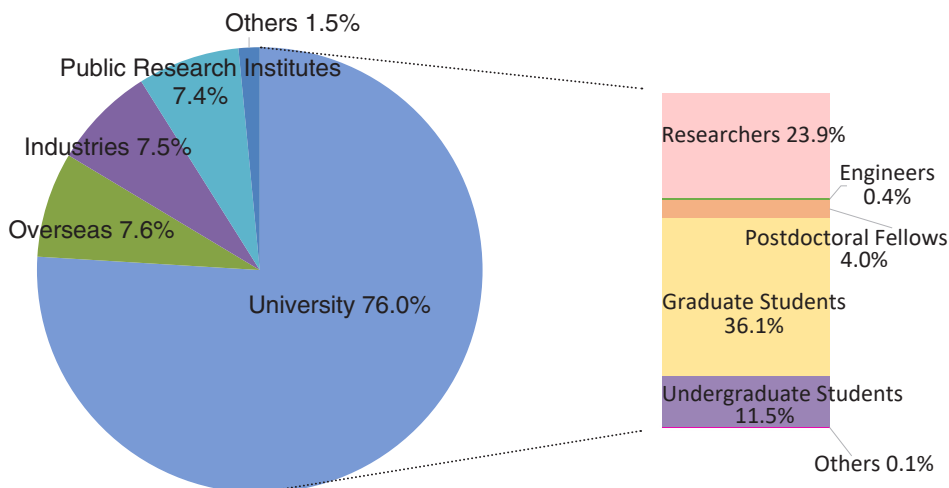


Figure 12: Distribution of users by institution and position.

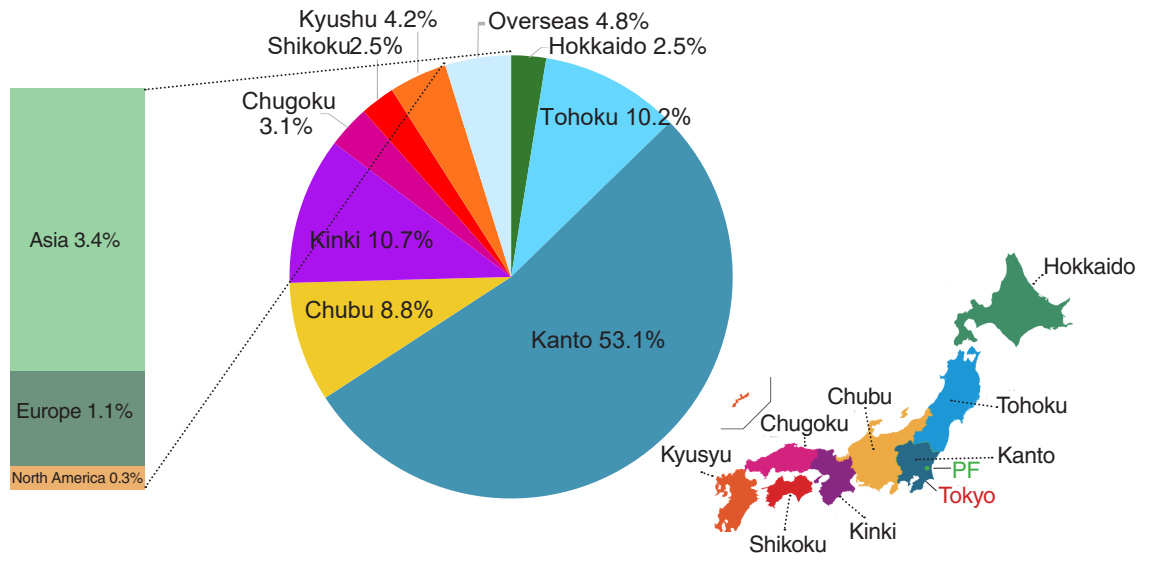


Figure 13: Regional distribution of spokespersons of proposals accepted in FY2018.

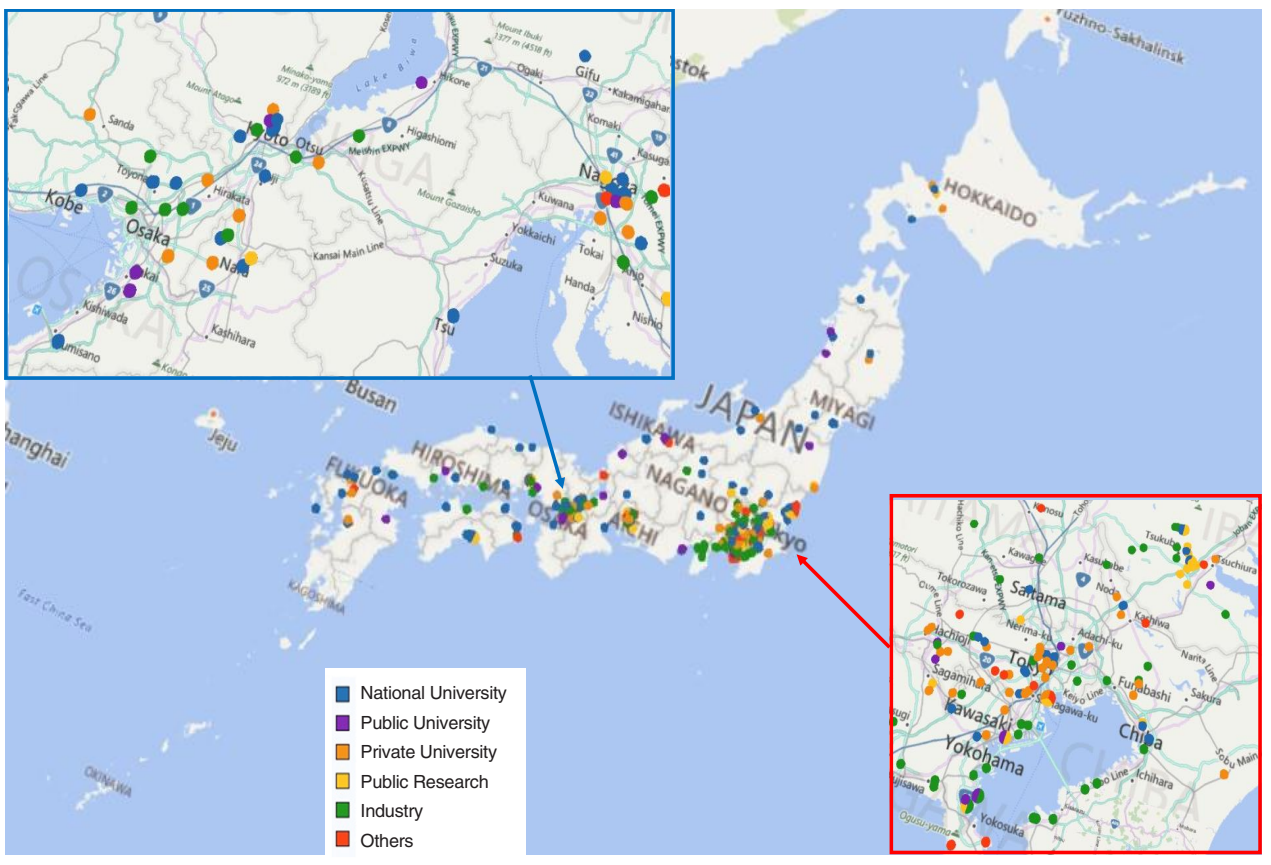
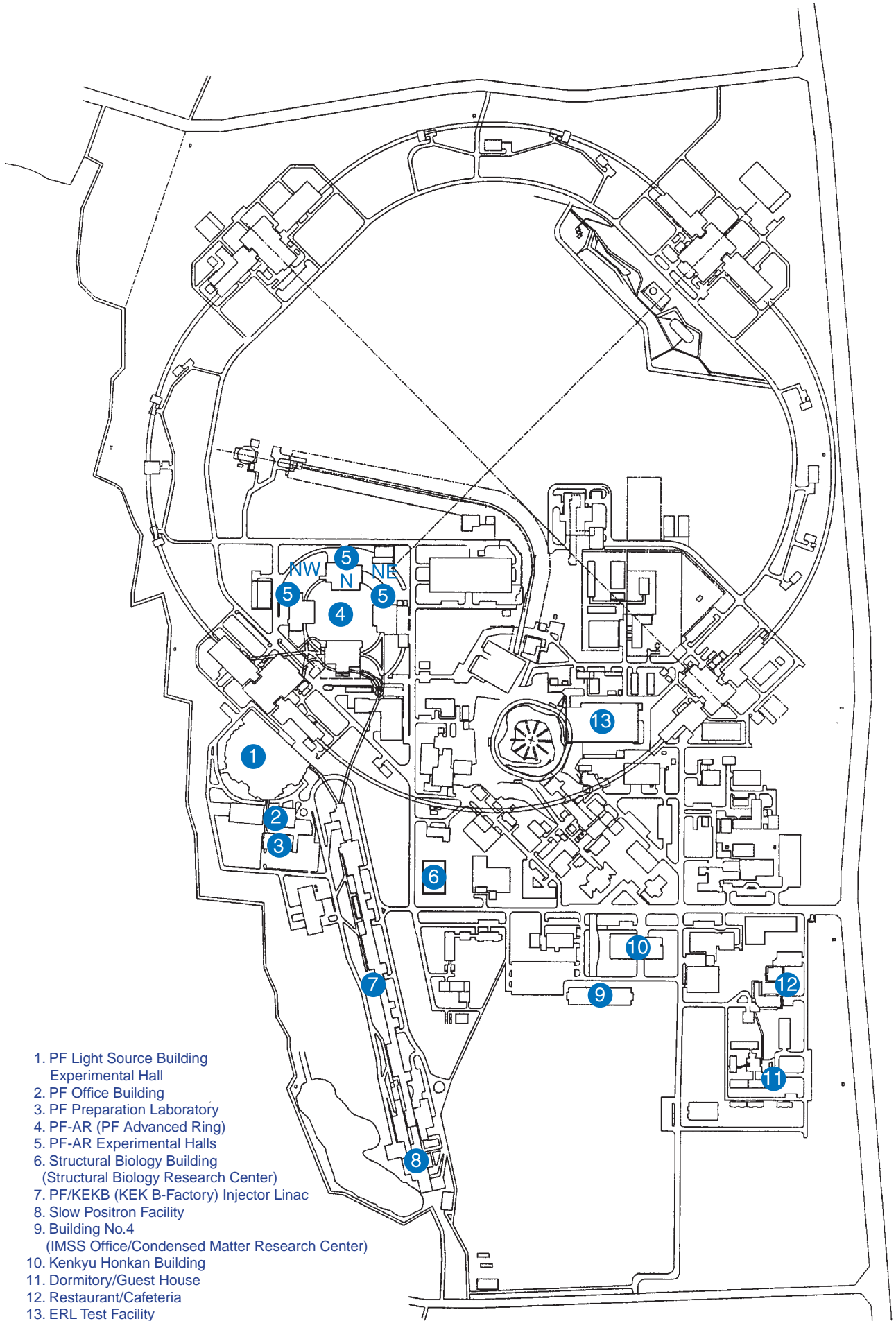


Figure 14: Geographical distribution of Photon Factory users in FY2018 (domestic users only).

APPENDICES

Site and Organization





- 1. PF Light Source Building
Experimental Hall
- 2. PF Office Building
- 3. PF Preparation Laboratory
- 4. PF-AR (PF Advanced Ring)
- 5. PF-AR Experimental Halls
- 6. Structural Biology Building
(Structural Biology Research Center)
- 7. PF/KEKB (KEK B-Factor) Injector Linac
- 8. Slow Positron Facility
- 9. Building No.4
(IMSS Office/Condensed Matter Research Center)
- 10. Kenkyu Honkan Building
- 11. Dormitory/Guest House
- 12. Restaurant/Cafeteria
- 13. ERL Test Facility

KEK consists of four research institutions, i.e., the Institute of Materials Structure Science (IMSS), the Institute of Particle and Nuclear Studies (IPNS), the Accelerator Laboratory (AL), and the Applied Research Laboratory (ARL). As shown in **Fig. 1**, the IMSS con-

stitutes the Synchrotron Radiation Science Divisions I and II, the Neutron Science Division, the Muon Science Division, the Structural Biology Research Center, the Condensed Matter Research Center and IMSS Instrument R&D Team.

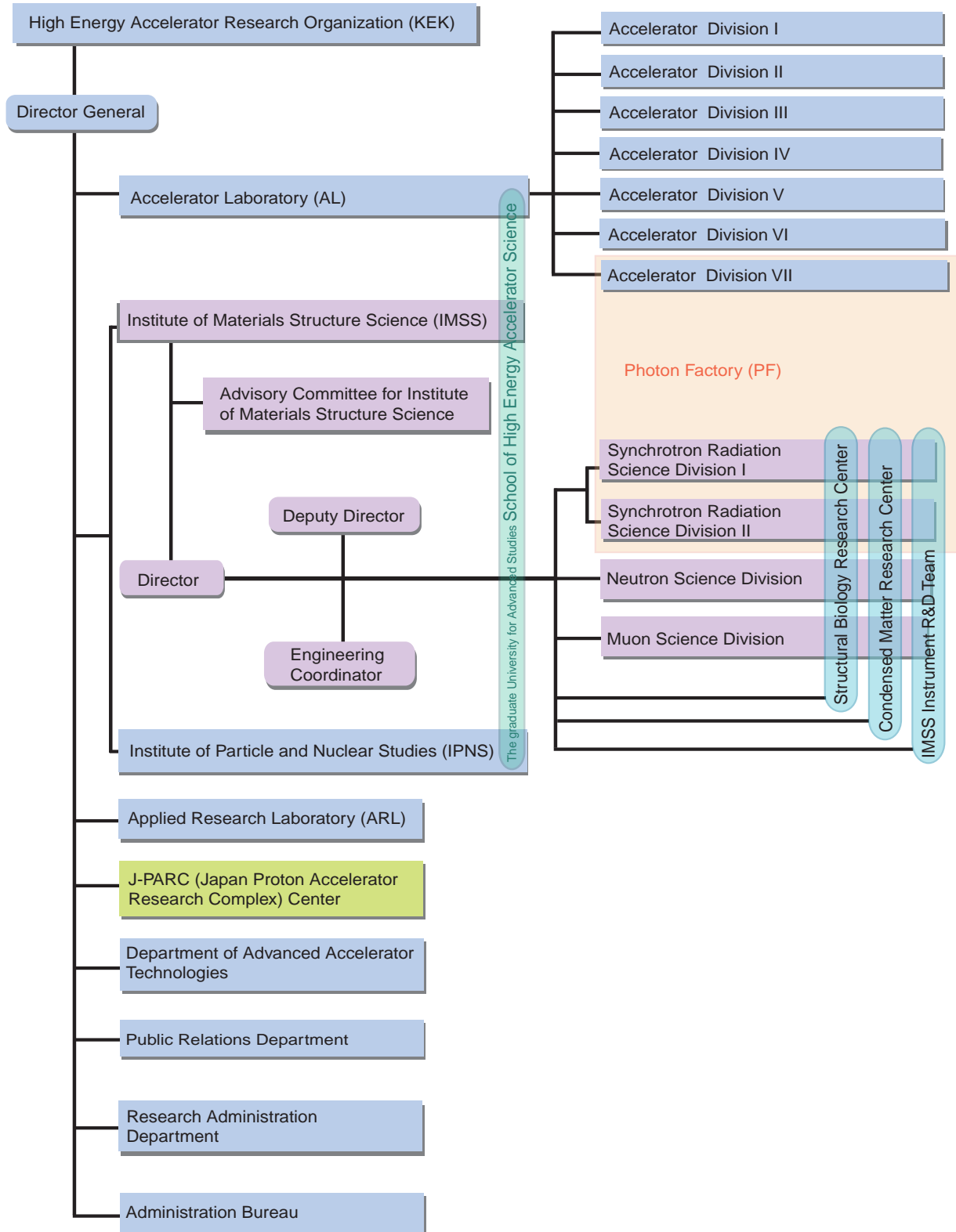


Figure 1: Organization chart of KEK.

Photon Factory (PF) consists of two divisions of the IMSS (the Synchrotron Radiation Science Divisions I and II) and the Accelerator Division VII of the AL as shown in the organization chart of Fig. 2. The staff members of the PF are listed in Table 1. Synchrotron Radiation Science Divisions I and II consist of five beamline groups (electronic structure group, condensed matter group, materials chemistry group, life sciences group and slow positron group), four engineering and

administration groups (beamline engineering & technical services group, safety group, user support & dissemination group and industrial application research group) and two working groups (ultrafast dynamics group and advanced detector R&D group). The Accelerator Division VII has seven groups, which are named Light Source Group I to VII. The missions of each group are described in parentheses of Fig. 2.

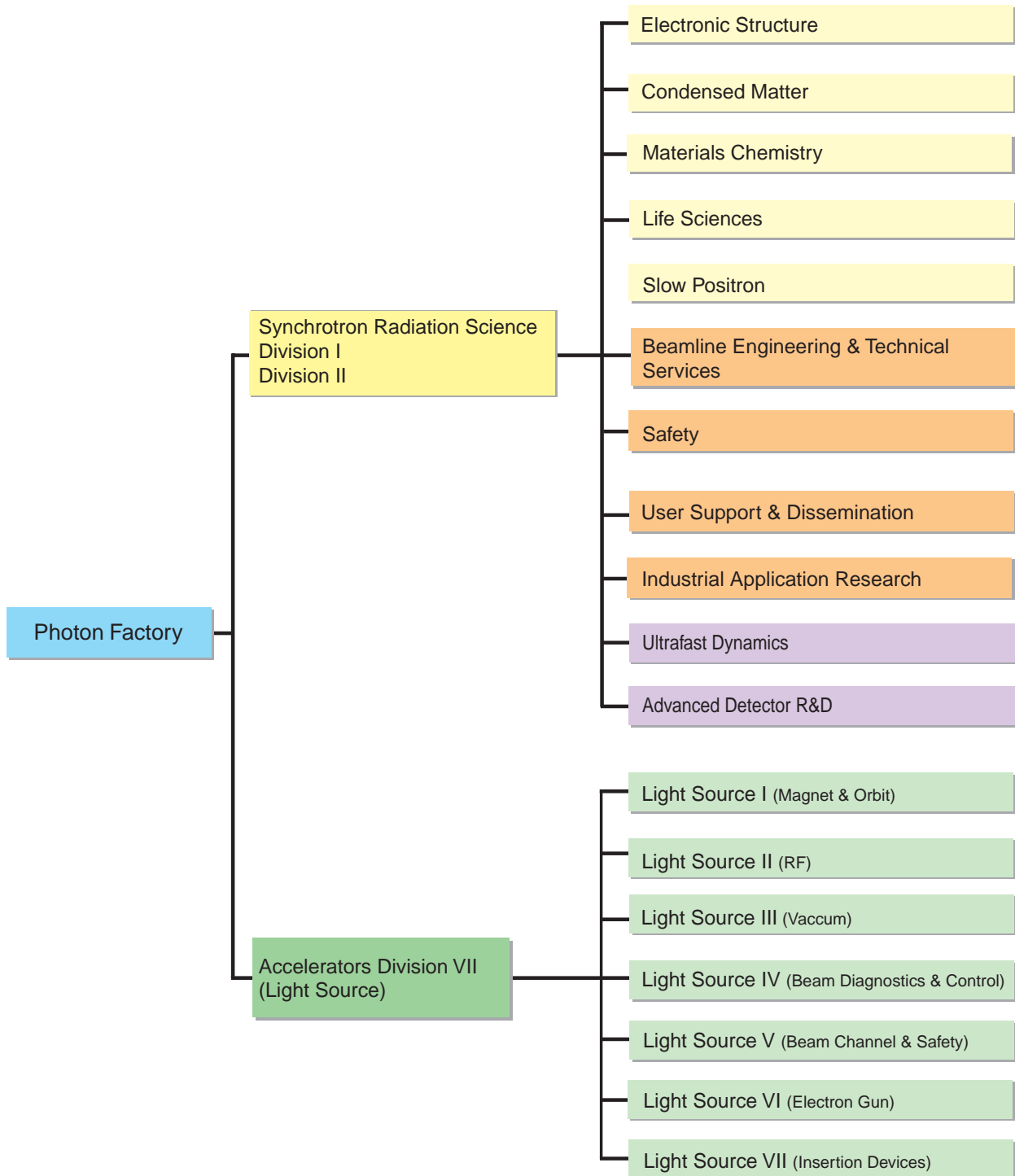


Figure 2: Organization chart of PF (as of March 31, 2019) .

Table 1: Staff members of the Photon Factory.

Group	Name	*Position Title	**Additional Group	Remarks
Research Staff				
IMSS Director	KOSUGI, Nobuhiro	P		
IMSS Deputy Director	ADACHI, Shin-ichi	P		
Synchrotron Radiation Science Division I & II				
Electronic Structure Group				
◎	KUMIGASHIRA, Hiroshi	P		
○	HORIBA, Koji	AP		
	AMEMIYA, Kenta	P	BETS · UD · AD	
	MASE, Kazuhiko	AP		
	ONO, Kanta	AP	AD	
	HAWAI, Takafumi	ASP		
	SAKAMAKI, Masako	ASP	AD	~Sep. 30, 2018
	SHIMADA, Hiroyuki	ASP		
	YUKAWA, Ryu	ASP		
	KITAMURA, Miho	PD		
	OBATA, Yukiko	PD		
	TSUKAHARA, Hiroshi	R		
	SHIGA, Daisuke	RA		
	(KITAJIMA, Yoshinori, ADACHI, Jun-ichi)			
Condensed Matter Group				
◎	KUMAI, Reiji	P	AD	
○	NAKAO, Hironori	AP	UD	
	ADACHI, Shin-ichi	P	UD · AD	
	FUNAMORI, Nobumasa	P		
	KISHIMOTO, Shunji	P	UD	
	MURAKAMI, Youichi	P		
	HIRANO, Keiichi	AP		
	IWANO, Kaoru	AP		
	NOZAWA, Shunsuke	AP	S · UD	
	SAGAYAMA, Hajime	AP		
	FUKAYA, Ryo	ASP		
	FUKUMOTO, Keiki	ASP		
	HARUKI, Rie	R	AD	
	HASHIMOTO, Ryo	ASP		
	TABATA, Chihiro	R		~Oct. 31, 2018
	TAMATSUKURI, Hiromu	R		
	YAMAGUCHI, Tokitake	R		
	KIYEGAWA, Takumi			
	(SUGIYAMA, Hiroshi)	SF		
Materials Chemistry Group				
◎	KIMURA, Masao	P	IAR	
○	ABE, Hitoshi	AP		
	NITANI, Hiroaki	ASP	BETS · S	
	TAKEICHI, Yasuo	ASP	AD	
	NIWA, Yasuhiro	E	BETS · S · UD	
	WATANABE, Toshiki	R		
	(KIMIJIMA, Ken'ichi)			
Life Sciences Group				
◎	SENDA, Toshiya	P		
○	MATSUGAKI, Naohiro	AP	S	
	KATO, Ryuichi	AP	S	
	KAWASAKI, Masato	AP		
	MORIYA, Toshio	AP		
	SHIMIZU, Nobutaka	AP	BETS · S	Sep. 1, 2018~
	TANABE, Mikio	AP		
	YUMOTO, Fumiaki	AP		
	ADACHI, Naruhiko	ASP		
	HIKITA, Masahide	ASP		

Group	Name	*Position Title	**Additional Group	Remarks
	SENDA, Miki	ASP		
	YAMADA, Yusuke	ASP	S	
	TAKAGI, Hideaki	ASP		
	SHINODA, Akira	PD		
	TOMITA, Shougo	PD		~Jun. 30, 2018
	GIANNOPOULOU, Evdokia	R		
	Anastasia	R		
	HARADA, Ayaka	R		
	KOBAYASHI, Jun	R		Aug. 16, 2018~
	KOIWAI, Koutaro	R		
	KUWABARA, Naoyuki	R		~Jun. 30, 2018
	MILLER, Simon	R		~Dec. 31, 2018
	NAGASE, Lisa	R		
	OHARA, Maki	R		
	YONEZAWA, Kento	R		
	YOSHIDA, Hisashi	R		~Sep. 30, 2018
	<i>(IGARASHI, Noriyuki, HYODO, Kazuyuki, USAMI, Noriko)</i>			
Slow Positron Group				
	◎ NAGAI, Yasuyoshi	P		
	○ HYODO, Toshio	DF		
	MOCHIZUKI, Izumi	ASP	S	
Beamline Engineering & Technical Service Group				
	◎ IGARASHI, Noriyuki	AP	LS · S · AD	
	○ KOYAMA, Atsushi	SE	S	
	SUGIYAMA, Hiroshi	ASP	CM · S	
	WAKABAYASHI, Daisuke	ASP		
	YAMASHITA, Shohei	ASP		
	MORI, Takeharu	EE	S	
	TOYOSHIMA, Akio	EE	S · UD	
	UCHIDA, Yoshinori	EE	S	
	KIKUCHI, Takashi	E	S · UD	
	SAITO, Yuuki	E	S	
	TANAKA, Hirokazu	E	S · UD	
	MATSUOKA, Ai	AE	S	
	ISHII, Haruno	TA	S	
	NAGATANI, Yasuko	TS		
	SUZUKI, Yoshio	R		
	<i>(AMEMIYA, Kenta, SHIMIZU, Nobutaka, KITAJIMA, Yoshinori, NITANI, Hiroaki, KOSUGE, Takashi, NIWA, Yasuhiro)</i>			
Safety Group				
	◎ KITAJIMA, Yoshinori	AP	ES · BETS	
	○ KOSUGE, Takashi	SE	BETS · UD · AD	
	<i>(ADACHI, Jun-ichi, IGARASHI, Noriyuki, KATO, Ryuichi, MATSUGAKI, Naohiro, NOZAWA, Shunsuke, SHIMIZU, Nobutaka, NITANI, Hiroaki, SUGIYAMA, Hiroshi, YAMADA, Yusuke, MOCHIZUKI, Izumi, KOYAMA, Atsushi, TOYOSHIMA, Akio, MORI, Takeharu, UCHIDA, Yoshinori, KIKUCHI, Takashi, SAITO, Yuuki, TANAKA, Hirokazu, NIWA, Yasuhiro, MATSUOKA, Ai, ISHII, Haruno)</i>			
User Support & Dissemination Group				
	◎ HYODO, Kazuyuki	AP	LS	
	○ BAN, Hiroshi	ScF	IAR	
	USAMI, Noriko	AP	LS	
	OHSHIMA, Hiroko	TS		
Industrial Application Research Group				
	◎ KIMURA, Masao	P	MC	
	○ BAN, Hiroshi	ScF	USD	
	KIMIJIMA, Ken'ichi	AP	MC	
Ultrafast Dynamics Working Group				
	◎ ADACHI, Jun-ichi	AP	ES · S	

Group	Name	*Position Title	**Additional Group	Remarks
	YAMAMOTO, Shigeru	P		
	MASUDA, Shinichi	R		
	(ADACHI, Shin-ichi, AMEMIYA, Kenta, KISHIMOTO, Shunji, NAKAO, Hironori, NOZAWA, Shunsuke, KOSUGE, Takashi, TOYOSHIMA, Akio, KIKUCHI, Takashi, NIWA, Yasuhiro, TANAKA, Hirokazu)			
	Advanced Detector R&D Working Group			
	◎ KISHIMOTO, Shunji	P	CM · UD	
	(ADACHI, Shin-ichi, KUMAI, Reiji, AMEMIYA, Kenta, ONO, Kanta, IGARASHI, Noriyuki, TAKEICHI, Yasuo, SAKAMAKI, Masako, HARUKI, Rie, KOSUGE, Takashi)			
Accelerator Division VII				
	Light Source I			
	◎ NAKAMURA, Norio	P		
	KOBAYASHI, Yukinori	P		
	HARADA, Kentaro	AP		
	MITSUDA, Chikaori	AP		
	OZAKI, Toshiyuki	SF		
	SHIMADA, Miho	AP		
	SHIMOSAKI, Yoshito	AP		
	TAKAKI, Hiroyuki	AP		
	UEDA, Akira	EE		
	NAGAHASHI, Shinya	E		
	TANAKA, Olga	ASP		
	HIGASHI, Nao	ASP		
	Light Source II			
	◎ SAKANAKA, Shogo	P		
	YAMAMOTO, Naoto	ASP		
	TAKAHASHI, Takeshi	EE		
	Light Source III			
	◎ HONDA, Tohru	P		
	TANIMOTO, Yasunori	AP		
	JIN, Xiuguang	ASP		
	SASAKI, Hiroyuki	ASP		
	YAMAMOTO, Masahiro	ASP		
	UCHIYAMA, Takashi	E		
	NOGAMI, Takashi	E		
	ASAOKA, Seiji	SF		
	Light Source IV			
	◎ OBINA, Takashi	P		
	TAKAI, Ryota	AP		
	TADANO, Mikito	SE		
	SAGEHASHI, Hidenori	E		
	Light Source V			
	◎ MIYAUCHI, Hiroshi	AP		
	HAGA, Kaiichi	AP		
	NIGORIKAWA, Kazuyuki	EE		
	SATO, Yoshihiro	E		
	TAHARA, Toshihiro	E		
	Light Source VI			
	◎ KATO, Ryukou	P		
	HONDA, Yosuke	ASP		
	Light Source VII			
	◎ TSUCHIYA, Kimichika	AP		
	ADACHI, Masahiro	ASP		
	EGUCHI, Shu	TA		
	SHIOYA, Tatsuro	SF		

Name	(Affiliation)	Remarks
Visiting Professor		
ASAKURA, Kiyotaka	(Hokkaido Univ.)	
KAMIKUBO, Hironari	(Nara Inst. of Science & Tech.)	
KONDO, Hiroshi	(Keio Univ.)	
KOSHIHARA, Shinya	(Tokyo Tech)	
MORITOMO, Yutaka	(Univ. of Tsukuba)	
NAGASHIMA, Yasuyuki	(Tokyo Univ. of Science)	
OHKUMA, Haruo	(Osaka Univ.)	
OKUBO, Masataka	(AIST)	
SAKASHITA, Hitoshi	(AIST)	
TAKAHASHI, Yoshio	(The Univ. of Tokyo)	
YAO, Min	(Hokkaido Univ.)	
Visiting Associate Professor		
NIWA, Ryusuke	(Univ. of Tsukuba)	
The Graduate University for Advanced Studies (SOKENDAI)		
AIZAWA, Kyohei		
FURIHATA, Hirotake		
HARANO, Takayuki		
KAMEZAWA, Chika		
KONOSHITA, Aya		
MIKI, Hiromi		
MIYAZAWA, Tetusya		
YAMAGUCHI, Takaaki		
YU, Hong Yang		

◎ Group Leader ○ Sub Group Leader

*Position Title

P	Professor	SE	Senior Engineer
AP	Associate Professor	EE	Expert Engineer
ASP	Assistant Professor	E	Engineer
PD	Postdoctoral Fellow	AE	Associate Engineer
R	Researcher	TA	Technical Associate
SF	Senior Fellow	TS	Technical Specialist
ScF	Scientific Fellow	DF	Diamond Fellow
RA	Research Assistant		

**Synchrotron Radiation Science Division (*Italic: additional posts*)

ES	Electronic Structure
CM	Condensed Matter
MC	Materials Chemistry
LS	Life Sciences
SP	Slow Positron
BETS	Beamline Engineering & Technical Services
S	Safty
USD	User Support and Dissemination
IAR	Industrial Application Research
UD	Ultrafast Dynamics
AD	Advanced Detector R&D

Member Photo



1 KUMIGASHIRA, Hiroshi	45 UNJOH, Atsuko	88 HIRANO, Keiichi
2 KIMURA, Masao	46 TANAKA, Olga	89 MIYAUCHI, Hiroshi
3 NOMURA, Masaharu	47 FURIHATA, Hirotake	90 HONDA, Tohru
4 NAGAI, Yasuyoshi	48 KATO, Ryuichi	91 IKEDA, Kiyoshi
5 SENDA, Toshiya	49 YAMASHITA, Shohei	92 ADACHI, Masahiro
6 ADACHI, Shin-ichi	50 SHINODA, Akira	93 MASUDA, Shinich
7 KOSUGI, Nobuhiro	51 NAKAO, Hironori	94 ASAOKA, Seiji
8 AMEMIYA, Kenta	52 KAMENASHI, Momoko	95 KIKEGAWA, Takumi
9 KOBAYASHI, Yukinori	53 UENO, Tetsuro	96 HARUKI, Rie
10 FURUKAWA, Kazuro	54 NUMAZAKI, Saori	97 KOYAMA, Atsushi
11 TANABE, Mikio	55 GIANNOPOULOU, Evdokia Anastasia	98 MATSUGAKI, Naohiro
12 INABA, Kazue	56 ZENIYA, Tomoko	99 KATO, Ryukou
13 IWANO, Kaoru	57 OHSHIMA, Hiroko	100 TSUCHIYA, Kimichika
14 KOIWAI, Kotaro	58 HAYASHI, Yoko	101 KUMAI, Reiji
15 MISUMI, Yoko	59 UTSUNO, Emi	102 HASHIMOTO, Ryo
16 NOGAMI, Takashi	60 TOYAMA, Hisako	103 TAHARA, Toshihiro
17 SUZUKI, Yuta	61 TAKAHASHI, Yoshimi	104 HIKITA, Masahide
18 KONOSHITA, Aya	62 UEDA, Akira	105 DAS, Gangadhar
19 SAGAYAMA, Hajime	63 WANG, Kun	106 ADACHI, Naruhiko
20 MATSUMARU, Hiroyuki	64 SHIMADA, Miho	107 MUKHERJEE, Suman
21 KUWABARA, Naoyuki	65 KOBARI, Miyuki	108 BHUNIA, Satyaban
22 MASE, Kazuhiko	66 NAKAJIMA, Mieko	109 FUNAMORI, Nobumasa
23 USAMI, Noriko	67 TANAKA, Makiko	110 TOYOSHIMA, Akio
24 MOCHIZUKI, Izumi	68 SAITO, Akane	111 YONEZAWA, Kento
25 FUKUMOTO, Keiki	69 SASAJIMA, Kumiko	112 BHATTACHARYYA, Arpan
26 YUKAWA, Ryu	70 MASUDA, Chiho	113 KIKUCHI, Takashi
27 TABATA, Chihiro	71 SUKEGAWA, Rieko	114 EGUCHI, Shu
28 YAMAMOTO, Ryosuke	72 NAGATA, Naomi	115 TANIMOTO, Yasunori
29 ISHII, Haruno	73 BAN, Hiroshi	116 UCHIYAMA, Takashi
30 TAMATSUKURI, Hiromu	74 KIKUCHI, Akemi	117 TAKAI, Ryota
31 KOSUGE, Takashi	75 ABE, Hitoshi	118 KITAJIMA, Yoshinori
32 FUKAYA, Ryo	76 HYODO, Toshio	119 HORIBA, Koji
33 NOZAWA, Shunsuke	77 YAMAMOTO, Shigeru	120 MITSUDA, Chikaori
34 YAMADA, Yusuke	78 WATANABE, Toshiki	121 NAKAMURA, Norio
35 KISHIMOTO, Shunji	79 YUMOTO, Fumiaki	122 SAGEHASHI, Hidenori
36 TOMITA, Shogo	80 HARANO, Takayuki	123 MURAKAMI, Youichi
37 YAMASAKI, Tazuko	81 UCHIDA, Yoshinori	124 NIGORIKAWA, Kazuyuki
38 AOKI, Tamie	82 NITANI, Hiroaki	125 OBINA, Takashi
39 MIKI, Hiromi	83 TAKAHASHI, Masatsuyo	126 ADACHI, Junichi
40 OHARA, Maki	84 KOIDE, Tsuneharu	127 IGARASHI, Noriyuki
41 IGARASHI, Miho	85 HYODO, Kazuyuki	128 KAMEZAWA, Chika
42 HORI, Akiko	86 KIMIJIMA, Ken'ichi	129 MORI, Takeharu
43 SENDA, Miki	87 OHNO, Masaki	130 HARADA, Kentaro

Editorial Note

Editorial Board

Masahide Hikita, Miho Kitamura, Takashi Kosuge,
Reiji Kumai, Chikaori Mitsuda, Kanta Ono, Hiroyuki Takagi, Shohei Yamashita,
Kaoru Iwano (Editor in Chief)

Editorial, Design & Layout

Yoko Misumi, Tazuko Yamasaki

Cover Design

Hiroko Ohshima

We, the editorial board would like to thank all the users and
the staffs who have contributed to the editing of this "PF Highlights 2018".

Cover Photos

Top: ARPES images observed for anatase TiO₂ (001) surface (Highlight 1-12)
Upper Middle: Structure of horse TLR9 in complex with CpG DNA and 5'-xCx DNA (Highlight 4-3)
Lower Middle: The effect of KDE on 2D (Highlight 5-1)
Bottom: Overview of 5'-xCx DNA binding site. (Highlight 4-3)

Photon Factory

1-1 Oho, Tsukuba, Ibaraki 305-0801 Japan

Institute of Materials Structure Science
High Energy Accelerator Research Organization (KEK)

